Numerical simulation of wave propagation in 3D basin models and their effects on nonlinear structures response

Valeria Paz Soto Moncada

THESE DE DOCTORAT

NNT: 2023UPAST079

université PARIS-SACLAY

Simulation numérique de propagation des ondes dans modèles de bassin et leurs effets sur la réponse des structures non linéaires

Numerical simulation of wave propagation in 3D basin models and their effects on nonlinear structures response

Thèse de doctorat de l'université Paris-Saclay

École doctorale n° 579, sciences mécaniques et énergétiques, matériaux et géosciences (SMEMaG)
Spécialité de doctorat: Génie Civile
Graduate School: Sciences de l'ingénierie et des systèmes
Référent: CentraleSupélec

Thèse préparée dans l'unité de recherche **LMPS - Laboratoire de Mécanique Paris-Saclay (Université Paris-Saclay, CentraleSupélec, ENS Paris-Saclay, CNRS)**, sous la direction de **Fernando Lopez-Caballero**, Professeur

Thèse soutenue à Paris-Saclay, le 23 juin 2023, par

Valeria Paz SOTO MONCADA

Composition du jury

Membres du jury avec voix déliberative

Etienne BERTRAND Directeur de recherche, Université Gustave Eiffel - IFSTTAR	Président
Cécile CORNOU Directrice de recherche, IRD, Université Grenoble Alpes	Rapportrice
Panagiotis KOTRONIS Professeur des universités, Ecole Centrale de Nantes	Rapporteur
Cédric GIRY Maître de conférences, Université Paris-Saclay, ENS	Examinateur
Esteban SÁEZ Associate Professor, Pontificia Universidad Católica de Chile	Examinateur
Irmela ZENTNER Ingénieure de recherche, EDF R&D	Examinatrice

université PARIS-SACLAY

ÉCOLE DOCTORALE
Sciences mécaniques et énergétiques, matériaux et géosciences (SMEMAG)

Titre: Simulation numérique de propagation des ondes dans modèles de bassin et leurs effets sur la réponse des structures non linéaires

Mots clés: effect de bassin, facteurs d'aggravation, ondes des surface, interaction sol-structure, modelisation SEM-FEM

Résumé: Les matériaux contenus dans les bassins sédimentaires modifient les caractéristiques du mouvement du sol (EGM) en cas de séisme par le piégeage d'énergie, la résonance et la génération des ondes de surface en bord du bassin. En général, ces effets sont définis comme des *effets de site* et ils sont pris en compte par des proxys associés à la structure unidimensionnelle (1D). Pour l'évaluation des risques dans le cadre de la méthodologie de Performance Based Earthquake Engineering (PBEE), les effets sont considérés en termes d'une mesure d'intensité (IM). La présence du bassin, i.e., la géométrie tridimensionnelle (3D), peut être approximée par des facteurs d'aggravation ou d'ajustement (AGF). Ce facteur est généralement défini comme le rapport entre les cas 3D et 1D de l'IM calculé avec les composantes horizontales des signaux à partir d'une approche d'incidence d'ondes planes. Cependant, la composante particulière des ondes de surface, décrite par un mouvement du sol plus complexe, est rarement mesurée de manière explicite. Cette complexité provient spécifiquement du fait que les ondes de surface ont un contenu à basse fréquence et incluent à la fois des composantes verticales et rotationnelles.

Ce travail évalue l'impact des effets de bassin, avec un intérêt pour la génération des ondes de surface, sur les dommages sismiques des structures non linéaires. Des simulations numériques sont nécessaires pour introduire le champ d'ondes complexe dans la structure. La méthode de réduction de domaine (DRM) est utilisée ici dans une approche couplée SEM-FEM 3D. Cela permet d'étudier la propagation des ondes depuis la faille jusqu'à la structure. Par conséquent, en suivant la méthodologie PBEE, ce modèle est capable de quantifier et de contraster les effets de bassin couplés simultanément sur l'aléa sismique et la demande structurelle.

Afin de quantifier correctement les ondes de surface générées, une caractérisation basée sur le produit intérieur normalisé (NIP) est validée par rapport à d'autres procédures d'identification. Ensuite, l'évaluation de l'aléa sismique est définie en termes de caractérisation des ondes de surface et des AGF. L'étude est réalisée à partir de modèles sismiques paramétriques, avec des géométries de bassin simplifiées et des propriétés de matériaux homogènes. Deux types de sources sismiques sont simulées : des ondes planes sous incidence verticale et des sources ponctuelles, profondes et superficielles, de type double-couple. L'effet du contraste d'impédance à l'interface sédiments-roche est également évalué. Des simulations de bassin des sites d'Argostoli (île de Céphalonie, Grèce) et de Cadarache (France) sont étudiées afin de s'approcher de scénarios réalistes.

Finalement, l'étape suivante de la méthodologie PBEE, concernant la réponse de la structure, est réalisée avec une structure non-linéaire et un bassin simplifié. La variabilité spatiale est étudiée en plaçant la structure dans différentes positions, ce qui modifie le champ des ondes arrivant à la fondation de la structure. Les résultats sont ensuite comparés à ceux obtenus par les méthodologies traditionnelles afin de vérifier si le modèle entièrement couplé de la faille à la structure augmente la demande structurelle sismique.

université PARIS-SACLAY

ÉCOLE DOCTORALE
Sciences mécaniques et énergétiques, matériaux et géosciences (SMEMAG)

Title: Numerical simulation of wave propagation in 3D basin models and their effects on nonlinear structures response

Keywords: basin effects, aggravation factors, surface waves, soil-structure interaction, SEM-FEM modelling

Abstract: Sedimentary materials enclosed in basins modify the earthquake ground motion (EGM) characteristics by energy trapping, resonance and surface wave generation at the basin edge. Usually, these are defined as *site effects* and are considered by proxies associated with the one-dimensional (1D) structure beneath. In the context of hazard assessment with the Performance-Based Earthquake Engineering (PBEE) methodology, they are considered to modify the EGM in terms of an intensity measure (IM). The effects of the basin presence, i.e., the three-dimensional (3D) geometry, can be further approximated by aggravation or adjustment factors (AGF). This factor is traditionally defined as the ratio between the 3D and 1D cases of the IM computed with the horizontal components of motions using a plane wave approach. However, the particular surface wave part of the ground motion, described with a more complex shaking, is never explicitly measured. This complexity comes specifically from the fact that surface waves are defined by low-frequency content and include both vertical and rotational components.

With this regard, the current work assesses the impact of basin effects, with interest in surface wave generation, on the seismic damage of nonlinear structures. In order to introduce the complex input wavefield into the structure, numerical simulations are needed. In this case, a coupled 3D SEM-FEM approach is used, employing the Domain Reduction Method (DRM). As a result, a complete-time wave propagation analysis from the earthquake source to the structure can be investigated. Therefore, following the PBEE methodology, this model is able to quantify and contrast the coupled basin effects simultaneously on the seismic hazard and structural demand analyses.

As an initial step, in order to quantify the generated surface waves correctly, a characterization based on the normalized inner product (NIP) is validated against other surface-wave-identification procedures. Then, the seismic hazard evaluation here is defined in terms of surface wave characterization and the AGFs. The study is carried out with parametric seismic scenarios, with simplified basin geometries and homogeneous material properties. Two types of seismic sources are simulated: plane waves with vertical incidence and deep and shallow double-couple point sources. In addition, the effect of the impedance contrast at the sediment-bedrock interface is also assessed. Moreover, to approach realistic scenarios, basin simulations of the Argostoli (Kefalonia island, Greece) and Cadarache (France) sites are investigated.

Furthermore, the subsequent step of the PBEE methodology, regarding the structural and damage analyses, is performed using a nonlinear structure and the basin simplified case. The spatial variability is investigated by placing the structure in different positions, hence modifying the ground motion wave field arriving at the structure's foundation. The results are further contrasted with those obtained from traditional methodologies to check if the fully coupled model from the source to the structure increases the seismic structural demand.

“La réalité est là et nous sommes en elle, la comprenant chacun à notre façon mais en elle."

Julio Cortázar, *Marelle*

Acknowledgments

I would like to start this section by thanking my professor, Fernando Lopez-Caballero. You are one of a kind, and I couldn't be more grateful for being your student. Since the beginning, including covid times, I felt supported, and you always had the right words (and ideas) to guide me in this journey. Thank you for pushing me to do things that were out of my comfort zone; those experiences have really contributed to my professional development.

I would like to extend my sincere gratitude to Etienne Bertrand for being the president of my jury. Additionally, I am sincerely grateful to Panagiotis Kotronis and Cécile Cornou for their time and commitment to reviewing this thesis and to the jury members Irmela Zentner, Cédric Giry and Esteban Sáez. The expertise in their own fields of each member of the jury has helped in providing an external perspective into this research, thank you for your valuable feedback and suggestions.

I would like to acknowledge the financial and intellectual support provided by the project MODULATE. I appreciate the valuable insights and discussions from the meetings on the project. I especially want to thank Kristel Meza-Fajardo and Charisis Chatzigogos for the shared information and support.

Additionally, I appreciate the contribution and cooperation during the different parts of my research from Michail Korres, David Castro, Andrea Riaño and Julián Daza. I would also like to say some words to Dyvia Madhavan and Aurélie Thomann. Your course on communication skills for researchers profoundly impacted my life.

Furthermore, I would like to thank my friends and colleagues from the LMPS laboratory: Denis, Faisal, David, Andrea, Christian, Yilun, Amar, Michail, Martin, Christina, Roman, Sara, Filippo, Fanny, Julián, Juan Camilo, Exneyder, Amanda, Kuralay, Mouhammed, Nadine. You have made my time here really special, and I appreciate all the moments we shared together.

Finally, I would like to thank my parents, Andrés and Susana, and grandparents, Mario, Luisa, Humberto and Iris, for their unconditional support, love and for always encouraging my curiosity about the world. All the time and energy you have dedicated, sharing your own countless experiences, have shaped the person I have become, and for that I am immensely grateful. I would also like to thank my little sisters, Camila and Paulina, for all the memories we have created together. I miss you every day and can't wait to be laughing again next to you. To the family I've found in France, Ramon and Watson. Ramon, this accomplishment would not have been possible without your love, encouragement, patience and caring. You were there for me even when I wasn't. You are my biggest support and make me happy every day.

Synthèse en français

Les matériaux contenus dans les bassins sédimentaires modifient les caractéristiques du mouvement du sol (EGM) en cas de séisme par une combination associé au piégeage d'énergie, la résonance et la génération des ondes de surface en bord du bassin.

En général, ces effets sont définis comme des effets de site et ils sont pris en compte par des proxys associés à la structure unidimensionnelle (1D). Pour l'évaluation des risques dans le cadre de la méthodologie de Performance Based Earthquake Engineering (PBEE), les effets sont considérés en termes d'une mesure d'intensité (IM). La présence du bassin, i.e., la géométrie tridimensionnelle (3D), peut être approximée par des facteurs d'aggravation ou d'ajustement (AGF). Ce facteur est généralement défini comme le rapport entre les cas 3D et 1D de l'IM calculé avec les composantes horizontales des signaux à partir d'une approche d'incidence d'ondes planes. Cependant, la composante particulière des ondes de surface, décrite par un mouvement du sol plus complexe, est rarement mesurée de manière explicite. Cette complexité provient spécifiquement du fait que les ondes de surface ont un contenu à basse fréquence et incluent à la fois des composantes verticales et rotationnelles.

Ce travail évalue l'impact des effets de bassin, avec un intérêt pour la génération des ondes de surface, sur les dommages sismiques des structures non linéaires placés. Des simulations numériques sont nécessaires pour introduire le champ d'ondes complexes dans la structure. La méthode de réduction de domaine (DRM) est utilisée ici dans une approche couplée SEM-FEM 3D. Cela permet d'étudier la propagation des ondes en forme directe depuis la faille jusqu'à la structure. Par conséquent, en suivant la méthodologie PBEE, ce modèle est capable de quantifier et de contraster les effets de bassin couplés simultanément sur l'aléa sismique et la demande structurelle.

Afin de quantifier correctement les ondes de surface générées, une caractérisation basée sur le produit intérieur normalisé (NIP, Meza-Fajardo et al., 2016) est validée par rapport à d'autres procédures d'identification proposées par la littérature : Polarisation de 6 composantes (6CPol, Sollberger et al., 2018), et MUSIC/MUSIQUE (Schmidt, 1986; Hobiger, 2011). La méthodologie NIP présent des avantages par rapport aux autres. En effet, son application nécessite des historiques temporels simples à trois composantes, ce qui le rend plus adapté à la quantification de l'effet de bassin sur les ondes de surface.

Ensuite, l'évaluation de l'aléa sismique est définie en termes de caractérisation des ondes de surface et des AGF. L'étude est réalisée à partir de modèles sismiques paramétriques, avec des géométries de bassin simplifiées et des propriétés de matériaux homogènes. Deux types

de sources sismiques sont simulées : des ondes planes sous incidence verticale et des sources ponctuelles, profondes et superficielles, de type double-couple. L'effet du contraste d'impédance à l'interface sédiments-roche est également évalué. Les résultats montrent que la localisation de la source sismique est aussi importante que les propriétés du bassin pour la génération des ondes de surface.

Des simulations de bassin des sites d'Argostoli (île de Céphalonie, Grèce) et de Cadarache (France) sont étudiées afin de s'approcher de scénarios réalistes. Malgré la complexification des mouvements du sol et l'observation de nouveaux phénomènes tels que les effets de champ proche, il est possible de constater que les caractéristiques des ondes de surface suivent les mêmes tendances que dans les cas les plus simples. Les résultats soulignent l'importance du contraste d'impédance pour la conversion d'énergie sur les bords du bassin.

Finalement, l'étape suivante de la méthodologie PBEE, concernant la réponse de la structure, est réalisée avec une structure non-linéaire et un bassin simplifié. La non-linéarité de la structure est modélisée par l'approche de la section multifibre.

La variabilité spatiale est étudiée en plaçant la structure dans différentes positions, ce qui modifie le champ des ondes arrivant à la fondation de la structure. Les résultats sont ensuite comparés à ceux obtenus par les méthodologies traditionnelles afin de vérifier si le modèle entièrement couplé de la faille à la structure augmente la demande structurelle sismique.

Les résultats indiquent que l'effet des bassins sur les dommages structurels peut être estimé de manière simplifiée en utilisant une combinaison d'un prédicteur de comportement structurel et d'AGF dérivés des mouvements du sol en champ libre. Cependant, ces facteurs doivent être correctement prédits, en incluant à la fois la variabilité du bassin et de la source.

Contents

List of Figures

List of Tables

Introduction

Background and Motivations

Rivers, and the presence of freshwater, have been essential for the development of animal life. Human and animal establishments near sedimentary basins have been documented to be over thousands of years (Berger et al., 2016; Alcaraz-Castaño et al., 2021; Tan et al., 2022; Gao et al., 2022, among others). Nowadays, important economic capitals (Los Angeles, Tokyo, Mexico City) are settled in sedimentary basins. These zones are particularly prone to be affected by a particular natural phenomenon: earthquakes. Earthquakes create seismic waves resulting in ground shaking in the surrounding area (Baker et al., 2021). Combined with proximity to active faults, the presence of sedimentary materials has been a significant factor in the severity of the observed damages, numerous fatalities and economic losses. For instance, after significant earthquakes in Northridge (1994) and Kobe (1995), severe damage occurred close to the basin edge. Similar observations can be made for several basins all over the world, such as San Francisco, Kanto and Mexico City (Gilbert et al., 1907; Furumura et al., 2008; Ghofrani and Atkinson, 2015; Cruz-Atienza et al., 2016)

Furthermore, any infrastructure has to be constructed considering the seismic damages (Cornell C. Allin, 1968; Anderson and Brune, 1999). According to Day (2012), four main factors cause structural damage during an earthquake: the strength of shaking, the duration of shaking, the type of subsurface conditions and the type of buildings. Therefore, to investigate the engineering response of any infrastructure, the knowledge of the characteristics of seismic ground motion is a key point. The seismic wavefield observed in a specified location is a result of phenomena occurring simultaneously at various scales (Semblat and Pecker, 2009), as described by Figure 1:

- Regional scale: from the seismic source (*S*),
- Local scale: at the site, including surficial geological structures (*L*) and interaction with structures (*SSI*).

The distortion produced in the incoming wavefield by subsurface geological irregularities is usually called *site effects* and is a crucial part of the propagation process (Semblat and Pecker, 2009). The seismic response modifications are observed as increased amplitudes, duration lengthening, and significant ground strains (schematically represented by the records in Figure 1). These

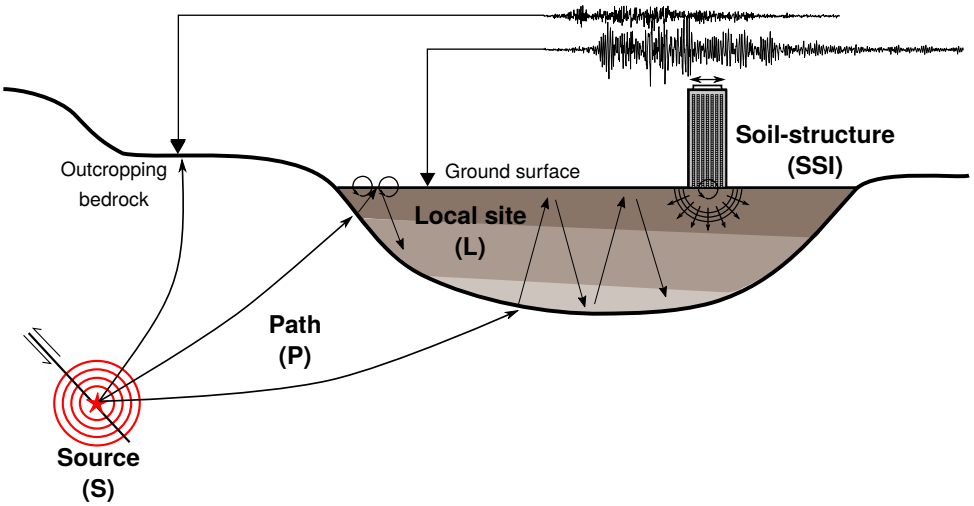

Figure 1: The problems assessed in this thesis: from source (S), path (P) and local site (L) effects to soil structure interaction (SSI).

are produced due to the local geological and geometrical conditions near the free surface. Commonly, the subsurface comprises layers of sedimentary materials, described with lower density and elastic modulus than the surrounding bedrock. Soft sedimentary materials close to the surface amplify the ground motion due to the decrease of seismic velocities and enclose the seismic energy by reflections, refraction and resonance (Kawase and Aki, 1989; Anderson, 2007). Moreover, the geometry enclosed by basins creates multi-dimensional seismic motion. These are usually called *basin effects*, which can be understood as the combination of all the wave propagation within them, making it a complex problem. Surface waves are generated at the borders, propagated horizontally inside the basin and reflected back and forth across the basin, increasing the duration of the signal (Sanchez-Sesma, 1987). Specifically, these types of waves are created by the interaction of the wavefield with the properties of the sediments and their geometry. They are frequency dependent so they will travel at different velocities depending on the properties of the sediments (Anderson, 2007). According to Cruz-Atienza et al. (2016), the basin's structure is responsible for the Mexico City basin's damage due to surface wave energy generated at the borders.

As observed, one of the main challenges is the accurate estimation of the ground motion characteristics for the efficient evaluation of the impact on the performance of structures. Due to the random nature of earthquakes, determining the structural response induced by seismic loading would be more effective in probabilistic than deterministic terms (Vamvatsikos, 2015). In that direction, developed by the Pacific Earthquake Engineering Research (PEER) Center, the Performance-based Earthquake Engineering (PBEE) presents a framework based on the evaluation of the engineering model in terms of different levels of the design (risk of collapse, fatalities, repair costs and post-earthquake loss) (Krawinkler, 1999; Porter, 2003; Baker et al., 2021). Risk analysis requires a hazard analysis and depends on the *exposure* of assets to those hazards and the *vulnerability* of the exposed assets to ground motion and other earthquake effects. There-

fore, the objective can be translated as a risk assessment analysis performed in four sequential stages, each connected to the previous one through a performance metric. Figure 2 schematically represents the required stages, where $p\left[X|Y\right]$ is the probability of X conditioned to Y and $\lambda\left[X|Y\right]$ is the ocurrence frequency of X given Y.

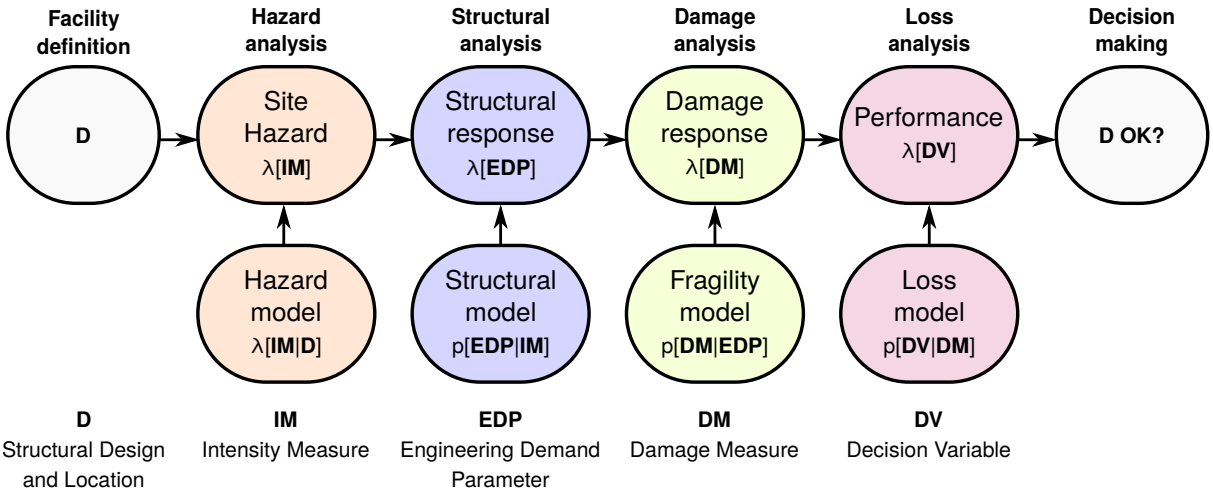

Figure 2: The probabilistic definition of the risk assessment according to the PBEE methodology. After (Porter, 2003).

The framework can be represented by the integral formulation (Bazzurro and Cornell, 1999), given by

$$\lambda\left(DV > x\right) = \int_{\mathbf{DM}}\int_{\mathbf{EDP}}\int_{\mathbf{IM}} P\left(DV > x \mid \mathbf{DM}\right) f\left(\mathbf{DM} \mid \mathbf{EDP}\right) f\left(\mathbf{EDP} \mid \mathbf{IM}\right) \mid d\lambda\left(\mathbf{IM}\right) \mid d\mathbf{EDP} d\mathbf{DM} \quad (1)$$

which estimates the frequency of a decision variable DV of exceeding a threshold x. For instance, decisions supported by this procedure can be the safety management of any facility, the calibration of design standards, the evaluation of potential losses, or potential mitigations. Usually, in the form of a vector, **DM** is a damage measure indicating the damage states of each component in the structure, **EDP** is a vector of engineering demand parameters, and **IM** is a ground motion intensity measure, which is, in general, a scalar, but can also be a vector under certain conditions (Baker et al., 2021).

The first step of the PBEE requires a *Hazard Analysis*, which refers to the characterization of natural phenomena resulting from earthquakes. The step quantitatively estimates the ground motion hazard, solving the physics of multiple earthquake source ruptures and the resulting propagation of seismic waves up to a precise location site. Because earthquake-induced ground motions are complex, the hazard is commonly estimated using an Intensity Measure (IM) parameter that characterizes them (e.g., peak ground acceleration, response spectra, duration). The result of these calculations in a probabilistic manner is the ground motion hazard curve, which

quantifies the distribution of levels of a selected IM versus the associated rates of exceedance (Bommer, 2002).

In general, they can be predicted by either the use of (i) recorded time histories, (ii) ground-motion prediction equations (GMPEs), or (iii) physics-based simulations (PBSs). Using historical time-histories requires a selection of compatible records from large data sets or generating synthetic motions from signal processing techniques (Bommer and Acevedo, 2004; Zentner, 2014; Baraschino et al., 2022, among others). Since in the next step of the PBEE methodology, non-linear dynamic soil-structure interaction analysis ought to be performed, the selection process is of crucial importance but usually present several issues, such as not enough available data for the defined region or the sought magnitude, or they are inadequate to represent the tested model. Alternatively, the GMPEs use indirect, approximate, or statistical approaches to integrate the earthquake source, directivity, path, attenuation and scattering, basin, and site effects (Douglas and Aochi, 2008). Hence, they are specific to each region of the world. Finally, the PBS uses numerical methods and models, incorporating the source and the resulting wave propagation explicitly (Paolucci et al., 2014; Taborda and Roten, 2015; Maufroy et al., 2016; Riaño et al., 2020). Therefore, they can estimate the earthquake ground motions time series explicitly. For instance, the PBS has been helpful in reproducing historical earthquake responses (Taborda and Bielak, 2014; Takemura et al., 2015; Smerzini et al., 2022, among others) and contributing to the seismic hazard assessment in determined regions (Tarbali et al., 2019; Castro-Cruz et al., 2021, among others).

The subsequent step is devoted to the *Structural Analysis*, where the dynamic response of the structure of interest is quantified through an Engineering Demand Parameter (EDP). This value is conditioned to the seismic excitation input for different seismic intensity levels, $p\left[EDP|IM\right]$. Generally, the structure can be modelled as a series of structural components defined by its properties (i.e., mass, damping, stiffness) to where the hazard is applied to perform a (nonlinear) time-domain analysis. Hence, the resulting EDP can be determined for a specific element or involving the entire structure, respectively local or global parameters, such as deformation or forces, floor spectral acceleration or inter-story drift (Cosenza and Manfredi, 2000; Rathje and Saygili, 2008; de Silva, 2020, among others).

The third step is the *Damage Analysis*, which refers to the estimation of the physical damage or functional failure at the structural components conditioned by the structural response model, quantified through Damage Measures (DM). They are conditioned on the structural response, $p\left[DM|EDP\right]$, defined with fragility or vulnerability functions. The DMs are defined as failure criteria with respect to some outcome of interest, commonly as different damage levels (light, moderate, severe) (Porter, 2003; Saez et al., 2011; Ghisbain, 2014; Zentner, 2017; Khalil and Lopez-Caballero, 2021).

Finally, the final stage of the PBEE is the *Loss Analysis*, which refers to the characterization of consequences, achieved by the definition of a Decision Variable (DV) parameter conditioned on the DM, $p\left[DV|DM\right]$. Therefore, the DV are consequences metrics, such as repair costs and duration, fatalities/injuries and economic loss (Baker et al., 2021). It is worth noting that this last

step is not considered in this work.

Traditionally, the site effects are accounted for in the PBEE methodology directly on the seismic hazard analysis. Since it is usually accepted that site amplification is mainly a one-dimensional effect (Semblat and Pecker, 2009; Berge-Thierry et al., 2019), modern seismic codes account for the site effects exclusively by this 1D process, defined as the amplification due to impedance contrast in layered sediments. However, as stated before, the geometry of the deposit (i.e., basin effects) is also a governing factor, inducing additional modifications in the ground motions. In order to consider the latter, several approaches have been defined in the literature (Makra et al., 2005; Psarropoulos et al., 2007; Gelagoti et al., 2012; Iyisan and Khanbabazadeh, 2013; Riga et al., 2016; Zhu et al., 2016, 2018, 2020; Amini et al., 2022; Ayoubi et al., 2021; Korres et al., 2023). One of them is with aggravation factors, accounting for the additional amplification produced by the basin effects against the 1D case, which allow to add them directly to the codes. For instance, this approach has been used by Bard (2021), who defined the site term in a GMPE by a 1D site response plus “correction factors", where the AGF was one of them (besides nonlinear response and topographic effects). The term “*aggravation*” does not necessarily mean that the inclusion of the basin geometry is always detrimental compared to the one-dimensional response. In some cases, the spatial distribution in some basin regions could result in a general deamplification, as observed by Pitilakis et al. (2015).

However, the AGFs focus mainly on the amplification of horizontal components because it is expected that the motion to be predominantly in that direction (Anderson, 2007), but that assumes that the ground motion is composed mainly of S-waves, neglecting the effect of the source location. To date, there are no techniques for ground motion quantification which consider the entire effects of the basin, i.e., surface waves: rotational and vertical components. Besides, the ground motion hazard calculation is performed first and then their results serve as input in the risk analysis (Baker et al., 2021). If the surface wave effect seeks to be incorporated into the full PBEE methodology, they should also be joined in the subsequent steps concerning the structural response. The ground motion excitation input to the structure is only applied in the horizontal components. However, it has been observed that rotational and vertical components, including directivity effects, can increase the observed structural damage (Cornou et al., 2003b; Narayan, 2012; Guidotti et al., 2018; Guéguen and Astorga, 2021; Kato and Wang, 2021; Vicencio and Alexander, 2019; Castellani et al., 2012; Smerzini et al., 2009; Nazarov et al., 2015; Falamarz-Sheikhabadi and Ghafory-Ashtiany, 2015; Ktenidou et al., 2016; Meza Fajardo and Papageorgiou, 2018, among others). While numerous examples in the literature have shown how soil-structure interaction analyses are an excellent way to tackle the issue (using a coupled approach both in the hazard and structural demand, e.g., Lombaert et al., 2005; Lombaert and Clouteau, 2006; Matinmanesh and Asheghabadi, 2011; Hökelekli and Al-Helwani, 2020; de Silva, 2020; Arboleda-Monsalve et al., 2020, among others), no proper investigation have been focused directly on the complex propagation produced by the basin incorporation.

Concerning the quantification of basin effects within the PBEE framework, the PBSs represent a great tool to model the source-to-structure wave propagation (Ichimura et al., 2017a; Abell

et al., 2018; Zhang et al., 2020; McCallen et al., 2021a,b; Zhang and Taciroglu, 2021). They can explicitly consider the different phenomena acting simultaneously as in Figure 1: the earthquake source, propagation path, local site effects and nonlinear behaviour of subsurface soil and structure (Poursartip et al., 2020). Since the problem happens at different scales, from tenths of kilometres to tens of meters, each scale commonly uses a distinctive numerical approach to perform the wave propagation. For instance, the most used formulations at a regional scale are the finite difference (FDM) or the spectral element method (SEM). In contrast, at a local scale, the finite element method is the preferred (Poursartip et al., 2020). In order to exploit the advantages of each method in its respective scale, the coupling technique called the *Domain Reduction Method* (DRM, Bielak et al., 2003) have been proposed. It is based on a weak-coupling approach, i.e., the solution is performed in two separate steps, where first, the free-field ground shaking is computed by an auxiliary simulation of the geological domain at a large scale without the structure and then injected as an equivalent nodal force distribution at the boundary of a small-scale domain including the structure.

Therefore, making use of PBSs and the DRM, the seismic risk in a probabilistic framework can be assessed, specifically by (i) the proper definition of an excitation source on the regional scale and characterization of the realistic 3D geological and mechanical properties, which will allow defining the ground motion on the scale of the site to perform the hazard analysis; and also (ii) the suitable definition of a constitutive model for the (nonlinear) behaviour of soil and structure, to execute the hazard and damage analyses; all in a coupled approach (Jeremić et al., 2009; Ichimura et al., 2017a,b; Abell et al., 2018; Hori et al., 2018; Nguyen et al., 2022; Korres et al., 2023; Kusanovic et al., 2023, among others).

Objectives

This thesis pretends to accurately characterize the ground motions induced in basins and their effects on nonlinear structures. Figure 3 represent the working framework: numerical source-to-structure simulations are performed from the regional to the local scale, as observed at the top. As ground motions in basins usually consist of surface waves generated by the conversion of incident waves in sedimentary deposits, the work is accomplished in three main axes and their relation: aggravation factors and surface waves at a regional scale, and structural performance, at a local scale.

More specifically, the following significant questions try to be answered:

1. What are the methods able to correctly characterize surface waves? How they can be easily characterized following a hazard analisys?

2. How are surface waves affecting the amplification observed in the basin? Can surface waves be estimated based on basin-structure setting parameters?

3. How much is the structural performance affected by the basin presence? Can this effect be estimated from some IMs for the seismic hazard evaluation?

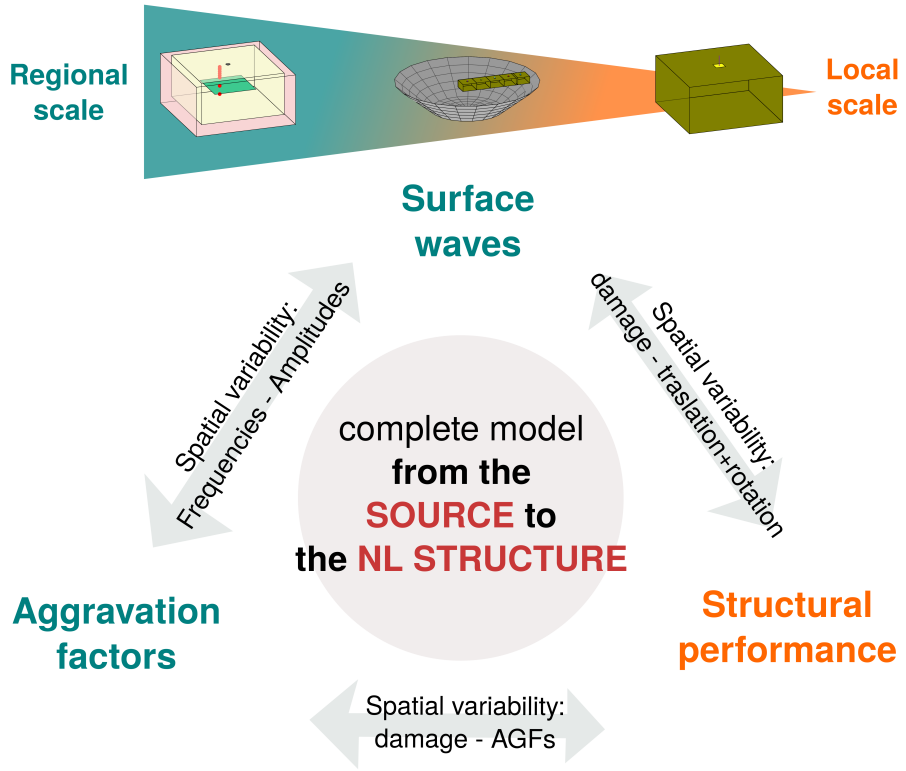

Figure 3: Framework of the thesis.

ANR MODULATE

The present work is placed within the framework of the project MODULATE (Modelling long-period ground motions and assessment of their effects on large-scale infrastructures) from the French National Research Agency (ANR). The final objective is the development of tools and guidelines that allow assessing the long-period ground motion at a site located in a sedimentary basin into the performance of real large-scale structures.

Outline

This thesis is organized into four main chapters, as follows. Chapters 2 and 4 are self-contained as a journal paper (under review and under preparation, respectively).

Chapter 1 dedicates to the validation of the surface waves' identification procedure defined as the Normalized Inner Product (NIP) (Meza-Fajardo et al., 2015; Meza-Fajardo and Papageorgiou, 2016). This chapter consists of a preliminary step for characterizing ground motion in basin models. Theoretical elements concerning the surface wave properties are discussed, essential for the formulation of the identification process. The validation is presented by contrasting the NIP with two other procedures: the Multiple signal classification (MUSIC) and the six-component polarization method (6CPol). Their capabilities are checked for wave fields with increasing com-

plexity, such as theoretical waves, and an MASW test including material heterogeneities and real recorded data signals.

Chapters 2 and 3 focus on the identification of the basin-setting conditions for the surface wave generation by exploiting the high-fidelity 3D numerical tool, SEM3D. In **Chapter 2**, numerical simulations are performed in canonical basins to cover a series of physical parameter configurations. The spatial variability of the surface wave characteristics and ground motion amplification in the basin is calculated and contrasted. **Chapter 3** further investigates the surface waves and amplification patterns on numerical simulation of two real basin models: Argostoli, located in Kefalonia island, Greece, and Cadarache in southern France. The sites were selected for their extensive geological, geophysical and geotechnical characterization, which allows the construction of reliable 3D physics-based numerical models previously validated in the literature. These models examine the effects of the heterogeneity of the shallow layers and the seismic-source azimuth, depth and type on the basin amplification.

Chapter 4 aims at quantifying the impact of basin effects on the performance of nonlinear structures through the framework of PBEE. The structural and damage analyses are performed in a coupled process with the help of the domain reduction method (DRM). A traditional methodology is first applied to compute the reference case of the selected nonlinear structure. The choice of an appropriate intensity measure, engineering demand parameter and damage measure is evaluated in this simple case. Then, the basin effects are evaluated in terms of two models, with and without the basin geometry. Consequently, the differences observed in the seismic performance of these structures in the presence of surface waves are quantified.

A small explanation of the formulation in SEM3D is presented in Appendix A, including a validation of the methodology against a reference amplification in a basin.

Chapter 1

Surface wave characterization

Contents

1.1 Introduction

As the number of large-scale structures increases, such as high-rise buildings and suspension bridges, the correct determination of long-period ground motion becomes an important subject to have an accurate response for seismic design (Koketsu and Miyake, 2008). Specifically, in the Performance Based Earthquake Engineering (PBEE) methodology proposed by the Pacific Earthquake Engineering Research (PEER) center (Porter, 2003; Günay and Mosalam, 2012), the first step is devoted to the seismic hazard analysis, in which the ground motion characterization are identified in terms of some ground motion or intensity measures (IMs).

The intense long-period ground motion observed in seismograms is generated, in general, from two phenomena linked to the distance to the source, namely the near- and far-source ground motion. Near-fault ground motion is mainly generated from the fault rupture directivity and is defined by short duration. In contrast, far-source ground motion can be generated by large earthquakes far from the source in sedimentary basins by the creation of surface waves, which increase the duration of the signal (e.g. Miura and Midorikawa, 2001; Cruz-Atienza et al., 2016; Viens and Denolle, 2019, among others). Hence, in order to correctly determine the seismic response of structures placed inside sedimentary basins, an important step is to incorporate surface waves and their characteristics in the analysis procedures. However, they are poorly included into the seismic analysis because of their more complex characteristics and effects on the ground motions.

A key element would be then the ability to estimate surface wave characteristics from ground motions quantitatively in order to have an IM representing the presence of the surface waves in the ground motion. This Chapter develops the methodologies that will be used in the next chapters to quantitatively study the surface waves and their dependency on the parameters of the basin-seismic setting.

This Chapter aims to evaluate methodologies for the characterization of surface waves from ground motion signals. For that, the Chapter starts by explaining the wave propagation principles to understand surface wave propagation characteristics. Then, three methodologies that are able to identify surface waves from ground motions are selected, namely the Normalized Inner Product (NIP), MUSIC and the Six-Degrees-of-Freedom Polarization Analysis (6CPol). Their capabilities will be evaluated via three examples with increasing complexity: a theoretical Rayleigh wave signal (Subsection 1.6.1), a synthetically generated Rayleigh wave (Subsection 1.6.2) and real data signals (Subsection 1.6.3). The influence of the material properties heterogeneity on the surface wave characteristics is investigated in Subsection 1.6.2.

1.2 The wave equation in solid media

This section describes the fundamental concepts, starting from the waveform in 3D mediums. Using the notation of bold for vectors, the waveform of a tridimensional plane wave in an elastic

homogeneous medium is a solution of the partial differential wave equation

$$\nabla^2 \mathbf{u} = \frac{1}{\nu^2} \frac{\partial^2 \mathbf{u}}{\partial t^2} \tag{1.1}$$

where $\mathbf{u}(\mathbf{r}, t)$ is an (unknown) three-dimensional displacement field, dependent on the spatial $\mathbf{r}$ and temporal t variables. The standard solution of this equation can be expressed as

$$\mathbf{u}\left(\mathbf{r}, t\right) = A \cos\left[\omega t - \mathbf{k} \cdot \mathbf{r} + \phi\right] = A \exp i \left(\mathbf{k} \cdot \mathbf{r} - \omega t + \phi\right) \cdot \mathbf{p} \tag{1.2}$$

where A is the amplitude of the wave, and

$$\mathbf{r} = \begin{pmatrix} x \\ y \\ z \end{pmatrix} \tag{1.3}$$

defines the coordinates of a point in three-dimensional space, t is the time, $\mathbf{k} = \omega \cdot \mathbf{s}$ is the radial wavevector and $\mathbf{s} = (s_x, s_y, s_z)$ is the slowness vector, which describes a harmonic plane wave travelling in the $\mathbf{s}$ direction. The vector $\mathbf{p}$ is the polarization vector, which is a constant unitary vector describing the particle displacement direction.

1.3 Body waves

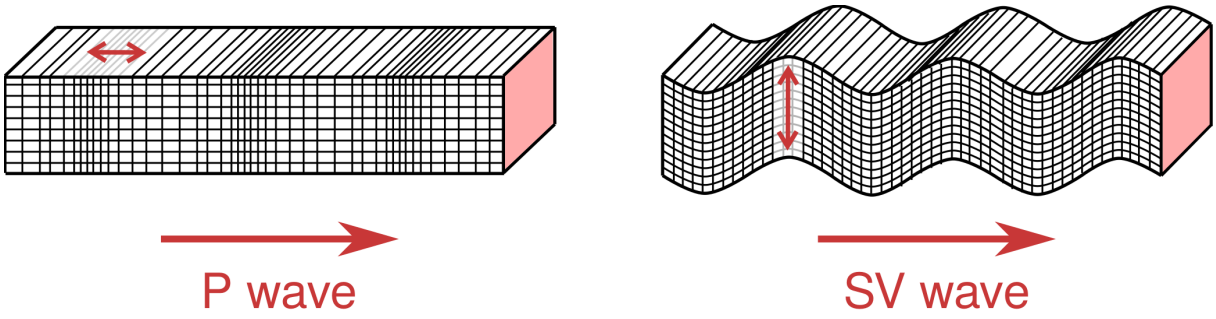

Figure 1.1: Illustration of ground motion displacement caused by compressional (P wave) and shear (SV waves) waves. After Shearer (1999).

From the previous propagation equation, and in the absence of any sources, two body-wave types propagate in infinite homogeneous elastic media: P (longitudinal, compressional - dilatational) and S (shear) waves, associated to volumetric and distortion deformation, respectively. When the distance from the source is large enough, the wavefront can be approximated by plane waves with parallel seismic rays. In this case, Equation 1.2 reduces to a one-dimensional (1D) wave equation.

For a plane wave travelling in the $\pm x$ direction, as in Figure 1.1, two types of waves are propagated. The first is a P-wave travelling with a speed v_p in the $\pm x$ direction, where the particles

are displaced parallel to the direction of the propagation, as represented in Figure 1.1 on the left. The second case is described by an S-wave travelling with speed v_s in the $\pm x$ direction. The equation allows two particle motions, both perpendicular to the direction of propagation: a vertically polarized SH-wave and a horizontally polarized SV-wave.

For an unbounded homogeneous isotropic elastic 3D medium, the equation of motion can be written as

$$(\lambda + \mu)\, \nabla\, (\nabla \cdot \mathbf{u}\,) + \mu \nabla^2 \mathbf{u} = \rho \frac{\partial^2 \mathbf{u}}{\partial t^2} \tag{1.4}$$

where λ and μ are the Lamé parameters and ρ is the density of the medium. Then, three cases are possible (Krebes, 2019):

1. The slowness **s** is parallel to the particle displacement **u**, i.e., $\mathbf{u} = a \cdot \mathbf{s}$ with a a constant at any given time. Then, the Equation 1.2 becomes:

$$\left((\lambda + \mu)\, s^2 + \left(\mu s^2 - \rho\right)\right) a \cdot \mathbf{s} = 0 \Rightarrow v^2 = \frac{1}{s^2} = \frac{\lambda + 2\mu}{\rho} \tag{1.5}$$

   which is a plane wave traveling in the **s** direction with speed v, with particles displaced parallel to the **s** direction.

2. The slowness **s**, which is the same than applying the divergence in Equation 1.2, from it is obtained:

$$v^2 = \frac{1}{s^2} = \frac{\mu}{\rho} \tag{1.6}$$

   that describes a plane wave travelling in the **s** direction with speed v, but this time the particles are displaced perpendicular to the **s** direction.

3. The other case is that s and u are neither parallel nor perpendicular; in this case, the Equation 1.2 show no solution.

The Lamé parameters, λ and μ, are two elastic constants associated with the mechanical properties of the medium. They are always positive, so the P-wave velocity is always larger than the S-wave velocity.

The wave vector **k** describe the propagation direction. In a more generalized way, any plane wave can be described as travelling in a 3D medium with the polar angles θ, denoting the inclination with respect to the z direction, and ϕ, or azimuth. The wave vector becomes:

$$\mathbf{k} = k \cdot \mathbf{r} = \begin{pmatrix} \sin\theta \cdot \cos\phi \\ \sin\theta \cdot \sin\phi \\ \cos\theta \end{pmatrix} \tag{1.7}$$

For P-waves, the polarization vector **p** is defined as:

$$\mathbf{p}_P = (\sin\theta \cdot \cos\phi, \sin\theta \cdot \sin\phi, \cos\theta)^T \tag{1.8}$$

describing a particle motion parallel to the wave vector **k** for P-waves.

As informed previously, the S-wave can be separated into two types: SH and SV waves. SV waves describe a particle motion in the vertical direction, orthogonal to the wave vector. The polarization vector $\mathbf{p}_{SV}$ is then

$$\mathbf{p}_{SV} = (-\cos\theta \cdot \cos\phi, -\cos\theta \cdot \sin\phi, \sin\theta)^T \tag{1.9}$$

For SH waves, which exhibit translational particle motion orthogonal to the wave vector, the polarization vector $\mathbf{p}_{SH}$ is

$$\mathbf{p}_{SH} = (-\sin\phi, \cos\phi, 0)^T \tag{1.10}$$

Moreover, the Equation 1.2 can be generalized to consider multiple harmonic waves of different frequencies using the inverse Fourier transform:

$$f(\mathbf{x}, t) = \frac{1}{2\pi} \int_{-\infty}^{\infty} F(\omega) \exp\left[i\left(\frac{\omega}{C(\omega)}\mathbf{s}(\mathbf{x}) - \omega t\right)\right] d\omega \tag{1.11}$$

where $F(\omega)$ is the complex spectrum of $f(\mathbf{x}, t)$ and can be represented as a real ($\Re$) and a imaginary part ($\Im$) as

$$F(\omega) = \Re(\omega) + i\Im(\omega) = A(\omega)\exp[i\Phi(\omega)] \tag{1.12}$$

where

$$A(\omega) = \left[\Re(\omega)^2 + \Im(\omega)^2\right]^{1/2} \tag{1.13}$$

is the amplitude spectrum and

$$\Phi(\omega) = \tan^{-1}[\Re(\omega) + \Im(\omega)] \tag{1.14}$$

is the phase spectrum. With the Fourier transform,

$$F(\omega) = \int_{-\infty}^{\infty} f(t)\exp[i\omega t]\, dt \tag{1.15}$$

the spectrum of the time function $f(t)$, $F(\omega)$, can be represented.

1.3.1 Reflection and refraction

Before were presented elementary solutions of the wave equation for propagation in homogeneous media, which are body waves of P and S types. In reality, Earth materials are not homogeneous, and their characteristics vary spatially. When waves propagate from one medium to another with different properties, some energy is reflected into the first medium, and the other is transmitted or refracted into the second. The theory of this reflection and refraction was first developed by Knott (1899) and Zoeppritz (1919).

In elastic media, incident body waves (P and S) will be reflected and refracted due to the Huygens principle and will, in general, generate reflected waves. Incident P and SV-waves create both reflected P and SV-waves, while incident SH-waves creates only reflected SH-waves. The phenomenon, called *mode conversion* occurs between two media of different material properties and also at the free surface. The case of the reflection at the free surface is of particular interest for the formation of Rayleigh surface waves. The boundary imposes a stress-free condition at the free surface, or null normal stresses.

1.4 Surface waves

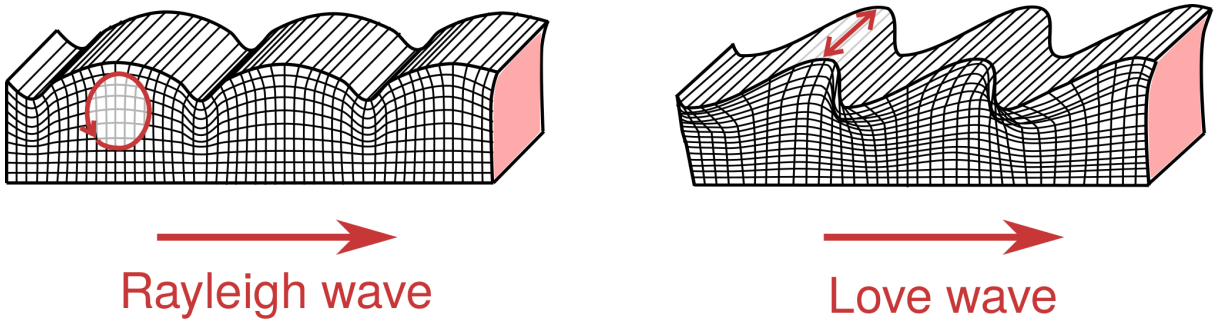

Figure 1.2: Illustration of ground motion displacement caused by Rayleigh and Love waves. After Shearer (1999).

The presence of a free surface on an elastic medium offers the reflection of body waves, as seen in the previous section. At the Earth's surface and under certain conditions, the constructive interference of body waves with the free surface will generate *surface waves*. They are called surface waves because they propagate along the boundary of a body rather than its interior (Foti et al., 2015). Surface waves have been helpful in determining the local structure (Haskell, 1953; Tokimatsu, 1997; Foti et al., 2015, among others), in general, with their dispersive nature. Some of the characteristics above are important to describe the wave source, the propagating medium, to the estimation of site effects.

These waves propagate at the surface, and their amplitudes decrease exponentially with depth. They originate from the stress-free condition at the boundary of the domain. They are important in seismology as they produce large amplitudes of surface ground motion, especially in low frequencies or long periods. This work will focus on two types of surface waves: Rayleigh and Love (Figure 1.2).

1.4.1 Rayleigh waves

Under the condition of a free-horizontal surface is present, Rayleigh waves are generated by the reflection of P and SV on the border, i.e., they can be generated on the surface of a homogeneous halfspace. The particle motion will then be a sum of the P component of motion u_P and the

SV component of motion u_{SV}, propagating in the horizontal direction given by the wave vector $\mathbf{k} = k\,(\cos\phi, \sin\phi, 0)^T$. The polarization vector of a Rayleigh wave is given by

$$\mathbf{p}_R = (-\sin\xi \cdot \cos\phi, -\sin\xi \cdot \sin\phi, \cos\xi)^T \tag{1.16}$$

where ξ is the ellipticity of the Rayleigh wave. Equation 1.16 defines the particle motion of a single monochromatic Rayleigh wave as $\mathbf{u} = (\mathbf{u}_X, \mathbf{u}_Y, \mathbf{u}_Z)$ (Sollberger et al., 2018):

$$\mathbf{u}_X = -A \sin\xi \cos\phi \cos(\omega t - \mathbf{k}\cdot\mathbf{r} + \psi) \tag{1.17}$$

$$\mathbf{u}_Y = -A \sin\xi \sin\phi \cos(\omega t - \mathbf{k}\cdot\mathbf{r} + \psi) \tag{1.18}$$

$$\mathbf{u}_Z = -A \cos\xi \cos(\omega t - \mathbf{k}\cdot\mathbf{r} + \pi/2\psi) \tag{1.19}$$

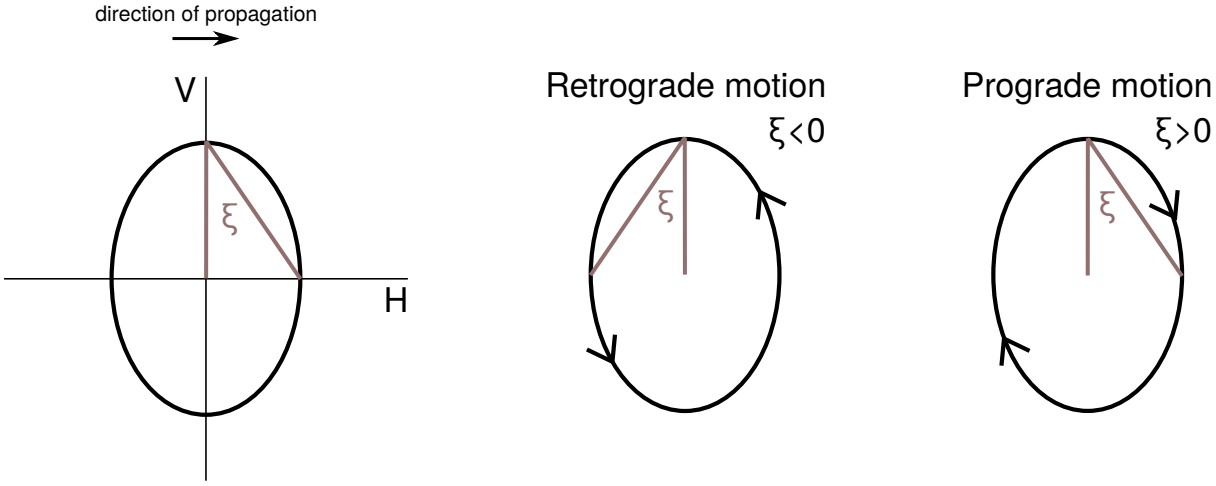

Figure 1.3: Ellipticity definition for Rayleigh waves exhibiting retrograde or prograde motion. After Maranò et al. (2017).

These equations describe an elliptical particle trajectory (Figure 1.3), due to the phase shift by $\pm 90^o$ between the SV-wave on the vertical component and P-wave in the horizontal component. The value ξ

$$\xi = \tan^{-1}\left(\frac{H}{V}\right) \tag{1.20}$$

defines the ratio of horizontal and vertical axes of the ellipse along which particles are moving in the propagation. In transient or real signals, the particle path is very unlike ellipses but remains in the vertical plane. This delay is never far from 90 degrees (Keilis-Borok, 1989).

In a homogeneous halfspace, particles at the surface disturbed by a Rayleigh wave will experience a counterclockwise or retrograde elliptical motion, where $\xi < 0$ (Achenbach, 1973). In this case, the maximum vertical displacement is retarded by a time of $\pi/2\omega$ in comparison with the maximum horizontal displacement. This motion is preferred of the fundamental mode (Gribler and Mikesell, 2019). In contrast, it could also happen that the vertical displacement is advanced by a time of $\pi/2\omega$, to which it is said that the Rayleigh wave describes a prograde

motion, where $\xi > 0$. This case happens in a homogeneous halfspace at a certain depth (Aki and Richards, 1980), or at the surface in sedimentary basins and shallow layers for determined frequency ranges (Malischewsky et al., 2008).

When the medium they propagate has layers of different material properties, they need the right combination of frequency and angle of incidence to generate constructive interference of body waves. By Snell's law, the angle of incidence depends on the velocity of the medium, so they travel with different velocities at different frequencies, i.e., they show dispersive behaviour (Anderson, 2007).

1.4.2 Love waves

The Love waves are SH-waves guided by the surface. The name is after the mathematician A. E. H. Love, who worked out their properties. In a horizontal halfspace, they exist only if a low-velocity layer $v_1 < v_2$ is over a halfspace with higher velocity v_2. The surface then acts as a waveguide.

They are formed with multiple interferences of SH in the free surface (Shearer, 1999), so their particle motion is always parallel to the surface and transversal to their direction of propagation (Figure 1.2 on the right). The polarization vector of Love waves is given by

$$\mathbf{p}_R = (-\sin\phi, \cos\phi, 0)^T \tag{1.21}$$

which defines the particle motion of a Love wave as $\mathbf{u} = (\mathbf{u}_X, \mathbf{u}_Y, \mathbf{u}_Z)$ (Sollberger et al., 2018):

$$\mathbf{u}_X = -A\sin\phi\cos(\omega t - \mathbf{k}\cdot\mathbf{r} + \psi) \tag{1.22}$$

$$\mathbf{u}_Y = -A\cos\phi\cos(\omega t - \mathbf{k}\cdot\mathbf{r} + \psi) \tag{1.23}$$

$$\mathbf{u}_Z = 0 \tag{1.24}$$

Contrary to Rayleigh waves, Love waves are always dispersive. As Love waves follow the same polarization as SH waves, more than one station is needed to differentiate them. The vertical SH wave induces the same motion everywhere on the surface, while the Love wave shows periodic reversals every half wavelength in the direction of propagation (Anderson, 2007).

1.4.3 Summary of the main properties of surface waves

In summary, the main characteristics of surface waves that can be important to be described in earthquake engineering are:

- Geometric dispersion: defined as the variation of velocity propagation with frequency in surface waves. Due to dispersion, surface waves are observed on seismograms of distant surface earthquakes as wave trains of large amplitudes arriving at different times, first arrivals corresponding to waves of longer periods (Udias et al., 2013). Based on this dispersive nature, they have been helpful in determining subsurface structure (Tokimatsu, 1997;

Aki and Richards, 1980; Foti et al., 2015), assuming the Earth as a sequence of horizontal layers having different elastic properties. The form of the dispersion curve, which represents the dependence of the frequency on the velocity, depends on the characteristics of the medium, namely the wave velocity and thickness of the sediments.

- Polarization: The term refers to the particle motion observed, and is key to discriminate between strong linear particle motion (e.g., P, S and Love waves) and elliptical particle motion (e.g., Rayleigh waves) (Hendrick and Hearn, 1999).

- Attenuation: With distance, body and surface waves decay amplitudes due to the energy spreading. Due to their origin of vanishing stresses at the boundary of a domain, surface waves have an exponential decay of displacement in depth away from the free surface due to geometrical spreading, and most of the strain energy is confined within a depth of one wavelength λ (Achenbach, 1973). Since their radiation pattern is essentially two-dimensional (Foti et al., 2015), the amplitude decay rate of surface waves with distance r at the free surface is of $1/\sqrt{r}$. Anelastic attenuation will also be present in the propagation as a result of material adsorption. This attenuation is usually represented by the dimensionless quality factor, Q:

$$\frac{1}{Q\left(f\right)} = -\frac{\Delta E}{2\pi E} \tag{1.25}$$

where E is the peak strain energy and ΔE is the energy loss per cycle at a given frequency, which can be approximated as an exponential decay in the amplitude with distance.

1.5 Overview of methodologies for identification of surface waves from time signals

The determination of site effects is important in the seismic hazard assessment. The wavefield of a determined location is a combination of body and surface waves, the latter having more significance inside sedimentary basins (Cornou and Bard, 2003; Moczo et al., 2018; Riga et al., 2018, 2016; Marafi et al., 2017; Meza-Fajardo et al., 2015; Meza-Fajardo and Papageorgiou, 2016, among others). Because of the fact that surface waves "*absorb*" the path characteristics in their propagation, they are usually used as an inexpensive method to investigate the local soil structure (elastic properties of the earth, density and thickness of layers) (Haskell, 1953). However, the link between wavefield and structure is possible only making some hypothesis such as the semi-infinite dimension of the layers. Basin presence is heterogeneous enough, being a structure with both vertical and lateral variations. Therefore, the surface wave field cannot be derived with the exact formulas presented before, because they can only be formulated for simple geometry configurations (Keilis-Borok, 1989). Thus, this investigation pretend to do the *inverse* problem: in complex geometrical problems (basins), where these hypothesis do not hold, to investigate how surface waves characteristics are linked to the basin geometry or source. This has as objective to

relate in a next step the surface waves generation with the amplification of the ground motion in basin geometries (Chapters 2 and 3) and their subsequent effect on structural response (Chapter 4).

To fulfill the objective, the surface wave characteristics need to be estimated from ground motions. In the literature, several methodologies have been developed to identify the wavefield types and their characteristics. Usually, the techniques can be divided in two groups: (i) the ones who perform a *polarization* analysis from single stations (ii) and the ones who use multiple stations to compute a coherent summation of signals of the same polarization (Greenhalgh et al., 2008). Polarization parameters should be correctly defined, since they could give crucial information about the surface wave influence on the ground motion. For instance, the polarization azimuth angle could be important in the seismic hazard for the evaluation of directivity effects, the definition of the approach direction of the wave and the determination of geological features. Additionally, the translational and rotational amplitudes obtained from the polarization analyses could be associated to the intensity characterization of the ground motions.

In this part of the work, the capacity to determine quantifiable information of the surface waves of three selected methodologies is investigated, namely the Normalized Inner Product (NIP, Meza-Fajardo et al., 2015), the Six Degrees-of-Freedom Polarization Analysis (6CPol, Sollberger et al., 2018) and the Multiple Signal Classification (MUSIC, Schmidt, 1986). The first two are single-station polarization analyses, while the latter is described as a beamforming method associated with a coherent summation from multiple stations. These methodologies have been validated for simple signals as well as real signals from sedimentary basins after earthquakes: NIP (Meza-Fajardo et al., 2015, 2021; Heresi et al., 2020; Meza-Fajardo et al., 2019), 6C-POL (Sollberger et al., 2018, 2020), and MUSIC/MUSIQUE (Cornou et al., 2003a,b; Imtiaz et al., 2017, 2020; Hobiger, 2011; Hobiger et al., 2016).

The three methodologies are compared, knowing that in this work some features are seeked:

- they have to be able to extract parameters of the surface waves in an quantifiable manner in order to be added into the PBEE methodology, e.g., as a (single) measure.
- since the spatial variability in basins is an important subject, an adequate methodology has to be able to process a high number of data in acceptable time.

A short description of the methodologies will be introduced hereafter. For more details refer to the references provided in each subsection.

1.5.1 Normalized inner product (NIP)

The Normalized Inner Product Procedure is a time-frequency polarization analysis to separate the surface waves from the time signals proposed in Meza-Fajardo et al. (2015). Since surface waves have a very distinct polarization pattern, a filter based on the correlation between two orthogonal components can be used to separate them. The procedure is briefly described here.

More details can be found in Meza-Fajardo et al. (2015) and Meza-Fajardo and Papageorgiou (2016).

From the displacement time signals, $\mathbf{u}(t) = (\mathbf{u}_x(t), \mathbf{u}_y(t), \mathbf{u}_z(t))^T$, for each component x, y and z, a time-frequency representation is obtained. Given a time function $h(t)$, the Stockwell Transform $\mathbf{S}(\tau, f)$ (Stockwell et al., 1996) is defined as:

$$\mathbf{S}(\tau, f) = \int_{-\infty}^{\infty} h(t) \frac{|f|}{\sqrt{2\pi}} \exp\left[-\frac{(\tau - t)^2 f^2}{2}\right] \exp[-2\pi i f t]\, dt \tag{1.26}$$

The Stockwell transform preserves the signal's phase, allowing it to correlate two components in the time-frequency domain. The Stockwell transform can also be written as:

$$\mathbf{S}(\tau, f) = A(\tau, f) \exp(i\phi(\tau, f)) \tag{1.27}$$

where the amplitude A and the phase ϕ are frequency (f) and time (τ) dependent.

The inverse of the Stockwell transform is also required to convert the time-frequency signal back to the time domain,

$$h(t) = \int_{-\infty}^{\infty} \left[\int_{-\infty}^{\infty} \mathbf{S}(\tau, f)\, d\tau\right] \exp[-2\pi i f t]\, df \tag{1.28}$$

To filter surface waves, Meza-Fajardo et al. (2015) makes use of the Normalized Inner Product (NIP). By its general definition, the NIP is an autocorrelation coefficient between two arbitrary signals, m and n, given by the equation

$$\mathbf{NIP}_{m,n}(\tau, f) = \frac{\Re[\mathbf{S}_m(\tau, f)]\,\Re[\mathbf{S}_n(\tau, f)] + \Im[\mathbf{S}_m(\tau, f)]\,\Im[\mathbf{S}_n(\tau, f)]}{A_m(\tau, f)\, A_n(\tau, f)} \tag{1.29}$$

where $\Re$ and $\Im$ are the real and imaginary parts of the transform. Values of NIP close to 1 represent a high correlation between signals. This feature is used for the identification of the polarization angle of surface waves by filtering regions of high values of NIP in the time-frequency space.

As previously stated, prograde Rayleigh, retrograde Rayleigh and Love waves will all be polarized in a vertical plane, which can be characterized by an angle with respect to the North. This angle of polarization, $\theta(\tau, f)$, can be found by minimizing the correlation between the horizontal components according to the following relation:

$$\theta(\tau, f) = \frac{1}{2} \tan^{-1}\left\{2\frac{IP[S_N(\tau, f), S_E(\tau, f)]}{A_N^2(\tau, f) - A_E^2(\tau, f)}\right\} \tag{1.30}$$

where IP is the Inner product, computed as the numerator of Equation 1.29, i.e., the NIP not normalized by the signals' amplitudes. In this case, the correlation is performed with the two orthogonal horizontal components of the ground motion, represented by the subscript N and E, the north and east component of the signal. The angle $\theta(\tau, f)$ expresses the preferential hori-

zontal direction to where the motion is polarized. Then, the signals are rotated in the direction of θ, separating the polarized motion in one component, $S_R(\tau, f)$, from its tranverse component, $S_T(\tau, f)$. The relation with the original directions can be obtained by a rotation matrix, given by

$$\begin{pmatrix} \mathbf{S}_R(t,f) \\ \mathbf{S}_T(t,f) \end{pmatrix} = \begin{bmatrix} \cos\theta & \sin\theta \\ -\sin\theta & \cos\theta \end{bmatrix} \begin{pmatrix} \mathbf{S}_N(t,f) \\ \mathbf{S}_E(t,f) \end{pmatrix} \tag{1.31}$$

Once the polarized wave in the time-frequency domain $\mathbf{S}_R(\tau, f)$ is obtained, the wave type is discriminated. The particle motion of Rayleigh waves rests in a vertical plane while the horizontal and the vertical components have a phase difference of $+\pi/2$ for prograde waves and $-\pi/2$ degrees for retrograde waves. This feature allows the generation of a filter in the $\tau - f$ domain where the correlation between the vertical phase shifted wave $\mathbf{S}_{\overline{V}}(\tau, f)$ and the polarized wave is high ($NIP\left(\mathbf{S}_R(\tau, f), \mathbf{S}_{\overline{V}}(\tau, f)\right) > 0.8$), assuming prograde or retrograde motion. Moreover, the particle motion of Love waves lies only on the horizontal plane. Therefore, if a low NIP value is found between the polarised wave $S_R(\tau, f)$ and the vertical shifted wave $\mathbf{S}_{\overline{V}}(\tau, f)$, it can be assumed that the wave corresponds to a Love wave. Finally, the polarized signal in $\tau - f$ domain is inverted to obtain the time signal of the extracted wave.

The initially calculated angle θ relies upon the $\tau - f$ domain, so the extracted signals average angle is calculated using the polarized extracted wave in time, $x_{pol}(t)$, and the north and east components of the signal, $x_E(t)$ and $x_N(t)$:

$$\tan\theta_r = \frac{\mathbf{S}_{EP}}{\mathbf{S}_{NP}} = \frac{x_E x_{pol}}{x_N x_{pol}} \tag{1.32}$$

The angle θ_r is a reference angle, so to obtain the real angle of polarization of the wave θ is determined by

$$\theta = \theta_r + \pi\left[1 - sign\left(\mathbf{S}_{EP}\right)\right] + \pi\left[1 - sign\left(\mathbf{S}_{NP}\right)\right] sign\left(S_{NP}\right)/2 \tag{1.33}$$

In the last step, the extracted waves are discriminated with a correlation coefficient C_{PV} computed in the time domain between the polarized ($x_{pol}(t)$) and shifted vertical ($x_{\overline{V}}(t)$) signals

$$C_{P\overline{V}} = \frac{\sum_{i=1}^{t} x_{pol}(i) x_{\overline{V}}(i)}{\left[\left(\sum_{i=1}^{t} x_{pol}(i) x_{pol}(i)\right)\left(\sum_{i=1}^{t} x_{\overline{V}}(i) x_{\overline{V}}(i)\right)\right]^{1/2}} \tag{1.34}$$

If $C_{PV} > 0.7$, the extracted wave is accepted as a Rayleigh wave and if $C_{PV} < 0.3$, it is accepted as a Love wave (Meza-Fajardo et al., 2015; Meza-Fajardo and Papageorgiou, 2016). It should be noted that this technique is performed for each wave train separately.

As already stated, the seismic hazard needs to be characterized in terms of some intensity measures. For that reason, the main characteristics of the signals can be further analyzed. Meza-Fajardo et al. (2021) made an effort to quantitatively characterize generated surface waves in the Nobi and Kanto basins during major earthquakes. For that, they defined the central frequency of

the waves f_{cen} as

$$f_{cen} = \underset{(\tau,f)}{argmax} \left\{ S_P \left(\tau, f \right) \right\} \tag{1.35}$$

which is the frequency associated with the maximum amplitude of the S-Transform of the extracted waves. Since the result of this procedure is the signal time series, any other ground motion parameter (such as peak values and spectral responses) can also be computed.

1.5.2 Multiple signal classification (MUSIC)

The procedure MUSIQUE (Hobiger et al., 2016) determine the wave vector first with the MUSIC algorithm (Schmidt, 1986). This subsection is based mainly on the works of Cornou et al. (2003b) and Hobiger et al. (2016).

First, the original MUSIC approach determines the azimuth θ and slowness s of the most energetic contributions crossing simultaneously N sensors (N an arbitrary number such that they describe a two-dimensional seismic array). The azimuth direction defines the radial component (where the incident wavefront is coming from), while the transverse component is orthogonal to this direction (Hobiger et al., 2016).

The algorithm is developed to separate the signal and noise subspaces and performed at each frequency individually, f. The signal is pre-filtered with a small-band Chebyshev filter around the desired frequency. Then, the signal is divided into time windows of several length periods. This procedure is performed for each time-frequency window.

Supposing the array is composed by N three-component sensors, the covariance matrix $\mathbf{S}_i$ is defined as

$$\mathbf{S}_i \left(f \right) = \mathbb{E} \left(\mathbf{X}_i \left(f \right) \overline{\mathbf{X}}_i \left(f \right) \right) \tag{1.36}$$

by averaging ($\mathbb{E}$) over a small range of frequencies around the central frequency f the product of the signal data vector $\mathbf{X}_i \left(f \right)$ and its conjugate $\overline{\mathbf{X}}_i \left(f \right)$. This complex vector $\mathbf{X}_i \left(f \right)$ is of size $N \times 1$ for each component $i = x, y, z$. Then, a single covariance matrix $\mathbf{S}$ is computed by summing the three components,

$$\mathbf{S} = \mathbf{S}_x + \mathbf{S}_y + \mathbf{S}_z \tag{1.37}$$

The signal and noise subspaces are determined by computing the eigenvectors and eigenvalues of the covariance matrix $\mathbf{S}$. If a number q of wave arrivals want to be identified, the q larger eigenvalues determine the signal subspace and the $N - q$ smaller the noise subspace, $\mathbf{G}$. Only the signal with the largest eigenvalue (most energetic wave) is used in this case.

Since the signal and noise subspace are orthogonal (Cornou et al., 2003b), the signal direction vector $a \left(\mathbf{k} \right)$ is identified by maximizing the MUSIC functional P by a 2-D grid search:

$$P \left(\mathbf{k} \right) = \frac{1}{\overline{\mathbf{a} \left(\mathbf{k} \right)} \mathbf{G} \overline{\mathbf{G}} \mathbf{a} \left(\mathbf{k} \right)} \tag{1.38}$$

where $a\left(\mathbf{k}\right)$

$$a\left(\mathbf{k}\right) = \exp\left(-i\mathbf{R}\mathbf{k}\right)/\sqrt{N} \tag{1.39}$$

with **R** the matrix of sensors positions and k the wave vector:

$$\mathbf{k} = -2\pi f\, s\left(f\right) \cdot \left(\sin\theta, \cos\theta, 0\right)^T \tag{1.40}$$

The wave vector is defined by the signal back azimuth θ and apparent propagation slowness s, so the signal properties can be determined by finding the peak in the MUSIC functional P.

Then, the radial and transverse components of motion can be separated by a projection of the North and East components in the obtained azimuth θ:

$$\mathbf{S}_{radial} = -\sin\left(\theta\right)\mathbf{S}_E - \cos\left(\theta\right)\mathbf{S}_N \tag{1.41}$$

$$\mathbf{S}_{transverse} = \cos\left(\theta\right)\mathbf{S}_E - \sin\left(\theta\right)\mathbf{S}_N \tag{1.42}$$

MUSIC can discriminate the type of the dominant wave during the selected window and frequency based on the components' energies:

$$E_{vert} = \sum_k \overline{\mathbf{S}}_{vert} \cdot \mathbf{S}_{vert} \tag{1.43}$$

$$E_{radial} = \sum_k \overline{\mathbf{S}}_{radial} \cdot \mathbf{S}_{radial} \tag{1.44}$$

$$E_{transverse} = \sum_k \overline{\mathbf{S}}_{transverse} \cdot \mathbf{S}_{transverse} \tag{1.45}$$

If most of the energy is carried out by the transverse component than the radial and vertical combined, then the incident wave is identified as Love. Otherwise, the wave is identified as a possible Rayleigh wave.

As recalled before, in this work, this procedure will be used only to verify the results of the NIP when more than one station is available. The original signal will be filtered close to the central frequency f_{cen} obtained by the NIP (Equation 1.35). The verification will be made in terms of the azimuth and the type of identified wave.

1.5.3 Six component (6-C) Polarization Method

The six-component $(6-C)$ polarization analysis was proposed by Sollberger et al. (2018) to identify wave type and characteristics. Its name comes from using the three rotational components and the three translational components of motion from a single sensor. By also using the measurements of the rotational motions, ambiguities in the parameter estimation of the wavefield by using only translational components are eliminated (Maranò and Fäh, 2013). This procedure can obtain the local velocities and direction angles (inclination and azimuth) of body and surface

waves. The full description of the method is found in the work of Sollberger et al. (2018).

The method assumes plane wave propagation fronts, and the polarization model is inferred for each type of wave. The polarization vector is known for the translational motion components from sections 1.3 and 1.4. Now, the polarization vector **v** will have six components, described also adding the rotational motion components. The rotations are computed as follows:

$$\begin{pmatrix} \omega_x \\ \omega_y \\ \omega_z \end{pmatrix} = \frac{1}{2} \begin{pmatrix} \frac{\partial u_z}{\partial y} - \frac{\partial u_y}{\partial z} \\ \frac{\partial u_x}{\partial z} - \frac{\partial u_z}{\partial x} \\ \frac{\partial u_y}{\partial x} - \frac{\partial u_x}{\partial y} \end{pmatrix} \tag{1.46}$$

The boundary conditions at the free-surface imply the vertical stress tensor is zero, so the rotational motions become:

$$\begin{pmatrix} \omega_x \\ \omega_y \\ \omega_z \end{pmatrix} = \begin{pmatrix} \frac{\partial u_z}{\partial y} \\ -\frac{\partial u_z}{\partial x} \\ \frac{1}{2}\frac{\partial u_y}{\partial x} - \frac{\partial u_x}{\partial y} \end{pmatrix} \tag{1.47}$$

The 6-C wavefield at position **r** and time t can now be described with the translations and rotations as:

$$\Omega\left(\mathbf{r}, t\right) = A\omega\mathbf{v}\sin\left(\omega t - \mathbf{kr} + \phi\right) \tag{1.48}$$

where **v** is the polarization vector, including the rotational components.

In general, the rotational components are phase-shifted by $\pi/2$ with respect to the displacements. For that reason, translational velocities are used. Then, to have the same units between the translational and rotational signals, velocities are scaled by a factor p_s. If $p_s = 1/\beta_s$, where β_s is the local soil shear wave velocity (under the station), the amplitudes of translational and rotational components are comparable.

The polarization pure vectors **v** are defined for each type of wave at the free surface and account for the incident and the reflected wave in the case of body waves. Since the focus here are the surface waves, the polarization vector will be shown only for Rayleigh and Love waves.

For a Rayleigh wave, the polarization vector $\mathbf{v}_R$ is given by

$$\mathbf{v}_R = \begin{pmatrix} jp_s\sin\left(\xi\right)\cos\left(\phi\right) \\ jp_s\sin\left(\xi\right)\sin\left(\phi\right) \\ -p_s\cos\left(\xi\right) \\ \frac{1}{\beta_s}\cos\left(\xi\right)\sin\left(\phi\right) \\ -\frac{1}{\beta_s}\cos\left(\xi\right)\cos\left(\phi\right) \\ 0 \end{pmatrix} \tag{1.49}$$

where j indicates the phase-shift of $\pi/2$ between the horizontal components compared to the vertical and rotational components.

For Love waves, $\mathbf{v}_L$ is given by

$$\mathbf{v}_L = \begin{pmatrix} p_s \sin(\phi) \\ -p_s \cos(\phi) \\ 0 \\ 0 \\ 0 \\ \frac{1}{2\beta} \end{pmatrix} \tag{1.50}$$

From the polarization vectors, it is possible to notice that P-, SV- and Rayleigh waves can generate rocking or rotation over the horizontal components, while SH- and Love waves can only generate torsion or rotation over the vertical component.

Then, the matrix $\Omega_R(\mathbf{r}, t)$ describe the complete wavefield

$$\Omega_R(\mathbf{r}, t) = (\Omega_1, \Omega_2, \Omega_3, \Omega_4, \Omega_5, \Omega_6)^T(\mathbf{r}, t) \tag{1.51}$$

$$\Omega_R(\mathbf{r}, t) = (p_s u_x, p_s u_y, p_s u_z, \omega_x, \omega_y, \omega_z)^T(\mathbf{r}, t) \tag{1.52}$$

The method tries to find the polarization vector that best describes the data. The procedure starts by computing the analytic (complex-valued) signal $\tilde{\Omega}_R$ with the Hilbert transform:

$$\tilde{\Omega}_R(\mathbf{r}, t) = \tilde{\Omega}_R(\mathbf{r}, t) + jH\left[\tilde{\Omega}_R(\mathbf{r}, t)\right] \tag{1.53}$$

where $H[\bullet]$ is the Hilbert transform, which is the signal phase-shifted by $\pi/2$. Similar to MUSIC, the method constructs a coherency matrix with the product of the signal vector with its conjugate average over a time window of length W:

$$\mathbf{C}(\mathbf{r}, t) = \frac{1}{W} \sum_{i=i_0-W/2}^{i_0+W/2} \tilde{\Omega}_R(\mathbf{r}, t_i)\, \overline{\tilde{\Omega}_R}(\mathbf{r}, t) \tag{1.54}$$

The following is similar to MUSIC. The eigenvalues and eigenvectors are computed, and a likelihood function L is sought to be minimized. In this case, however, the parameters from the wavefield vector $\mathbf{v}$ are searched. The wavefield vector $\mathbf{v}(\mathbf{m})$ depends now on the polarization parameters $\mathbf{m}$, depending on each type of wave. For Rayleigh waves, $\mathbf{m}_R = (\phi, \xi, \beta)^T$ is defined by the azimuth ϕ, the wave ellipticity ξ and the local propagation velocity β. For Love waves, $\mathbf{m}_L = (\phi, \beta)^T$ can be defined by the azimuth ϕ and the local propagation velocity β. This method's advantage is that each wave type's parameters can be examined independently.

Once the parameters are retrieved, the determined type signal can be isolated by rotating the recorded signal Ω onto the polarization direction $\mathbf{v}(\mathbf{m})$.

1.6 Validation of the three identification methodologies

From the description of the three methods, some differences can be extracted. The NIP and the 6CPol take advantage of the particular polarization of surface waves (particle motion) to determine their characteristics based on one station. The MUSIC procedure needs arrays of seismic sensors as it searches for a dominant direction of propagation and propagation velocity (which determine the wave vector) of the signal passing through the array. Then, it discriminates the type of wave in terms of energy. Having the final objective of determining surface wave characteristics for seismic hazard analysis in mind, the NIP method clearly gives advantages for its simplicity. In the following chapters of the work, the NIP will be used because it needs little information (only three orthogonal time histories) and its formulation is faster (no grid search of parameters). The objective of the following is then to verify if a simple method (NIP) can be used to do the analyses for the inclusion of basin effects in the seismic design of infrastructures.

Therefore, the three methods will be compared in order to validate the accuracy of the NIP method by analyzing simultaneously problems with increasing wavefield complexity. In subsection 1.6.1, a simple theoretical signal is used, representing a Retrograde Rayleigh wave, where all the wave parameters are inherently known. Then, in subsection 1.6.2, the surface waves generated in a numerical MASW test are analyzed. In this case, the polarization direction is known as well as the medium properties. The complexity of the MASW problem then escalate when heterogeneities of the properties are added. Finally, in subsection 1.6.3 the most intricate media is investigated with real signals.

1.6.1 Application to theoretical signal

A first simple validation process will be conducted for the three procedures to simple theoric data. The signal is a pure Rayleigh wave passing through a set of monitors, used by Hobiger et al. (2011) in a similar validation procedure. This section aims to confirm that the three methodologies discover proper Rayleigh wave parameters. The characteristics of the motion are described hereafter.

1.6.1.1 Description of the signal

The analytical signal generated is a pure cosine of a frequency $f_c = 0.77$ Hz, a propagation velocity V_R of 1.69 km/s, and a propagation direction described by an azimuth with respect to the North of $\theta = 30^o$. The signal has a total time of 20 s.

The ellipticity of the wave is $\xi = 5$ (Equation 1.20), describing a retrograde motion. Figures 1.4 and 1.5 show the signal in time and time-frequency domain, with the Stockwell transform S, respectively.

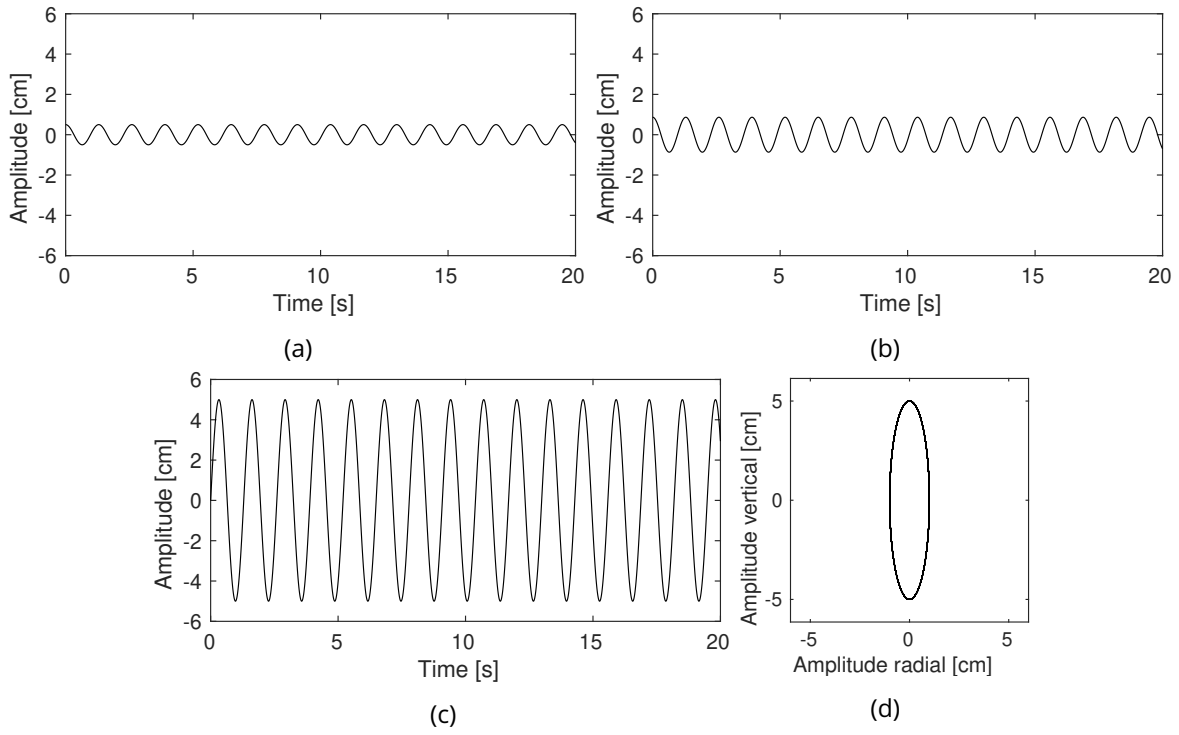

Figure 1.4: Synthetic signal (displacements) in time domain in (a) $East$ (b) $North$ (c) $Vertical$ components and (d) radial versus vertical.

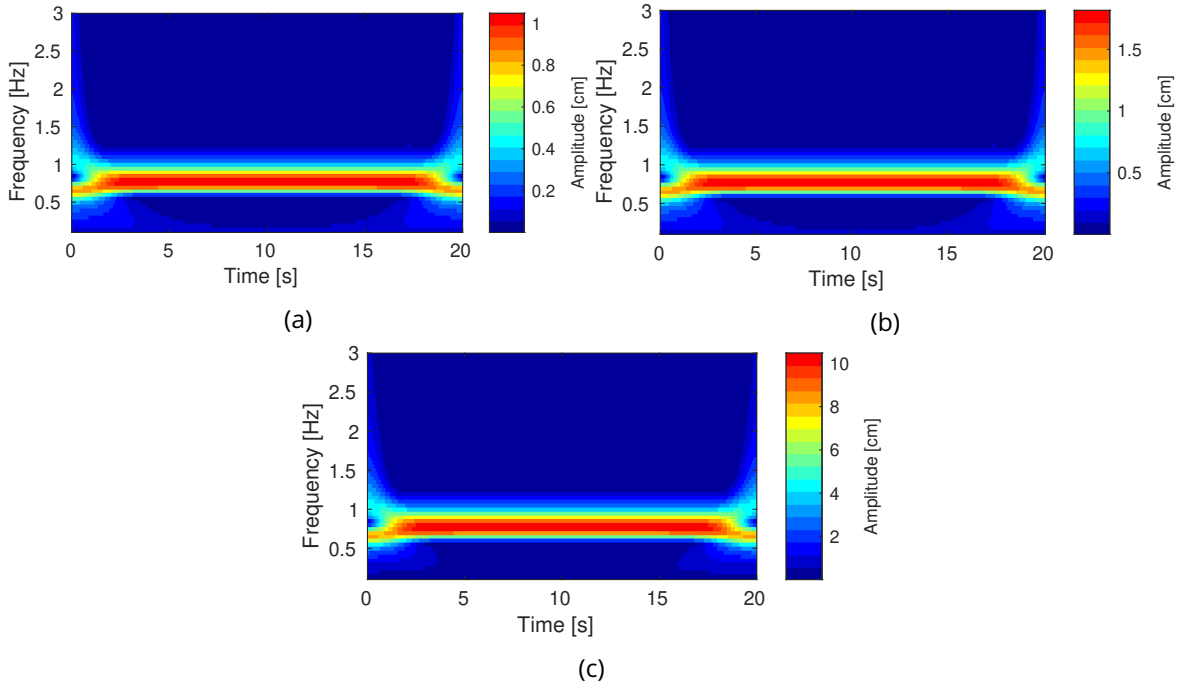

Figure 1.5: Representation of the synthetic signal in time-frequency domain in (a) S_N (b) S_E (c) S_V components using the Stockwell transform.

1.6.1.2 NIP

The validation of the NIP procedure for the synthetic signal is provided next. From the horizontal components signals $\mathbf{S}_N$ and $\mathbf{S}_E$ in $\tau - f$ domain from Figure 1.5, the angle of polarization $\theta\,(t, f)$ is computed using Equation 1.31.

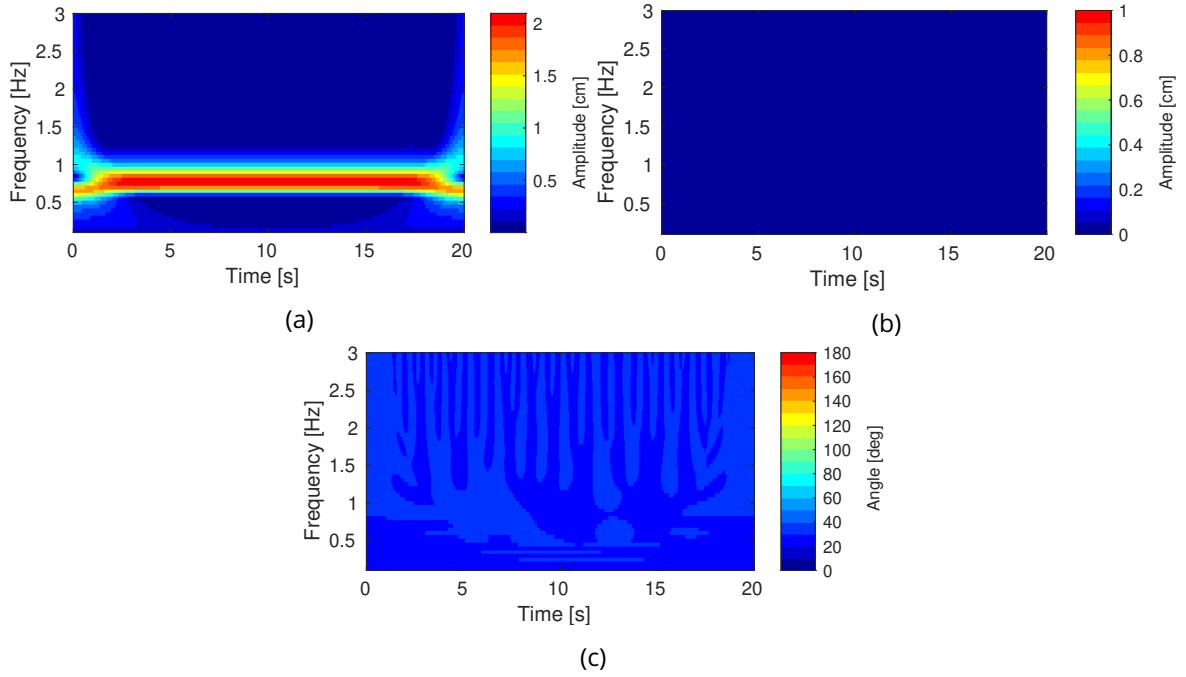

Figure 1.6: Using the NIP methodology, the (a) radial S_R and (b) transverse $\mathbf{S}_T$ components can be obtained in the time-frequency domain, including the (c) polarization angle θ of the wave.

The radial $\mathbf{S}_R\,(t, f)$ and transverse $\mathbf{S}_T\,(t, f)$ components are obtained from Equation 1.31. The angle of polarization $\theta\,(t, f)$ is obtained by selecting the angle where the $NIP\,(S_R, S_T)$ (between the two horizontal orthogonal components) is minimum. The analysis result in the $\mathbf{S}_R\,(t, f)$, $\mathbf{S}_T\,(t, f)$ and $\theta\,(t, f)$ displayed in Figure 1.6. Generally, most energy is close to the signal's frequency (0.77 Hz). From this Figure is observed that for an angle close to 30^o (Figure 1.6(c)), all the energy remains in the radial component, as it was expected (Figure 1.6(a)).

Next, zones in the $t-f$ domain with high cross-correlation between the radial and vertical are searched and filtered with the $NIP\,(\mathbf{S}_R, \mathbf{S}_{\overline{V}})$ (Figure 1.7a and b, after the filtering). The notation $\overline{V}$ refers to the phase-shifted vertical component, as the radial and vertical components are 90^o out-of-phase for Rayleigh waves. A value $NIP > 0.8$ is selected to have a good correlation. A cosine interpolation for NIP between 0.7 and 0.8 is used for a smoother filter avoiding any artefacts. The filter is then

$$F\,(x) = \begin{cases} 0 & \text{if } x \leq 0.7 \\ \frac{1}{2}\cos\left[\frac{\pi(x-.8)}{0.1}\right] + \frac{1}{2} & \text{if } 0.7 < x < 0.8 \\ 1 & \text{if } x \geq 0.8 \end{cases} \tag{1.55}$$

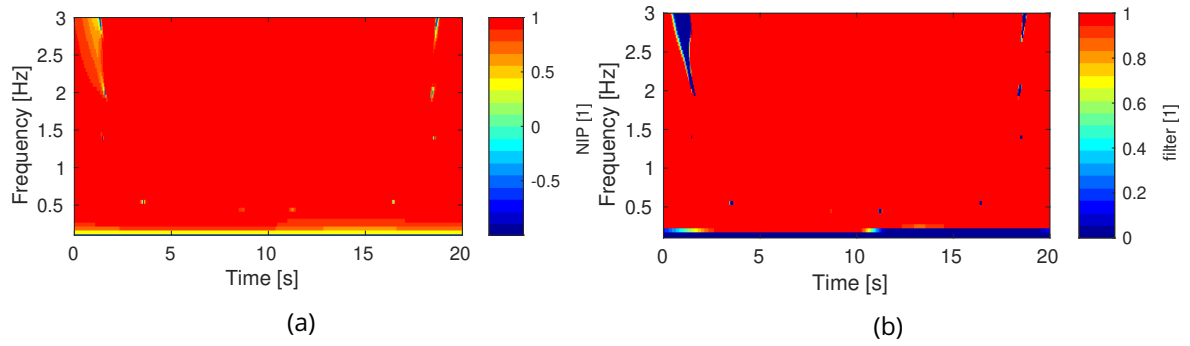

(a) (b)

Figure 1.7: (a) $NIP\left(\mathbf{S}_R, \mathbf{S}_{\overline{V}}\right)$ between the horizontal radial $\mathbf{S}_R$ and shifted vertical $\mathbf{S}_{\overline{V}}$ and (b) filter for high values $NIP\left(\mathbf{S}_R, \mathbf{S}_{\overline{V}}\right) > 0.7$.

where $x = NIP\left(\mathbf{S}_R, \mathbf{S}_{\overline{V}}\right)$. Then, $\mathbf{S}_R\left(t, f\right)$, $\mathbf{S}_T\left(t, f\right)$ and $\mathbf{S}_{\overline{V}}\left(t, f\right)$ are filtered and inverted with Equation 1.28, to obtain $x_R\left(t\right)$ and $x_{\overline{V}}\left(t\right)$, the horizontal al vertical isolated Rayleigh wave in the time domain, respectively. The vertical component is shifted to its original phase with the Hilbert transform H. Once the signal is isolated, the average azimuth is computed in time with Equation 1.34, which gives a value $\theta_R = 30°$. The results demonstrate that the NIP is capable of obtain the correct wavefield parameters.

1.6.1.3 6C Polarization Analysis

In addition to the translational components of Figure 1.4, for the 6C Polarization Analysis (6C-POL) procedure, the rotational components of the analyzed Rayleigh wave are computed theorically. The analysis is performed in acceleration for translational components and rotational velocities (Figures 1.8 and 1.9, respectively). The slowness factor ρ_s is selected as $1/v_R$.

The 6C-POL is performed by the open-source code of Sollberger et al. (2020) (available in `https://github.com/solldavid/6DOF_processing_tutorial` and also as a python toolbox, TwistPy). This code can make the analysis in the time or in the time-frequency domain.

In order to fit a polarization model to the data, two main methods are available: MUSIC and DOT. The MUSIC method was previously explained in section 1.5.2, and the DOT method is computed by using the dot product to minimize the angle between a theoretical model and the dominant polarization of the data in a vector formulation (Sollberger et al., 2020). For more information, please refer to Sollberger et al. (2020). With this code, the data was analyzed between 0 and 2 Hz, and the time-frequency domain was frequency-dependently discretized, selected as one time the wavelength and 0.01 times the frequency.

A total of 6040 time-frequency windows are analized in a total processing time of approximately 20 minutes (in each window the polarization model of Rayleigh wave is fitted to the observed data by grid-exploring the parameter space). In Figure 1.10, the likelihood is presented, ranging between 0 and 1. This parameter is 1 when the theoric and data polarization vector are parallel (for the DOT method). High values were obtained ($L > 0.8$), representing a good data fit for Rayleigh waves present in the data.

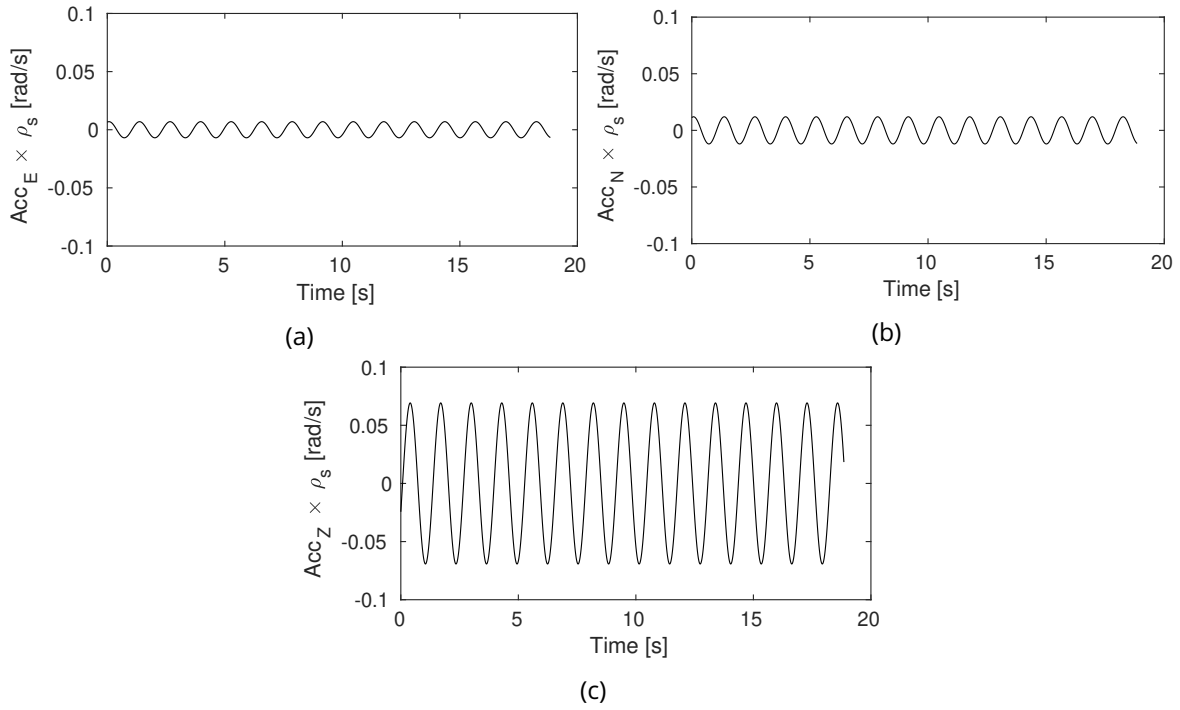

Figure 1.8: Acceleration time series in (a) $east$ (b) $north$ (c) $vertical$ components for the signals of Figure 1.4.

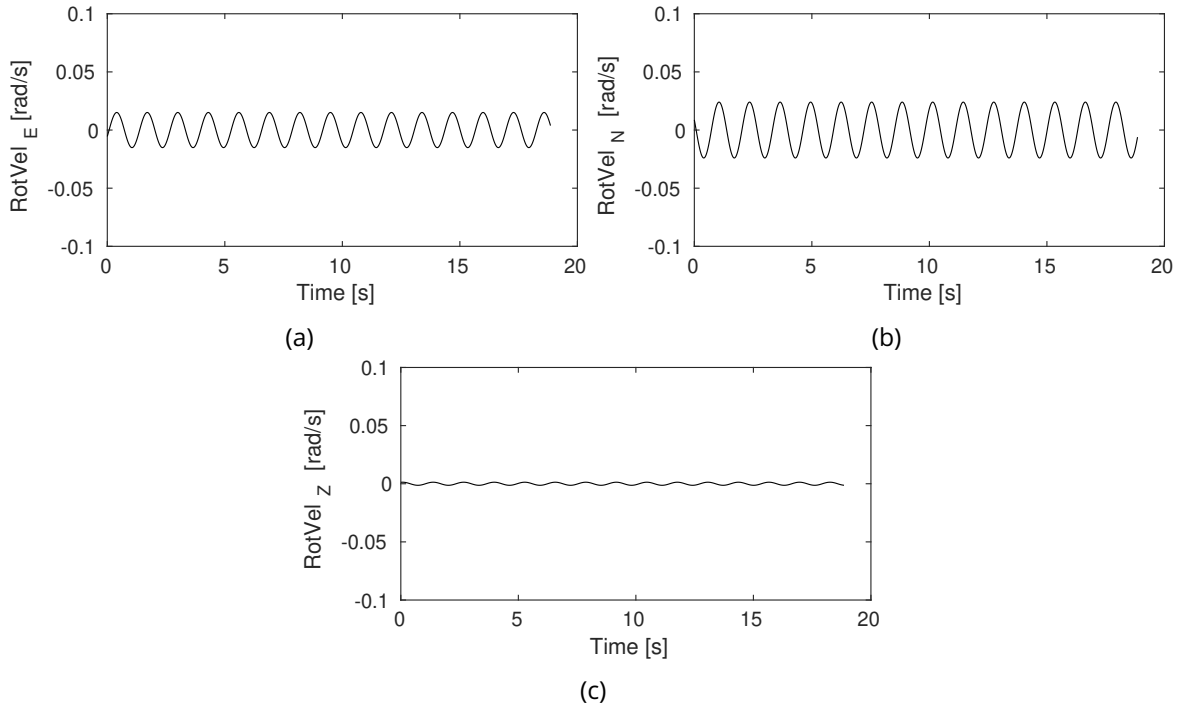

Figure 1.9: Rotational velocity time series in (a) $east$ (b) $north$ (c) $vertical$ components for the signals of Figure 1.4.

Moreover, characterization results for the wave are presented in Figure 1.11 in the time-frequency domain. The obtained azimuth, close to $30°$ is in excellent agreement with the theoric

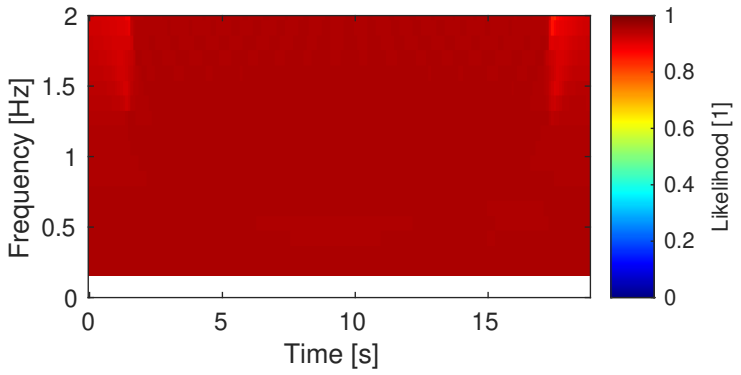

Figure 1.10: Likelihood of the 6C-POL procedure.

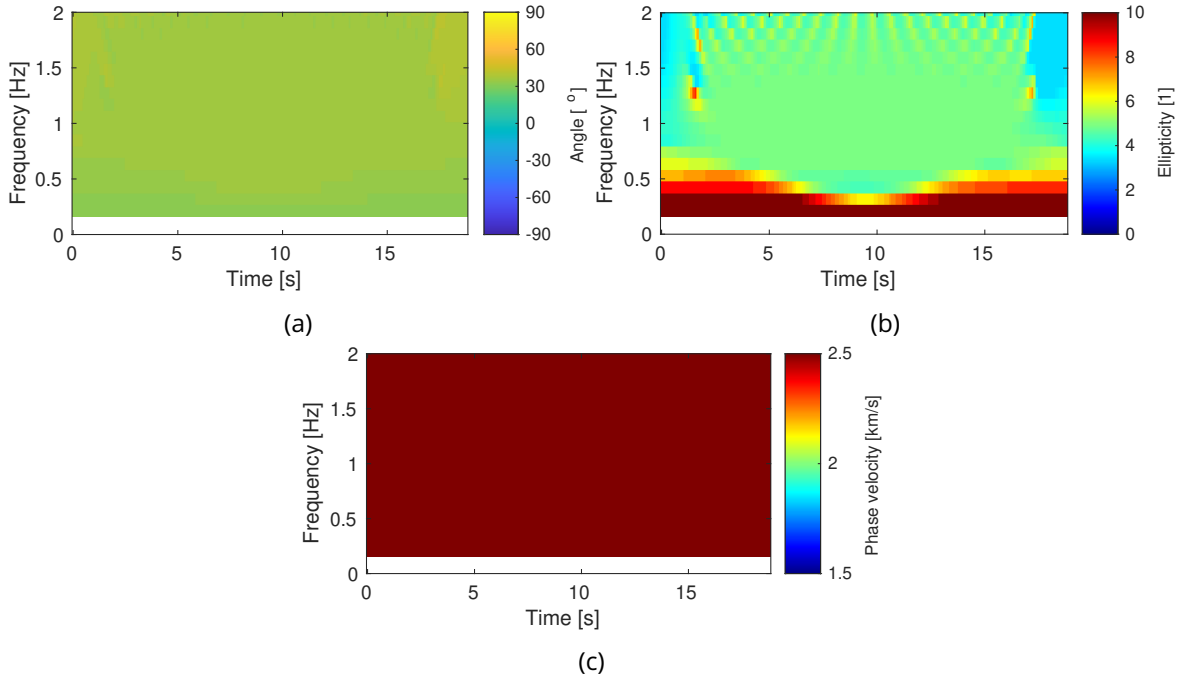

Figure 1.11: Time-frequency domain (a) azimuth, (b) ellipticity and (c) phase velocity obtained by the 6C-POL procedure.

in the whole domain. Besides, while more fluctuation in the ellipticity is observed, the obtained ξ from the data is similar to the theoric one ($\xi = 5$) in the frequency of interest. The phase velocity, on the contrary, is over-estimated. This parameter, in general, tends to be more unstable than the others as expressed by Zerva and Zhang (1996); Cornou et al. (2003b).

1.6.1.4 MUSIC

The MUSIC procedure demands a grid of stations. For the MUSIQUE procedure, the signal passes through 8 seismic stations, regularly spaced on a ring of a 1.0 km radius surrounding a central station (as displayed in Figure 1.12). The registered signal will have a delay depending on its position, as seen in Figure 1.12 on the left. The signal will be analyzed only around the desired

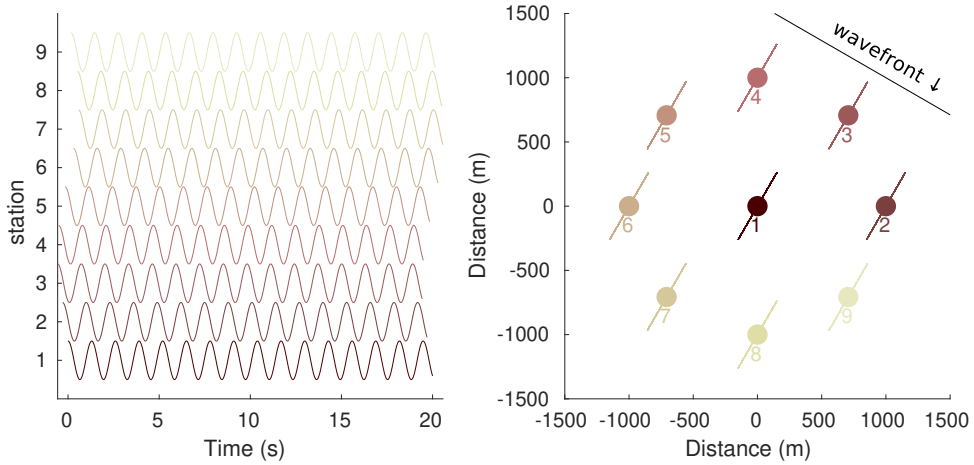

Figure 1.12: Synthetically generated signal passing through 9 stations, used for the MUSIC method application.

frequency, filtered with a Chevyshev filter and separated into time windows of three times the wavelength ($t_s = 3.9$ s).

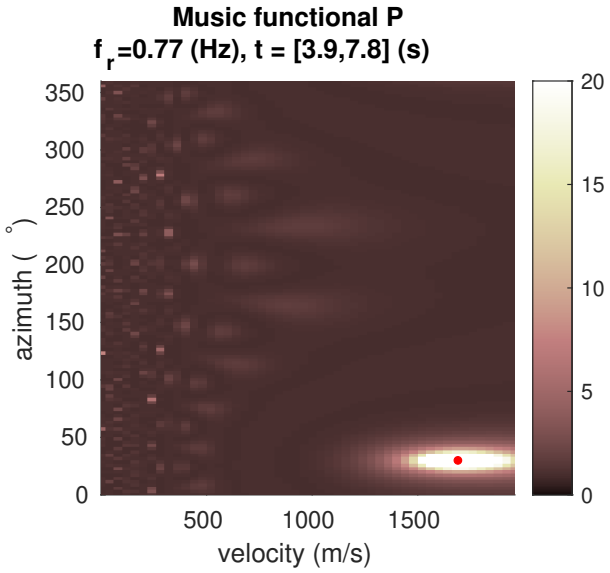

Figure 1.13: MUSIC functional P, to find the velocity and azimuth of the Rayleigh wave signal. The red dot shows the real wave parameters.

Figure 1.13 shows the functional P, or likelihood, in terms of the velocity and azimuth. The function has a maximum value around the real value parameters, described by a red dot, where the azimuth (in the vertical axis) is better retrieved than the velocity of propagation in the horizontal direction. This result is in agreement with the previously obtained with the 6C-Pol procedure.

The findings of this section lead to the partial conclusion that the three approaches can recover the right wave parameters (polarization azimuth angle) from simple data. However, there are key differences in terms of the amount of input data needed. The MUSIC needs a handful of receivers and the 6CPol the rotational components, while the NIP only needs a three-component

seismogram. For that reason, in more realistic scenarios only one method should be preferred. Next, a more complex case is modelled by using a numerical MASW test, in order to contrast the three methodologies.

1.6.2 Application to synthetically generated signals (MASW test)

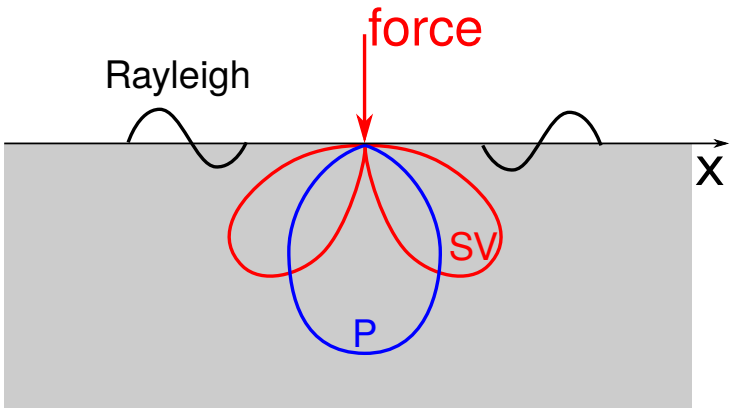

Figure 1.14: Schematic representation of a vertical force acting on the free surface, with the generation of P, SV and Rayleigh waves. Modified from Kennett and Fichtner (2020).

A more realistic scenario will be examined in this section with synthetically generated Rayleigh waves (MASW test). Rayleigh waves in an elastic halfspace can be generated by an impulsive vertical force acting on the free surface, commonly named as *active-source* seismic test (Foti et al., 2015; Igel, 2016, among others). The reaction of the ground from this impulse can be approximated by a force dipole represented in Figure 1.14. P-wave radiation is produced with the largest radiation oriented vertically. SV-wave radiation is generated with a propagation angle of around 45 degrees to the vertical. Besides, a significant fraction of energy is carried out in the form of fundamental mode Rayleigh waves (Kennett and Fichtner, 2020). Since geometric attenuation is higher for body waves than for surface waves, as seen in previous chapters, at a distance of the order of one or two wavelengths from the source, the wavefield is dominated by Rayleigh waves (Foti et al., 2015). Therefore, this section makes use of the experiment to validate the identification methodologies in numerically simulated Rayleigh waves.

The presented numerical simulation of an active source seismic experiment was performed by Riaño and Lopez-Caballero (2021) in a 3D spectral element method (SEM) model. The realistic model represents the site of Argostoli, located in Kefalonia island, western Greece region. The objective of the original work was to retrieve the shear wave velocity profile with the Multichannel Analysis of Surface Waves (MASW) technique (Park et al., 1998), by using the frequency-dependent phase velocity of Rayleigh waves. In this work, the simulated time histories at the surface will be used to evaluate the surface wave characteristics with the NIP, MUSIC and 6C Pol methodologies. For the sake of briefty, more details about the obtained results of the MASW inversion are not provided here, please refer to Riaño and Lopez-Caballero (2021).

1.6.2.1 Description of the model

A simulation of the MASW technique in the Argostoli basin was performed, situated on the Island of Kefalonia, Greece. During the project SINAPS@ (Cushing et al., 2016), an accelerometer network ARGONET was installed, and the geomechanical properties of the site are well characterized (Sbaa et al., 2017; Cushing et al., 2016, 2020; Berge-Thierry et al., 2020, among others).

The simulation was carried out in SEM3D (CEA and CentraleSupélec and IPGP and CNRS, 2017). The model size for the MASW test is selected to fully contain the basin and avoid reflections at the borders, of dimensions (East-West, North-South and Depth) of about $9 \times 9 \times 1$ km. The mesh is not-honouring, i.e., the mesh does not follow the geometrical interfaces, and the material properties are assigned to each *Gauss-Lobato-Legendre* (GLL) point independently. Thanks to this technique, the mesh is constituted by regular elements of a minimum size of $5 \times 5 \times 5$ m at the surface and a maximum size of $45 \times 45 \times 45$ m in deeper parts of the model, with a total of 15 million elements for a maximum frequency of 30 Hz.

The 3D structure of the Argostoli basin was described extensively by several authors (e.g. Cushing et al., 2016, 2020). Particularly, for the local scale, the material properties of the sediment fill and the surrounding rock were developed by Cushing et al. (2020), based on dispersion curves. Three soil layers were identified, soft-soil, stiff-soil and bedrock, with shear wave velocity V_s values dependent on the depth z in meters, given by the expressions and Figure 1.15. The units of V_s are in m/s.

$$V_{s,softsoil}(z) = \begin{cases} 250 & 0 \leq z \leq 2 \\ 9.2z + 122 & 2 < z \leq 26 \\ 4.5z + 242 & z > 26 \end{cases} \quad (1.56)$$

$$V_{s,stiffsoil}(z) = 1.5h + 650 \quad (1.57)$$

$$V_{s,bedrock}(z) = \begin{cases} 11.7z + 650 & 0 \leq z \leq 30 \\ 4.7z + 858 & 30 < z \leq 400 \\ 0.8z + 2430 & 400 < z \leq 1000 \\ 3230 & z > 1000 \end{cases} \quad (1.58)$$

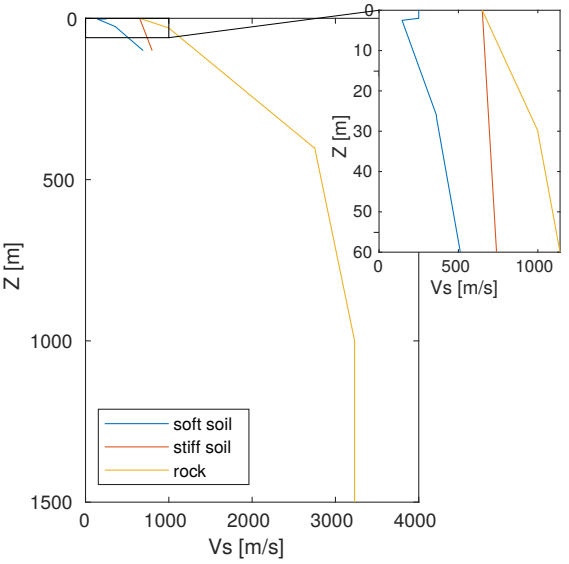

Figure 1.15: Shear wave velocity (V_S) model for the three layers of the Argostoli basin. Modified from Riaño and Lopez-Caballero (2021) and Cushing et al. (2020).

Figure 1.16 shows the velocity model for a selected section of the model where the interface between layers can be observed. The minimum shear wave velocity is $V_s = 168$ m/s located at 2-meters depth and the maximum depth of the sediments is approximately 150 m (Cushing

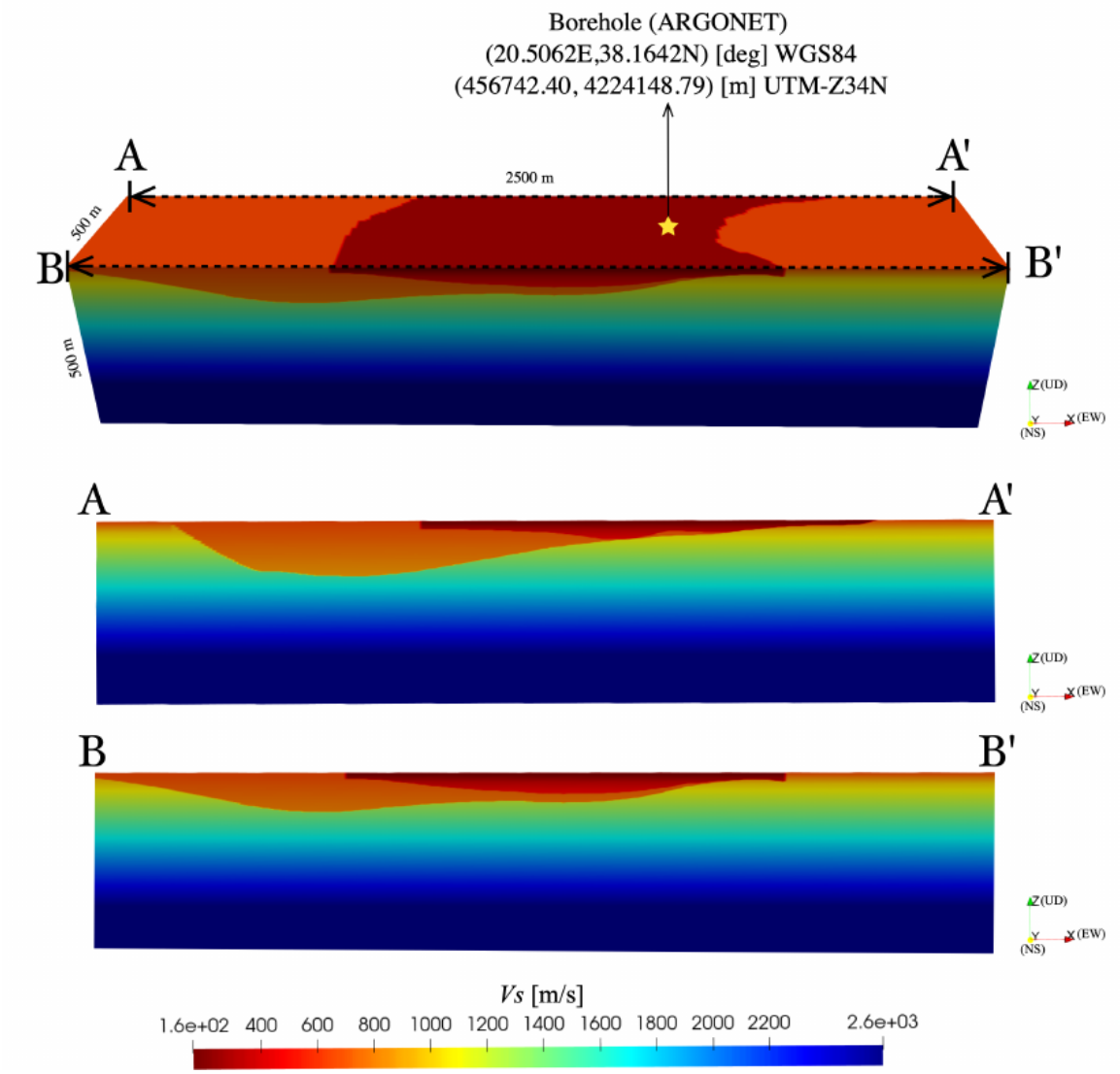

Figure 1.16: Shear wave velocity section of a small portion of the numerical model used for the MASW simulation. The basin-setting is observed around the ARGONET station, where the vertical load has been applied. Retrieved from Riaño and Lopez-Caballero (2021).

et al., 2020). The compressional wave velocity V_p is defined in terms of the V_s. The density ρ is 2400 kg/m^3 for the soft soil, 2800 kg/m^3 for the stiff soil and 3300 kg/m^3 for the bedrock. The Figure also displays the ARGONET station position in the soft sediments area, where the active source load was applied for the MASW test.

In Riaño and Lopez-Caballero (2021), the MASW procedure was carried out to extract the V_s profile in the ARGONET borehole site. The active source load (Figure 1.17a) was applied at the surface in the ARGONET coordinates (Figure 1.17a in blue). The stations of the linear array were displayed in the East-West direction every 2 m, with an offset from the source of 20 m. The simulation time was set to 4 s, and to be performed in 2000 CPU processors a total wall clock of 12 hours was required. Figure 1.18 shows the recorded horizontal (left) and vertical (right)

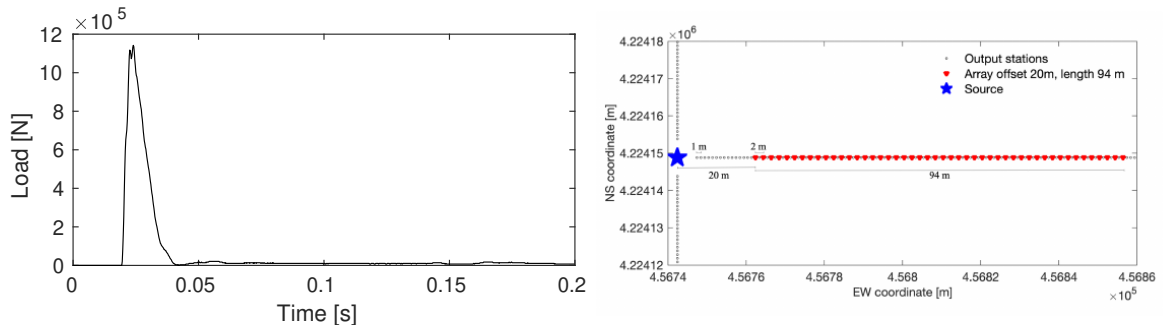

(a) (b)

Figure 1.17: (a) Applied vertical impulsive force and (b) stations selected for MASW test simulation. The blue star represents the position of the force. Retrieved from Riaño and Lopez-Caballero (2021).

displacements time series at the stations.

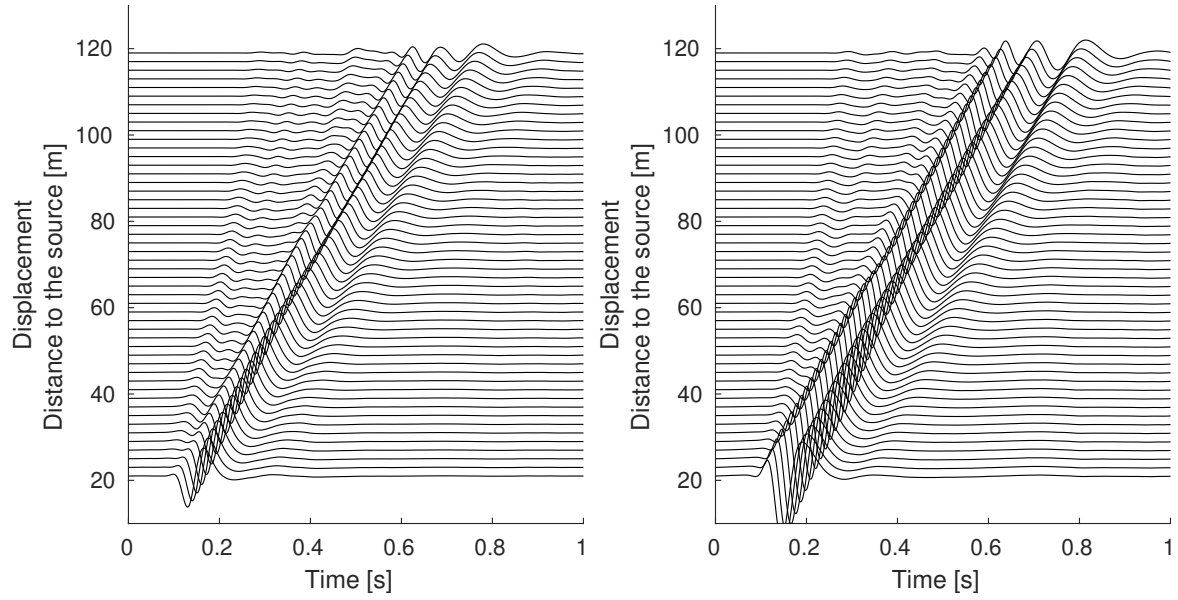

(a) Horizontal (b) Vertical

Figure 1.18: Obtained seismograms (displacement time series) from simulated MASW test along the array.

Due to the simulation characteristics (i.e., maximum frequency, loading case), the surface wave analysis is performed between 5 and 20 Hz.

1.6.2.2 Time signals of the extracted surface waves

One of the advantages of the 6C-polarization and NIP procedures is that time histories of the surface waves can be obtained directly from the ground motions. For this reason, the extracted signals are compared against the original displacement time histories for all the monitors along the array.

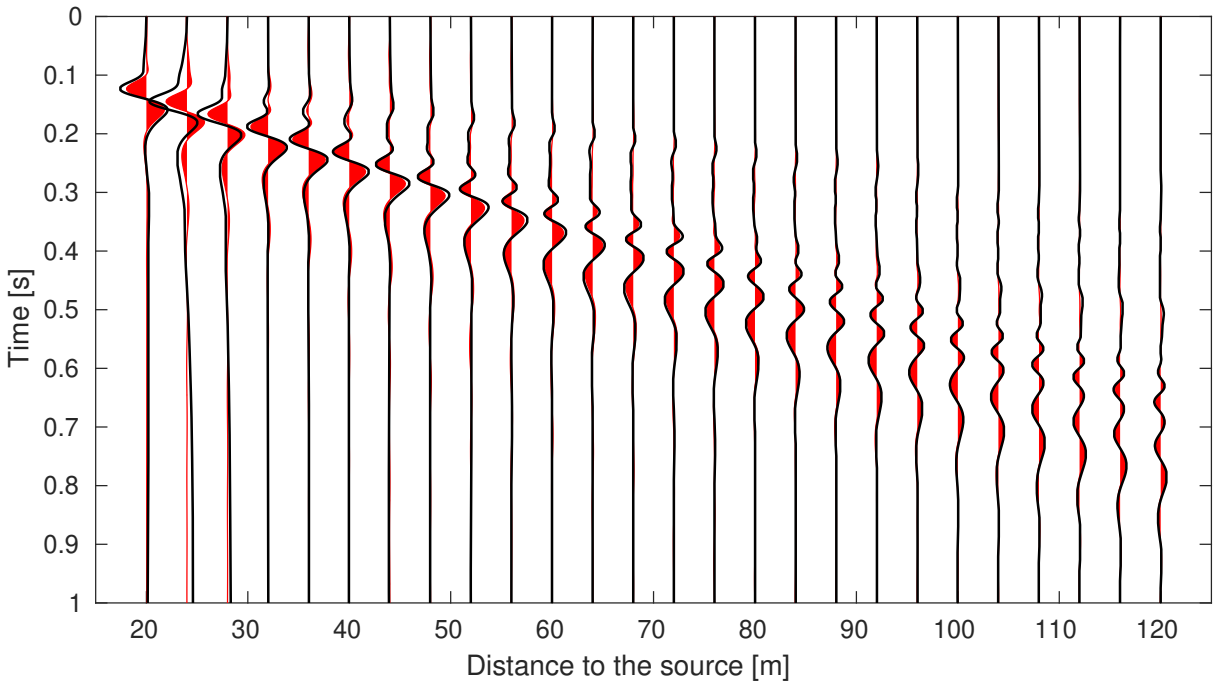

Figure 1.19: Extracted Rayleigh waves (in red), obtained with the NIP method, compared to the total displacement (in black).

For the NIP procedure in Figure 1.19, the displacement time histories are represented in red for the extracted waves and in black for the original signal. As expected, it can be seen that most of the original signal is classified as a Retrograde Rayleigh wave.

For the 6C-Pol methodology, rotations are needed and computed numerically with:

$$\begin{pmatrix} \omega_x \\ \omega_y \\ \omega_z \end{pmatrix} = \begin{pmatrix} \frac{\Delta u_z}{\Delta y} \\ -\frac{\Delta u_z}{\Delta x} \\ \frac{1}{2}\frac{\Delta u_y}{\Delta x} - \frac{\Delta u_x}{\Delta y} \end{pmatrix} \tag{1.59}$$

where $\Delta x = \Delta y = \Delta z = 4$ m is the distance between two receivers.

Only six signals from the array were chosen for examination because the 6C-Pol technique requires more calculation time, associated to the fact that it needs a grid search for the parameters in the frequency-time domain. Figure 1.20 presents the vertical $\ddot{u}_z$ and horizontal $\ddot{u}_x$ accelerations and the rotational velocity $\dot{\omega}_y$ over the y direction in the selected positions. The scaling parameter $p_s = 1/168$ s/m is selected from the minimum value of the shear wave velocity model (Riaño and Lopez-Caballero, 2021). With this value, amplitudes of the rotational velocity and the horizontal acceleration are comparable.

The outcome is similar to the NIP technique for the 6CPol in Figure 1.21, considering most of the signal in general is identified and isolated as a Rayleigh wave, for translational and rotational motions. The majority of the signal is correctly isolated as a Rayleigh wave using both techniques, NIP and 6CPol. Because of the output of MUSIC method is the energy and not directly the time signals, only their estimated surface waves parameters are going to be investigated in the next

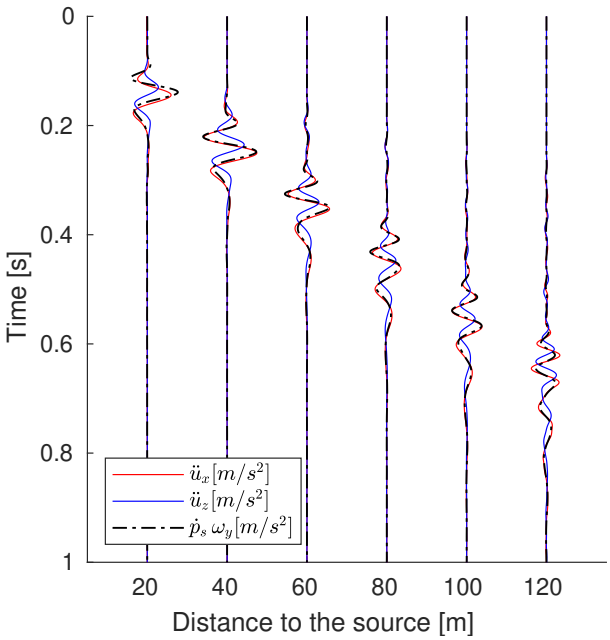

Figure 1.20: Accelerations (blue z, red x) and rotational velocity (black) in six selected receivers, used as input in the 6CPol.

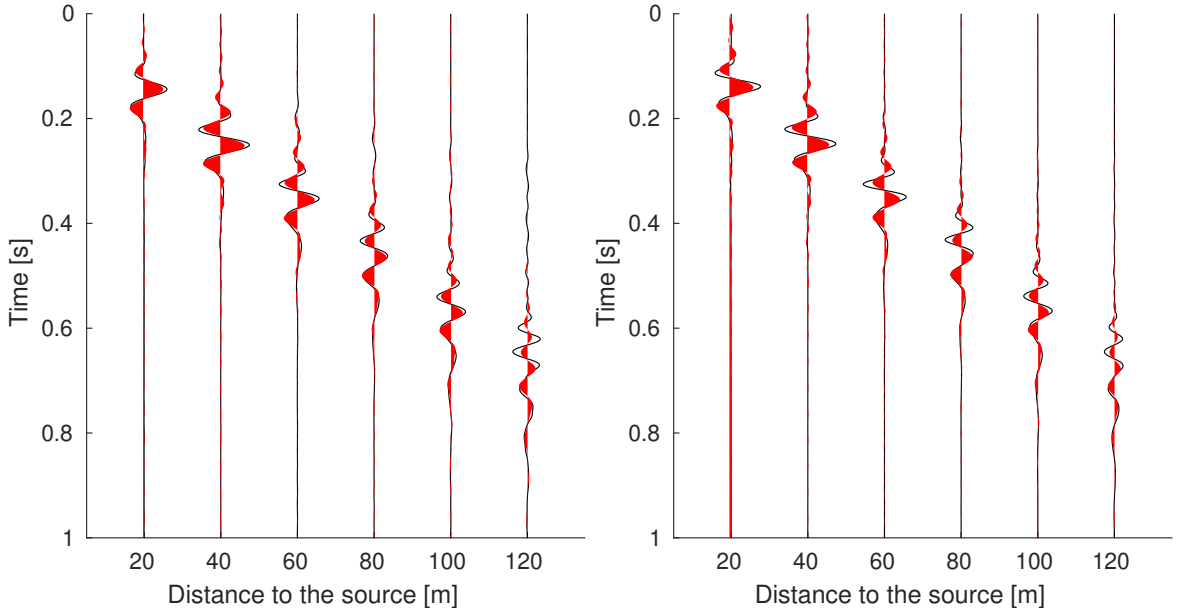

(a) Translational vertical acceleration

(b) Rotational velocity in the x component

Figure 1.21: Isolated wave with the 6CPol (in red) in comparison to the original signal (in black).

subsection.

1.6.2.3 Surface wave parameters

The surface waves characteristics parameters such as the azimuth of the polarization, amplitude of the horizontal/vertical components and carried energy allow to give an insigth into the pro-

portion of surface waves in the wavefield (Cornou and Bard, 2003; Meza-Fajardo et al., 2021). As a result, the parameters pretend to directly quantify the amplification of the ground motion induced by surface waves. Therefore, the surface wave characteristics obtained with the three methodologies in the MASW test are presented next.

First, the MUSIC procedure requires multiple recorders, so the analysis was done including all the stations. The results are presented for three frequencies: 5, 10 and 15 Hz (Figure 1.22 for one selected time-window). The time window length in this case is frequency dependent and selected as ten times the period (the inverse of the analyzed frequency).

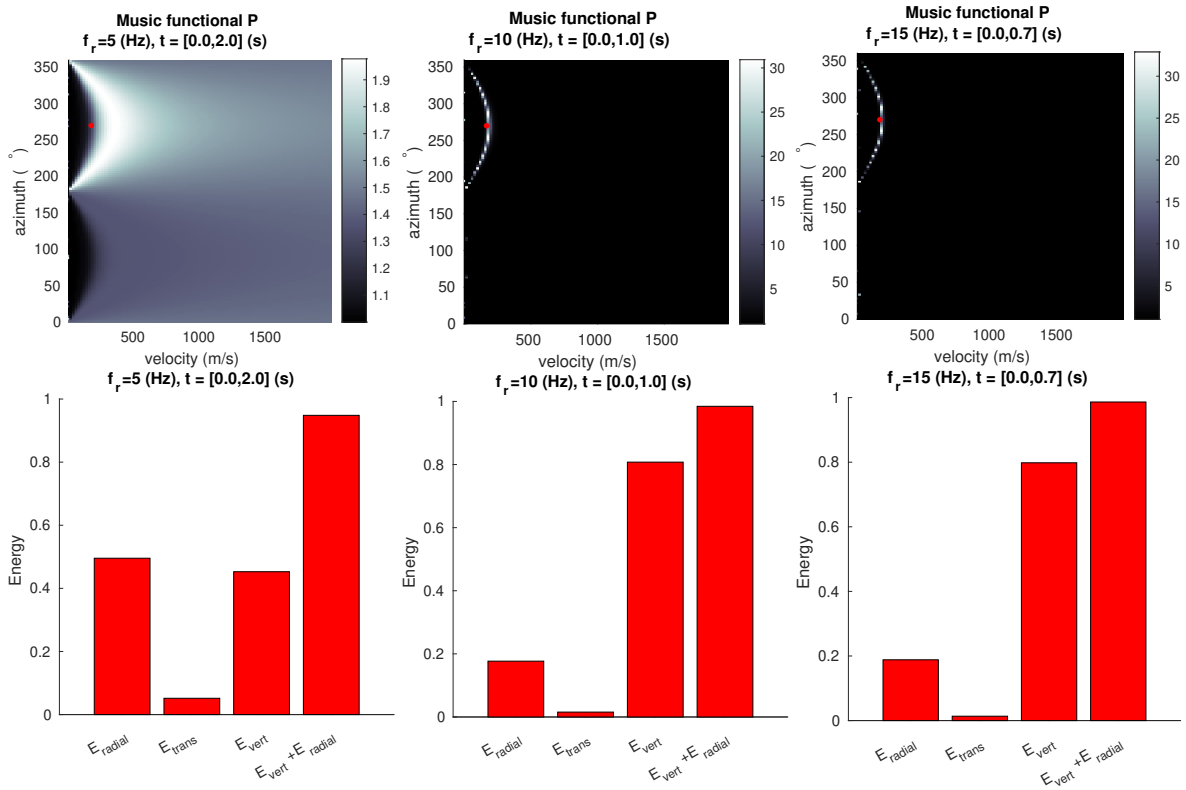

(a) 5 Hz (b) 10 Hz (c) 15 Hz

Figure 1.22: MUSIC analysis of MASW test for three different frequencies: (a) 5 Hz, (b) 10 Hz and (c) 15 Hz. The upper figure shows the parameters grid, where higher value of the functional P is searched to determine the wave vector. The lower figure show the distribution of energies in the selected time window.

In the lower frequency of 5 Hz, the wave parameters are poorly estimated by the MUSIC functional P as shown in Figure 1.22a. However, for higher frequencies (10 and 20 Hz in Figures 1.22b and 1.22c, respectively), the results can retrieve the correct wave parameters (azimuth and velocity). The obtained velocity of the Rayleigh wave is close to the shear wave velocity properties at the surface for higher frequencies, while for 5 Hz the obtained velocity seems to be higher, similar to expected values from the dispersion theory.

Alternatively, for the 6CPol method, the parameters are shown in the time-frequency space in Figure 1.23. The likelihood is presented in Figure 1.23, higher values are observed from 5 to

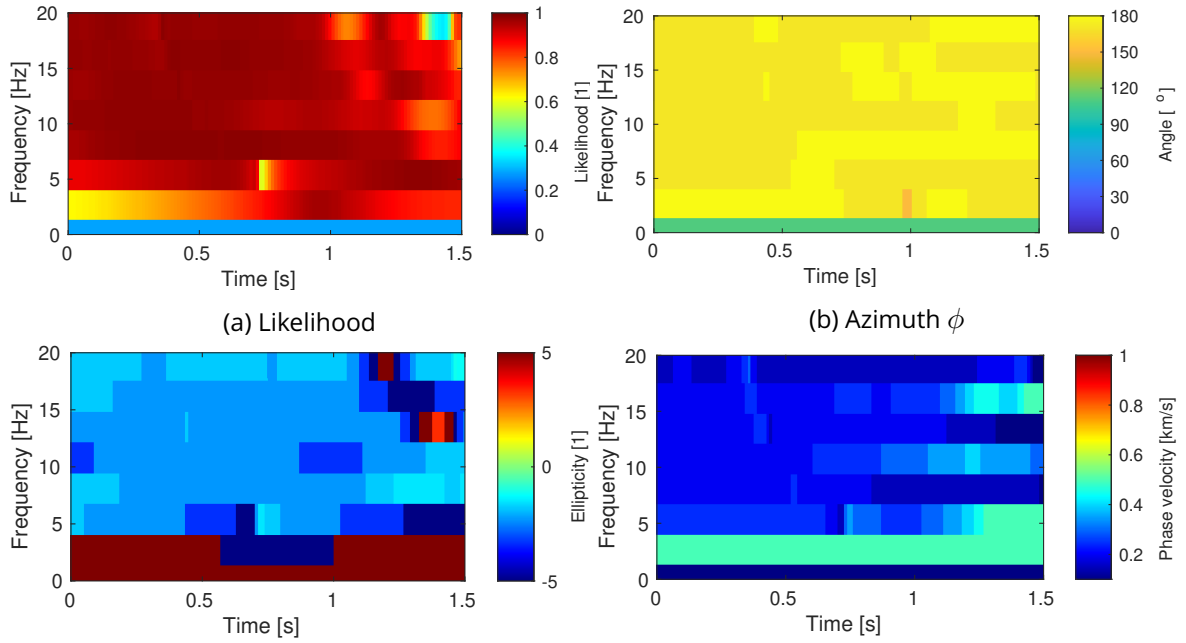

(a) Likelihood (b) Azimuth ϕ

(c) Ellipticity ξ (d) Phase velocity v_R

Figure 1.23: Time-frequency domain (a) Likelihood, (b) azimuth, (c) ellipticity (d) phase velocity and obtained by the 6CPol in one station of the MASW array.

20 Hz. The angle is close to $180°$, associated to a wave propagating from the west to the east, for all frequencies and times on the grid. The phase velocity seems to increase with increasing frequency, showing the expected dispersion with frequency. The obtained ellipticity is negative, assuming a retrograde polarized motion of the Rayleigh waves.

Finally, the surface wave parameters, namely the azimuth, central frequency f_{cen}, maximum amplitude A_{POL} and correlation coefficient between the polarized and vertical components C_{PV} are obtained for the NIP method. The NIP was applied at each receiver independently, so the spatial variability of the parameters along the MASW array can be assessed as shown in Figure 1.24 in red dots. In terms of the correlation factor between the polarized and vertical components, C_{PV}, good results are obtained with the NIP, where $C_{PV} > 0.7$ in most of the array. As expected, the azimuth coincides with the Rayleigh wave travelling from west to east. The central frequency f_{cen} varies between 12 and 15 Hz, mainly due to the source characteristics. In addition, the amplitude of the extracted Rayleigh waves exhibits a good agreement with the theoretical amplitude decrease as $1/\sqrt{r}$, signalled in the Figure by a black line.

The three methodologies have been contrasted and their capacity is herein briefly discussed. The MUSIC, NIP and 6CPol are able to find the polarization direction (azimuth angle) and the proportion of the surface waves in the total ground motion correctly (NIP and 6CPol with the time histories, MUSIC with the carried energy). Nevertheless, because the NIP only requires a single station, the spatial variability of the polarization characteristics within the array could be assessed. The obtention of varying values at different locations is practical for finding a relation between surface wave characteristics with basin amplification patterns.

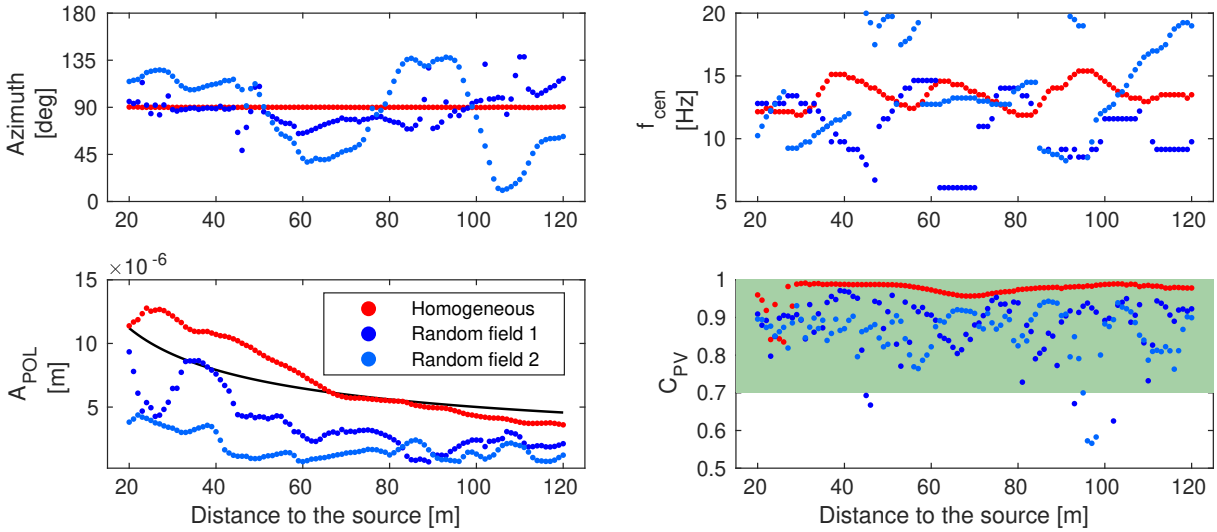

Figure 1.24: Rayleigh wave characteristics obtained by the NIP along the MASW array: Azimuth of the polarized direction of motion, central frequency f_{cen}, maximum amplitude of the horizontal polarized wave A_{POL} and correlation coefficient C_{PV}, between polarized and shifted vertical wave, to discriminate the obtention of the wave. In red, the results when using homogeneous properties and in blue when fluctuaction of the material properties are added to the sedimentary layers.

For instance, in some practical cases, when soil material heterogeneities are present, the wave characteristics are expected to change within close distances (El Haber et al., 2019). The next section is dedicated to the evaluation of the surface waves properties propagating from the same MASW experiment in a heterogeneous soil media.

1.6.2.4 Effects of the material heterogeneities

The numerical simulation of the active MASW test generates surface waves propagating horizontally along the receivers. The influence of spatially variable material properties on the surface wave characteristics is investigated in this section. It is well know that the waves will be scattered due to small-scale heterogeneities in the soil properties (Greenhalgh et al., 2008; Gatti et al., 2017; Svay et al., 2017; Imtiaz et al., 2017, among others). Therefore, limitations of the identification methodologies to a scattered wavefield are discussed. For the sake of briefty, only the NIP method is used.

In general, a random heterogeneous media is numerically modelled by a random field, composed by an autocorrelation function imposed on a homogeneous background. The function is described in terms of the length scale of the heterogeneity and the standard deviation of the material properties' fluctuation. In this example, the heterogeneities have been added to the shear wave velocity, V_s, of the sediment layers (soft and stiff soil), following the work of de Carvalho Paludo et al. (2019), and all the other material parameters have remained constant. The field was generated with a Von Karman auto-correlation function with correlation lengths ℓ_{C-x},ℓ_{C-y} and ℓ_{C-z} equal to 50 m and coefficient of variation $CV = 0.3$. These values are less than

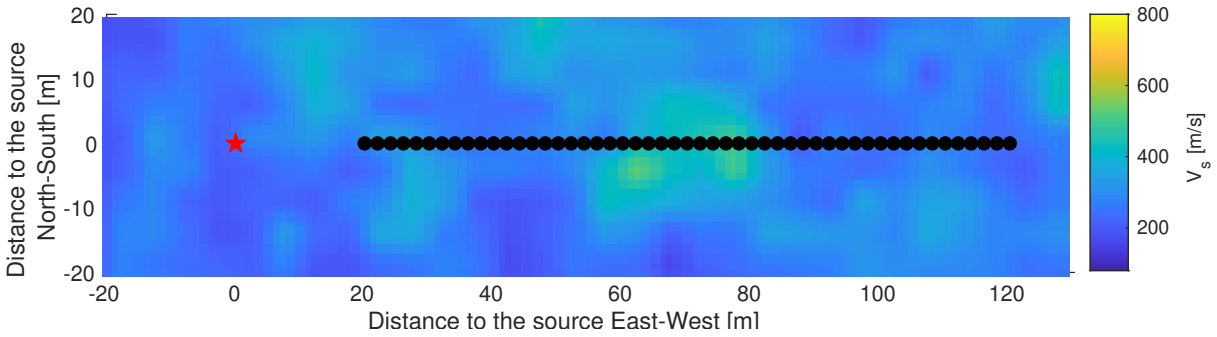

(a) XY plane at the surface ($z = 0$ m).

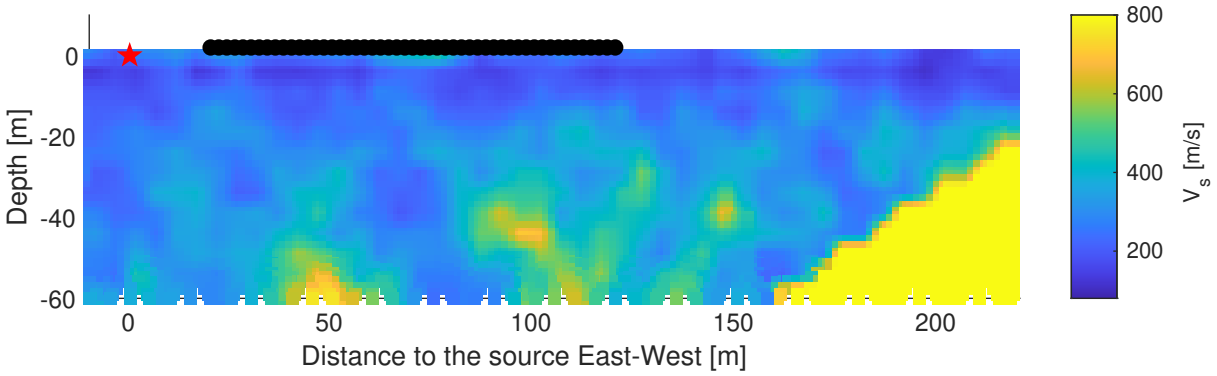

(b) XZ along the array.

Figure 1.25: Shear wave velocity V_s of the sediment at the surface, generated by a random field evaluated at the GLL points of the mesh. The source and position of the selected monitors are displayed by the red star and the black dots, respectively. The sediments-bedrock interface can be seen between the sediments and the yellow area in the bottom right of Figure b which correspond to bedrock materials.

the depth of the sedimentary basin, allowing a significant scattering of the waves (Tchawe et al., 2021). In this part, two different random seeds are used to provide two different random fields. The V_s values extrapolated in the SEM3D model for one of the studied cases are presented in Figure 1.25.

The seismograms contrasting the heterogeneous to the homogeneous case are displayed in Figure 1.26, showing higher attenuation of the main Rayleigh wave with distance when heterogeneities are present.

The scattered behavior in the heterogeneous model is evaluated next with two approaches: local directivity δ and coherency functions. A first insight into the wave scattering produced by the heterogeneous media can be given by the parameter δ (Arias, 1996), associated to the local directivity of ground motion, in order to check if the angle of propagation of the surface wave is deflected due to the heterogeneous media. Arias (1996) defined the dominant orientation of the horizontal ground motion as a value δ:

$$\delta = \frac{\left[(I_{xx} - I_{yy})^2 + 4I_{xy}^2\right]^{1/2}}{I_{xx} + I_{yy}} \tag{1.60}$$

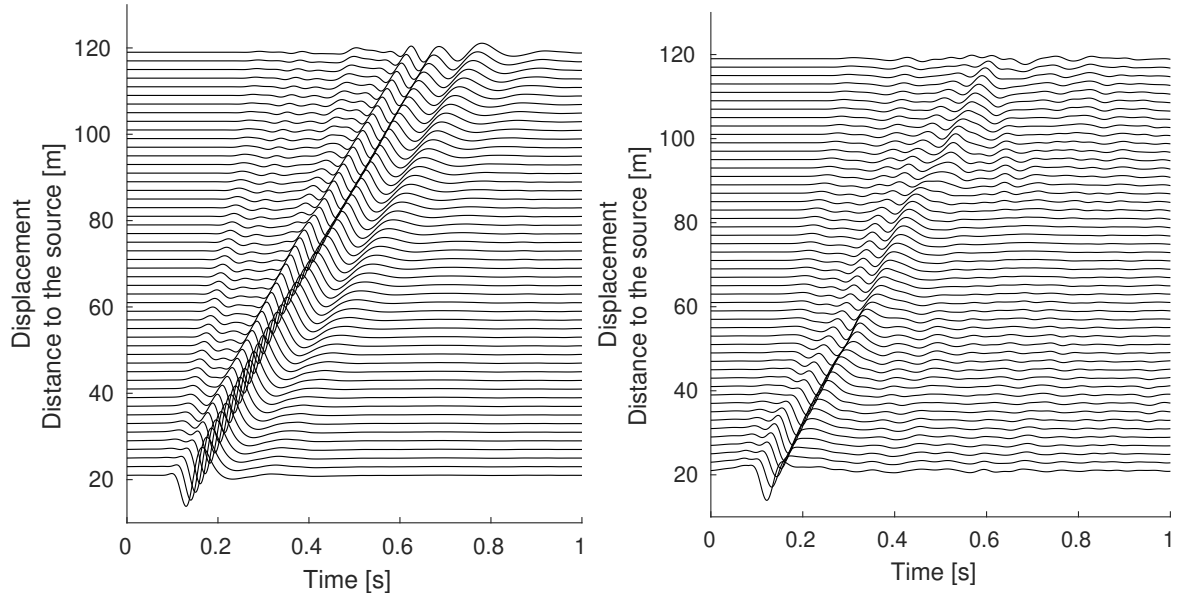

Figure 1.26: Horizontal displacement histories using (a) the homogeneous model presented in the previous section and (b) a heterogeneous model using a random field to generate the soil properties.

where I_{rs} is the Arias Intensity between the component r and the component s computed as:

$$I_{rs} = \frac{\pi}{2g} \int_0^{t_0} a_r(t) a_s(t) dt \tag{1.61}$$

The local directivity δ ranges between $[0, 1]$, and it is close to zero when the two components are comparable and close to the unit when the ground motion has one preferential direction. Clearly shown by Figure 1.27, the homogeneous case shows a δ close to 1, since the wave is polarized in the x-direction. When heterogeneities are added into the material, in contrast, this preferential direction blurs, showing an extensive range of directionality values, representing various dominant orientations (Arias, 1996; Xu et al., 2003).

Additionally, the spatial variability of the heterogeous effect on the surface waves ground motion can be analyzed with coherency functions, which represent a measure of relation between two signals. Traditionally, the coherency for two ground motions (subscript j and k) is defined by Abrahamson et al. (1991) as

$$\gamma_{jk}(f) = \frac{S_{jk}(f)}{\sqrt{S_{jj}(f) \cdot S_{kk}(f)}} \tag{1.62}$$

where $S(f)$ is the smoothed cross-spectrum computed with the power spectral density and f is the frequency. One specific type of coherency function is used here, called the plane wave coherency function γ_{jk}^{PW}, representing an unlagged coherency by removing the wave passage effects assuming a plane wave incidence (Abrahamson et al., 1991; Svay et al., 2017). This proce-

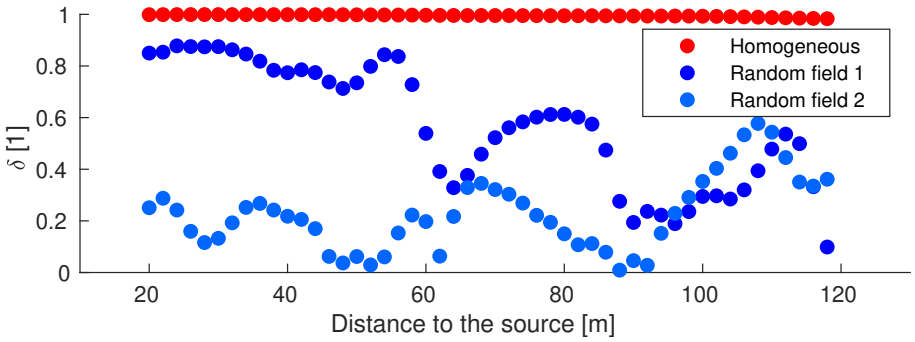

Figure 1.27: Directionality δ values for the horizontal components of the signals along the array, representing a unique dominant orientation when the value is close to 1 (Arias, 1996). In red, the results when using homogeneous properties and in blue when fluctuaction of the material properties are added to the sedimentary layers.

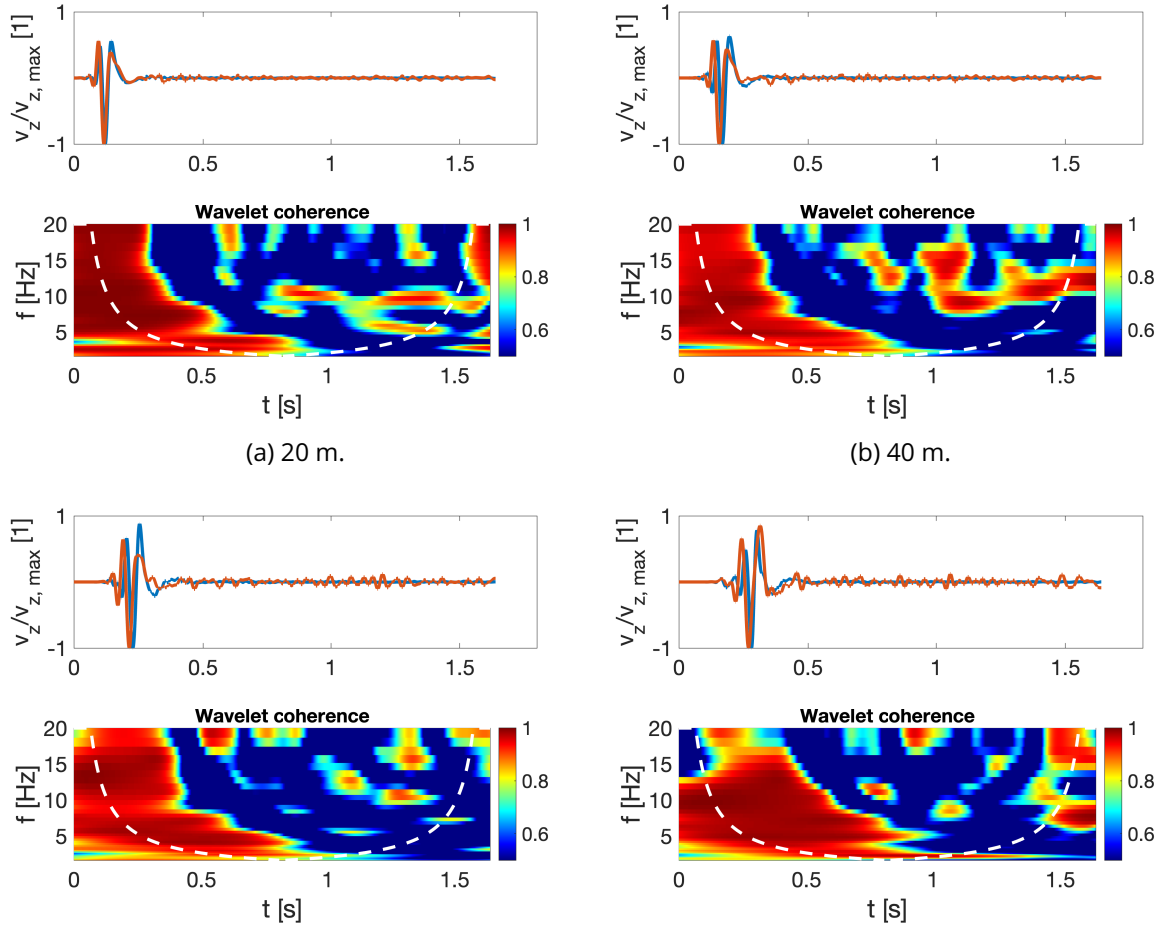

(a) 20 m. (b) 40 m.

(c) 60 m. (d) 80 m.

Figure 1.28: Wavelet coherence between the homogeneous and heterogeneous signals in the time-frequency domain at different positions along the array.

dure demands a time shift computed as

$$\Delta t = d_{jk}/C_{app} \tag{1.63}$$

where d_{jk} is the distance between the two sensors and C_{app} is the apparent velocity. C_{app} between two stations is calculated using the cross-correlation function (Elgamal et al., 1996).

In the recent work of Mao et al. (2020), the coherency has been revisited with the wavelet formulation in order to known the coherency function in the time-frequency domain, $\Gamma(f,t)$. In this example, instead on comparing the coherence between sensors at different positions, the wavelet coherence is computed between the time signals of homogeneous against the heterogeneous model to determine their differences in the time-frequency domain. Only the random field associated to one seed is selected. Before the computation of Γ, the signals are shifted with Equation 1.63 independently for both models because their apparent velocity is different. The upper plots of Figure 1.28 show the time signals in the heterogeneous and homogeneous model after this time shift is applied, where the strong motion coincides between the two models. The spatial variability of wavelet coherence is also analyzed for 4 different locations of the array. From the figures, it is possible to recognize a persistent scattering of the waves due to the effects of the heterogeneities over the whole array, translated as a loss of coherence on the high frequency range (from 10 to 20 Hz) after the passage of the surface wave. The results obtained from the two approaches, i.e., directivity and coherence, indicate that the heterogeneous material induces a deflection on the arrival direction of the seismic wave, and a generation of “noise" not coherent with the original signal.

The next step is then to evaluate the influence of the heterogeneous media specifically on the surface wave characterization. The differences on the direction of propagation, maximum amplitudes and frequencies are analyzed with the NIP and shown with the blue dots in Figure 1.24 for two different random fields (RF). It can be observed that, compared to the homogeneous case, the azimuth angle of polarization in the heterogenous case is similar to the homogeneous case up to 50 meters away from the source. Then, due to the fluctuation of properties, the azimuth changes direction in $\pm 30°$ for the RF1 and $\pm 30°$ for the RF2, which may be associated with an increase of V_s at the surface (Figure 1.25) and also to a decrease in the local directivity in Figure 1.27. The finding could be related to a multi-pathing problem: the scattered waves overlap and interfere with each other (Greenhalgh et al., 2008). In this case, the literature suggests a direction of arrival error when using a single station approach as with the NIP method.

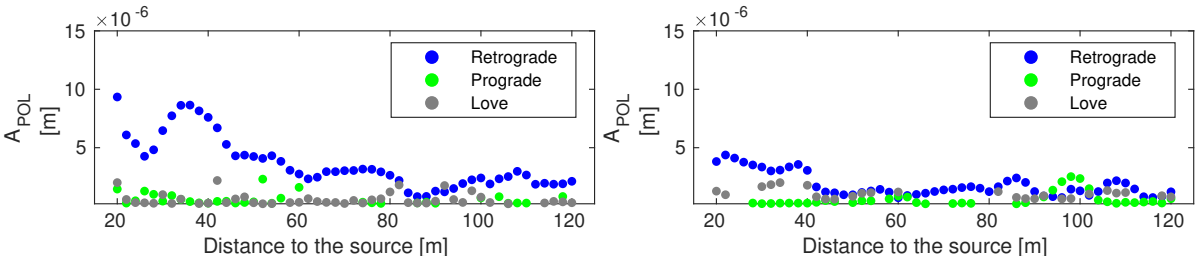

(a) Random field 1.

(b) Random field 2.

Figure 1.29: Maximum amplitude of the surface waves A_{POL} extracted via the NIP procedure. The Prograde Rayleigh and Love waves have been considered to see is scattering from heterogeneities can be identified as surface waves.

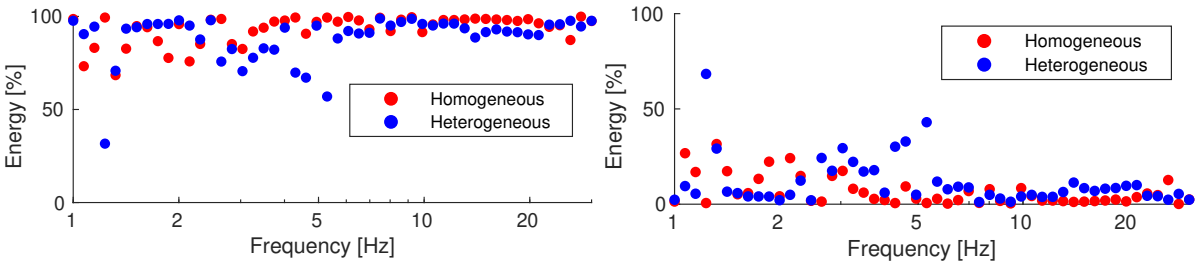

(a) Vertical + radial energy.

(b) Transversal energy

Figure 1.30: Energy obtained from the MUSIC procedure for different analyzed frequencies. In red, the results when using homogeneous properties and in blue when fluctuaction of the material properties are added to the sedimentary layers.

Moreover, Prograde Rayleigh and Love waves are searched with the NIP to evaluate the effects of heterogeneities in generating other types of surface waves. Figure 1.29 shows the amplitudes along the array. Besides the decrease in the amplitude of Rayleigh waves when heterogeneities are present, it is possible to observe the generation of Prograde and Love waves, but in small amplitudes. Finally, Figure 1.30 shows the distribution of energy with frequency computed with MUSIC for the homogeneous and heterogeneous (in red and blue, respectively). While, it is observed that most of the energy is carried by the vertical plus radial energy associated with Rayleigh waves, in the heterogeneous case, some of the energy is present in the transversal component. This result is similar to the generation of other wave types and the loss of coherence obtained before, which evidences comparable findings between the methodologies even if heterogeneities are present.

To partially conclude this section, the heterogeneities decrease the amplitudes of the generated surface waves. This can be further explained by the scattering of the wave also observed in the change in directionality and loss of coherence. The results are in agreement with other studies where heterogeneities have been included in the numerical simulation of wave propagation (e.g. Chammas et al., 2003; Tchawe et al., 2021; Touhami et al., 2022, among others).

1.6.3 Application to real signals

In Sections 1.6.1 and 1.6.2, the investigation was predominantly focused on checking if the methodologies could obtain the correct surface wave parameters, since the source and the soil structure in the site of interest were already known. Furthermore, it was observed that the heterogeneities of the materials would influence the amplitudes and characteristics of the surface waves. In this section, the capacity of the three methodologies is assessed by applying them to real signals, where the wave propagation problem is uncertain due to source, path and site effects, with phenomena such as the slip distribution, source-to-site distance, travel path geology, attenuation, scattering of seismic wave propagations, site geology, and site topography (Kawase, 2003; Anderson, 2007; Svay et al., 2017, among others).

1.6.3.1 Description of the ground motions

The data measurements analyzed were obtained from the vertical network ARGONET in the Argostoli basin, Kefalonia Island, Greece. In this area, the rotational motion signals are available from the rotational signals installed by the SINAPS@ project (Berge-Thierry et al., 2017; Sbaa et al., 2017; Perron et al., 2018b) in `http://argonet-kefalonia.org/data/postseismic_event_data/`. The site was selected because it was the object of extensive studies regarding site effects, including surface waves, rotational components and spatial variability (Imtiaz et al., 2014, 2020; Sbaa et al., 2017; Perron et al., 2018b; Svay et al., 2017, among others).

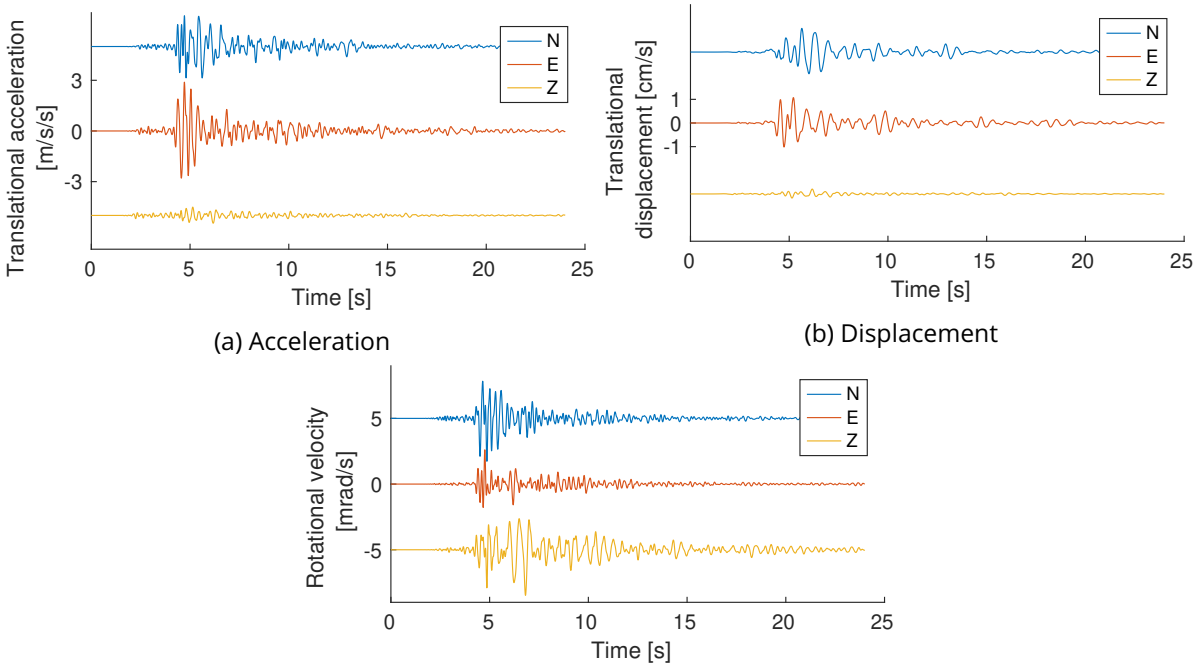

(a) Acceleration

(b) Displacement

(c) Rotational velocity

Figure 1.31: Selected real signal (magnitude $M_L = 5$, distance to the source $R = 20.6$ km) in the ARGONET station, composed of translational and rotational sensors. From Sbaa et al. (2017).

Since basins will amplify the ground motions amplitudes and generate surface waves, a phenomenon that will be analyzed extendedly in the following chapters, the signals are selected to be located in soft soil inside the basin. The array is located in the same position as ARGONET, corresponding to the “phase 3" of the dataset installed and described by Sbaa et al. (2017). The selected signal is from a record with magnitude $M_L = 5.0$, hypocenter distance of 20.57 km and depth of 18.4 km. The signals were filtered with a fourth-order Butterworth bandpass between 0.1 and 10 Hz. The accelerations and displacement time histories are presented in Figure 1.31, the latter used for the NIP analysis in the right part. It is noted that a low amplitude of the vertical component characterizes the original signal. Figure 1.31c presents the signal obtained by the rotational sensor. The north (N) and east (E) components represent the rocking around those axes, and the vertical (Z) component is the torsion.

In real data, the heterogeneities present in the soil and the soil geometry will influence the

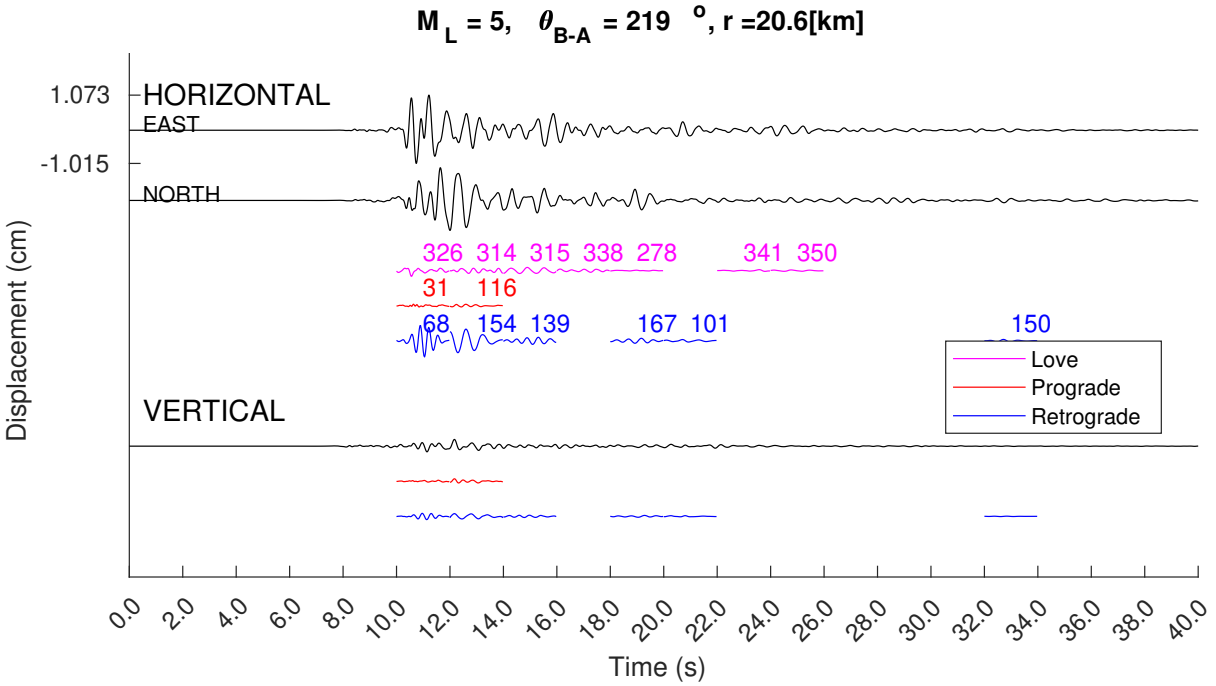

Figure 1.32: Comparison between the original signals, in black, against the isolated surface waves (NIP) for the selected signal. The signal was analyzed in 2 seconds- time windows, and the polarized direction is also depicted in degrees above each extracted wave.

spatial variability of the ground motion (Svay et al., 2017), and also the generated surface waves as observed in subsection 1.6.2.4. The multiple reflections will generate multiple types of waves arriving at the same moment. For that reason, the signal was divided into time windows of 2 s, following recommendations considering a time window of three to five periods of length (Hobiger et al., 2016; Imtiaz et al., 2017; Sollberger et al., 2020).

1.6.3.2 Results

The extracted waves with the NIP procedure are represented in colours in Figure 1.32. Above each extracted wave, the number is the azimuth of the corresponding wave with respect to the North. From this Figure, it is interesting to see what proportion of the original signal is identified as surface waves. Only waves with a $C_{PV} > 0.7$ for Rayleigh or $C_{PV} < 0.1$ for Love waves are displayed. Generally, the recognized Retrograde Rayleigh waves have higher amplitude with diverse azimuths. Love waves are polarized mainly in the northwest direction (approximately azimuth $N310$ to $N350$).

As for the other methodologies, the time-domain parameters obtained with the MUSIC and DOT algorithm in the 6CPol methodology are presented in Figure 1.33, for the signal displayed in Figure 1.31. A low likelihood is obtained with the two algorithms to find the polarization vector. Greenhalgh et al. (2018) exhibited some limitations of single station 6C polarization analysis. For instance, the time of the window selected impacts the analysis because the noise may not be cancelled out completely, independently of the SNR ratio. Sbaa et al. (2017) stated that for the

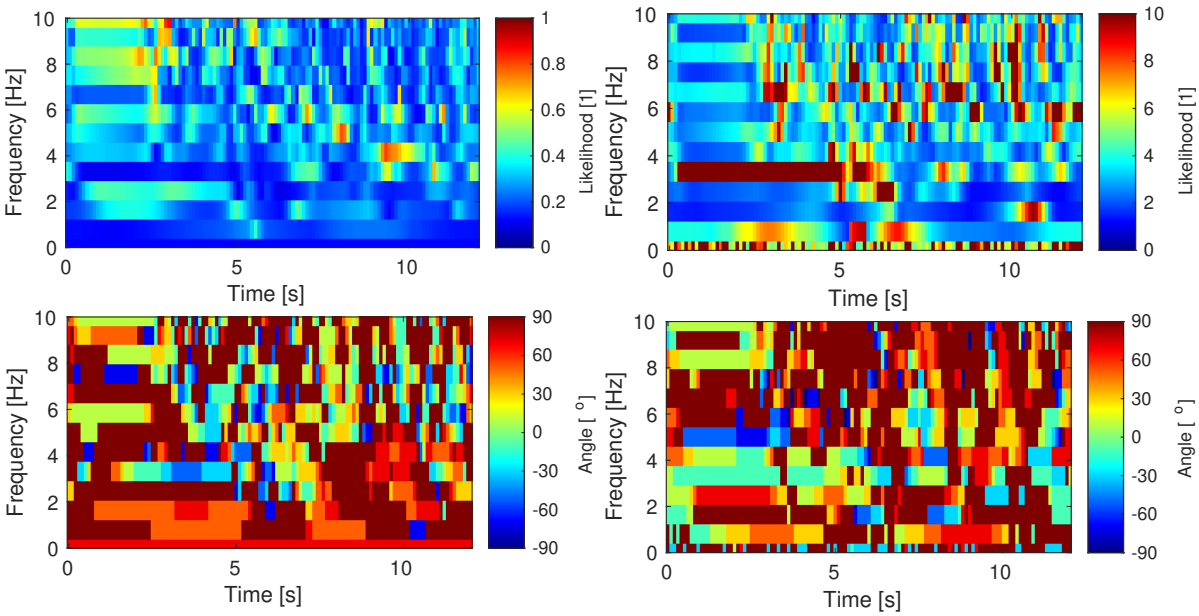

(a) DOT (b) MUSIC

Figure 1.33: Rayleigh wave characterization with the 6Pol processing procedure (Sollberger et al., 2020), using two algorithms to obtain the polarization vector.

selected signal, the rotational sensor had a higher noise level than the translational sensor, which may have impacted the accuracy of the methodology once the signal was complexified.

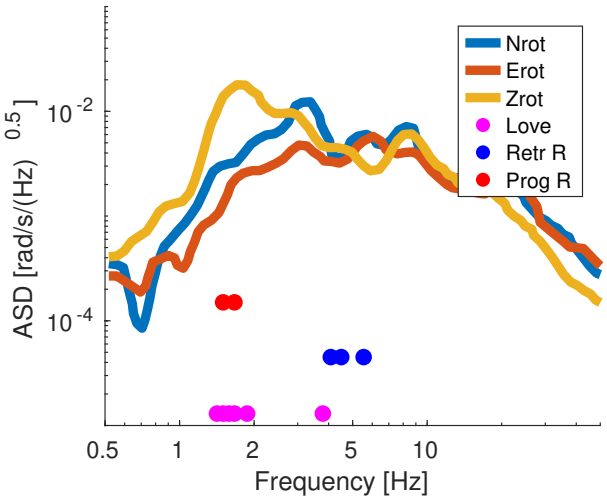

Figure 1.34: Amplification Spectral Ratio (ASR) of the rotational velocity computed by Sbaa et al. (2017) against the central frequency f_{cen} of the extracted waves (NIP) depicted as points in the bottom part of the figure.

Moreover, for the same data presented in this section, Sbaa et al. (2017) related the torsion with Love waves and rocking with Raleigh waves, assuming that the earthquakes were sufficiently distant. Compared to rock sites, the sites located in soft soil had a higher amount of torsion, while rocking had comparable values. That result would indicate that Love waves were amplified (or

created) inside the lower S-wave velocity sediments inside the basin. To further relate the extracted surface waves with the rotations, the results obtained with the NIP were compared with the Amplification Spectral Ratios (ASR) calculated by Sbaa et al. (2017) for the same event. Figure 1.34 clearly recognizes the surface wave influence on the rotational components. The rotation around the vertical axis $Zrot$, or torsion, shows a peak value between 1.5 and 2.0 Hz, which is consistent with the central frequency of the isolated Love waves around the predominant frequency ($f = 1.8$ Hz) of the sediments in the area. The central frequency of Retrograde Rayleigh waves is higher, close to 5 Hz.

Table 1.1: Selected events in the Argostoli basin for the computation of surface waves parameters. The data has been recovered from http://argonet-kefalonia.org/data/postseismic_event_data/

ID	Origin date/time	M_L	H [km]	R_{epi} [km]	Baz [deg]
633	2014/11/08 23:15:42.200	5.0	20.57	9.20	219.1
734	2014/11/24 07:20:32.100	4.1	24.96	19.79	320.7
366	2014/05/25 22:42:04.300	3.9	35.08	30.63	21.4
79	2014/03/18 00:50:52.200	3.5	21.12	10.18	273.9
825	2016/06/04 16:38:25	4.4	22.12	14.15	259.0
596	2014/11/05 14:22:24.800	4.2	18.02	7.01	193.4
813	2015/11/17 07:10:07	6.0	57.24	56.23	8.4
182	2014/04/04 01:59:34.700	3.8	16.79	11.21	277.9
229	2014/04/13 08:46:47.100	3.5	13.37	6.82	262.7
84	2014/03/18 06:29:39.500	3.4	23.49	15.55	276.1
370	2014/05/26 13:58:21.300	3.3	21.42	12.49	275.3
468	2014/08/03 18:15:24.100	2.9	17.96	7.54	248.3
357	2014/05/22 18:12:30.100	3.5	25.05	13.65	234.0
779	2015/03/31 15:48:41.100	4.3	20.45	17.05	4.6
88	2014/03/18 15:37:40.700	3.2	21.14	10.93	287.9
696	2014/11/14 15:40:01.300	3.1	19.80	8.88	220.0
145	2014/03/28 23:28:21.900	3.3	16.82	8.86	259.1
457	2014/07/24 00:23:11.900	3.6	18.87	12.65	287.5
421	2014/06/22 12:55:20.500	3.7	18.85	13.65	345.4
675	2014/11/12 06:31:37.500	4.1	19.80	14.20	347.9
638	2014/11/09 01:30:13.200	3.1	20.39	7.14	213.5

1.6.3.3 Effect of the source position

Imtiaz et al. (2014, 2020) investigated the surface waves' energy with the MUSIQUE technique for a different set of data (local magnitude $M_L = 2 - 5$, and epicentral distance $R = 0 - 200$ km) located in two soft-soil sites in Argostoli, near the position of ARGONET. They found that most of the energy is associated with surface waves, with frequencies higher than the fundamental frequency of the basin, and the obtained back-azimuth was related to the basin-edge directions. Moreover, Imtiaz et al. (2020) found dominant arrival directions of the basin-induced surface

waves for two stations near the ARGONET sensor with the MUSIQUE procedure. They concluded that these directions were presumably associated with the basin's 2D/3D geometry. In order to further validate the NIP with real signals, the 20 events of the original dataset in ARGONET with the higher signal-to-noise (SNR) ratio were selected and processed with the NIP (Table 1.1). The signals were filtered and separated in 2 s time windows.

The plot in Figure 1.35 depicts the propagation angle (the angle of the plot) against the central frequency (the radius of the plot) of the extracted surface waves, where the first two predominant frequencies of the area are displayed in white. In the same Figure, the distribution of energies with back azimuth obtained by Imtiaz et al. (2020) was superposed. It is worth noting that while the location of the stations in this work is not exactly the same as the work of Imtiaz et al. (2020), they are distanced within 250 meters approximately and over the same soil type. For both types of waves, it is possible to observe good agreement of the NIP with the previous results (MUSIQUE) for the azimuth angle. For Love waves in Figure 1.35a, most central frequencies are close to the peak obtained by HVSR in Sbaa et al. (2017) (f =1.57 Hz). Rayleigh waves are described primarily by higher frequencies (2 to 5 Hz). Generally, the predominant angle of surface waves differs from the back azimuth angle for the events (in Table 1.1), indicating that these waves are not coming directly from the source but from elsewhere, presumably from interactions with the local subsurface. Specifically, the Rayleigh wave azimuth range is $N120 \pm 30°$, while the Prograde wave is $N60 \pm 30°$, showing that the nature of these could be associated with the complex edges of the basin in the area.

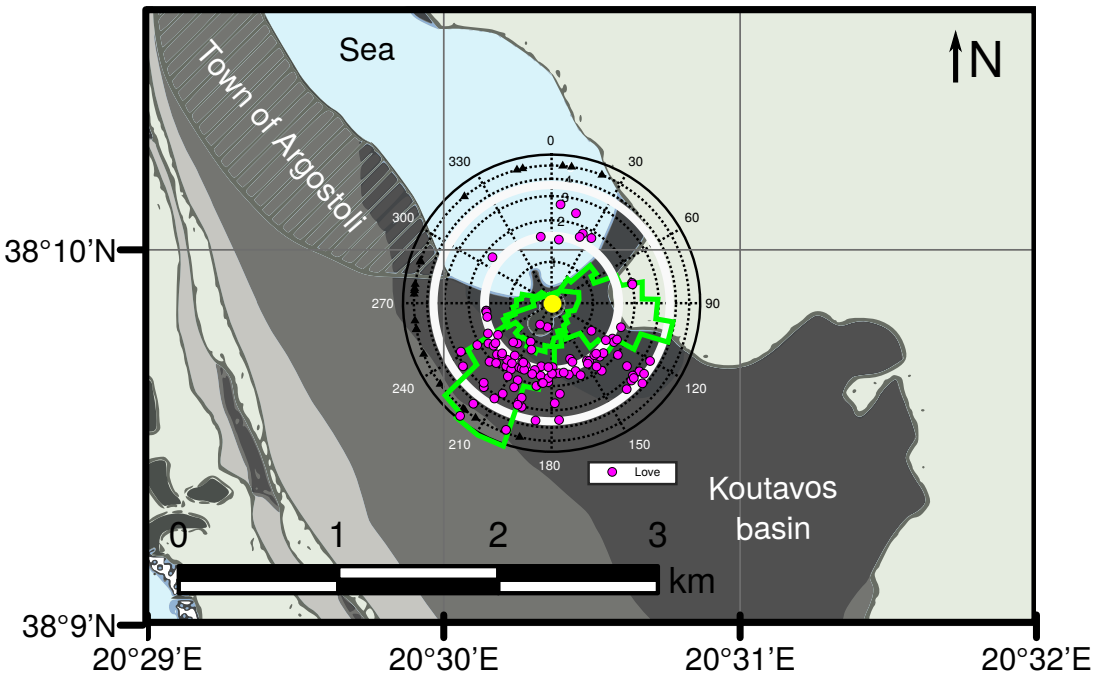

(a) Love

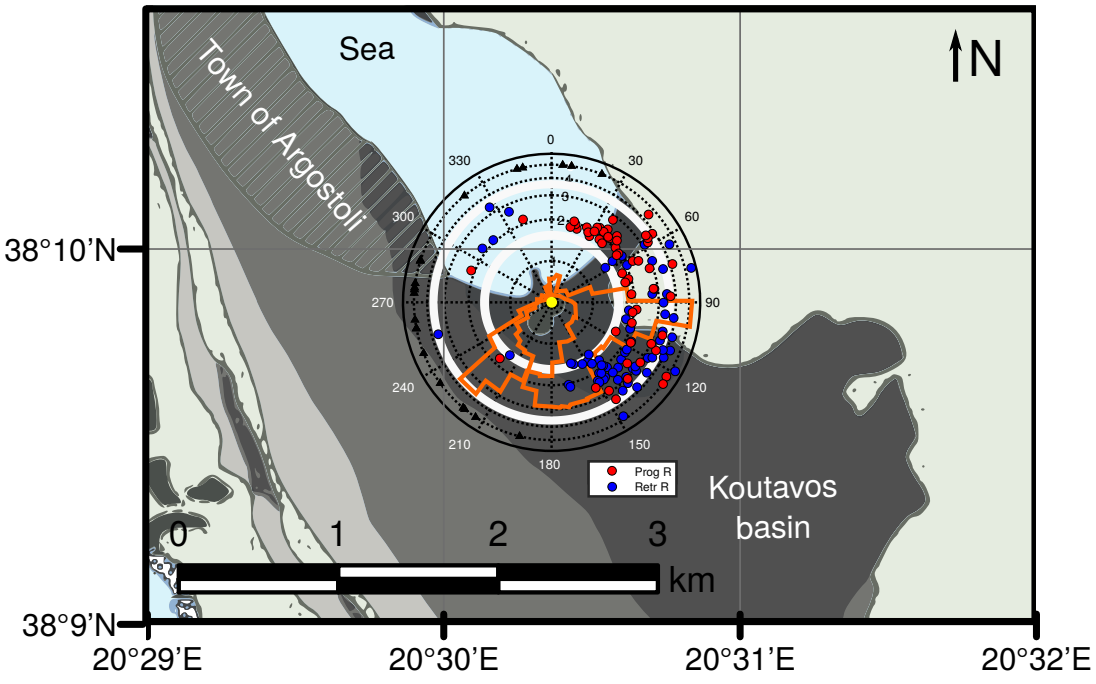

(b) Rayleigh

Figure 1.35: Azimuth of the signals obtained with the NIP for the (a) Love and (b) Rayleigh waves at the ARGONET station showing their relation with the basin borders. The Figure also presents the energy distribution obtained by MUSIQUE by Imtiaz et al. (2020) in continuous lines.

.

1.7 Concluding remarks

This Chapter introduces the methodology (NIP) used in the following chapters to evaluate long-period ground motions in the form of surface waves inside basins for the seismic hazard analysis, essential part of the PBEE methodology. Surface wave methodologies were explained and compared to obtain surface wave characteristics from ground motion signals with increasing complexity. The principal methodology used in this work will be the Normalized Inner Product (NIP) developed by Meza-Fajardo et al. (2015). Thus, in this Chapter, it was compared and analyzed against two other techniques (MUSIC/MUSIQUE (Schmidt, 1986; Hobiger et al., 2016) and 6CPol (Sollberger et al., 2018, 2020)) in its capacity to accurately characterize the surface waves.

The results have shown that for simple to complex data, the NIP has correctly estimated the parameters. Among the main advantages of the method in comparison with others can be argued:

- The capability of analyzing a large number of signals in small time, as it would be needed in the basin effect quantification. The NIP can obtain the dominant parameters easily with the correlation of components (Inner Product). The 6CPol and MUSIC techniques, in contrast, need a grid search of the parameters, so larger computational time is expected.

- The obtention of time signals. 6CPol and NIP can isolate the surface wave as a time signal, with three components, which could be a good advantage in e.g., evaluating the seismic performance of structures via time-histories analyses, in obtaining easily some ground motion parameters for seismic hazard. MUSIC, in contrast, can obtain just the energy of the total signal.

- The NIP need less data (only three-component seismogram). In contrast, the 6CPol requires the rotations (double of data) and MUSIC requires multiple stations (n times the data, depending on the number n of stations selected), so when analyzing surface stations in numerical simulations more storage would be necessary to characterize the same areas.

Therefore, in the following analyses of this work, only the NIP will be presented to describe the surface wave characteristics of the wavefield.

Chapter 2

Numerical simulation of amplification of seismic waves in 3D basins

Contents

2.1 Introduction

In the PBEE methodology, the seismic hazard analysis (SHA) estimates the ground motion (GM) hazard of a specific area (Kramer, 1996). This ground shaking is assessed quantitatively by determining the earthquake characteristics regarding intensity measures (IM), such as the peak ground acceleration (PGA) or the response spectra. The distribution of ground shaking amplitudes depends on the seismic wave propagation from source to site at the regional scale of tens to hundreds of kilometres (Figure 2.1). Regional scale heterogeneities and complexities in the subsurface induce modifications in amplitudes, frequency content and duration of the seismic ground motion. Mathematically, Boore (2003) comprised the conditioners of the ground motion $u(t)$ in the propagation by the equation

$$u(t) = S * P * L \tag{2.1}$$

where S is the contribution of the earthquake source effects, P are the path effects from source to site, and L is the local site effects due to small-scale geological conditions. Source and path effects influence the ground motions and the propagation and amplification of surface waves in the surficial soil layers (Boore, 2004).

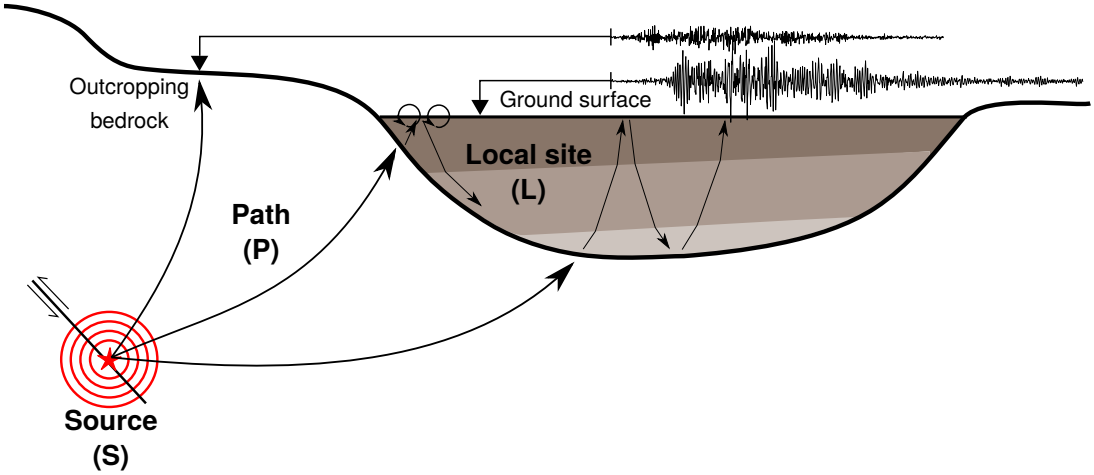

Figure 2.1: Representation of the seismic wave propagation from the source to site, depicting the source (S), path (P) and local site (L) contributions.

At the local scale, the complexity of the seismic phenomena can be expressed as a combination of different phenomena, as described by Parvez and Rosset (2014)

1. Geotechnical site conditions: amplification/reduction of seismic waves due to impedance contrast, resonance effect;

2. Geological site conditions : geometrical effects, such as the 2D/3D subsurface geometries (basin) or topography;

3. Effects on nonlinear response: attenuation of large amplitude waves due to soil non-elastic behavior, such as anelasticity or scattering.

In a smoothly varying medium, the propagation characteristics are governed by the vertical structure beneath each point on the propagation path (Woodhouse, 1974). Consequently, a first simplification of the problem is to characterize the site effects of the seismic site response by a single layer over a homogeneous infinite half-space (Kawase, 2003). Due to the reflection of body waves towards vertical incidence by Snell's law, it is generally assumed that the vertical component comprises only P waves and the horizontal only of S waves (Pilz et al., 2021). In a homogeneous media, assuming that the P and S waves are fully decoupled, the amplification factor $|U(\omega)|$ induced by either an S or P wave can be expressed as the spectral ratio of the surface motion concerning the outcrop motion, given by (Kawase, 2003)

$$|U(\omega)| = 2\sqrt{\cos^2(\kappa_1 h) + \gamma^2 \sin^2(\kappa_1 h)} \tag{2.2}$$

where h is the thickness of the layer, $\kappa_1 = \omega/\beta_s$ is the wavenumber at the surface layer and $\gamma = \rho_1\beta_1/\rho_2\beta_2$ is the impedance contrast between the two media with β is the shear wave velocity ρ the densities and the subscript 1 denotes the soil layer and 2 the half-space. Given that just a few parameters of the site are needed, this simplification is widely used in engineering practice: it is assumed that site effects are dominated by vertically propagating shear waves (SH type), since S wave has a larger amplitude as input and stronger contrast between layers (Kawase, 2003). This simplification would account for the amplification due to the impedance contrast and 1D resonance effects.

However, the hypothesis of infinite horizontal layering (1D) many times is not able to correctly model the wave propagation. Diverse studies have found differences between the analytical 1D solution and the modelled behavior of real data (Thompson et al., 2012; Kim and Hashash, 2013; Zalachoris and Rathje, 2015; Pilz et al., 2021, among others). Most of the differences come from the fact that the 2D/3D geology effect needs to be correctly captured, as the shape of the subsurface geology plays an important role in wave propagation. In reality, lower velocity sedimentary layers are confined by the surrounding rock to form sediment-filled basins (Kawase, 2003; Moczo et al., 2018), so parameters such as variable property layers, inclined bedrock, and inclined motion will affect the ground motion observed at the surface. These phenomena are commonly denominated *basin effects*.

Because the basin effects are complex phenomena, Kawase (2003) defined three model-oriented approaches to well identify the problem: ground motion modelling (characterization), numerical technique development and strong motion observation through the collection of observed data. The computational methods used for simulations of the events can be classified into three groups according to Poursartip et al. (2020): (i) analytical and semi-analytical methods, (ii) numerical methods and (iii) hybrid methods, which are a combination of the first two methods. Much of the early work on basin effects had analytical nature, focusing on the basin displacement response in simple two-dimensional geometries, such as the one developed by Tri-

funac team (Trifunac, 1971; Wong and Trifunac, 1974). Other theoretical developments were later produced by raypath and wavefront analyses as the work of Adams et al. (2003). However, analytical methods compute the wave motion in simple geologies, with homogeneous properties or simplified geology (Poursartip et al., 2020), so they cannot predict seismic response when irregularities or heterogeneities are present. In this case, the formulation becomes easily complex, so it is generally more efficient to make full 3D numerical simulations of the wavefield (Kennett and Fichtner, 2020).

In general, a wide variety of numerical methods have been used for computing the basin response, such as the finite difference method (Day et al., 2008; Iwaki and Iwata, 2008; Day et al., 2013; Aochi et al., 2013; Iyisan and Khanbabazadeh, 2013; Moczo et al., 2018; McCallen et al., 2021a, among others), finite element method (Bielak et al., 2000; Day et al., 2008; Gelagoti et al., 2012; Day et al., 2013; Riga et al., 2016; Meza-Fajardo et al., 2019; Riaño et al., 2020, among others), spectral element method (Stupazzini et al., 2009b; Smerzini et al., 2011; Castellani et al., 2012; Tchawe et al., 2021; De Martin et al., 2021; Touhami et al., 2022, among others) or Boundary element and boundary integral methods (Sanchez-Sesma and Luzon, 1995; Gil-Zepeda et al., 2002; Semblat et al., 2003, 2009, 2010; Lombaert and Clouteau, 2006; Meza-Fajardo et al., 2016; Amini et al., 2022, among others).

The basin effects in the ground motion are usually described by a significant amplification, prolongation of signal duration and differential motion. One of the most significant observations by Bard and Bouchon (1980a,b) were the generation of surface waves at the edges of basins due to the nonplanar interface propagating back and forth within the sediment cover. Several approaches evaluate the amplification due to basin effects in the literature (e.g. Semblat et al., 2009; Iyisan and Khanbabazadeh, 2013; Zhu et al., 2016; Riga et al., 2016; Zhu et al., 2018, 2020; Brissaud et al., 2020; Ayoubi et al., 2021, among others). The amplification factor (AF) is typically defined for basin effect quantification as a ratio of some ground motion parameter GMP_{BAS} inside the basin, over the same ground motion parameter at a reference point GMP_{REF}, without the presence of the basin:

$$AF = \frac{GMP_{BAS}}{GMP_{REF}} \tag{2.3}$$

The AF frequency dependency is connected to the selected GMP. Frequency-dependent GMPs, such as the spectral acceleration, can be useful in seismic risk analysis (Trifunac, 2012; Moczo et al., 2018).

In the engineering practice, i.e., seismic design codes, Ground Motion prediction Equations (GMPEs), the site effects are usually considered by a scalar correction to the ground motion depending on the site category (Bard, 2021). These are called site proxies, such as V_{s30} or the resonance frequency of the site (Stambouli et al., 2017). Another common practice to compute local site responses is obtaining free field ground motion at a reference bedrock with the GMPEs and then analysing site response with a column of soil to calculate the hazard at the ground surface (Ameri et al., 2017; Bard et al., 2020). A straightforward attempt to add the basin effects to the current seismic design is to evaluate the additional amplification of the basin effects against a

one-dimensional ($1D$) soil column. Therefore, the aggravation or adjustement factors (AGF) are defined as a ratio between the responses of the basin model ($3D$) and a horizontal $1D$ layered model (Faccioli and Chavez-Garcia, 2000). The AGF allow adding the amplification induced by the basin geometry directly to the horizontal translational components of ground motion used in seismic design. For instance, Bard (2021) defined the site term $\delta S2S_S$ in the GMPE by an equation that could be defined as the linear 1D site response plus “correction factors" depending on more complex site effects

$$\delta S2S_S = F_{1D} + F_{NL} + TAF + AGF + \phi_{S2S} \tag{2.4}$$

where F_{1D} accounts for the 1D linear site amplification, F_{NL} for modifications due to the non-linear site response, TAF is the topographic amplification factor, AGF the aggravation factor and ϕ_{S2S} the standard deviation. Each term relates to site condition proxies (SCP). The AGF parameter is, in general, computed by parametric numerical studies to evaluate the key parameters governing ground motion amplification in basins. Nevertheless, the AGFs focus mainly on the amplification of horizontal components, overlooking the generation of surface waves, whose rotational and vertical components are also present in the ground motion, and have been the cause of significant damage. Other parameters related to the source, such as its frequency, depth and angle of incidence to the basin, are also linked to basin response and to surface waves creation (Kawase, 2003; Wirth et al., 2019; Lai et al., 2020; O'Kane and Copley, 2021; Parla and Somala, 2022, among others). In addition, since most of the AGFs studies focus on the effects on the geometry or material properties of the basin, they are limited to plane-wave incidence and not to more realistic input scenarios (Makra et al., 2005; Psarropoulos et al., 2007; Gelagoti et al., 2012; Zhu and Thambiratnam, 2016; Ayoubi et al., 2021). Yet, recent studies, such as the one of Wirth et al. (2019) found that the position of different point sources impacts the basin amplification and generation of surface waves. Brissaud et al. (2020) used shallow sources to generate Rayleigh waves, highlighting the importance of input motion complexity in the posterior interaction with the basin geometry. From these studies can be drawn the importance of surface waves in the basin response and, therefore, understanding their generation is a mandatory step in the SHA for efficient site quantification.

The aim of this work is to perform an analysis of the effect of the geometry of the basin, dynamic material parameters and depth of the input motion on the basin-induced surface waves characteristics (e.g., the angle of polarization, central frequency, amplitude, among others), and their impact on the amplification of ground motion inside basins. At this point, two questions will be discussed:

1. How are surface waves related to key physical parameters, such as distance from the diffracting edge of the basin or material properties?

2. Can intensity measures parameters correlate with the apparition and characteristics of surface waves?

Hence, a numerical parametric investigation is presented based on a 3D numerical wave propagation simulation over simplified basins using the spectral element code SEM3D (CEA and CentraleSupélec and IPGP and CNRS, 2017). Two velocity contrasts between the material inside and outside the basin are evaluated. The influence of the depth of nine double couple (DC) point sources on the obtained response is also evaluated and compared to a vertically incident plane wave. As the response at the basin surface will be a combination of amplification due to changes in material properties, multiple reflections and generation of surface waves, the results from the simulations will be analyzed simultaneously with surface wave extraction and the calculation of the aggravation factor.

The methodology used in this Chapter for the surface wave characterization is the Normalized Inner Product (NIP) procedure (Meza-Fajardo et al. (2015),Meza-Fajardo and Papageorgiou (2016)). The result of this procedure are the time signals of the polarized waves (Rayleigh prograde, retrograde and Love) and their respective polarization angles. The advantages lie in the characterization of the predominant frequencies, maximum amplitudes, and durations from signals, using only three orthogonal translational components of the motion (north, east and vertical) from one independent station. In this work, the AGF will be defined in terms of the AF as

$$AGF(AF) = AF_{BAS}/AF_{LAY} \tag{2.5}$$

where BAS refers to the response from a model where the basin geometry is considered, and LAY is a model with the same properties, to which the soft sediments have been extended horizontally, generating a layered model.

The Chapter is organized as follows. First, in Section 2.2, a short review of the main results on the aggravation factors from the literature is presented to describe which basin-settings parameters affect the amplification response most. Second, Section 2.3 is devoted to characterising the earthquake ground motion with the Intensity Measures (IM). Third, the Section presents a parametrical study for a simplified basin to accomplish the Chapter objectives. *This chapter is adapted from a submitted publication.*

2.2 Parameters affecting the basin response

As previously stated, the basin effects combine amplification, resonance and surface wave generation, causing larger amplification and prolongation of signal duration and spatial variability or differential motion. The efforts to understand the basin response are mostly through numerical simulation, trying to relate the basin/source parameters with the corresponding amplification. The amplification factor (AF) can be defined at different locations within the basin, allowing the spatial variability of the amplification to be seen.

The early work of Bard and Bouchon (1985) discerns two distinct behaviors depending on the geometry and materials of the sediments. The first behavior corresponds to the *shallow basins*, where one-dimensional resonance predominates. In shallow basins, the arrival of surface waves

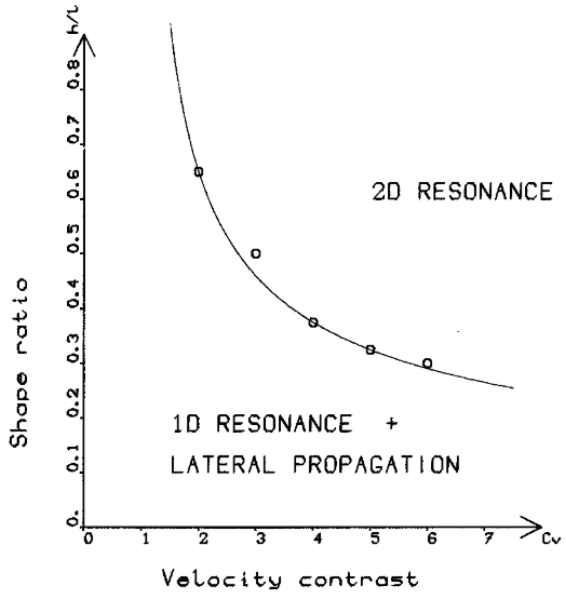

Figure 2.2: Velocity contrast versus shape ratio to discern the two main behaviors in basins. Retrieved from Bard and Bouchon (1985).

is well separated from the vertical resonance at the valley center, since they arrive at the center after the direct arrival. The second behavior corresponds to *deep basins*, characterized by two-dimensional resonance. In this case, the most significant amplification is observed in the valley center, decay towards the edges, and the ground motion is in phase across the whole valley (Bard and Bouchon, 1985).

The discrimination between the two behavior patterns is made through the basin properties associated with the geometry and the materials, shape ratio and the velocity contrast between sediment/bedrock, respectively (Figure 2.2). The shape ratio was defined for sine-shape valleys, but can be used for other shape type with equivalent shape ratio $h/2w$ where $2w$ is the total width over which the sediment thickness is more than half its maximum value (Bard and Bouchon, 1985). The resonance effects are larger in sedimentary basins with complex 2D/3D geometry where strong velocity contrast exists (Poggi et al., 2014). Besides, strong ground motion is significantly influenced by long-period surface waves that are produced at the edges of sedimentary basins by the conversion of body waves (Joyner, 2000). Bielak et al. (2000) described how different 3D modelling is from 1D. The ground motion is characterized by lower peaks and shorter duration, and a large spatial variability over short distance is observed.

Since in the 2D case, the in-plane (P-SV) and out-of-plane (SH) components of ground motion are orthogonal and do not interact with each other (Poggi et al., 2014), most of the amplification studies try to evaluate separately the two directions to simplify the analysis when conducting parametric studies. Among them, it has been found that the more important basin parameters are the impedance contrast between materials and the shape ratio of the basin (Douglas et al., 2009; Semblat et al., 2009; Iyisan and Khanbabazadeh, 2013; Riga et al., 2016; Zhu et al., 2016, 2018, 2020; Ayoubi et al., 2021; Brissaud et al., 2020; Amini et al., 2022). Several works evaluated

Table 2.1: Definition of the adimensional parameters by Ayoubi et al. (2021).

Parameter	Formula	Definition
π_1	ν_1	Poisson ratio sediments
π_2	ν_2	Poisson ratio bedrock
π_3	a/b	Shape ratio
π_4	V_{S2}/V_{S1}	Shear wave velocity ratio
π_5	$\frac{f_0 b}{V_{S1}}$	Dimensionless frequency
π_6	ρ_1/ρ_2	Density ratio
π_7	$\frac{(D+2a)}{b}$	Aspect ratio

the aggravation and amplification factors induced by an incident SH wave (e.g. Zhu et al., 2016; Zhu and Thambiratnam, 2016; Zhu et al., 2018; Iyisan and Khanbabazadeh, 2013; Gelagoti et al., 2012; Sohrabi-Bidar et al., 2010; Zhu et al., 2020), where the conclusions are variated. However, they all highlight the amplification produced by the combination of wavefield interaction, including the surface waves, concentrated towards the borders. Hence, the spatial distribution, i.e., the position of the site of interest concerning the basin geometry, is an influential parameter in the response. For that, some AGFs have been related to the location inside the basin, such as the different zones defined by Stambouli et al. (2018).

To parametrize the amplification response of basins, Ayoubi et al. (2021) defined seven dimensionless parameters (π_n with $n = [1, 7]$) in order to characterize the materials and shape of the basin and evaluate the amplification response. The parameters are displayed in Table 2.1, where the subscript 1 refers to the sediments and 2 to the bedrock. The geometrical parameters a, b and D refer to the width of the inclined boundary, depth of the sediments and width of the flat part of the basin, respectively. The dimensionless frequency, π_5, is defined in terms of the dominant frequency of the input motion, f_0 (or root mean frequency, RMS). The most significant parameters are dimensionless frequency, material velocity contrast and aspect ratio, similar to other studies (e.g. Riga et al., 2016; Zhu et al., 2016; Iyisan and Khanbabazadeh, 2013).

Parametric studies generally use vertically-incident plane waves as input, so the AF uses the input or source rock motion as a reference point (e.g., Semblat et al., 2009; Iyisan and Khanbabazadeh, 2013; Meza-Fajardo et al., 2016; Ayoubi et al., 2021). However, when there is no plane wave of vertical incidence, the reference point should not be considered as the input motion at any point outside the basin since the pattern of high-ground motion depends strongly on the direction from which the seismic energy enters the basin (Anderson, 2007). To overcome this, Kristek et al. (2018) proposed to consider as a reference the response of an additional model where the basin does not exist. This approach has also been used in other parametric studies where the seismic source is not defined as a plane wave of vertical incidence (Kamal and Rani, 2017; Brissaud et al., 2020).

Comparing the 2D and 3D modelling, Faccioli and Chavez-Garcia (2000) indicate that relative differences are only of quantitative nature and that the two-dimensional amplification becomes significant for lower periods. Similar findings come from Makra and Chávez-García (2016), who

compared the 2D and 3D responses for a realistic model of the Mygdonian basin in northern Greece. Although there were only slight variations between the 2D and 3D models, the 2D model may overestimate the surface wave amplitudes near the basin's edges. From those studies comes the effort to use 3D modelling in this work to accurately assess the generation of surface waves in basins.

Recently, studies have focused on the effects of more complex phenomena. For instance, Liu et al. (2021, 2022) studied the effects of real faults models on the amplification response of a simplified basin, where it was observed that basin and faults effects can appear simultaneously in the ground motions. The elastic behavior of soils has also been studied: nonlinearities can be important in near-surface layers (Seylabi et al., 2021) or near the edges of the basin (Gelagoti et al., 2012). With the increasing computational power, studies of the uncertainties of the parameters can be possible, as performed at large scale (Gatti et al., 2018; De Martin et al., 2021).

To summarize, the basin effects are complex since many basin/setting parameters are combined. Something to highlight in the latter studies is that surface waves may have been observed but have yet to be systematically quantified. This Chapter is then devoted to that with a simplified basin.

2.3 Earthquake Characterization of Ground Motion

The seismic response of a specific site needs to be characterised for the earthquake design of structures (Douglas and Aochi, 2008). This characterisation is made in terms of Intensity Measures (IMs). These are referred to as any parameter describing the earthquake-induced ground motion (Baker et al., 2021). In general, the ground motion is a function of amplitude, frequency and duration, so multiple IMs are considered necessary to comprehensively describe the ground motion severity (Aquib et al., 2022). Moreover, some ground-motion characteristics are important depending on the structure or consequences under consideration.

Different IMs account for the basin amplification response in the literature presented in section 2.2. In the following, a description of some of the most significant IMs is presented, focusing on the basin effects. The IMs have been classified as: peak values, spectral shape, duration and energy.

2.3.1 Peak values

The first and most easy to compute parameters are the peak values of the acceleration (PGA), velocity (PGV) and displacement (PGD) ground motions. Traditionally, the PGA is correlated to earthquake intensity (Trifunac and Brady, 1976). Typically, different vibration frequencies dominate the acceleration, velocity and displacement time series due to the predominant frequency reducing with integration. Therefore, PGA, PGV and PGD indicate the ground motion amplitude for high-, moderate-, and low-frequency bandwidth, respectively (Baker et al., 2021).

Some of the studies on basin effects usign the peak ground motions are Kawase (1996);

Narayan (2012); Ayoubi et al. (2021); Liu et al. (2021). This parameter type is used when evaluating spatial variability, especially when dealing with many data (De Martin et al., 2021; O'Kane and Copley, 2021).

2.3.2 Spectral shape

Since the amplification observed in the basin effects is distributed in a large frequency range, intensity measures should account this frequency dependency. Moreover, frequency content influence due to the dynamic response of a system is a function of the similarity between the frequencies of the excitation and the system of interest (Baker et al., 2021). In general, the site quantification works with the response spectra, which is the peak response of a single-degree-of freedom (SDOF) structure by computing the pseudo-spectral response in acceleration, velocity or displacement. This parameter account for amplitude and frequency content of a ground motion. In general, the spectral response at the frequency of the structure is a good indicator of the structural response.

Several basin effects studies have used the spectral shape to compute the aggravation factors (Makra et al., 2021). One of the most significant results relates to the 1D period of vibration of the sediment, T_0. This parameter constitutes a higher limit, where for $T > T_0$ no aggravation is observed (Faccioli and Chavez-Garcia, 2000; Riga et al., 2018; Zhu et al., 2020; Amini et al., 2022).

Comparisons of response spectra can be difficult because response spectra are not a direct reflection of ground motion records. The link between seismological theory is more informative when using the Fourier Amplitude spectra. $F(f)$ is a complex, absolute value associated with amplitude for a given frequency. Moreover, the complex argument $\arg(a(F(f)))$ is related to the phase angle associated with that frequency. Commonly, ratios of the Fourier spectra are used as amplification measures, such as transfer functions, standard spectral (SSR) ratios, and horizontal to vertical spectral (HVSR) ratios (Graves, 1993; Choi et al., 2005; Makra et al., 2005; Day et al., 2008; Iwaki and Iwata, 2008; Semblat et al., 2010; Iyisan and Khanbabazadeh, 2013; Day et al., 2013; Makra and Chávez-García, 2016; Pilz et al., 2018; Wirth et al., 2019; Brissaud et al., 2020; Makra et al., 2021; Stambouli et al., 2021, among others).

2.3.3 Duration and Energy

The duration of the signal strongly influences building response, associated to greater resonance and greater cumulative damage during nonlinear response. The most efficient parameter is the significant duration (D_S), defined as the time to which a specific percentage of the total energy imparted by the ground motion acceleration time series occurs, given by

$$D_{S5-X} = \frac{\int_0^{t_X} [a(t)]^2 \, dt}{\int_0^{\infty} [a(t)]^2 \, dt} - \frac{\int_0^{t_{5\%}} [a(t)]^2 \, dt}{\int_0^{\infty} [a(t)]^2 \, dt} \tag{2.6}$$

The threshold percentage is normally between 5% and $X = 75\%$ or $X = 95\%$. A D_{S5-75} generally includes all the P and S waves arrival, D_{S5-95} includes S and surface waves (Baker et al., 2021). The duration influences demands in linear and nonlinear systems.

Besides, two frequent metrics to account for the energy are the cumulatives Arias Intensity (I_a) (Arias, 1970) and the Cumulative Absolute Velocity (CAV), defined as

$$I_a = \frac{\pi}{2g} \int_0^t [a(t)]^2 \, dt \tag{2.7}$$

$$CAV = \int_0^{T_D} |a(t)| dt \tag{2.8}$$

where $a(t)$ is the acceleration time history, $\mid \bullet \mid$ is the absolute value and T_D is the significant duration, defined as the time difference of 5% and 95% energy thresholds under the acceleration of time history.

Despite the common knowledge of the lengthening of the ground motions due to the basin structure (Day et al., 2013; Kamal and Narayan, 2015; Pilz et al., 2018; Ayoubi et al., 2021, among others), only a few studies devoted to basin response directly computed the duration of the ground motion (Marafi et al., 2017; Touhami, 2020). Other investigations focus on energy parameters, which account for the duration indirectly. For instance, Novikova and Trifunac (1994) exposed the interest of using the duration to be related to the distance from the edge of the valley, to account basin-induced surface waves. Finally, the works of Stambouli et al. (2018); Moczo et al. (2018); Touhami (2020); Bustos et al. (2023) showed that the I_a and CAV are one of the most affected parameter when computing amplification or aggravation factors.

2.3.4 Multi-Component Ground Motion

When dealing with basin effects, specially in three dimensions, the directionality of the ground motion of the horizontal components is to be considered, due to changes on the induced wavefield caused by the propagation, reflection and refraction of seismic waves. In general, the directionality in the amplification is accounted by using the average or geometric mean of the two horizontal components (Marafi et al., 2017; Viens and Denolle, 2019; Wirth et al., 2019; Baraschino et al., 2022, among others). However, the geometric mean is not invariant to the orientation of the sensors, and does not work if a linearly polarized ground motion is aligned with one sensor component Boore et al. (2006). Consequently, an orientation-independent parameter was defined by Boore (2010) as the horizontal spectral amplitude over a rotation angle θ,

$$f_{ROT}(t) = f_X(t) \cdot \cos(\theta) + f_Y(t) \cdot \sin(\theta) \tag{2.9}$$

where $f_{ROT}(t, \theta)$ is a single time series obtained by rotating the horizontal X and Y components by the angle θ. The spectral response of $f_{ROT}(t)$ over the range $\theta = [0, \pi]$ is computed and for each oscillator period the *n*th fractiles are defined. Then, the $RotD50$ and $RotD100$ are

determined by the median and the maximum, as

$$IM_{RotD50} = \underset{\theta}{median}\left[IM\left(\theta\right)\right] \tag{2.10}$$

and

$$IM_{RotD100} = \max_{\theta}\left[IM\left(\theta\right)\right] \tag{2.11}$$

For simplified basins, i.e., 2D basin with plane wave incidence, the polarization direction of ground motion is known for in plane (P-SV) and out-of-plane (SH) input motions (Poggi et al., 2014), so this type of parameters is necessary when dealing with more complex modelling. For instance, Heresi et al. (2020); Daza et al. (2023) used the $RotD0, 50, 100$ to quantify the level of polarization, in order to evaluate the proportion of Rayleigh waves in the horizontal components of real signals in the Mexico city and Bogota basins. Similarly, Xu et al. (2003) used the δ parameter, defined as

$$\delta = \frac{\left[\left(I_{xx} - I_{yy}\right)^2 + 4I_{xy}^2\right]^{1/2}}{I_{xx} + I_{yy}} \tag{2.12}$$

with I_{ij}, the Arias intensity between i and j components. The values δ represents the dominant horizontal orientation, in order to evaluate the significance of basin effects in the directionality of ground motion.

2.4 Numerical model

2.4.1 Geometry and material properties of the basin

The models are three-dimensional sedimentary basins inserted into a homogeneous halfspace. The three-dimensional numerical simulation of seismic wave propagation was performed with the spectral element (SE) software $SEM3D$ (CEA and CentraleSupélec and IPGP and CNRS, 2017). The SE formulation used from the code as well as its main tools detailed in Appendix A, including a validation of the basin response against a reference solution.

The domain's total size is $40 \times 40 \times 25$ km^3 to avoid possible reflections at the edges of the domain and allow dynamic excitations far from the basin. SEM3D includes Perfectly Matched Layer (PML) absorbing elements at the boundaries of the mesh (Figure 2.3(a), coloured in yellow) to allow the outgoing wave to attenuate without re-entering the domain (Berenger, 1994).

A non-honouring meshing procedure is used, where the mechanical properties are interpolated at each Gauss-Lobatto-Legendre (GLL) point, so the mesh does not necessarily follow the geometry. The technique admits the creation of a mesh with rectangular hexahedral elements as displayed in Figure 2.3(b). For instance, Figure 2.3(c) shows how the material density ρ gradually interpolated between the basin's edge and the halfspace. The size of the elements was adapted to the wavelength for a maximum target frequency of 5 Hz, using five integration points per element in each direction. Figure 2.3(b) shows the elements' size, with a minimum element edge of 50 m closer to the center O at the surface to account for the smaller shear wave velocity inside

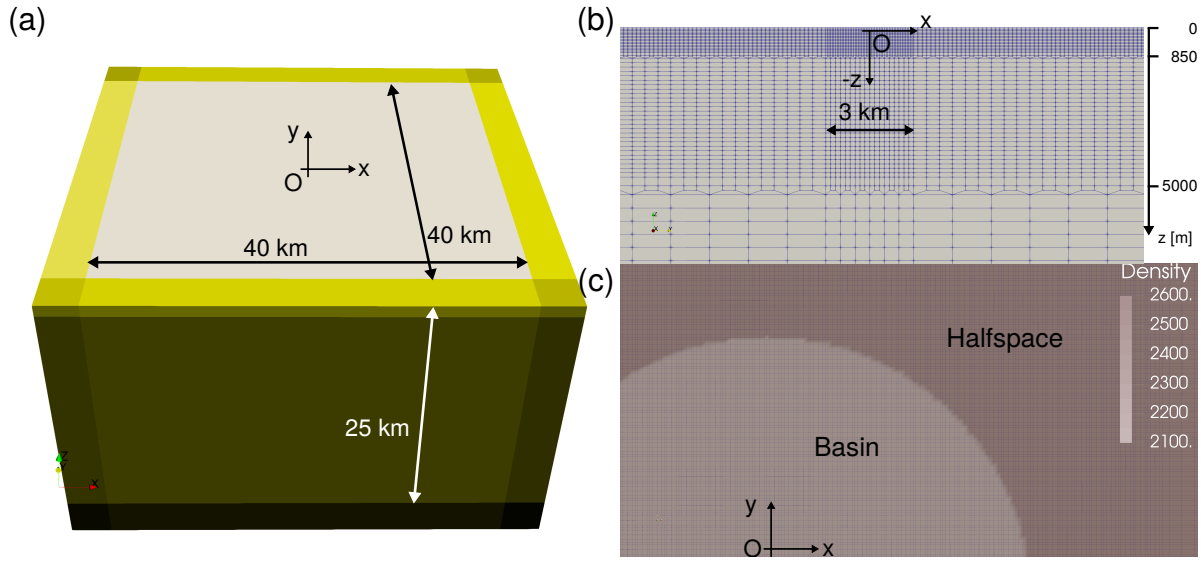

Figure 2.3: (a) Dimensions of the SEM domain, (b) interpolation of properties with the non-honouring technique and (c) element-size in different parts of the mesh.

the basin.

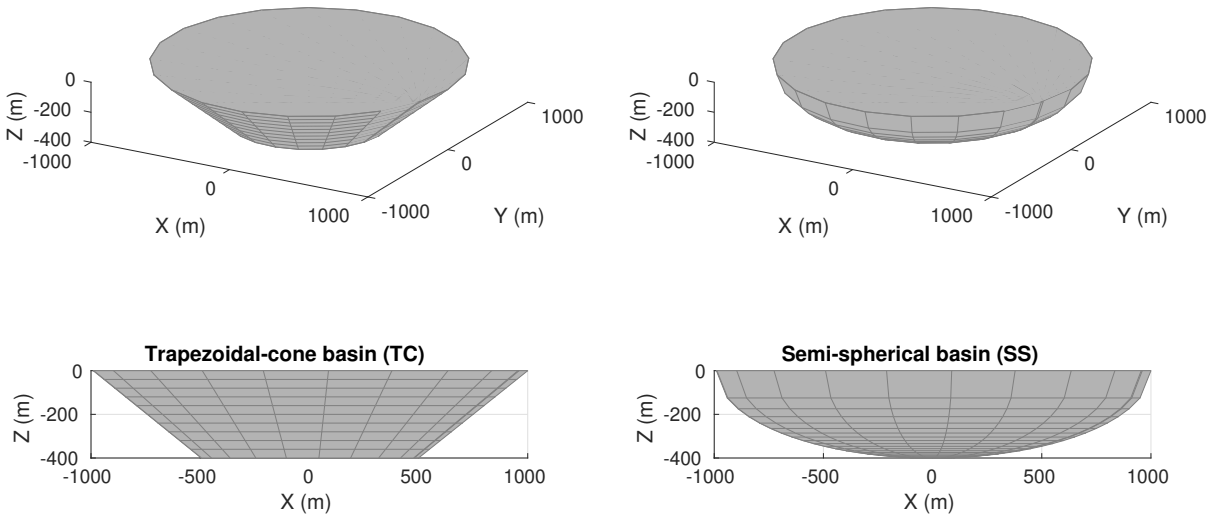

Figure 2.4: Geometries and dimensions of the selected basins: trapezoidal cone (TC) at the left and semi-sphere (SS) at the right.

In order to study the shape of the basin's influence on the generation of surface waves or AGF, the basins and halfspace will have a single homogeneous, linear elastic material. No material attenuation is introduced to the model. The mechanical material properties inside the basin and halfspace are given in Table 2.2. As material and geometrical properties of the sedimentary layers influence basin effects, two geometries and two material impedances are selected in a total of four combinations. Two velocity contrasts are considered by changing the shear velocity of the sedimentary material by 400 m/s to 900 m/s. In addition, two basin geometries are employed: a trapezoidal cone (TC) and a semi-sphere (SS), as shown in Figure 2.4. Both basins have the

Table 2.2: Material properties.

Material	V_s [m/s]	V_p [m/s]	ρ [kg/m^3]	ν
Basin	400 - 900	748 - 1684	2100	0.3
Half-space	2600	4700	2600	0.3

Table 2.3: Adimensional parameters for basin definition (Ayoubi et al., 2021).

		π_1	π_2	π_3	π_4	π_5	π_6	π_7'	f_0
Geometry	Vs [m/s]	ν_b	ν_{h-s}	$\frac{e}{H}$	$\frac{V_{s_{h-s}}}{V_{s_b}}$	$\frac{f_s H}{V_{s_b}}$	$\frac{\rho_{h-s}}{\rho_b}$	$\frac{2af_s}{V_{s_b}}$	$\frac{V_{s_b}}{4H}$
TC	900	0.3	0.3	1.25	2.89	0.79	0.81	1.97	0.56 Hz
	400	0.3	0.3	1.25	6.50	1.77	0.81	4.42	0.25 Hz
SS	900	0.3	0.3	2.50	2.89	0.79	0.81	1.97	0.56 Hz
	400	0.3	0.3	2.50	6.50	1.77	0.81	4.42	0.25 Hz

same circular surface section of radius $a = 1000$ m and a depth $H = 400$ m, hence the same shape ratio $a/H = 2.5$. The horizontal dimension of the edge of the TC basin is of $e = 500$ m, and for the SS the edge is equal to the radius of the basin $e = 1$ km.

According to the dimensionless parameters for defining basins of Ayoubi et al. (2021), the values π_n with $n = [1, 2, 3, 4, 6]$ associated with the geometry for the selected basins are described in Table 2.3, where the subscript b is associated with the basin material and $h - s$ with the halfspace. The parameter π_4 is the velocity contrast between soil and bedrock.

2.4.2 Seismic sources

In most aggravation studies, the incidence of the input motion is assumed either as a vertically incident plane wave (as in Riga et al., 2016; Zhu et al., 2018) or as an obliquely incident wave (as in Narayan, 2012; Amini et al., 2022). In order to evaluate the basin response to more realistic source scenarios, the seismic input will be imposed inside the domain as two types: a vertically incident plane shear wave polarized in the X direction and multiple independent double-couple (DC) point sources.

The source function is the same for the plane wave and the point sources, but vary in amplitude, described as moment time history in Figure 2.5 in (a) time and (b) frequencies. The dominant frequency f_s of the input is 1.77 Hz, which define the adimensional parameters π_5 and π_7' from Table 2.3. This excitation is proposed for a canonical basin case of the Euroseistest Verification and Validation Project (E2VP) (Chaljub et al., 2015; Maufroy et al., 2016).

The plane wave of vertical incidence is located at 10 km depth and inserted into the model through many point sources arranged in a horizontal plane, as shown in Gatti (2017). In each one of the point sources describing the plane wave, the moment time history shown in Figure 2.5 is imposed with the corresponding moment tensor for the correct definition of the vertical S-wave. In the 3D cases treated in this Chapter, the vertically incident S plane wave can be analyzed as an SV wave, as in-plane motion, or SH wave, as out-of-plane motion, depending on the selected

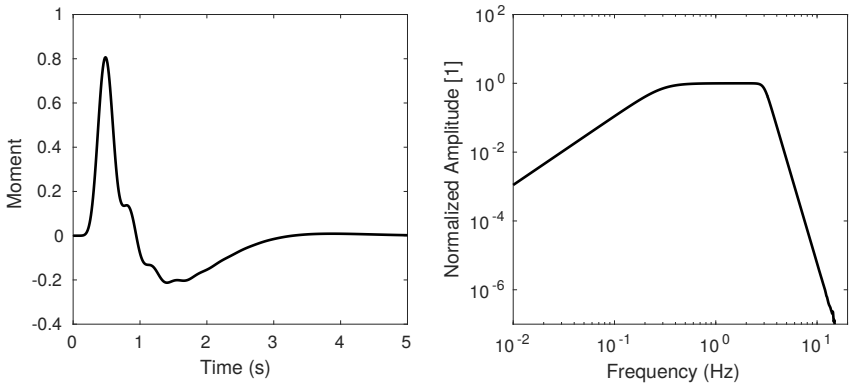

Figure 2.5: Dimensionless moment time history and corresponding amplitude Fourier spectra. The amplitude of the seismic moment is set differently to each point source and plane wave.

monitors on the surface.

The plane wave incidence will be contrasted against DC point sources (PS). These sources will be represented by the moment tensor, M:

$$M = \frac{1}{\sqrt{2}} \begin{bmatrix} 1 & 1 & 0 \\ 1 & -1 & 0 \\ 0 & 0 & 0 \end{bmatrix} \tag{2.13}$$

associated with a strike of $22.5°$, dip of $90.0°$ and rake of $0.0°$, which results in polarization motion in the X, Y, and Z components. The sources' epicenter are located at $x = -4000$ m and $y = 0$ m. The position of the sources, westward from the basin, results in the motion propagating in the positive X direction, impacting the basin from West (W) to East (E) (Figure 2.6).

The effects of source depth in basin amplification and surface wave generation are analyzed by nine different vertical positions, varying between 800 m and 14000 m. The name of each PS represents the angle between its vertical position to the basin center O at the surface. Thus, $PS_{11°}$ is the shallowest source, while $PS_{74°}$ is the deepest. Their positions are normalized with respect to height $H = 400$ m and basin radius $a = 1$ km in Figure 2.6.

Thus, for each configuration of 10 source types (1 vertically incident plane wave PW and 9 point sources PS_n), two basin geometries (TC and SS) and two velocity contrast between basin and bedrock (π_4 of 2.89 and 6.5), a total of 40 simulations were performed. The amplitude of all of the sources is normalized so that in a reference model without a basin, in a monitor located at the center O (coordinates [0,0,0] m), the maximum horizontal displacement is of 1.0 m.

2.5 Surface signal analysis in the basin

For each basin-source configuration, three independent $SEM3D$ simulations are necessary. The model where the basin is present can be represented as BAS in Figure 2.7(a). Two models are taken as reference: a model where the basin is not present, defined as REF , i.e. the model

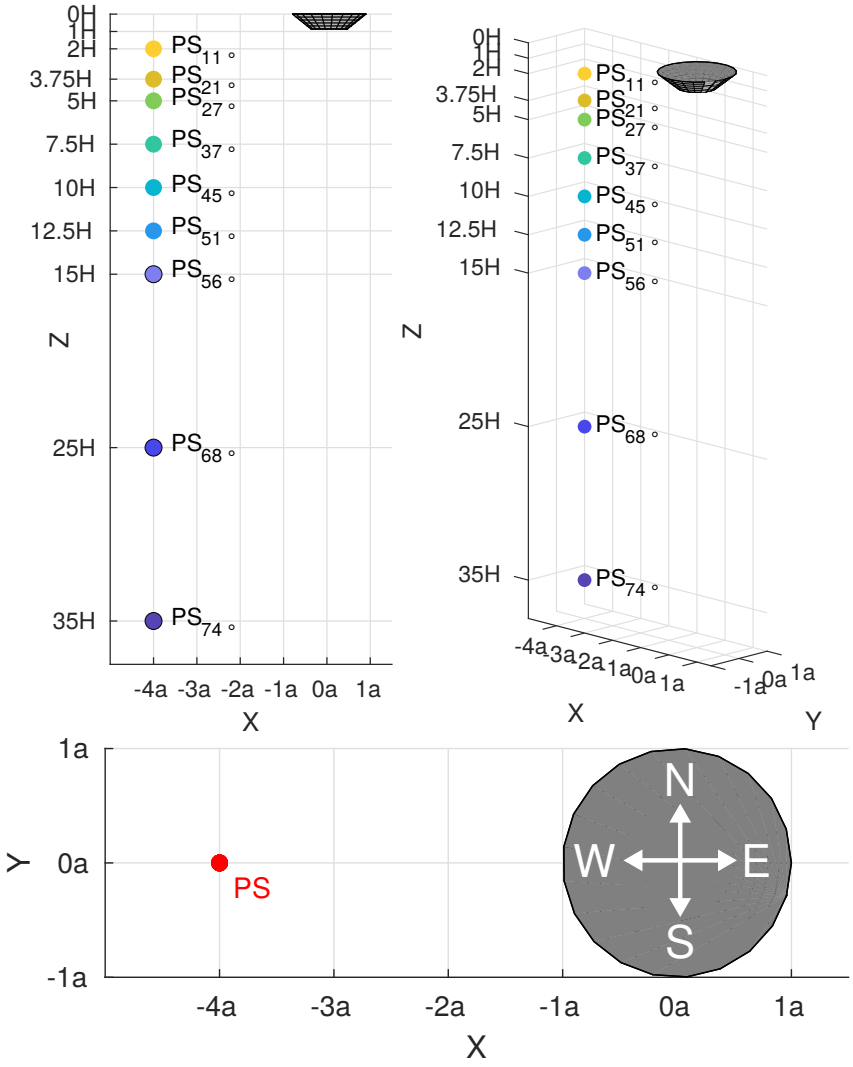

Figure 2.6: Geometry of the modeled basin and location of the sources, normalized by the halfwidth a and depth H of the basin.

consists only of the halfspace (Figure 2.7(b)); and the model where the sedimentary layer within the basin has extended laterally horizontally, with a thickness equal to the maximum thickness of the basin, defined as HOM in Figure 2.7(c). The latter is defined as two-dimensional (2D) instead of 1D, to account for the directionality coming from the point sources. Therefore, the difference between BAS and HOM is only inclusion of the basin edges.

Figure 2.8 shows the difference between the AF and the AGF for the displacement spectra (PSd) in one position inside the TC model with $V_s = 900$ m/s. The $AF_{2D}\{PSd\}$ (Equation 2.3) is amplified close to the predominant frequencies of the soil (vertical gray lines) inside the basin. However, as the $AF_{3D}\{PSd\}$ is not particularly amplified in the same frequencies, the $AGF\{PSd\}$ (Equation 2.5) will deamplified close to the predominant frequencies of the soil.

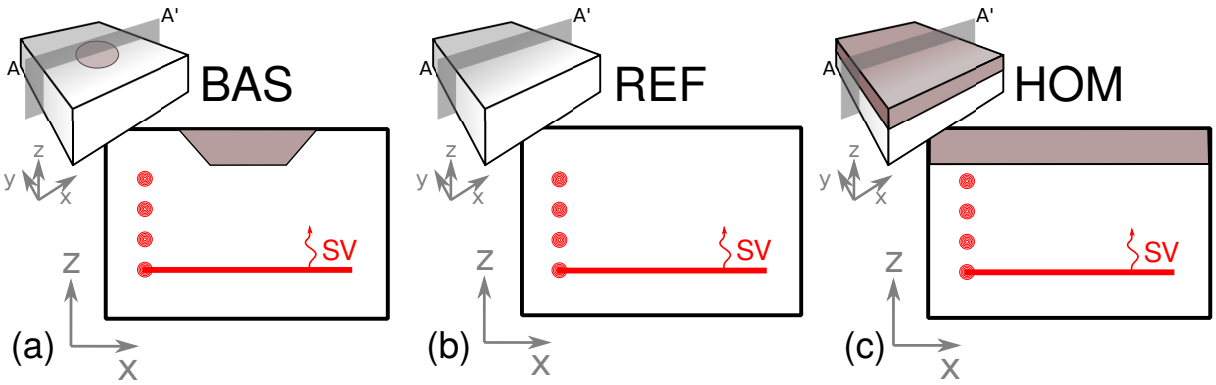

Figure 2.7: Representation of the three models used for the computation of the AGFs: BAS, including the basin, REF, only the halfspace and HOM or 2D model, where the sedimentary marterials are extended horizontally. The brown areas represent the sedimentary material.

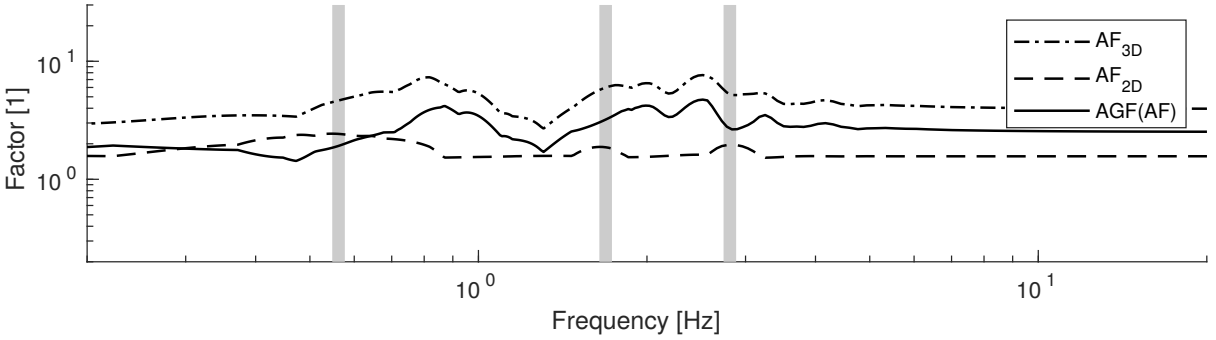

Figure 2.8: Comparison of AGF and AF computed in this work for a tipical case. The gray vertical lines represent the sediments predominant frequencies.

2.6 Results and discussion

In order to understand the effects of the surface waves on the basin amplification of the ground motion, surface wave characteristics are obtained in 3D models. Signals in the time domain are represented to qualitatively discern the creation of surface waves along the basin. Then, from these time signals, surface waves are extracted with the NIP method and characterised by their angle of polarisation, central frequency and maximum displacement.

The surface waves will be extracted from monitors located on a grid on the basin surface, spaced every 100 metres in both horizontal directions. Finally, the aggravation factor is calculated at the same positions.

In the first part, the analysis will focus on the basin response subjected to a plane wave (PW) approximation as input motion to verify the procedure. Then, the effect of different point source depth scenarios, basin geometry and basin-bedrock impedance contrast will be analysed.

As three-dimensional basins are used here, two profiles will be defined to present the results: $A - A'$, which is the vertical XZ plane passing through $y = 0$ (aligned with the EW direction), and $B - B'$, in YZ, which passes through $x = 0$ (aligned with the NS direction), for direction see Figure 2.6.

Both profiles divide the basin in its central part. The vertically incident S-wave can be analysed as an SV-wave (in-plane motion) in the $A-A'$ plane or as a SH-wave (out-of-plane motion) in the $B-B'$ plane.

2.6.1 Surface waves generated by a vertically incident plane S-wave

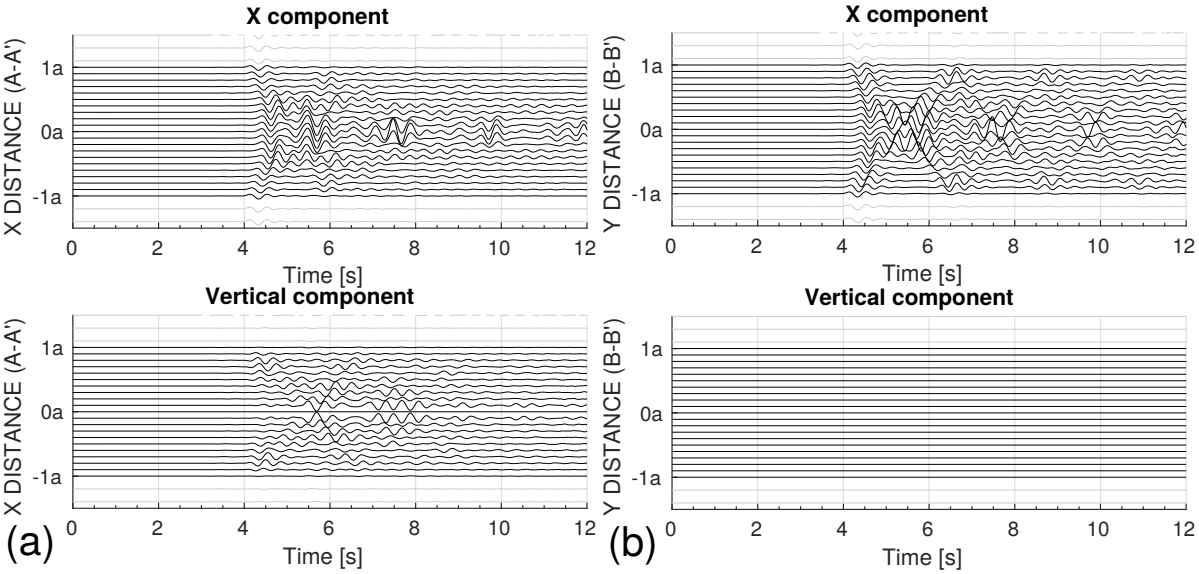

Figure 2.9: Acceleration time histories obtained at TC model for the vertically incident plane S-wave (PW) input motion. (a) profile $A-A'$ and (b) $B-B'$.

This part considers the response of the trapezoidal cone (TC) basin, with sediment shear wave velocity of $V_s = 900$ m/s, subjected to a vertically incident plane S-wave. The time domain representation for the plane wave is observed along the $A-A'$ and $B-B'$ profiles in Figure 2.9. As expected, the basin generates a parasitic vertical signal in profile $A-A'$. The effect on the horizontal accelerations is higher at the basin's centre, where surface waves are induced and trapped, reflected in the edges, travelling back and forth, increasing the signal duration. In the $B-B'$ plane, the surface wave arrival describes an X-pattern, observed by Kawase and Aki (1989) among others, for a SH-wave in a similar basin.

The amplification response can be observed over the surface with the horizontal particle motion (Figure 2.10). In red lines, the response in the REF model, without the basin, contrasts the amplification observed when the basin is added in black lines (BAS). In the central profile, the SH ($x = 0$) response predominates, but polarisations are seen in other areas.

In order to quantify the generation of surface waves and their propagation within the basin, three main characteristics are extracted with the NIP from the time signals: the maximum horizontal displacement, the central frequency and the angle of polarisation. As shown in Figure 2.9, the obtained signals exhibit multiple reflections causing surface waves to change their direction with time. Therefore, each signal is partitioned into 1.5-second time windows to evaluate their evolution with time.

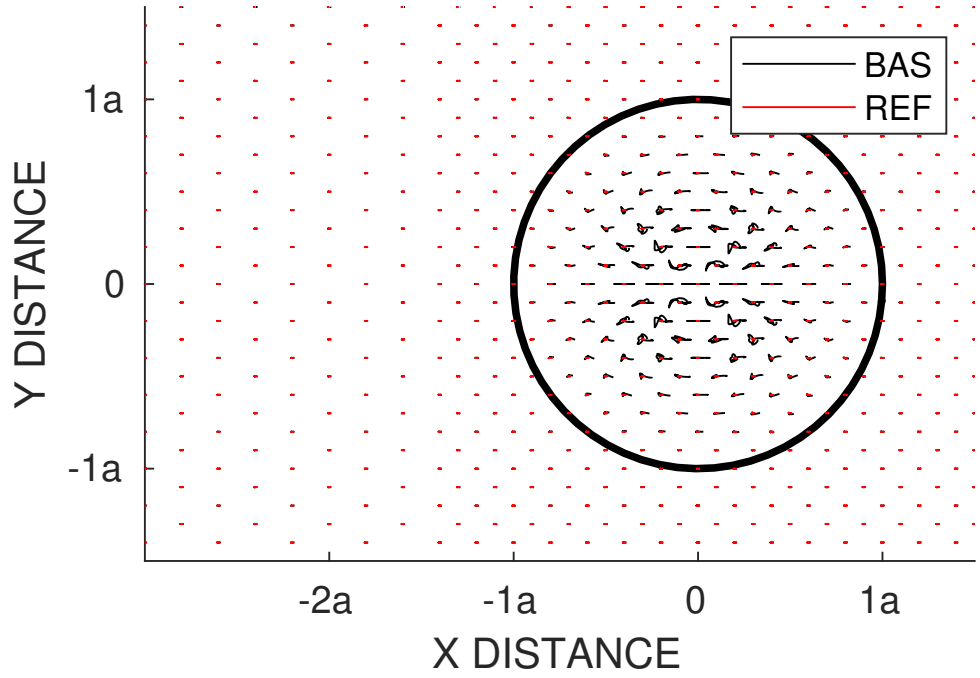

Figure 2.10: Particle motion at the surface in the time window $t = [4.50 - 6.00]$ s for the PW input motion. The basin amplification is shown as black lines for the BAS model in contrast with the reference model REF, without the basin, in red lines.

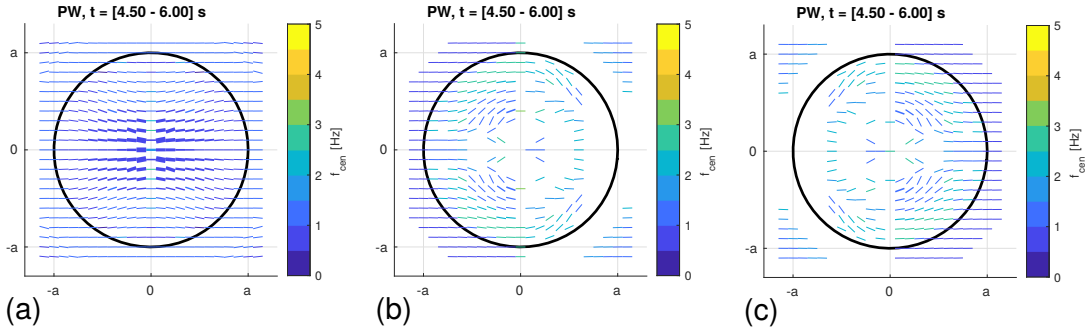

Figure 2.11: Spatial variability of the extracted surface waves: (a) Love, (b) Prograde Rayleigh and (c) Retrograde Rayleigh, in time window $t = [4.50 - 6.00]$ s for the PW input motion. The colour of the lines represents the central frequency f_{cen} and the thickness is proportional to the maximum amplitude of the wave in that position.

Figure 2.11 illustrates the extracted surface waves over the basin surface for the window $t = [4.50 - 6.00]$ s. The angle of polarisation, obtained with Equation 1.34, and two additional characteristics of the extracted waves are presented in Figure 2.11. First, the thickness of each segment is proportional to the maximum displacement of the extracted wave. Second, the colour is assigned by the central frequency (f_{cen}), defined as the frequency at which the maximum amplitude of the polarised wave is found in the Stockwell transform of the polarised wave (Meza-Fajardo and Papageorgiou, 2016). It is important to recall that an extracted wave is plotted in the figure only if the correlation coefficient C_{PV}, between the polarised and shifted vertical

wave is greater than 0.7 for Rayleigh waves and less than 0.3 for Love waves (Meza-Fajardo and Papageorgiou, 2016).

Only Love waves are detected in the $B - B'$ profile passing through the NS plane. Since Love waves propagate perpendicular to their polarisation, they are created at the edges and propagate toward the centre. This response demonstrates that the Love waves shown in Figure 2.9 in the $B - B'$ plane can be extracted using the NIP method as surface waves producing the X-pattern.

The tridimensional geometry of the basin generates additional surface waves not seen from the 2D profiles. Rayleigh waves seem to be generated from the East or West edges, where the polarisation of the waves is normal to the basin edge (Figure 2.11b and c). Then, they follow the basin edge as they propagate inside the basin. The decrease of the central frequency f_{cen} towards the centre stands in line with the findings of Narayan (2012). From the definition of the method, Rayleigh waves with prograde or retrograde polarisation have the same properties but an inverse angle of polarisation (Figure 2.11b and c). From this point on, only the retrograde Rayleigh wave will be depicted.

2.6.2 Surface waves for a shallow source ($PS_{11°}$) versus a deep source ($PS_{74°}$)

In order to compare the previous results for a more complex source, the shallower ($PS_{11°}$) and the deepest ($PS_{74°}$) point sources are selected in this section. It is important to recall that the amplitude of signals is normalised in the reference REF model without the presence of the basin.

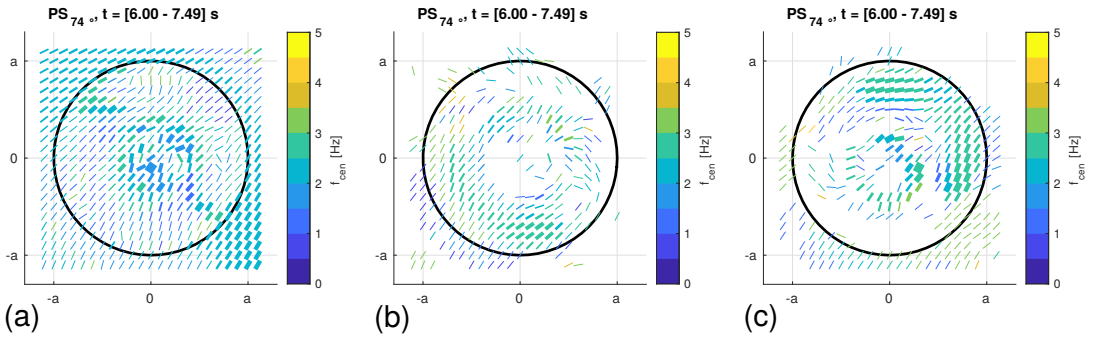

Figure 2.12: Spatial variability of the extracted surface waves: (a) Love, (b) Prograde Rayleigh and (c) Retrograde Rayleigh, for the $PS_{74°}$, in time $t = [6.00 - 7.50]$ [s]. The color description is found in Figure 2.11.

The response resembles the plane wave in the deep source $PS_{74°}$. Due to the point source characteristics, the polarisation angle outside the basin is nearly 50 °. As surface waves enter the basin, this angle is only slightly deflected. Love waves are generated in an azimuth close to $125°$ from the North, where the polarisation motion of the input follows the basin edges (Figure 2.12a). Then, they are amplified towards the centre of the basin. Rayleigh waves enter from an

azimuth close to $45°$ and get deflected by the basin edge (Figure 2.12b and c), following the same behaviour as the PW case.

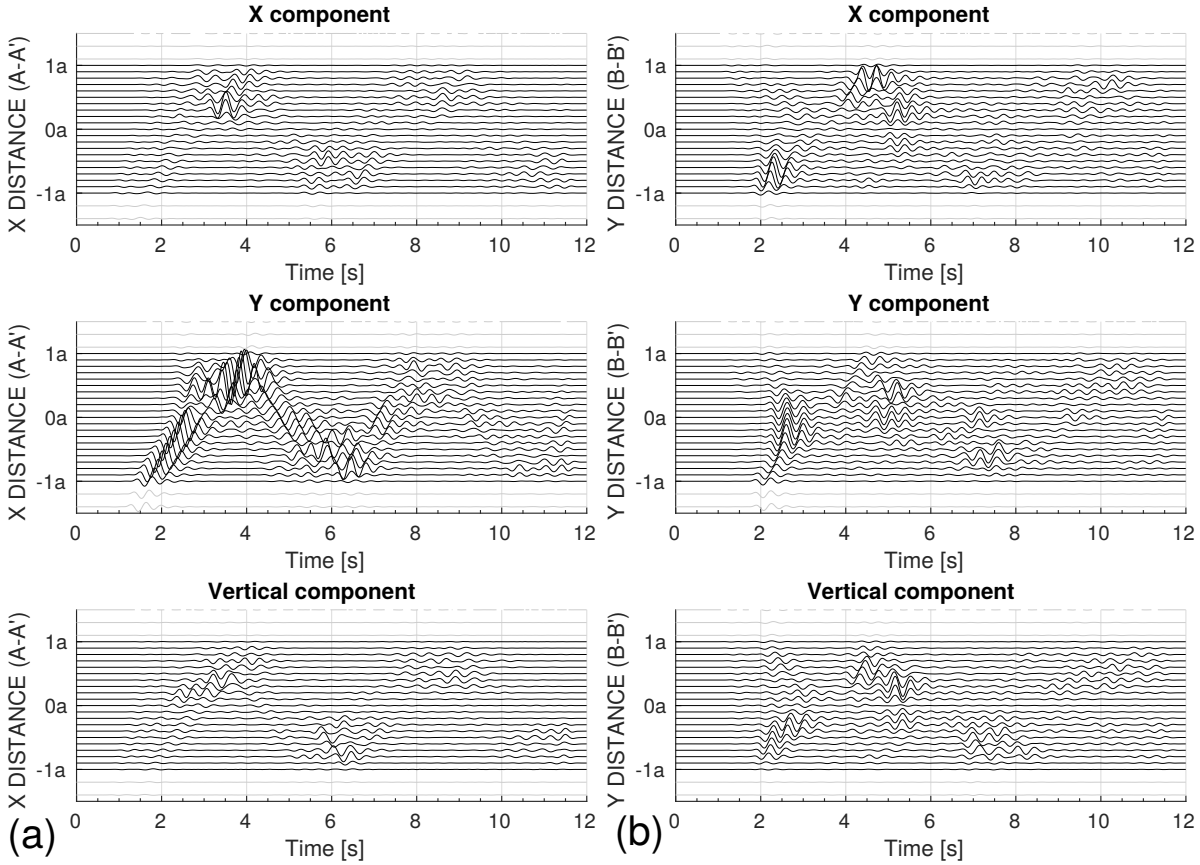

Figure 2.13: Acceleration time histories obtained at TC model for a point source input motion, $PS_{11°}$, located at [-4000,0,-800] m. (a) Profile $A - A'$ and (b) $B - B'$.

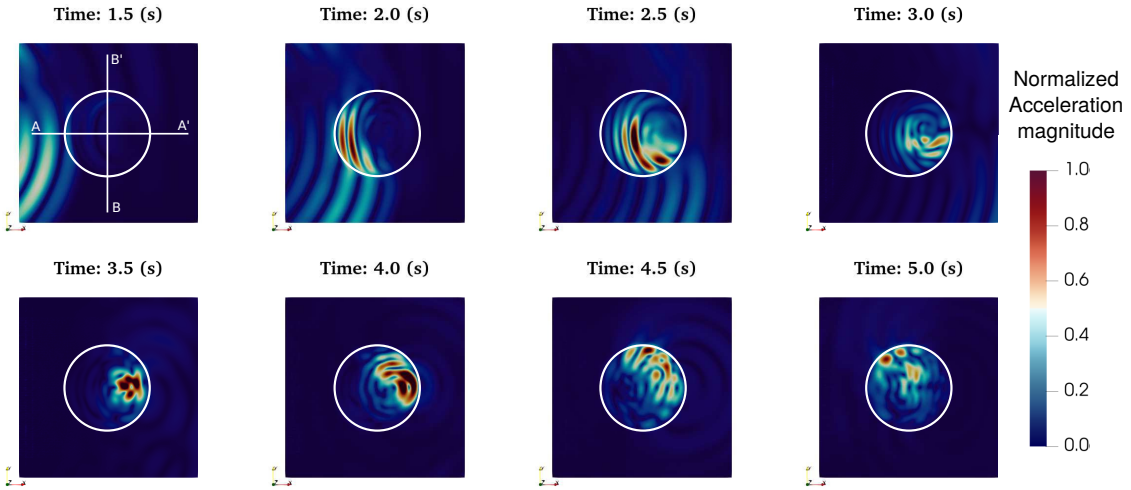

Figure 2.14: Snapshots from $t = 1.5 - 5.0$ s of the acceleration magnitude in the XY plane. The white circle represent the basin boundaries at the surface.

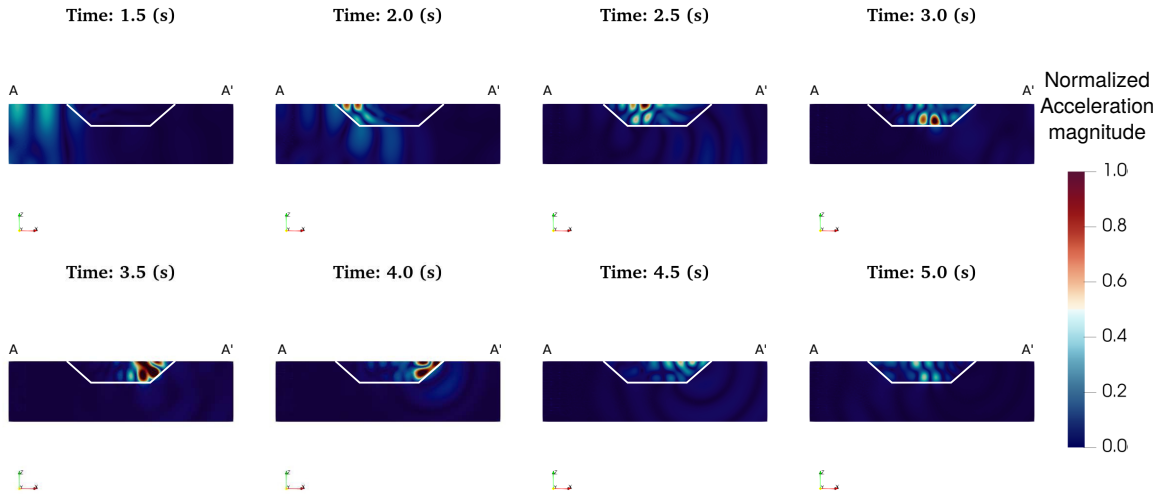

Figure 2.15: Snapshots from $t = 1.5 - 5.0$ s of the acceleration magnitude in the $A - A'$ plane. In white, the basin boundaries.

Contrary to the plane wave behavior and as expected, in the shallower source PS_{11° the surface motion is nonzero in all three directions, propagating from $[-4000 \text{ m}, 0 \text{ m}, -800 \text{ m}]$ or $[-4a, 0, -2H]$ (Figure 2.13). Reaching the western basin edge, at -1000 m or $-1a$, the profile $A - A'$ in Figure 2.13a displays how the wave travels toward the right edge from $-1a$ to $1a$. The same figure shows that the motion amplitude is higher in the Y component due to the moment tensor selected for the PS. The profile $B - B'$ shows the arrival time of the wave in the other orientation. Since the point source is centred on the Y axis, the wave's arrival at the basin edges is symmetrical but with different amplitudes on both sides.

To better understand the wave propagation for the same point-source case, PS_{11°, snapshots of the acceleration magnitude norm for different times are shown in the XY plane at the surface and the $A - A'$ profile in Figures 2.14 and 2.15, respectively. The wave arrives at the western edge and travels west-east inside the basin until it reaches the opposite edge, between 3.0 and 3.5 s. The maximum acceleration is a product of constructive wave interference at the opposite side, where a high concentration of energy is observed with complex directionality. The entire edge, in-depth, appears to influence this interference, as seen at 3.5 s in the $A - A'$ plane (Figure 2.15, bottom left). After 3.5 s, the wave propagates in the other direction, with a more complex motion. It can be seen that some energy reaches out from the basin at each reflection, but most of the energy remains trapped in the basin.

In order to contrast the influence of the source position in the polarisation of waves, Figure 2.16 on the left shows the particle ground motion along the surface for the PS_{11° on a small time window of $t = [1.5 - 3.0]$ s. The red lines illustrate the particle motion in the reference REF model: if the basin were not present, the particle motion for the shallow source would be induced by the input polarisation, showing larger variations of the polarisation angle across the basin. In contrast, the black lines illustrate how the motion is amplified inside the basin, showing a more complex motion due to the source position. When the wave first enters the basin at

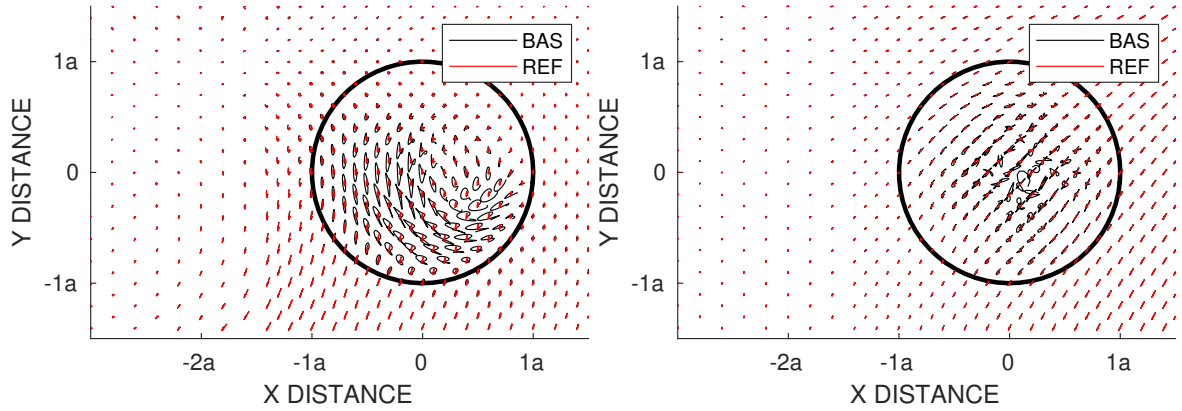

Figure 2.16: Particle motion along the basin for the source PS_{11° (left) and PS_{74° (right). The basin amplification is shown as black lines for the BAS model in contrast with the reference model REF, without the basin, in red lines.

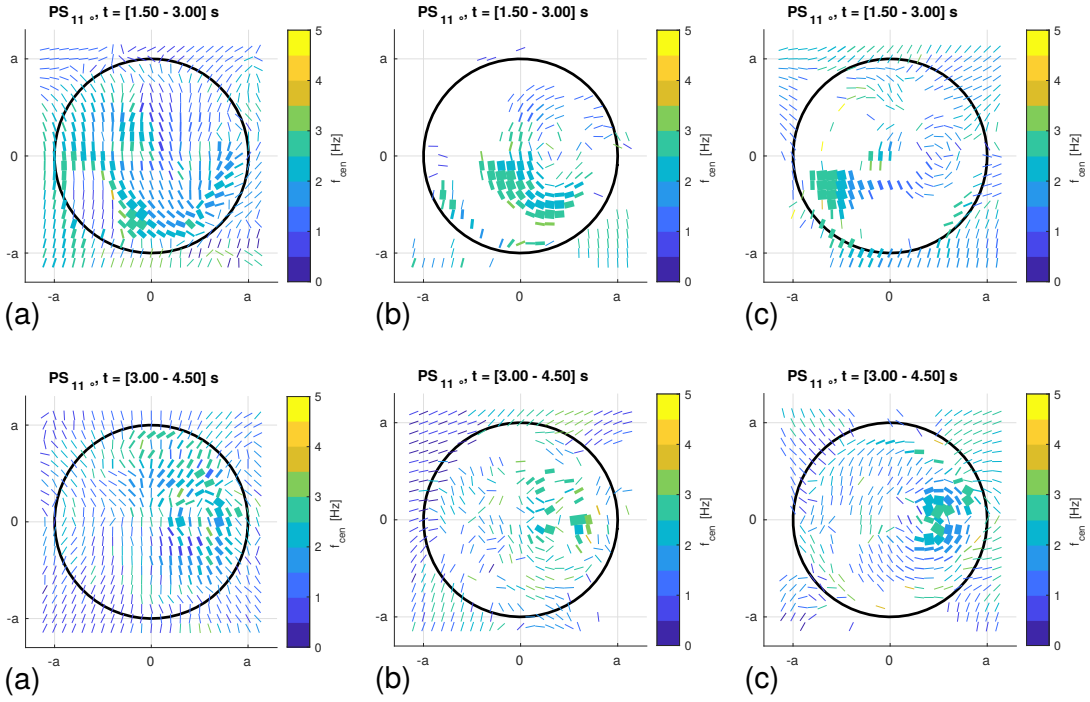

Figure 2.17: Spatial variability of the extracted surface waves: (a) Love, (b) Prograde Rayleigh and (c) Retrograde Rayleigh for the PS_{11°. Results from two separate time windows: $t = [3.00 - 4.50]$ s (top) and $t = [4.50 - 6.00]$ s (bottom). The color description is found in Figure 2.11.

the west border, the motion is aligned and defined by the source. This motion is congruent with the Love wave travelling from West to East, with a polarisation close to 180° extracted from the NIP methodology (Figure 2.17a). This motion could also be explained by a Rayleigh wave arriving between 1 and 3 seconds with an angle close to 180° (Figure 2.17b or c). Then, the waves approach the opposite edges in the time window $t = [4.50 - 6.00]$ s (Figure 2.17 bottom). The PS_{11° cause a high concentration of Love and Rayleigh waves, with polarisation angles of 0°

aligned to the North but slightly deflected.

The results indicate that this shallow source induces surface waves starting from the wave entrance to the basin and deflecting following the basin geometry. In this case, the creation of Love waves is privileged because the wave's polarisation direction coincides with the basin's edge. Rayleigh waves are created when the polarisation direction is perpendicular to the border, so they are not present directly in the west border. However, they are present in the centre of the basin. This area is exposed to waves propagating from the deepest part of the basin border seem to amplify the surface motion in Figure 2.15, so all the borders could play a role in the creation of Rayleigh waves.

2.6.3 Effects on the source depth on the surface waves characteristics

The impact of the source position on the creation of surface waves is next evaluated at the central monitor and the basin (TC) with a shear wave velocity $V_s = 900$ m/s. Figure 2.18 display the displacement time histories at the central monitor O for all the sources, from the shallower PS_{11° in yellow at the top to the deepest PS_{74° in blue and the PW input in black at the bottom of the figure.

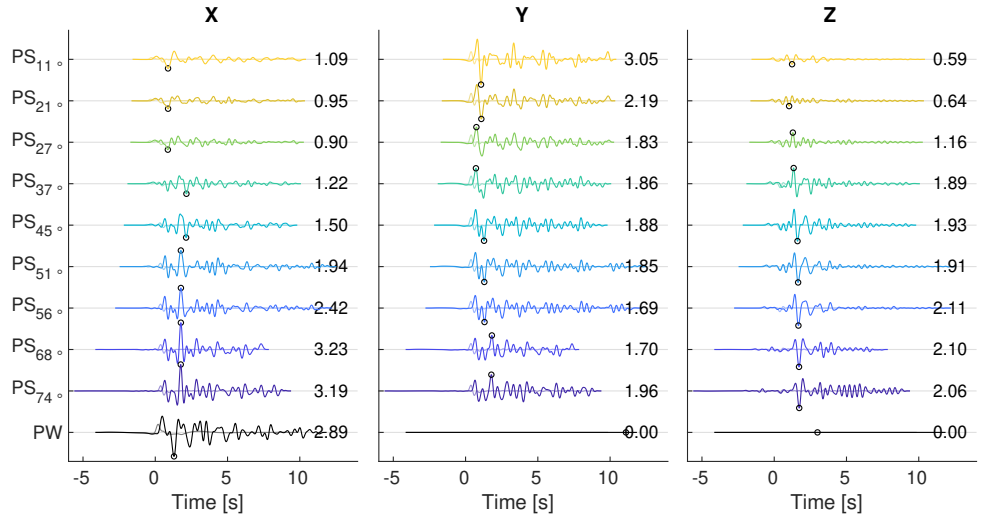

Figure 2.18: Displacement time histories obtained at TC model in the central monitor for all the sources, represented in different colours. The maximum displacement value is also mentioned. This value is normalised, so in the REF model, for each source, the obtained displacement is one m.

In Figures 2.19 and 2.20, each plot represents the evolution of the polarisation angle for the retrograde Rayleigh and Love waves, respectively. The angle is oriented in the figure so that it can be viewed in the north-south direction (0 degrees is North, 90 degrees is East). The radius in each plot represents the time, starting from the central part. The results for the shallowest source PS_{11° are in the upper left corner, and for the deepest source PS_{74° are in the lower right corner.

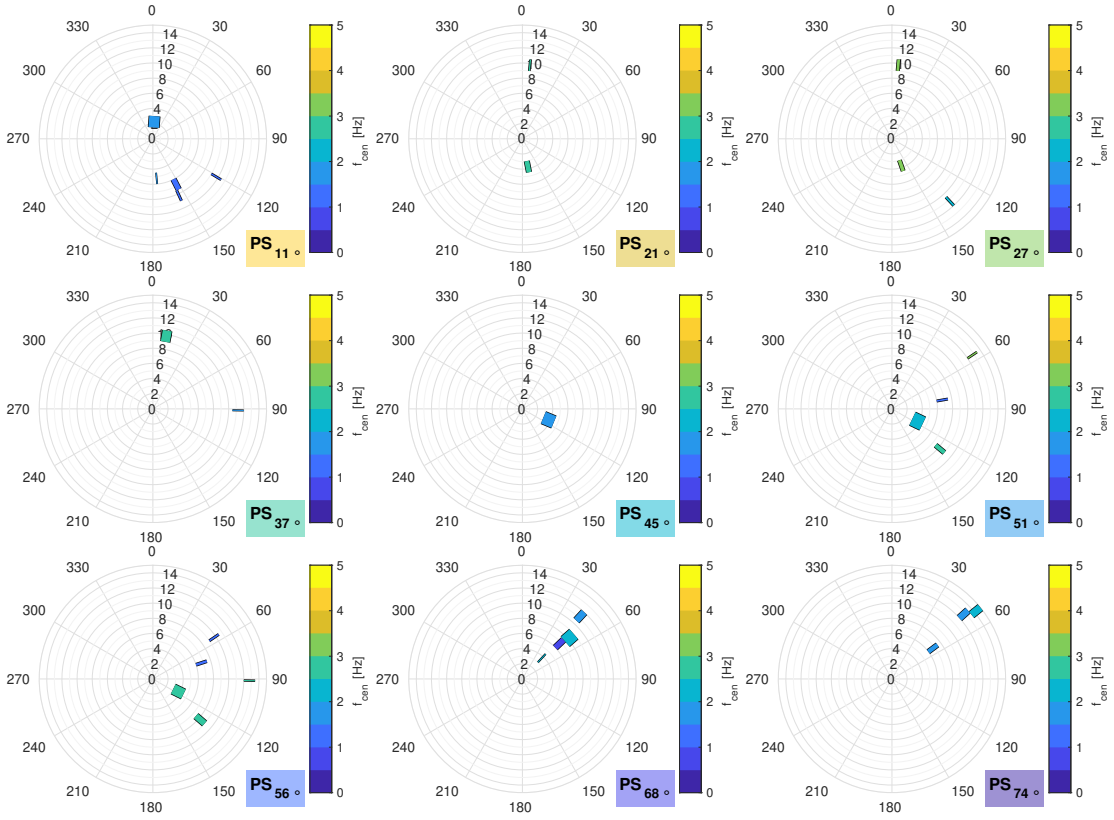

Figure 2.19: Time evolution of the extracted retrograde Rayleigh waves characteristics. Each plot represents a PS depth, from the shallower $PS_{11°}$, at the upper left, to the deepest, $PS_{74°}$, at the bottom right. The description is found in Figure 2.11.

For Rayleigh waves, in Figure 2.19, the angle of polarisation has different values in time, always in the quadrant $0° - 180°$. The polarisation angle of Love waves at the central position, in general, is stable in time (Figure 2.20), where maximum variation is seen for medium depth sources ($PS_{37°}$ to $PS_{56°}$). For both types of waves, as the depth of the source increases, the polarisation angle approaches a value of $45°$ or $225°$, which corresponds to the polarisation angle of the input motion. Therefore, the Love generation and propagation require the polarisation motion to be parallel to the basin's entrance. Thus, the results agree with those obtained in the previous section.

2.6.4 Spatial variability of the extracted surface waves characteristics with the basin geometry and material parameters

This section presents the influence of the spatial variation of the extracted surface wave characteristics with different geometry, material and source scenarios. Nine source depths, defined by the incidence angle of $11°, 21°, 27°, 37°, 45°, 51°, 56°, 68°$ and $74°$ are compared against the PW input. Two impedance contrast of $\pi_4 = 2.89$ and $\pi_4 = 6.50$ are evaluated. The characteristics of the extracted waves are presented in terms of amplitudes and frequencies. Besides, the impact of the basin geometry on the generation of surface waves is assessed with a semi-spherical

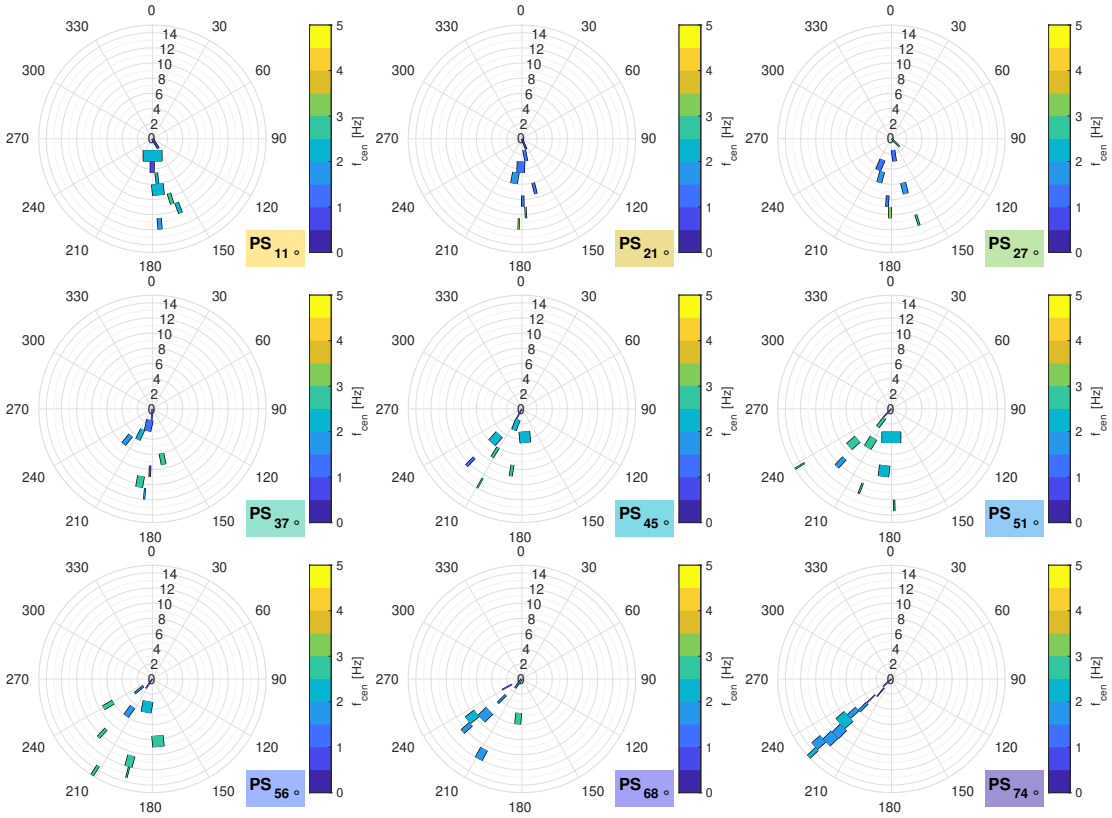

Figure 2.20: Time evolution of the extracted Love waves characteristics. Each plot represents a PS depth, from the shallower $PS_{11°}$, at the upper left, to the deepest, $PS_{74°}$, at the bottom right. The description is found in Figure 2.11.

basin (SS). According to Kamal and Narayan (2015), in the semi-spherical case, the entire basin influences the generation of surface waves, compared to the trapezoidal case, where only the edge of the basin influences the generation of surface waves. Both basin models have the same shape ratio, as shown in Figure 2.4.

2.6.4.1 Effect on the amplitude A_{POL} of the polarized extracted wave.

Figures 2.21 and 2.22 show the effect of source depth on the spatial variability of the maximum polarised wave amplitude A_{POL} of Love and Rayleigh waves, respectively. The x-axis represents the distance to the central point O, with $a = 1000$ m the radius of the basin. The plots on the left show the spatial variation on the X-axis or the $A - A'$ plane and the right on the $B - B'$ plane. The point sources are shown in colours, and the plane wave is black.

The maximum amplitude of Rayleigh waves is concentrated on the basin's eastern side (Figure 2.21), linked to the wave reflection at the opposite edge of the arrival. The reflection is more prominent in shallow PS sources from $PS_{11°}$ to $PS_{37°}$, where the wave impacts directly in the basin border. From an incidence angle of the wave greater than $56°$, the amplitude decreases and concentrates in the centre, approaching that of a plane wave. For the semi-spherical basin SS, only shallow sources have a recognisable amplification of Rayleigh waves linked with the wave

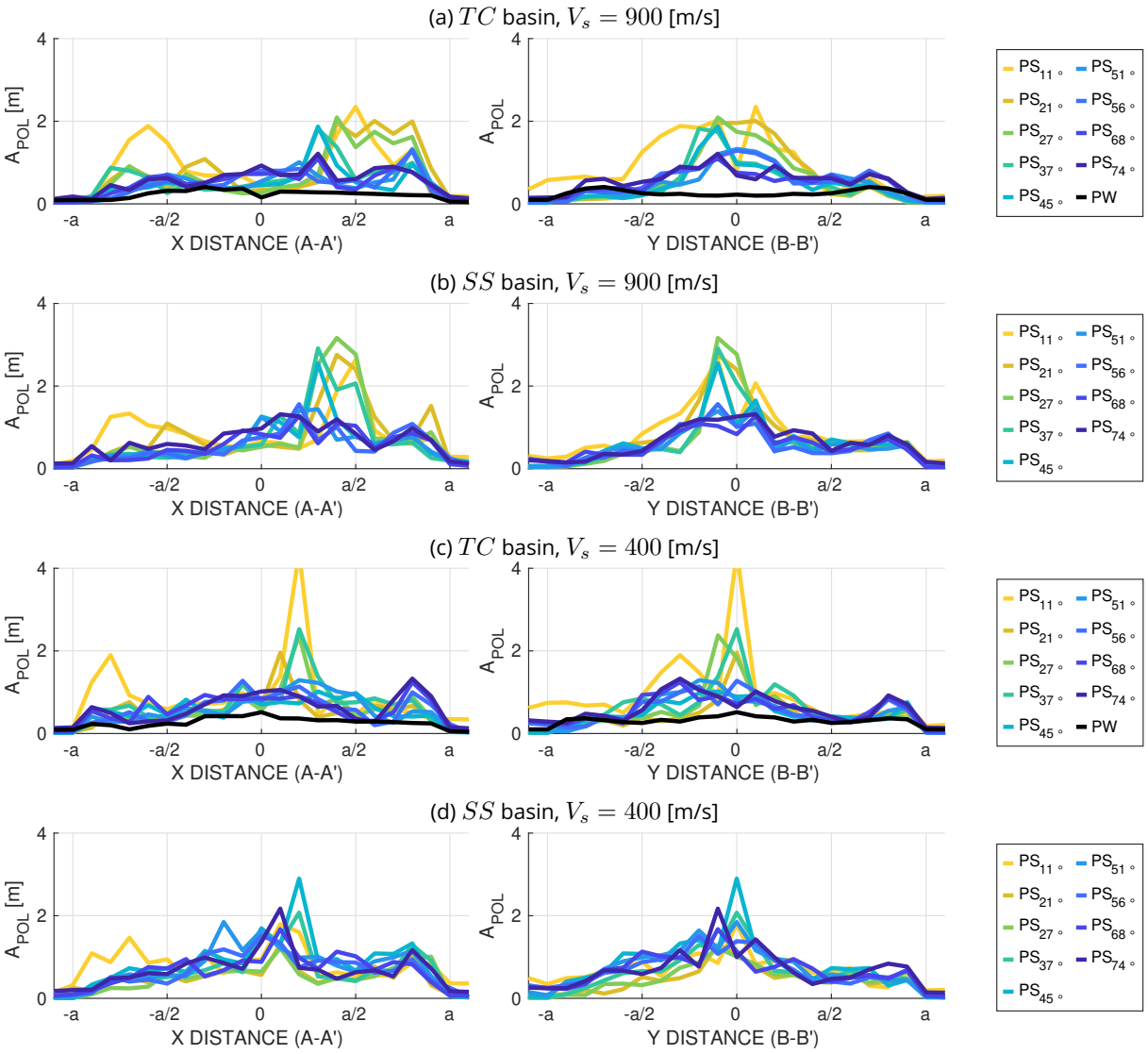

Figure 2.21: Spatial variability of the extracted retrograde Rayleigh wave, over the $A - A'$ (left) and $B - B'$ (right) planes for the TC and SS basin case and the shear wave velocities of the sedimentary materials $V_s = 900$ m/s and $V_s = 400$ m/s.

reflection. This reflection, however, does not appear to influence the spatial variability for low-rigidity sediments (Figure 2.21d). The impedance contrast affects A_{POL} displaying larger values for $V_s = 400$ m/s and inducing concentration of surface waves in different locations. In the case of $V_s = 400$ m/s, surface waves are mainly concentrated further away from the edge and in a narrower zone. This finding would indicate that the surface waves are rapidly deamplified within the basin for softer sediments. Nevertheless, edge-generated surface waves near the edges do not show substantial differences with basin geometry.

Love waves will have their maximum amplification towards the western edge (in $X = -a$). The amplification is independent of the source depth for the TC basin, but for the SS basin, amplification is only recognisable in shallow sources. Since the basin-bedrock interface is more

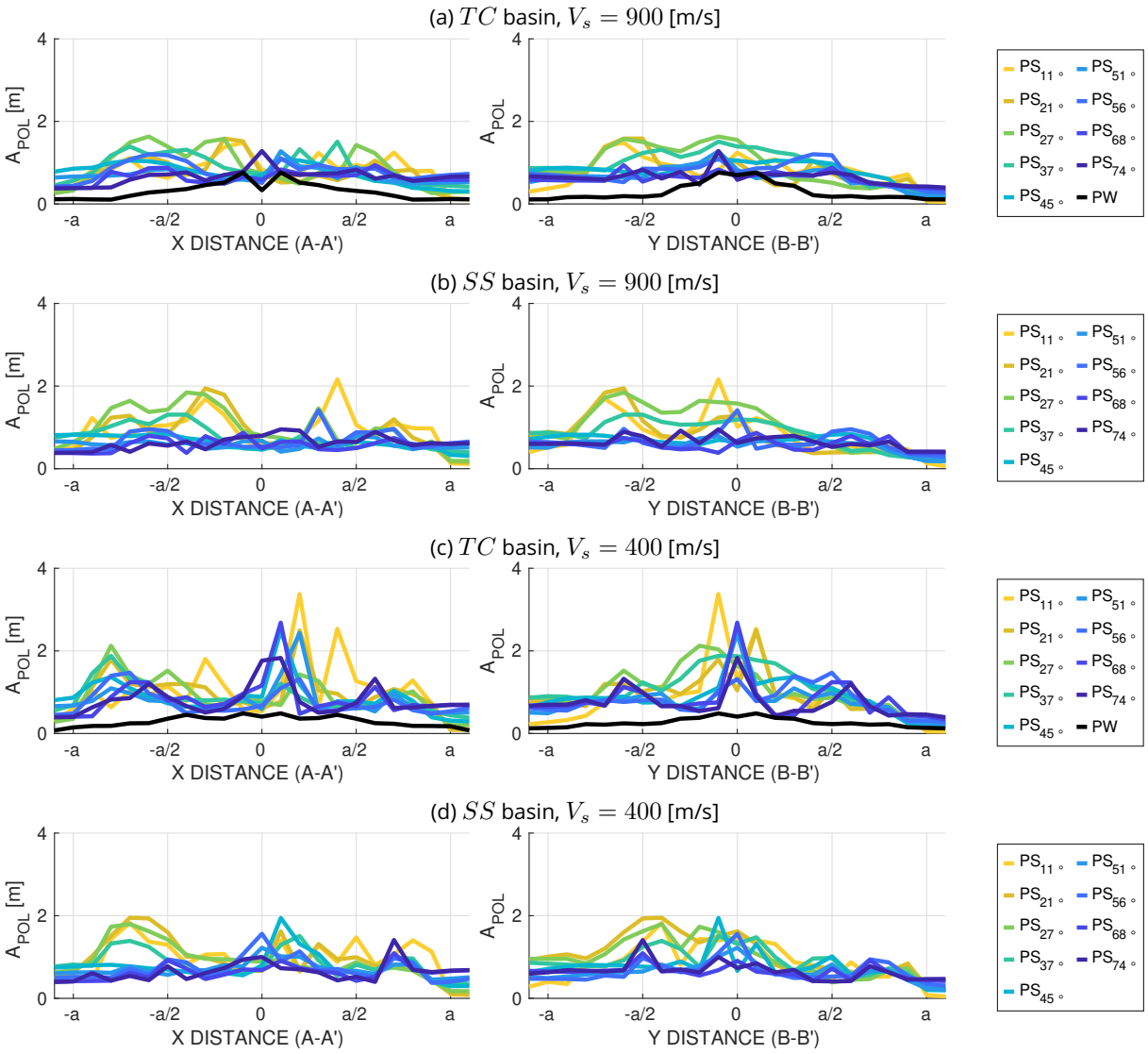

Figure 2.22: Spatial variability of the extracted Love wave, over the $A - A'$ (left) and $B - B'$ (right) planes for the TC and SS basin case and the shear wave velocities of the sedimentary materials $V_s = 900$ m/s and $V_s = 400$ m/s.

subtle in the SS basin, the edge reflections occur over a larger area, reducing the amplitudes of Love waves in this geometry.

2.6.4.2 Effect on the central frequency f_{cen} of the extracted waves.

The central frequency of the surface waves can also be necessary for their description since they influence the ground motion amplification inducing potential damage in buildings with those resonant frequencies. In the previous section, amplification is concentrated near the edges. Therefore, the spatial variability of this property is displayed against the distance to the centre.

The effect of impedance contrast, basin geometry, and source depth on the central frequency

(f_{cen}) of the extracted waves can be observed in Figure 2.23 for the point waves PS_{11° (yellow) and PS_{74° (blue). In the diagrams, each point represents an extracted signal, and the size is associated with its amplitude.

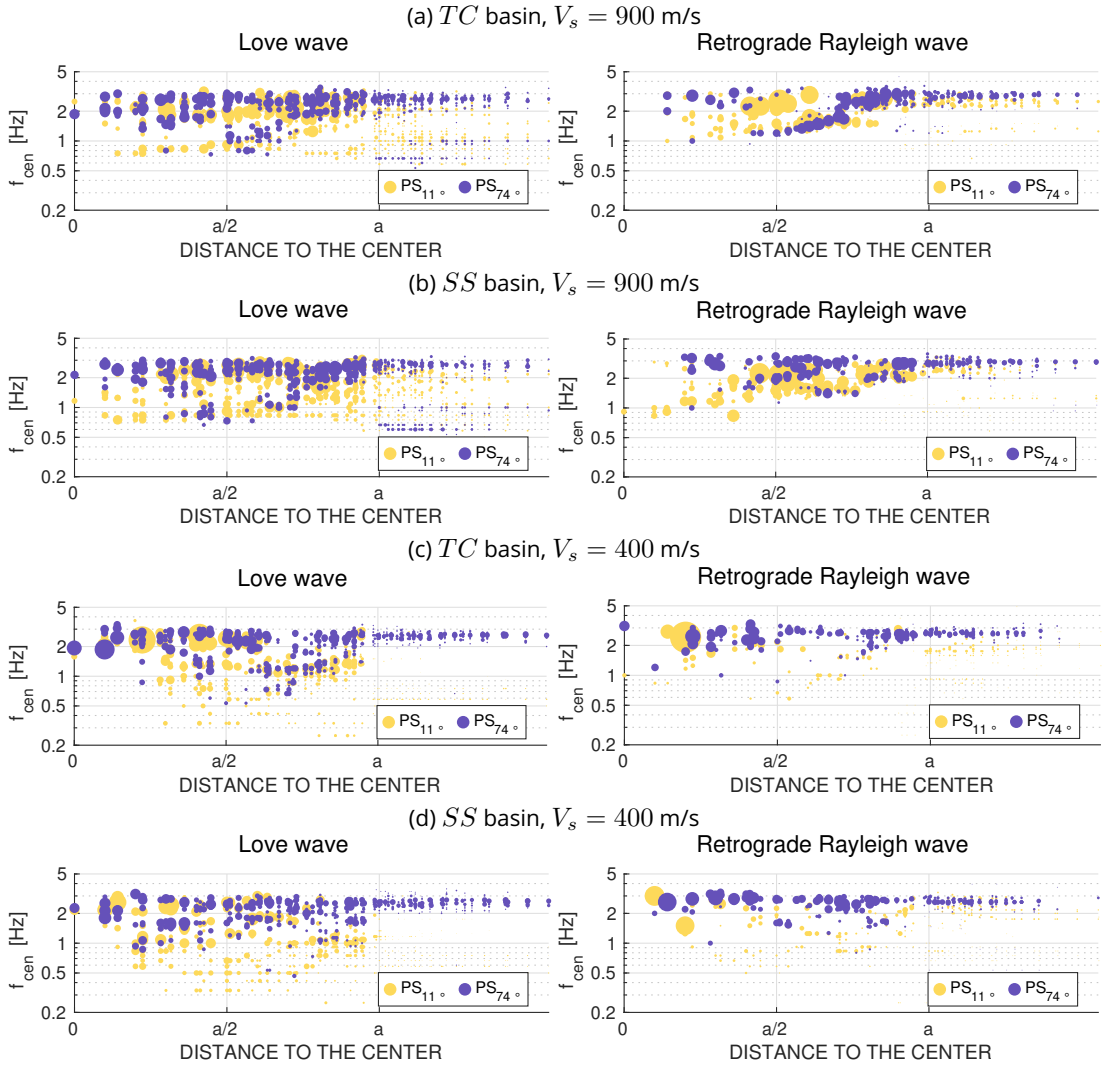

Figure 2.23: Spatial variability of the central frequencies (f_{cen}) of the extracted Love (left) and retrograde Rayleigh (right) waves over the $A - A'$ plane in the TC basin and the PS_{11°, in yellow, and PS_{74°, in blue, input motions, for shear wave velocities of the sedimentary materials $V_s = 900$ m/s (top) and $V_s = 400$ m/s (bottom).

For the PS input motions (Figure 2.23), the upper limit is $f_{cen} = 3.0$ Hz, related to the maximum frequency of the input motion (Figure 2.5). Generally, f_{cen} decreases as the surface waves (Love and Rayleigh) enter the basin from the edges. Love waves reach lower frequencies than Rayleigh waves, a similar response as the showed for Kanto and Nobi valleys in the work of Meza-Fajardo et al. (2021).

The effect of the impedance contrast can be seen as a decrease in the f_{cen}, but the results indicate that the f_0 value represents a lower limit of the central frequency of the extracted surface waves. The basin geometry, namely the difference between the TC and SS basins, does not

significantly affect the f_{cen}, as seen in Figure 2.23 for all case scenarios.

2.6.5 Impact of the basin-generated surface waves on the aggravation factor

Surface waves will impact the amplification of the ground motion inside the basin, as they are responsible for increasing the amplitudes and duration of the ground motion (Graves, 1993). In this last section, the spatial variability of the AGF with the same configurations is evaluated with Equation 2.5. The spatial variability of AGFs is then compared to the obtained with the extracted surface waves in the previous sections.

Two ground motion parameters are selected: the horizontal peak ground displacement,

$$PGD_H = \max_t \sqrt{u_x\left(t\right)^2 + u_y\left(t\right)^2} \tag{2.14}$$

and the displacement spectra of the horizontal components, PSD, with the $RotD50$, proposed by Boore (2010). The $RotD50$ is an orientation-independent spectral intensity measure, computed as

$$RotD50 = \underset{\theta}{median}\left[PSD_{5\%}\left(\theta\right)\right] \tag{2.15}$$

where the angle θ is defined by the rotation of their horizontal components. The $RotD50$ will be applied to account for the complex directivity pattern exposed by the surface waves with only one parameter for both horizontal components.

2.6.5.1 Effects on the $AGF\left\{PGD_H\right\}$

Figure 2.24 shows the $AGF\left\{PGD_H\right\}$ variation with the depth of the source and for the two impedance contrast. The maximum amplification factor in shallower sources is found towards the eastern edge of the basin, the edge opposite to the wave entrance, as could be observed before in the time signals. The $AGF\left\{PGD_H\right\}$ decreases while increasing depth, from a maximum value close to 6 at source PS_{11° to close to 2.5 at source PS_{74° in the $V_s = 900$ m/s case. Results from the literature suggest that these findings can be accounted for by increased wave interference and reflections at the opposite edge in sources closer to the surface. Narayan (2012) found that the average aggravation factor (AAGF), averaging over frequencies, for different edge slopes and a propagated SH wave increases with increasing angle of incidence. The found AAGF is minimum for an angle of 0 degrees, i.e., equal to the PW, shown in black in the figure, and maximum as it approaches 90 degrees, closer to the shallow sources. Panji and Mojtabazadeh-Hasanlouei (2021) studied the ground motions in basins for oblique incident SH waves and also found that the amplifications increased for waves closer to the surface. Larger $AGF\left\{PGD_H\right\}$ are also found next to the basin edges, higher for a $V_s = 400$ m/s.

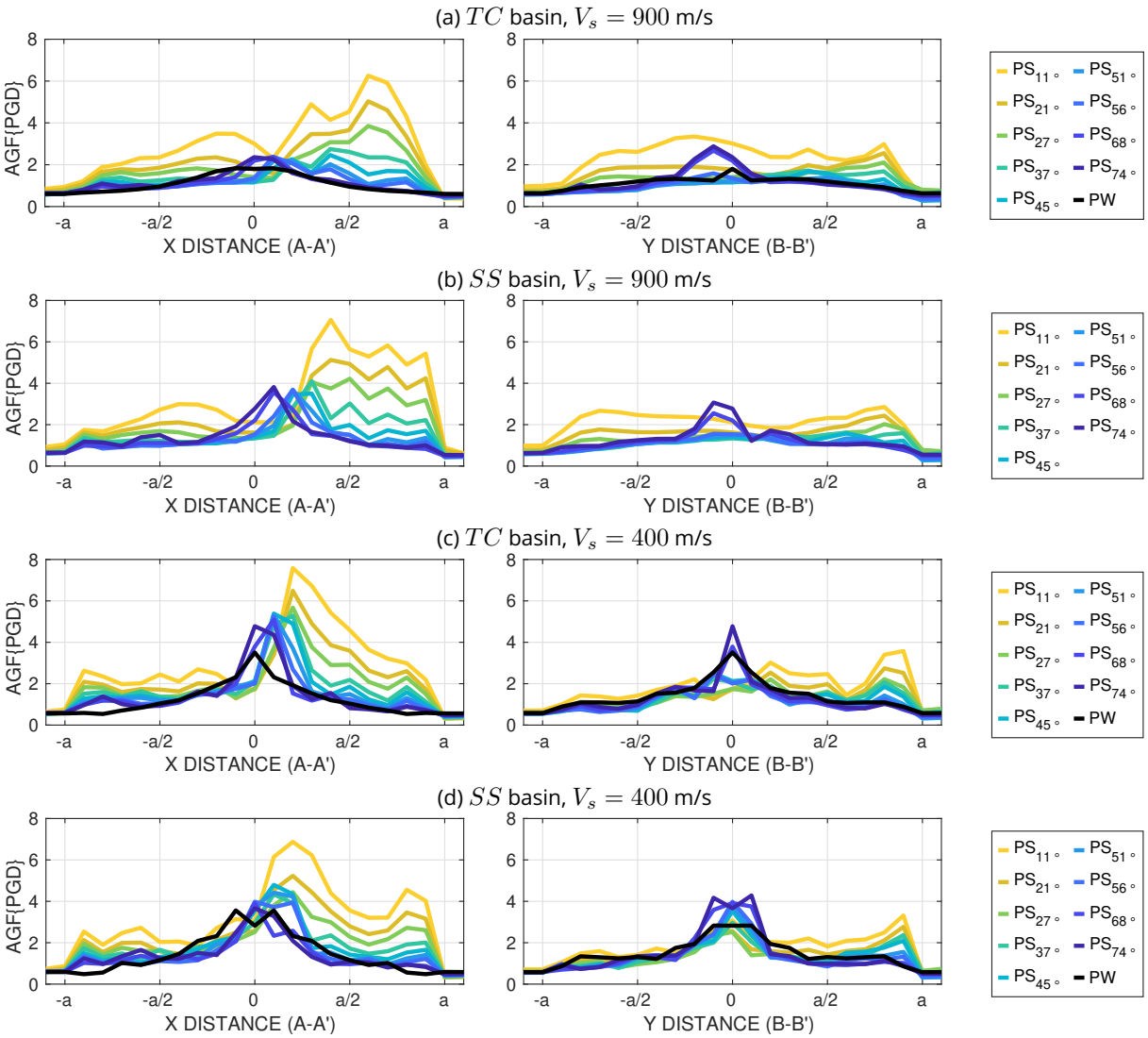

Figure 2.24: Spatial variability of the $AGF\ \{PGD_H\}$, over the $A - A'$ (left) and $B - B'$ planes.

2.6.5.2 Effects on the $AGF\ \{RotD50\}$

First, Figures 2.25 and 2.26 show the normalized horizontal $RotD50$ and vertical PSD and PSA, respectively, for all sources in the TC basin with $V_s = 900$ m/s. Figure 2.27 shows the same results but for the HOM model, where the sediment layer was extended horizontally. The responses show some amplification in the horizontal and vertical components, more significantly present in the range of frequencies of [1.0 - 3.0] Hz, which could be related to surface wave generation.

Figure 2.28 shows the aggravation factor $AGF\ \{RotD50\}$, calculated in two positions: at the centre O of the basin (Figure 2.28a) and in [0.6a, 0], where a high concentration of surface waves is obtained for the $V_s = 900$ m/s model. In general, it is observed that most of the variability is found starting at 0.6 Hz, which is the resonant frequency f_0 of the sedimentary layers. This frequency has been reported to be the minimum cutoff frequency by Narayan (2012)

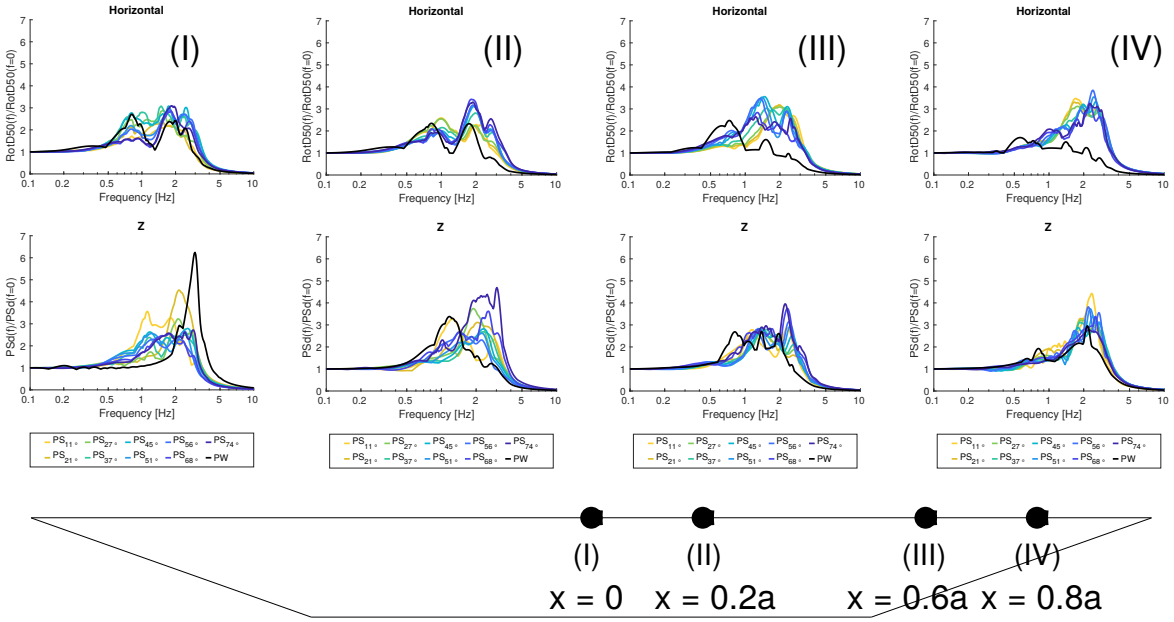

Figure 2.25: Normalized $RotD50$ for pseudo-spectral displacement, PSD, from horizontal components (top), and PSD from vertical component (bottom) for monitors located at the surface in the plane $A - A'$ ($y = 0$) and spatial variability in the east component: (I) $x = 0$ (II) $x = 0.2a$ (III) $x = 0.6a$ and (IV) $x = 0.8a$ with a the radius of the basin at the surface.

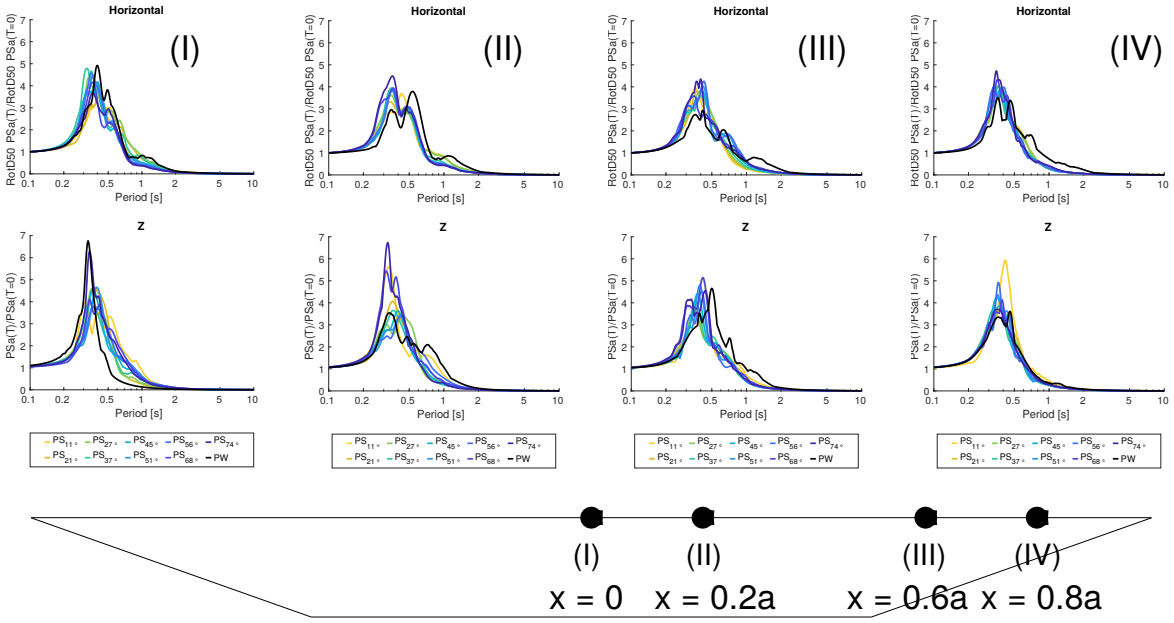

Figure 2.26: Normalized $RotD50$ for pseudo-spectral acceleration PSA, from horizontal components (top), and PSA from vertical component (bottom) for monitors located at the surface in the plane $A - A'$ ($y = 0$) and spatial variability in the east component: (I) $x = 0$ (II) $x = 0.2a$ (III) $x = 0.6a$ and (IV) $x = 0.8a$ with a the radius of the basin at the surface.

and is also the minimum frequency of surface wave creation observed in Section 2.6.4. In the central position, the $AGF\{RotD50\}$ varies between 1.0 and 3.0 approximately.

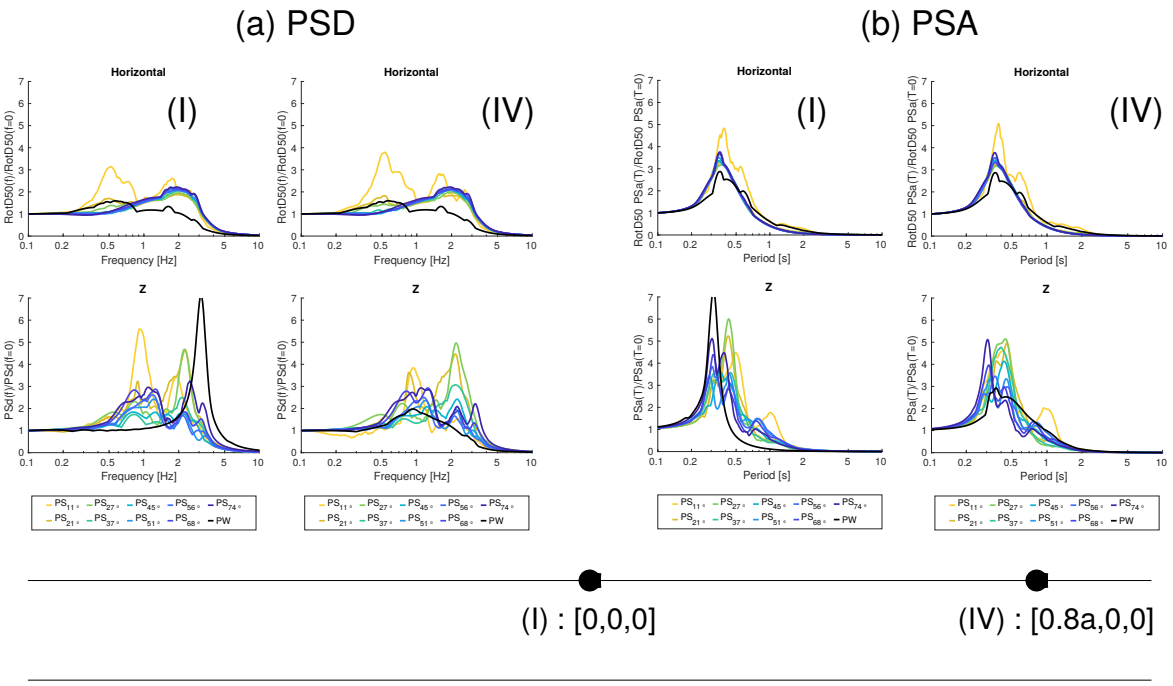

Figure 2.27: Normalized $RotD50$ from horizontal components (top) and vertical component (bottom) for monitors located at the surface in the plane $A - A'$ ($y = 0$) and spatial variability in the east component: (I) $x = 0$ and (IV) $x = 0.8a$ with a the radius of the basin at the surface.

In general, some frequencies are most modified, similarly for all sources, more distinctly observed in the PW case. However, considerable fluctuations are seen between the $AGF\{RotD50\}$ in the centre (Figure 2.28 on the left) with the $AGF\{RotD50\}$ where most energy is concentrated (Figure 2.28 on the right) for equal configurations. Therefore, the spatial variability, or in other words, the monitor's position inside the basin, has a more substantial influence on the $AGF\{RotD50\}$ than any frequency peak. In the most concentrated area (Figure 2.28 on the right), the more surficial sources will increase the $AGF\{RotD50\}$ up to values of 10, so the more influential parameters will be the source depth. Moreover, the effect of basin geometry is negligible in $AGF\{RotD50\}$. The impact of the shear wave velocity is observable of the $AGF\{RotD50\}$ only as a shift of the first peaks to lower frequencies in the softer material.

It can be seen that, compared to the plane wave, the point sources $PS_{68°}$ and $PS_{74°}$, in blue colours, are the only ones that are deep enough so that the aggravation factor approximates the plane wave in high frequencies. However, in any PS case, the low-frequency amplification observed by the PW case cannot be detected. This frequency is associated with the f_{cen} of Love waves extracted in section 2.6.4.

2.7 Concluding remarks

This Chapter presents a study on basin-generated surface waves through a parametric study of source and basin parameters. The basins have simple 3D configurations with homogeneous ma-

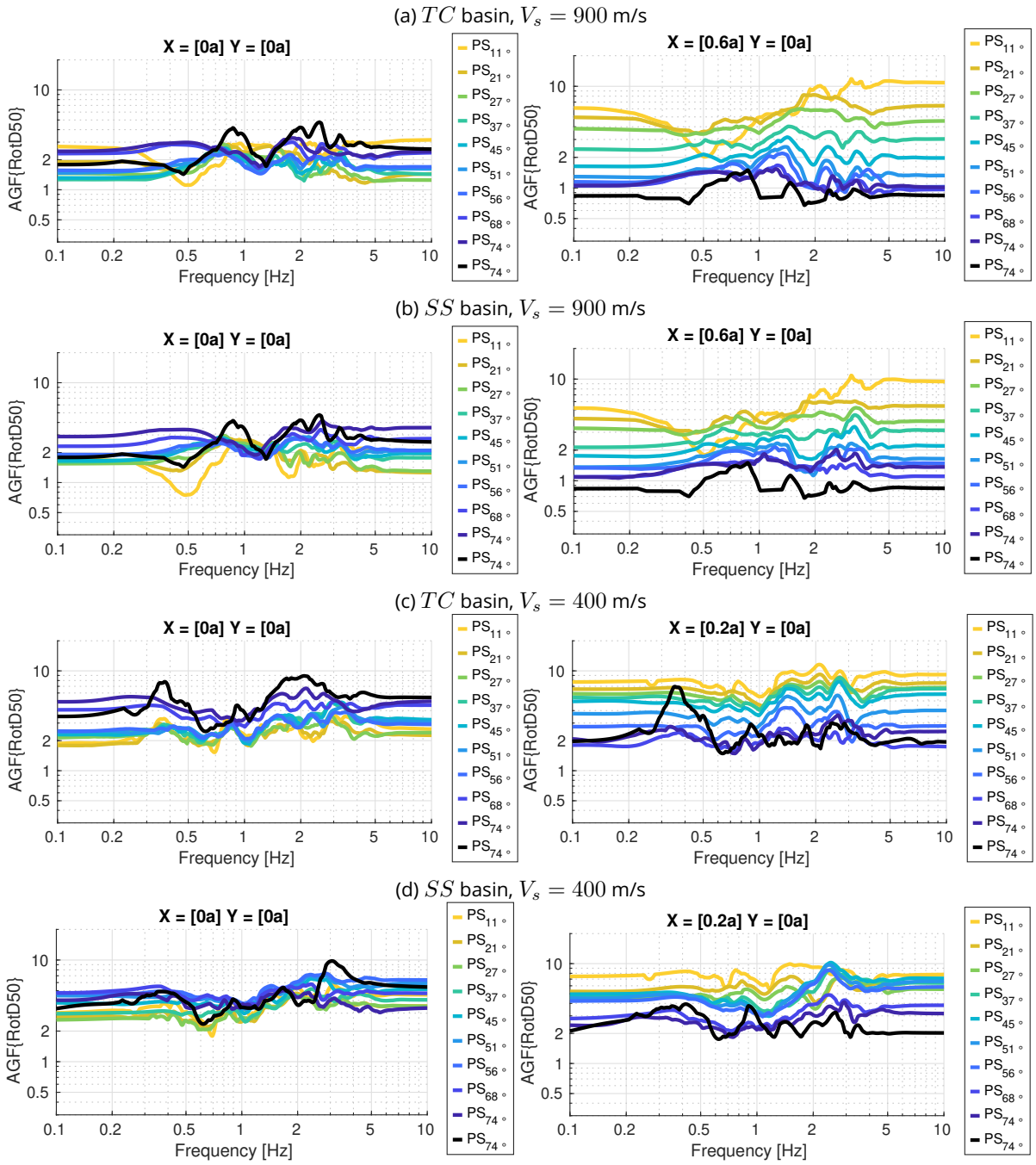

Figure 2.28: Aggravation factor $AGF\left\{RotD50\right\}$, from horizontal components. Two positions are selected: the basin central point O (0,0) m (left) and where most of the energy is concentrated, at (0.6a, 0) for a $V_s = 900$ m/s and (0.2a, 0) for a $V_s = 400$ m/s.

terials subjected to double couple (DC) point sources and a vertically incident plane S-wave. A total of 40 configurations were examined. The NIP procedure was applied to extract the time signals of surface waves, Love, prograde or retrograde Rayleigh waves, in different positions inside the basin and evaluate their characteristics (amplitude, angle of polarization and central frequency).

The results indicate that there are two class of surface waves generated, where the basin edge plays a major role:

- The first type of surface waves have high amplitudes and are generated in the first entrance and reflection inside the basin. The interface between sediments and bedrock acts as a reflection border where energy is concentrated. In shallow sources scenarios, the energy arrives directly and reflects in the opposite border, creating a high concentration of surface waves with complex propagation paths. For that reason, higher amplitudes up to values of 8 can be found in surficial sources with incidence angle from 11° to 27°, and in the TC basin. Since the border in the TC basin is sharper than in a semi-spherical (SS) basin, higher amplitudes of surface waves are found in the first geometry case.

- The second type of surface waves have smaller amplitudes and are concentrated toward the edge of the basin, generated later than the first type. In this case, the boundary shape influence the polarization angle, following the same angle.

In deeper sources, from incidence angles higher than 68°, or in the vertically incident plane wave, most of the characteristics of the surface waves are defined not by the basin but by the input motion. The polarization angle of surface waves is barely deflected by the edge, the central frequency is constant in all the basin positions and higher amplitudes are particularly concentrated in the central part of the basin. The fundamental frequency of the soil, f_0, represents a lower limit for the central frequency of the extracted surface waves.

The $AGF\left\{RotD50\right\}$ shows large spatial variations. This may be explained by the fact that the response from the layered model is very different from the basin response in cases of 3D geometry and complex (non-planar) sources. In these cases, the use of the AGF as means of applying the basin effects to the 2D might lose their validity. In terms of amplitudes, the spatial variability of surface wave creation follows the same trends as aggravation factors. This aspect can be particularly important in developing ways of integrating surface waves in seismic design through the aggravation factor. This study focused on horizontal components of surface waves. Further research could direct the efforts in estimating other parameters of the surface waves, such as the ellipticity of the Rayleigh waves, to consider vertical components of motion; and rotational components to account for rocking for the Rayleigh waves or torsion for the Love waves.

Finally, idealized geometries as the presented in this Chapter have been used to estimate basin amplification for realistic cases in the literature, such as in the works of Kawase and Aki (1989); Ayoubi et al. (2021), giving some insight into the key parameters governing amplification patterns. In this work, they have also given information about the relation between basin parameters and surface wave generation. More complex modelling is undoubtfully necessary if other features affecting the surface wave propagation phenomena want to the investigated, such as source effects (i.e., directivity, near-field, azimuthal dependency) or material layering.

Chapter 3

Amplification effects and surface wave generation in realistic basin models

Contents

3.1 Introduction

This Chapter is a continuation of Chapter 2, this time focusing on surface wave identification and characterization analysis in realistic basin models. The objective is to discern if the surface wave behavior changes when the basin structure is complexified or if canonical basins could be used to estimate the ground motion characteristics associated with basin-induced surface waves.

The amplification effects of strong ground motions in sedimentary basins has been extensively recognized from either recordings (Cadet et al., 2012; Ghofrani and Atkinson, 2015; Marafi et al., 2017; Pilz et al., 2018; Tsuno et al., 2022, among others) or numerical simulations (Olsen, 2000; Day et al., 2006, 2008; Salichon et al., 2010; Yoshimoto and Takemura, 2014; Moczo et al., 2018; Wirth et al., 2019; Viens and Denolle, 2019; Bustos et al., 2023, among others). The use of realistic basins allows consideration of other source settings that can influence amplification and can not be evaluated in idealized-shaped basin parametric analyses, such as the source effects (e.g., hypocenter location, directivity) or highly heterogeneous media effects (Day et al., 2006, 2008; Moczo et al., 2018; Wirth et al., 2019, among others).

Many of these studies have observed that the recorded intense long-period ground motions could be associated with surface wave generation at the basin edges. For instance, from a dense seismic array, Frankel et al. (2001) found that for strong recorded regional events (M 5.0 to 7.1), low-frequency (0.125-0.5 Hz) surface waves were created in the basin edge in the Santa Clara Valley, California. These surface waves arrived later, and their propagation direction was different from the earthquake's epicenter. Local events of smaller amplitude (M 2.5 to 2.8) generated high-frequency surface waves concentrated in a smaller basin area. Manea et al. (2017) studied the sedimentary deposit of Bucharest and the seismic wavefield characteristics were examined using the MUSIQUE method. Their results led to the conclusion of the impact of the 3D effects from the edges of the basin around the fundamental period of the sediments.

While the surface wave influence on the amplification is clearly recognizable from these studies, only a few of them have analyzed precisely the surface wave propagation in a quantifiable manner (e.g., Cornou et al., 2003b; Pilz et al., 2018; Heresi et al., 2020; Meza-Fajardo et al., 2021; Daza et al., 2023), which could be essential for their assessment in the seismic hazard. Some have used the normalized inner product (NIP) identification procedure (Heresi et al., 2020; Meza-Fajardo et al., 2021; Daza et al., 2023), focused on real recordings. From this context, numerical simulation is an excellent alternative since it can fully integrate source-to-site response, including large-scale earthquake scenarios with extended sources and complex basin geometries. Therefore, they can give an insight into how different parameters affect surface wave generation.

Therefore, in this Chapter, surface waves obtained from numerical simulations at a regional scale, including three-dimensional realistic basin sediments, are characterized using the normalized inner product (NIP). Consequently, this Chapter addresses the challenge of quantifying the spatial variability of the surface wave characteristics. The study expects to discern (i) if basin-generated surface waves can cause part of the observed basin amplification and (ii) if the surface wave behavior changes when the basin structure is complexified or if the findings for canonical

basins still hold. The study investigates the source effects on the basin amplification of surface waves with the comparison of (i) plane S-waves of vertical incidence, under the assumption that they generate surface waves from pure conversion from S waves in the basin edges; (ii) double couple point sources, and their corresponding location effects. Later, the near-field effects will also be investigated.

Two areas comprising basins were selected: the site of Argostoli, located in Greece, and the site of Cadarache, located in France. Both basins are well characterized and have been the focus of studies about site amplification: Argostoli (Touhami, 2020; Imtiaz et al., 2020; Cushing et al., 2020; Sbaa et al., 2017, among others) and Cadarache (Guyonet-Benaize, 2011; Castro-Cruz et al., 2021, 2022, among others). The Koutavos basin, located in Argostoli, Cephalonia Island, consists of two sub-basins, and a natural frequency of vibration of $f_0 = 1.5 - 1.7$ Hz has been previously estimated (Sbaa et al., 2017; Perron et al., 2018a; Hollender et al., 2018). The site of Cadarache, France, is a small basin with approximate dimensions of a few hundred meters wide and 50-150 m deep (Hollender et al., 2018). Ambient vibration studies have found resonant frequencies of the sediments close to $f_0 = 4.4$ Hz (Perron et al., 2018a; Hollender et al., 2011, 2018). The numerical simulations have been performed in the wave propagation software SEM3D, already presented by the research of Touhami (2020); Riaño and Lopez-Caballero (2021) for Argostoli, and in Castro-Cruz et al. (2021, 2022) for the Cadarache basin. Some of the data was directly retrieved from these studies. Both have been validated against real signals within the framework of the SINAPS@ project (Berge-Thierry et al., 2019).

The Chapter is divided into the results for the Argostoli basin, in Section 3.2 and for the Cadarache basin in Section 3.3.

3.2 Argostoli basin

The present analysis focuses on the Region of Argostoli basin, located on Cephalonia island, Greece. Multiple simulation data in the spectral element code SEM3D (CEA and CentraleSupélec and IPGP and CNRS, 2017) were taken from previously published studies and here are reinterpreted to investigate the spatial variability of the surface wave generation in the Argostoli basin. The simulation results were retrieved mainly from Touhami (2020); Touhami et al. (2022) and Riaño and Lopez-Caballero (2021). Specifically, the simulation of the vertically incident plane wave and point DC source from subsection 3.2.2 and subsection 3.2.3 were obtained from Riaño and Lopez-Caballero (2021). The simulations of the four different point sources from subsection 3.2.4 were performed for this work but were inspired by the results of similar sources discussed by Touhami (2020). A detailed description of the model will be presented in the following subsections.

More than to evaluate amplification effects via the amplification factor, which have already been computed, the aim of this and the following part is twofold: (i) to evaluate the characteristic of basin-induced surface waves under different seismic settings to understand how they are created and (ii) to check if the modification of the ground motion and amplification observed by

the previous studies can be explained or partially explained by the surface waves generation.

3.2.1 Regional model of Argostoli

The assumptions and properties of the Argostoli simulation at regional scale are presented hereafter. The local properties for the sediment layers that constitute the basin as well as the surficial bedrock were previously described in subsection 1.6.2 from the chapter 1. At regional scale (order of kilometers of depth), the material properties are extrapolated with the crustal model proposed by Haslinger et al. (1999) and is depicted in Table 3.1. The total dimension size of the domain (x, y, z) is of 24.6 km $\times$ 24.6 km $\times$ 61.2 km. The domain consist in a total of approximately 15 million hexahedral elements, a minimum element size of 25$\times$ m 25$\times$ m 25 m for a maximum frequency of 7 Hz. Additionally, the properties were included into the model with a non-honouring procedure (see Annex A.2). The material variation at the surface is observed in Figure 3.1a. Figure 3.1b displays the V_s across the profile $A - A'$, showing the basin edges and the increasing values with depth.

Table 3.1: Properties of the material for the crustal model proposed by Haslinger et al. (1999) for the Ionian region. V_p the P-wave velocity, V_s the S-wave velocity, ρ density, Q_p and Q_s, respectively the quality factor for P- and S-waves attenuation. Retrieved from Touhami (2020).

Depth [km]	V_p [km/s]	V_s [km/s]	ρ [kg/m^3]	Q_p	Q_s
0	3.50	1.90	2.4	300	150
0.5	5.47	2.70	2.8	300	150
2.0	5.50	2.86	2.8	300	150
5.0	6.00	3.23	2.9	300	150
10.0	6.20	3.23	2.9	300	150
15.0	6.48	3.40	3.0	300	150
20.0	6.70	3.80	3.0	300	150
30.0	6.75	3.81	3.1	300	150
40.0	8.00	4.66	3.3	1000	500

Table 3.2: Location and kinematic parameters of the DC point sources used in the Argostoli numerical model.

	Hypocenter [E,N]	Depth (km)	Strike (°)	Dip (°)	Slip (°)	M_w
Source 1 (S1)	[456190 4222570]	14	17	67	163	4.7
Source 2 (S2)	[450400 4229320]	14	17	67	163	4.7
Source 3 (S3)	[462625 4229320]	14	17	67	163	4.7
Source 4 (S4)	[450400 4229320]	5	17	67	163	4.7

In order to evaluate the impact of the source type in the basin's response, two input motions were used: a vertically incident plane S-wave with polarization over the NS direction and point sources. The two types of sources scenarios will cause a distinct wavefield, and consequently impact into the surface wave generation. As already discussed, the first will have only basin-edge

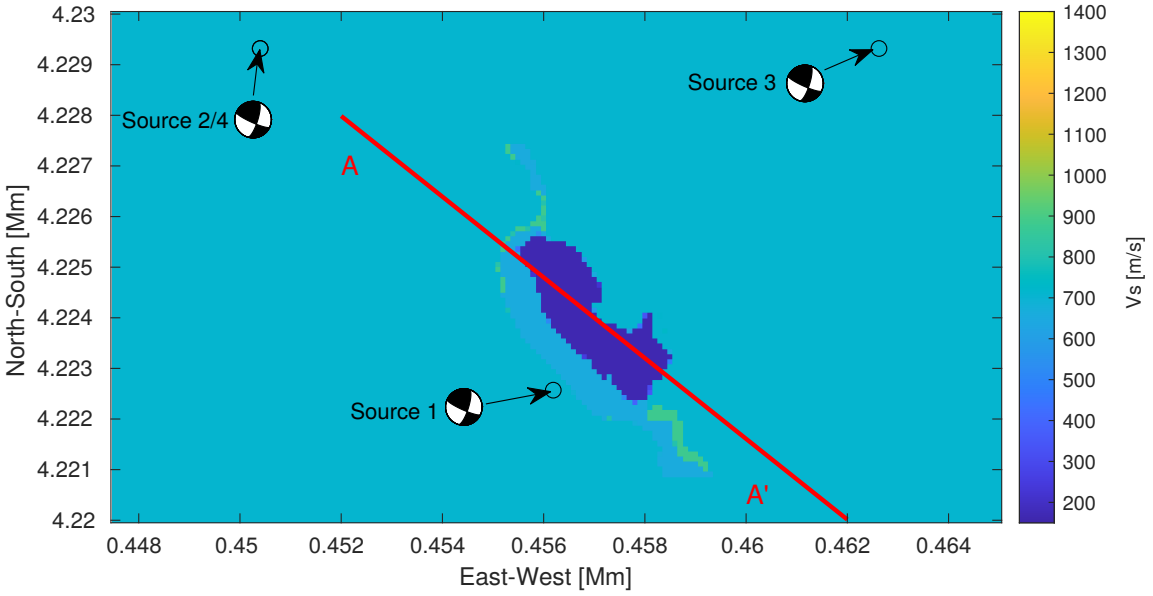

(a) $X - Y$ plane.

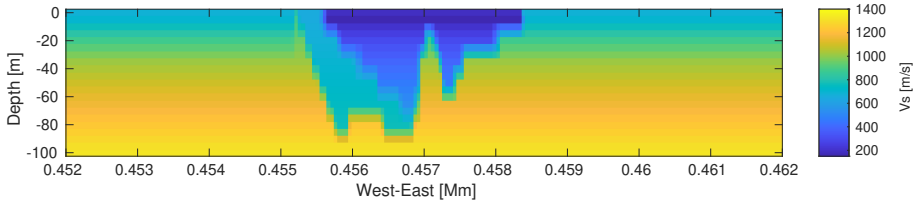

(b) $A - A'$

Figure 3.1: Spatial variability of the V_s (a) at the surface and (b) in the $A - A'$ cross section passing through the basin.

effects, while the latter basin-edge plus souce position effects. The location and fault mechanism of 4 point sources is described in Table 3.2.

3.2.2 Basin generated surface waves under plane wave loading

As for the plane wave, the source is discretized in a grid of sub-sources spaced at every GLL of the mesh, with a total dimension of 14.18 km $\times$ 14.18 km in the horizontal directions. So as to assure a correct plane wave approximation (see subsection A.1.2), this source is located at 20 km deep. The total simulation time is of 30 seconds. The Figure 3.2 displays the normalized velocity time-history and the Fourier spectrum of the force time histories inyected at each point subsource that constitute the plane wave source.

A first insight of the amplification due to the presence of the basin and the principal direction of the ground motions is displayed by the horizontal particle motion at the basin's surface in Figure 3.3 for different time windows. The two main sedimentary materials are delimited (check Figure 3.1). The basin effect can clearly be noticed inside the soft soil sediments delimited by the red line, where waves are amplified and trapped. Once the wave arrives to the basin ($t = [6 - 7]$

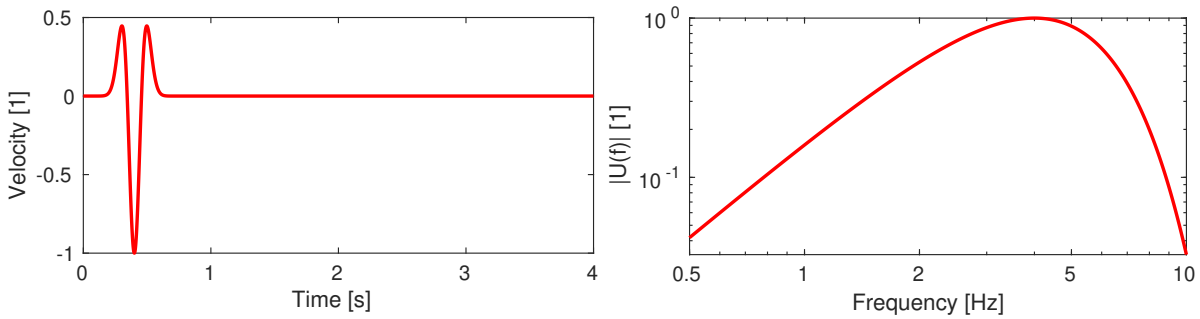

(a) Velocity time-histories

(b) Fourier spectrum

Figure 3.2: Normalized (a) time evolution and (b) Fourier spectrum of the source time function (velocity) inyected at each point subsource for the plane wave (PW) approximation.

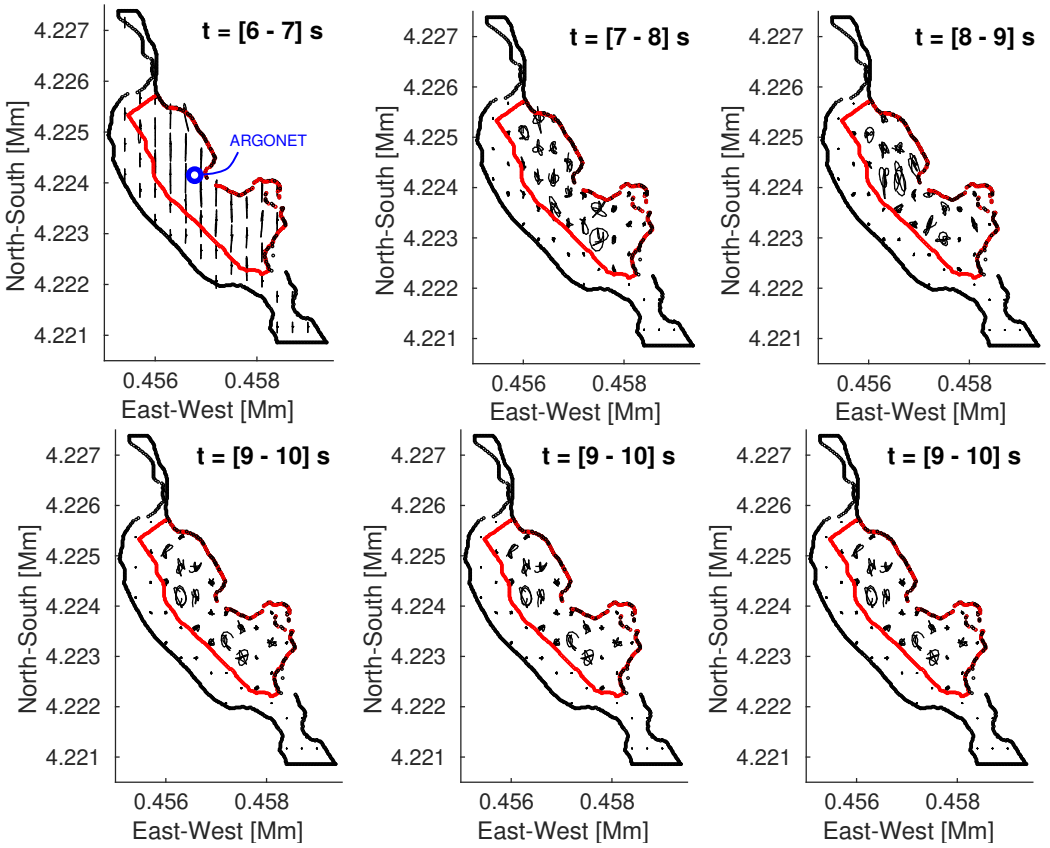

Figure 3.3: Horizontal particle displacements for different time windows, induced by the plane S-wave with vertical incidence polarized in the North-South direction. The location of the ARGONET station is depicted in blue at the first picture.

s), the motion is polarized in the same direction of the plane wave and somewhat amplified inside the soft sediments. Then, due to the reflections and surface waves generation, the ground movement shows a variety of dominant directions.

Again from Figure 3.3 multiple interferences of the plane wave with the basin are observed. In order to evaluate the time evolution of the surface waves, their main characteristics are extracted

from the displacement-time histories at the ARGONET station with the Normalized Inner Product (NIP) methodology. The signals are separated into 2.15-second time windows (approximately 3 wavelengths the frequency of the basin). In Figure 3.4, the original time signals in the x, y and z components are compared to the isolated surface waves. It is noted that some of the horizontal components are surface waves, while most of the vertical component is identified as Rayleigh waves, as expected for this kind of incident wave.

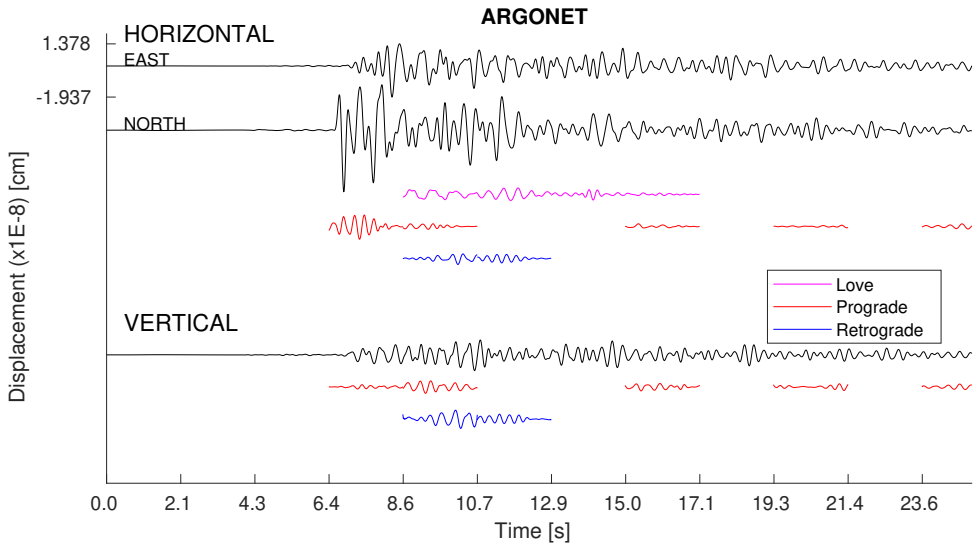

Figure 3.4: Comparison between the original signals, in black, against the isolated surface waves (NIP) for the signal in the Argonet station in the Plane wave simulation. The signal was analyzed in 2.1 s- time windows. The wave characteristics are better displayed in the next figure.

The time evolution of the waves' characteristics is displayed in Figure 3.5, from where preferential directions of the polarization azimuth angle are clearly observed for the three types of waves (Figure 3.5a). The central frequency f_{cen} of the Love waves remains close to the first fundamental frequency of vibration at the ARGONET site ($f = 1.8$ Hz), and it is higher for the Rayleigh waves (Figure 3.5c). These results are similar to the real recorded signals already analized in the Chapter 1. A conclusion can be drawn from Figure 3.5, the central frequency of the surface waves is stable with time, due to the fact that it depends in general to the material properties and geometry of the subsurface (Kawase and Aki, 1989).

The wavefield at different locations is expected to be different because of the basin site effects, which will alter the amplitude and frequency content of the ground motion, including the surface wave generation in the basin edges (Kawase, 2003; Riga et al., 2018, among others). In order to evaluate the spatial variability of the surface waves parameters, all the monitors inside the basin were analyzed with the NIP procedure. The spatial distribution of both maximum horizontal displacement amplitude (A_{POL}) and central frequency (f_{cen}) is presented in Figure 3.6. According to this Figure, it can be observed that the plane wave input induce surface waves mostly in the soft-sediments area (delimited in red), where higher amplitudes are associated to Love waves and in less extent to Prograde Rayleigh waves. The amplification is concentrated in the northern part of the basin, which is the deepest zone. Meza-Fajardo et al. (2019) studied the

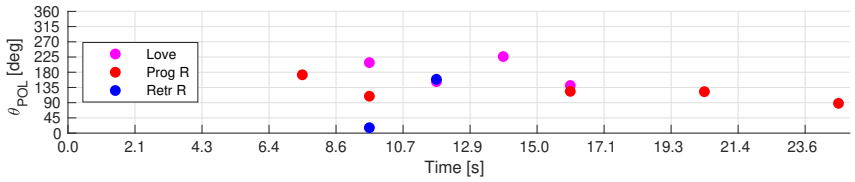

(a) Polarization azimuth angle

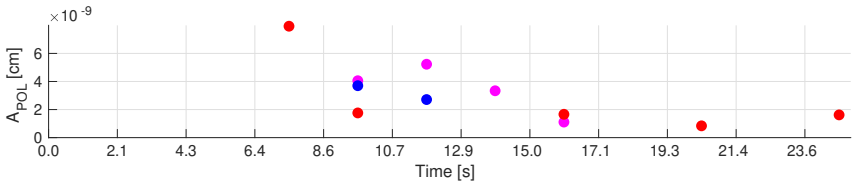

(b) Maximum displacement amplitude

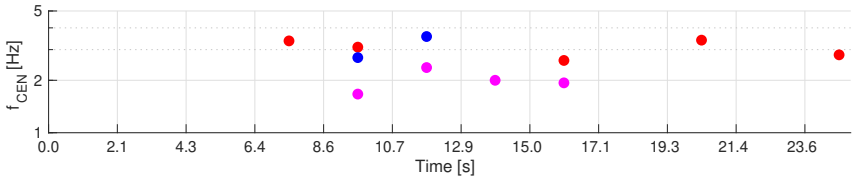

(c) Central frequency

Figure 3.5: Time evolution of the surface waves parameters from the isolated waves from Figure 3.4 at the ARGONET station, for the plane wave simulation in the Argostoli basin.

surface wave generation in a numerical simulation of a highly layered basin in Rome, Italy, using a vertically incident plane wave as input. The results presented here follow the same conclusions as the one obtained by the cited work, where amplification due to surface waves where mostly concentrated in the soft sediment parts. As for the central frequency, no specific trend of the spatial variability is observed for any type of surface waves, with f_{cen} around 2 to 5 Hz, partially atributed to the input frequency (Figure 3.2).

3.2.3 Basin response under point source loading

In this part, the effect of the source type and position is assessed by comparing the previous model with a more realistic source as input motion. In this case, surface wave parameters are expected to vary due to a combination of source and basin geometry effects. The surface wave generation is studied by a low magnitude earthquake scenario (Mw 4.7), modeled as a double couple (DC) point source located at 14 km depth, with strike $\phi_s = 17°$, dip $\delta = 67°$ and slip $\lambda = 163°$ angles. The focal mechanism is depicted in Figure 3.1. The source time function used is expressed by

$$f(t) = 1 - \left(1 + \frac{t - t_s}{\tau}\right) \exp\left(-\frac{t - t_s}{\tau}\right) \tag{3.1}$$

based in Brune (1970), where t_s is the time-shift and $\tau = 0.113$ s is the rise time. The location of four point sources is described in Table 3.2. For the sake of simplicity, in this section only results from the source S3 are described. The source S3 is located at the coordinates $[462625, 4229320]$, north-east from the basin (Source 3 in Figure 3.1). Close to the source, the velocity time histories

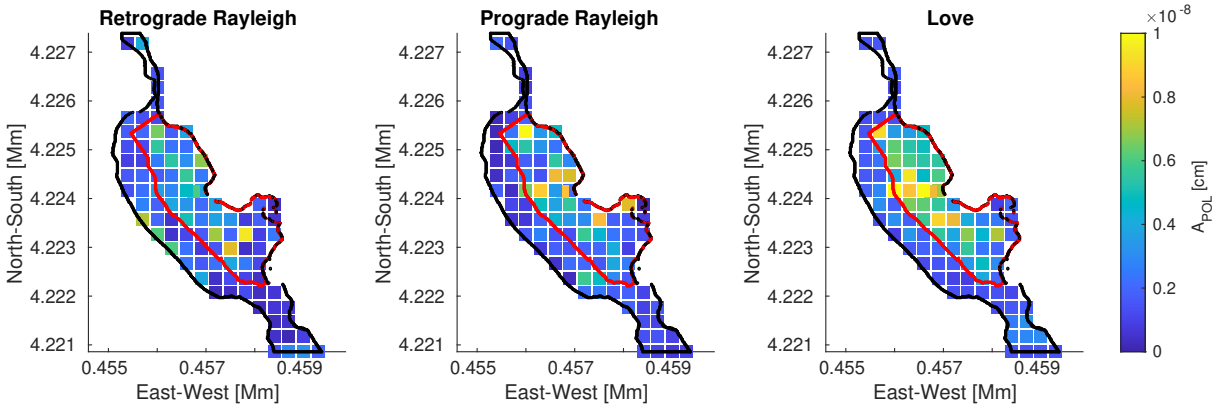

(a) Maximum amplitude of the polarized wave A_{POL}

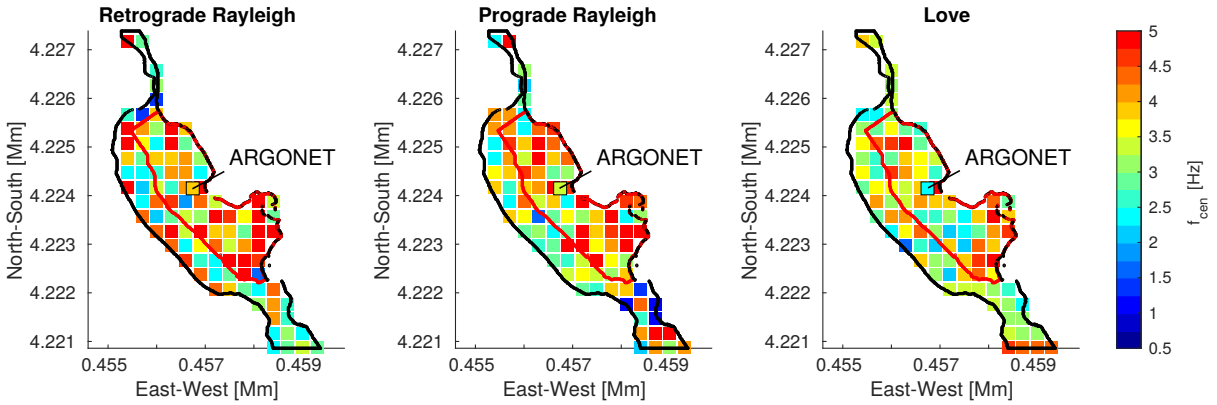

(b) Central frequency of the polarized wave f_{cen}

Figure 3.6: Spatial variability of the surface wave parameters in the Argostoli basin for vertically incident plane S-wave input polarized in the North-South direction.

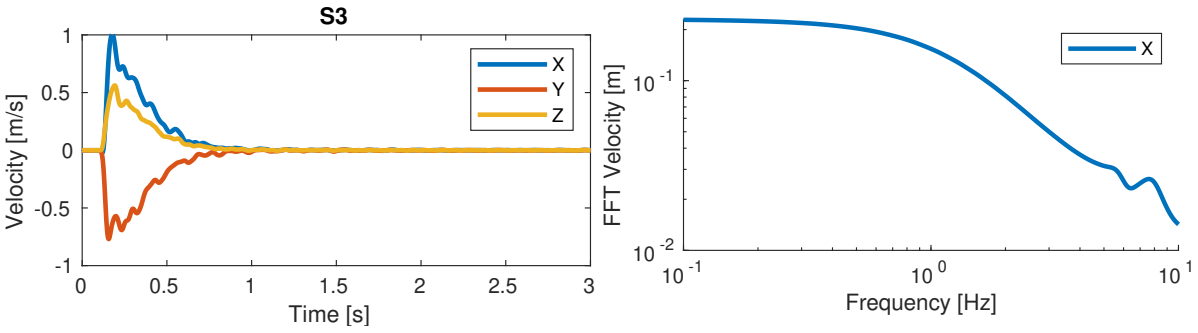

(a) Velocity time-histories

(b) Fourier spectrum

Figure 3.7: Normalized (a) time evolution and (b) Fourier spectrum of the source time function (velocity) inyected at the point source (PS) approximation.

obtained is the one presented in Figure 3.7 in time- and frequency-domain.

As in the previous case, the extracted surface waves at the basin surface are displayed in Figure 3.8. Despite the concentration of the surface waves in the softer sediments likewise the

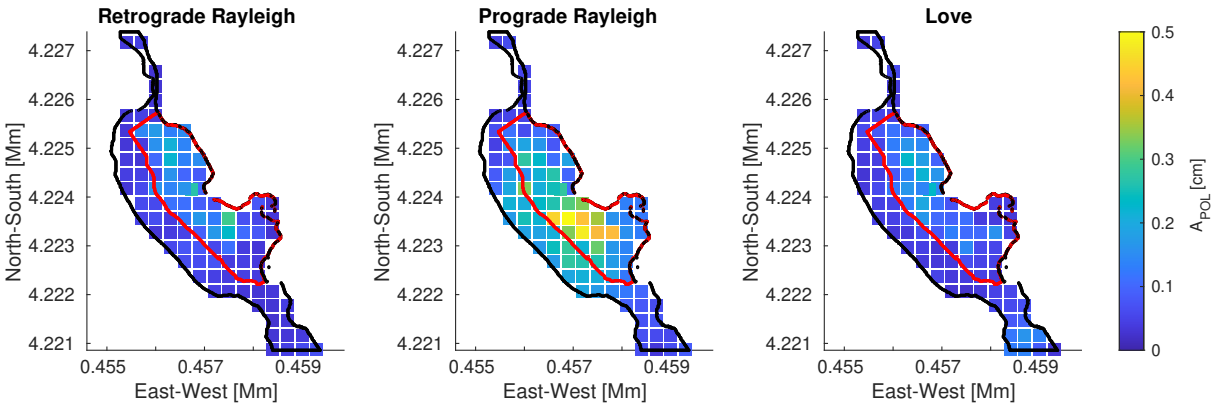

(a) Maximum amplitude of the polarized wave A_{POL}

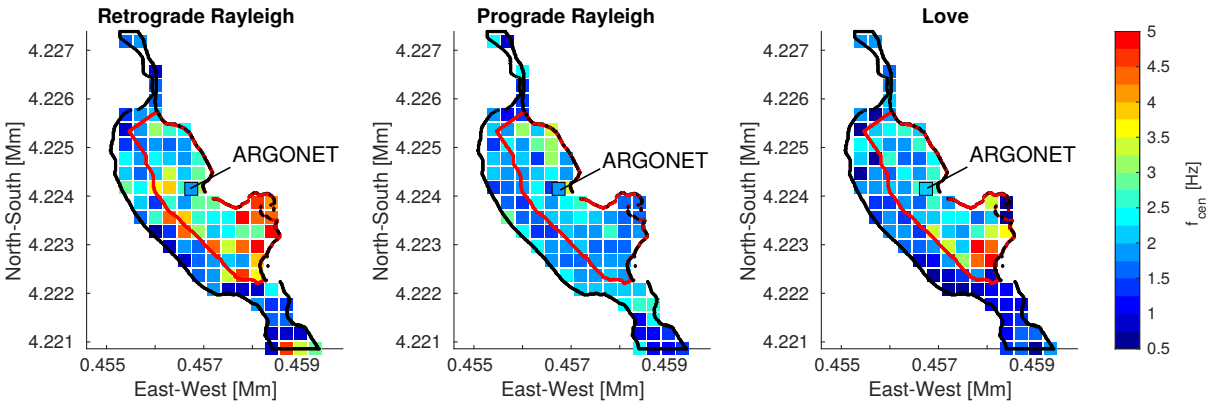

(b) Central frequency of the polarized wave f_{cen}

Figure 3.8: Spatial variability of the surface wave parameters in the Argostoli basin for the DC point source S3.

plane wave scenario, the response is different since it is governed by the generation of Prograde Rayleigh waves in the softer sediments instead of Love waves. The latter are also generated, but in a minor degree. Since surface waves are generated in the basin edges, the higher proportion of Rayleigh waves could be explained by the preferential direction of entrance (coming from the north-east, and impacting directly to the soft sediments area) in the PS case compared to the PW case.

In addition, some tendencies can be explicited concerning the central frequency (Figure 3.8b):

- the response is dominanted by a frequency of 1 to 2 Hz, related to the input frequency,
- in the softer sediments (delimited by red in the Figure) a slightly higher frequency around 2 - 3 Hz appears,
- the basin edge clearly interacts with the surface waves as f_{cen} increases up to 5 Hz, more predominantly at the south-western edges for Retrograde Rayleigh and Love waves.

These conclusions clearly show some discrepancies with the plane wave case scenario in terms of frequency. Furthermore, the results can be compared to the amplification response in

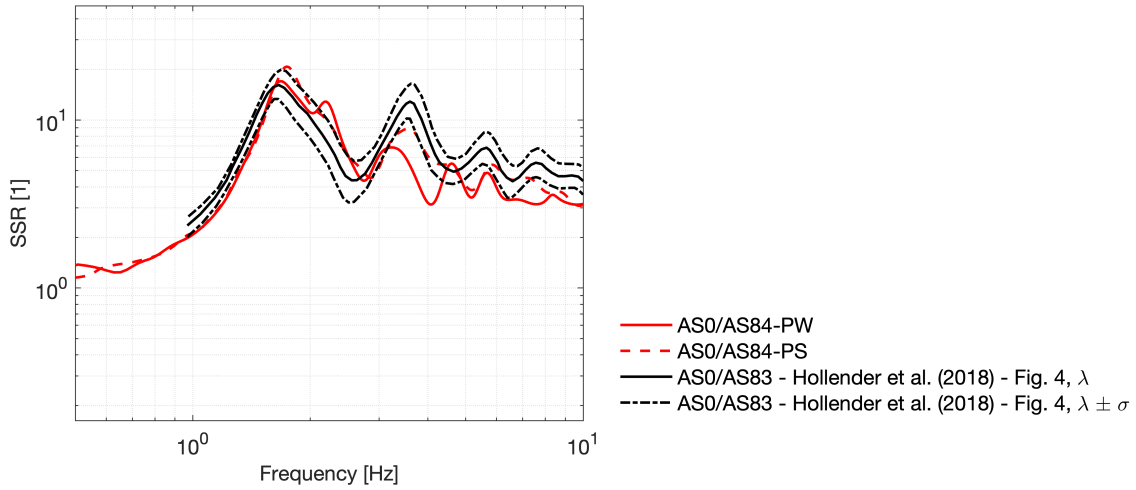

Figure 3.9: Surface/borehole SSR ratio comparing the results of the plane wave, point source inputs and experimental data. Reprinted from Riaño and Lopez-Caballero (2021).

the frequency domain computed with the standard spectral ratio (SSR). The SSR was computed by Riaño and Lopez-Caballero (2021) between the surface monitor (AS0) and the borehole station at bedrock level (AS84) and compared to experimental data in Figure 3.9, for the two analyzed sources: plane wave (PW) and DC point source (PS). The experimental SSR curves were retrieved from Hollender et al. (2018), and are compute based in a dataset of 436 events with magnitudes M_L 1.6 to M_w 6.4. The first peak in the SSR is associated to the resonance response of the basin, well reported in both types of input sources. Additionally, the response in higher peaks can be related to basin effects (e.g. Bonilla et al., 2002; Cornou and Bard, 2003).

The response of the second peak (around 3 to 4 Hz) is better accomplished by the PS and is certainly associated to the basin induced surface waves of Prograde Rayleigh type. Furthermore, the PW scenario is not fully able to replicate the full SSR. The PW scenario generates higher frequency surface waves, which are also illustrated in the Figure 3.9 as small peaks. Given the above, it is possible to conclude that surface waves impact in the higher frequency amplification response (Bowden and Tsai, 2017; O'Kane and Copley, 2021), and that while basin effects are related to surface wave generation, they depend not only of the basin geometry but also of the source characteristics (e.g. frequency, location). This latter point is further evaluated in the following subsection.

3.2.4 Impact of the source position

Since the basin is assymetrical, the source azimuth will influence the entrance of the wave and with that the basin induced surface waves (Wirth et al., 2019). Thus, the influence of the point source location in the surface wave generation is analyzed with 4 point sources, located in the positions displayed in Figure 3.1 and described in Table 3.2. The results presented in this subsection are inspired by the results of Touhami (2020), where a parametrical study on the position of

a DC point source on the Argostoli basin was conducted. All of them have the same kinematic parameters as the point source in the Subsection 3.2.3. The sources S1, S2 and S3 are located at depth 14 km. The S4 have the same hypocenter than the S2 but represents a shallow source with a depth of 5 km.

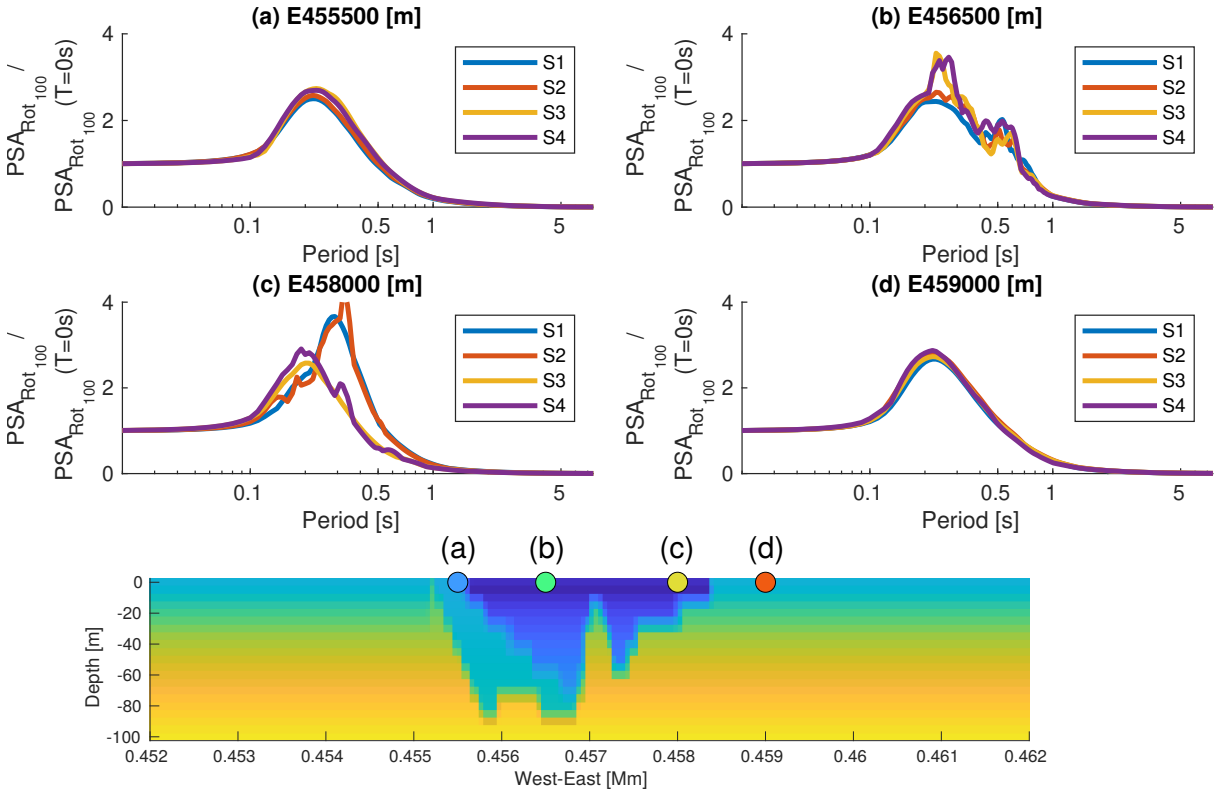

Figure 3.10: Normalized maximum spectral acceleration on the horizontal components (RotD100) at four positions along the $A - A'$ profile: (a) E4555500 m north-western part of the stiff sediments, (b) E456500 m deepest part of the basin, (c) E456500 m south-eastern part of the shallower basin and (d) E459000 m outside the basin. The lower figure displays the velocity profile and the relative positions selected.

For the sake of brevety, the crossection $A - A'$ have been defined in order to evaluate the response. The profile cuts the basin in half as seen in Figure 3.1b. Touhami (2020) evaluated the amplification effect in the pseudo spectral acceleration (PSA) for different periods, normalized by the PSA at a station located in rock. It was found that the Source 4, which is closer to the surface, contributed the most to the amplification to longer periods, while deeper sources (1 to 3) slightly amplified the response in the deepest zone of the basin (located at the northwest).

Since the observed wavefield is altered by the basin and the expected polarization is different from source to source, another way to evaluate the amplification response accounting possible directionalities of the ground motion is with the maximum acceleration response spectra over all orientations angles θ, i.e., the PSA_{Rot100} (Figure 3.10), defined as

$$PSA_{RotD100}(T) = \underset{\theta}{max}\left[PSA(\theta, T)\right] \tag{3.2}$$

The parameter PSA_{Rot100} was computed at four different positions along $A - A'$: (a) E4555000, at the northern part, on the stiff soil, (b) E4565000 and (c) E458000, located inside the soft sediments and (d) E459000, outside the basin. From Figure 3.10, differences between sources are only observed in the soft sediments (Figure 3.10b and c).

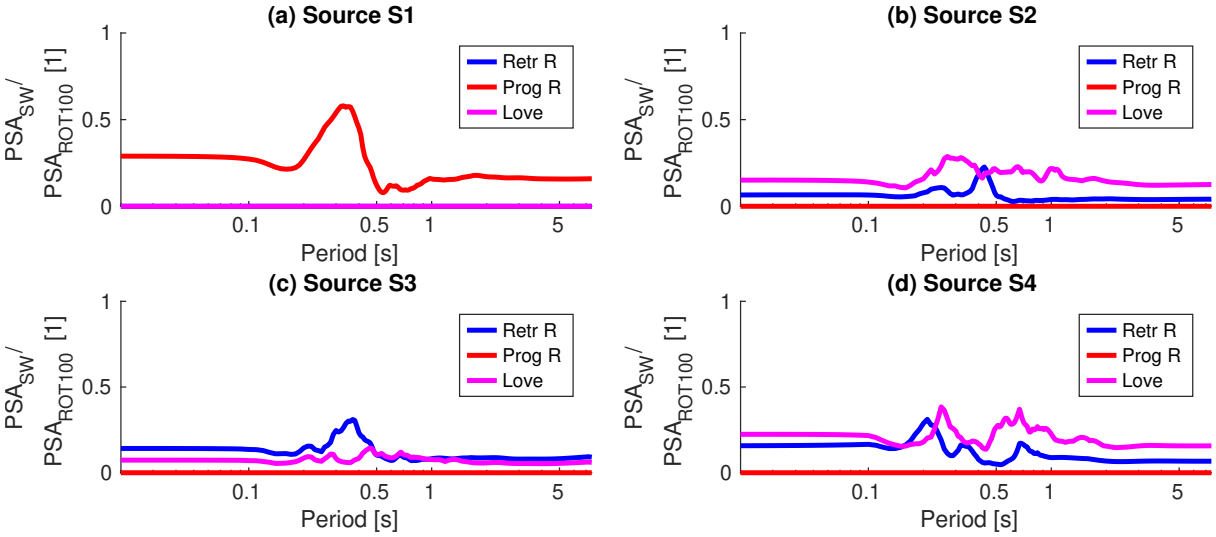

Figure 3.11: Spectral acceleration ratio between the horizontal polarized surface wave and the total signal at the deepest part of the basin (E456500 m).

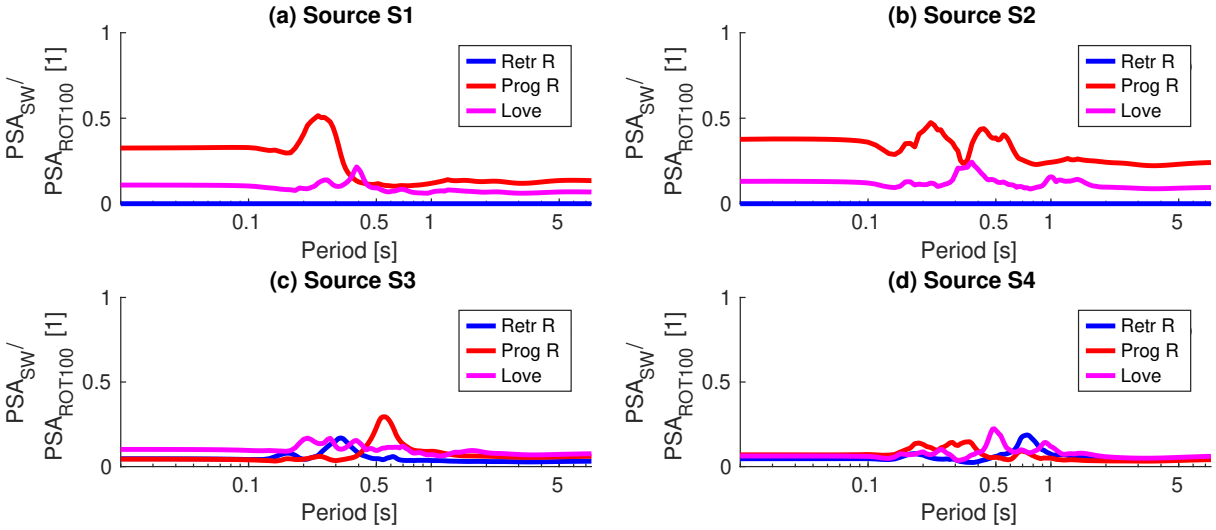

Figure 3.12: Spectral acceleration ratio between the horizontal polarized surface wave and the total signal at the south-eastern edge of the basin (E458000 m).

Furthermore, the surface waves are extracted from the signals at the same positions with the NIP. Then, from the time signal of the horizontal polarized component of the three types of waves, the pseudo spectral acceleration response is computed (PSA_{SW}). The ratio PSA_{SW}/PSA_{Rot100} shows the proportion of surface waves in the total signal (Daza et al., 2023). If a value close to 1 is obtained, then a high proportion of surface waves are present in the associated period. The quo-

tient is computed at positions E4565000 and E458000, inside the basin, and displayed in Figures 3.11 and 3.12, respectively. From them, some conclusions can be drawn. Firstly, the amplification in the deepest part, higher in the sources S2, S3 and S4, are associated to both Love and Rayleigh waves (Figure 3.11b,c and d). Secondly, the amplifications observed in the southern edge (Figure 3.10c), predominantly with the sources S1 and S2, are related principally to Prograde Rayleigh waves (Figure 3.12a and b).

Now, the effect of the source location on the spatial variability of surface waves can be further analyzed along the $A - A'$. The Figure 3.13 displays the peak amplitudes of the displacement imposed by the 4 sources for the three types of waves. From the figure, it is observed that practically no surface waves are generated outside the basin. The shallow source (S4) is the one that present higher amplitudes of induced surface waves in the Argostoli basin. For the shallow source, the effect on the depth is mainly observed closer to the incident border (at the left on the figure). However, Rayleigh waves are particularly influenced by the shallow source in the edges, amplified only in the S4 scenario. No significant differences are observed between the prograde or retrograde polarizations. Moreover, an interesting result is observed for Love waves. The shallow source generates Love waves when they enter the basin in the stiff materials. For the other sources, the amplification $A_{POL,Love}$ is independent of the source position on the softer sediments, similar to the observed on the canonical basins in Chapter 2.

Moreover, Figure 3.14 confirms the fact that the obtained surface waves are induced by the basin edges. The conclusion can be established because no specific relation is observed between the backazimuth, computed as the angle between the source and the monitor position, and the obtained polarization angle of the surface waves, which can be related to the direction of propagation of the waves.

3.2.5 Source position effect on the amplification of surface waves

Furthermore, to investigate the source location effects on the amplification of surface waves, the amplification factor is defined as

$$AF_{PS/PW} = \frac{PGD_{PS}^{SW}}{PGD_{PW}^{SW}} \tag{3.3}$$

where the maximum horizontal amplitudes (A_{POL} or PGD^{SW}) of each point source (PS) is compared against the vertically incident plane wave. The analysis of this amplification factor pretends to contrast two phenomena. First, the fact that the plane S-wave input generates surface waves only because of the conversion of S waves to surface waves in the basin edges. On the other hand, in the double couple PS, the generated surface waves will be converted into a more complex pattern due to the influence of the point source incidence combined with the basin edge effects. Thus, the ratio is a qualitative way to check which zones are extra influenced by the source location.

In Figure 3.15, the spatial variability of the $AF_{PS/PW}$ shows slightly higher values for the

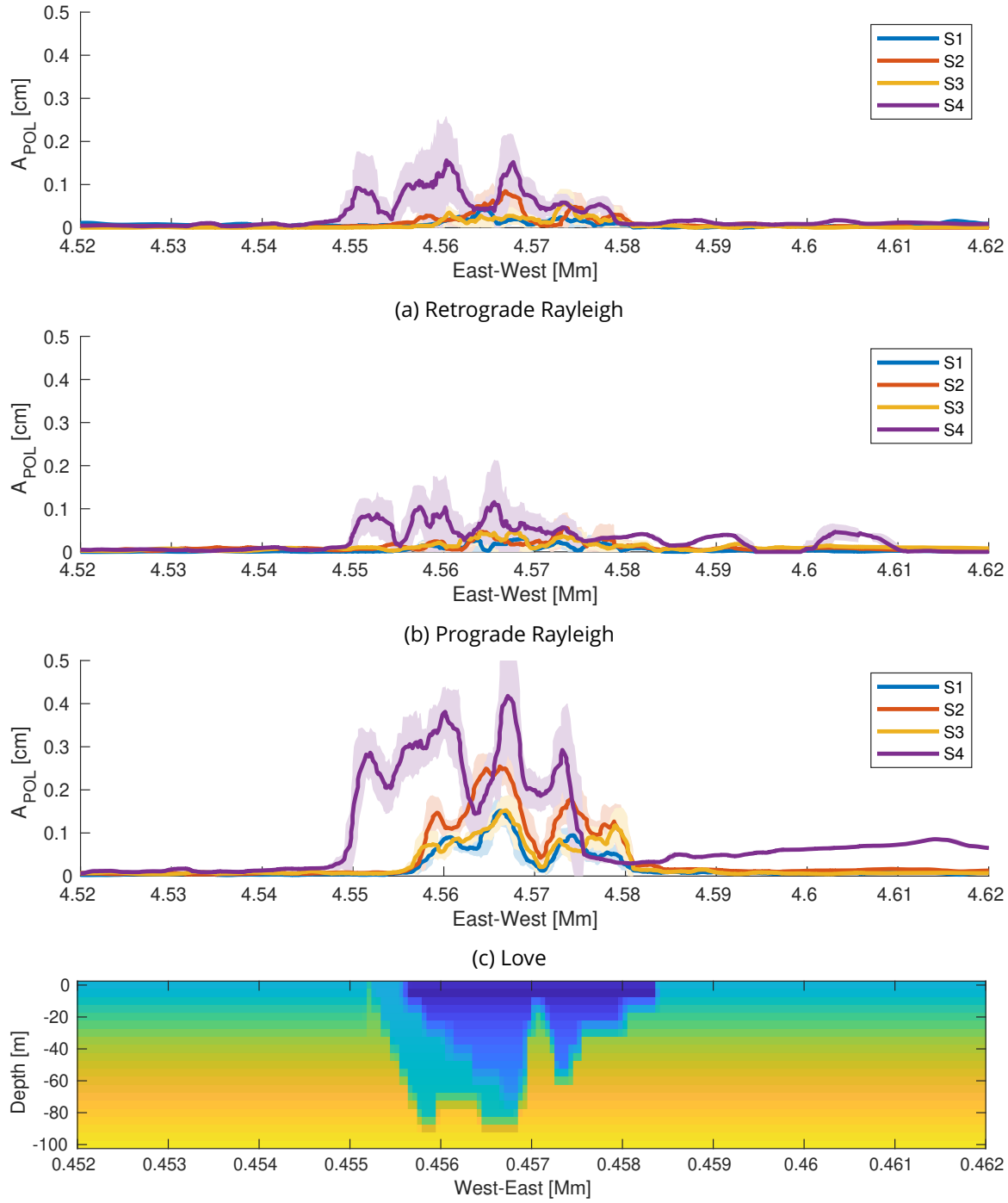

(a) Retrograde Rayleigh

(b) Prograde Rayleigh

(c) Love

(d) $A - A'$

Figure 3.13: Maximum horizontal displacement along the $A - A$ (a) retrograde and (b) prograde Rayleigh and (c) Love waves. (d) is the $A - A$ cross section displaying the shear wave velocity 2D profile.

Rayleigh waves of prograde polarization than for the Love waves. The unrealistic high values (between 10^6 and 10^8) are explained by the significant difference between the amplitudes of the point sources and the plane wave input motions. Thus, while the analysis results are only

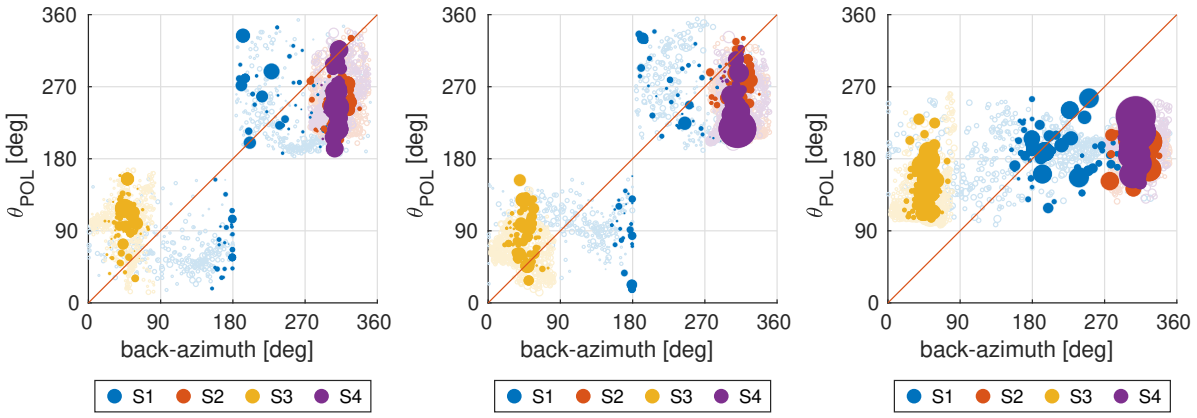

(a) Retrograde Rayleigh (b) Prograde Rayleigh (c) Love

Figure 3.14: Relation between the backazimuth and the polarization angle of the surface waves inside the basin for 4 different PS. In the background the surface waves for monitors outside the basin.

of a qualitative manner, they remain comparable between sources. Results show the shallow source certainly induces more basin-edge surface waves (Wirth et al., 2019, Chapter 2 of this manuscript).

Moreover, only the three deep sources (S1, S2 and S3) are evaluated to evaluate the source position. Source-azimuth dependence on the surface wave generation is clearly recognized as the source S1 present lower AF values. This result can be argued by the velocity contrast difference in the incident edge for the three PS. The velocity contrast in the northern and eastern edges for S2 and S3, respectively, is larger than in the western edge for S1, due to the presence of the stiff sediments, thus affecting the incidence in the basin and the surface wave-energy transmission into the basin (Lai et al., 2020; Brissaud et al., 2020).

3.2.5.1 Partial conclusions

The spatial variability of the basin-induced surface waves in the Argostoli basin has been assessed with physics-based simulations. In realistic basins, the source azimuth influences the amplification pattern and also the generation of long-period surface waves (e.g. Wirth et al., 2019; Daza et al., 2023). Therefore, in this Section, the source location effect has been investigated with four double couple point sources (PS) and compared to a more general case of a vertical plane wave motion.

Partial conclusions can be drawn from the results. The source azimuth effect influences the basin-edge generation of surface waves, predominantly of Rayleigh type, partially responsible for the higher frequency amplification response ($f > f_0$, f_0 the fundamental frequency of the site). The effects can be related to basin-setting parameters, such as the velocity contrast at the incident edges of the basin where the surface waves are presumably generated.

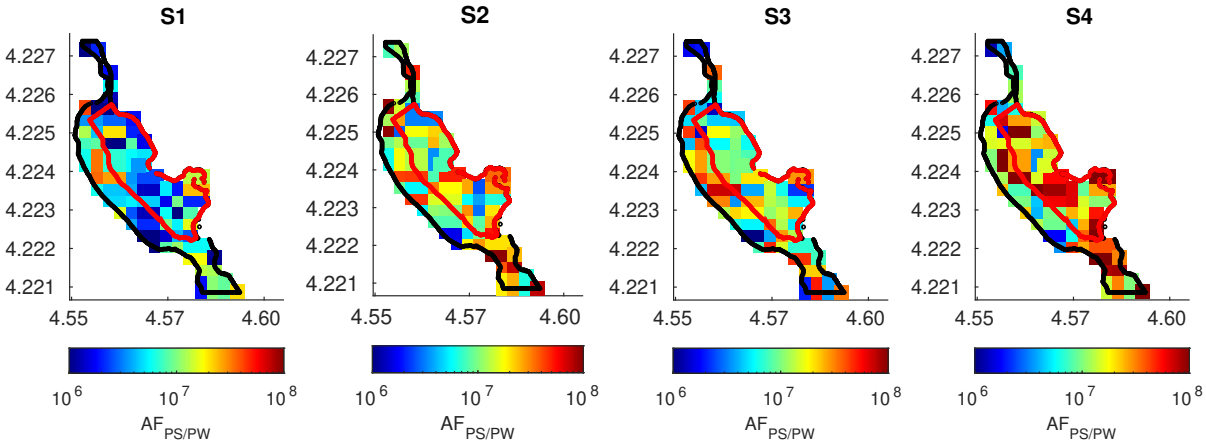

(a) Prograde Rayleigh waves

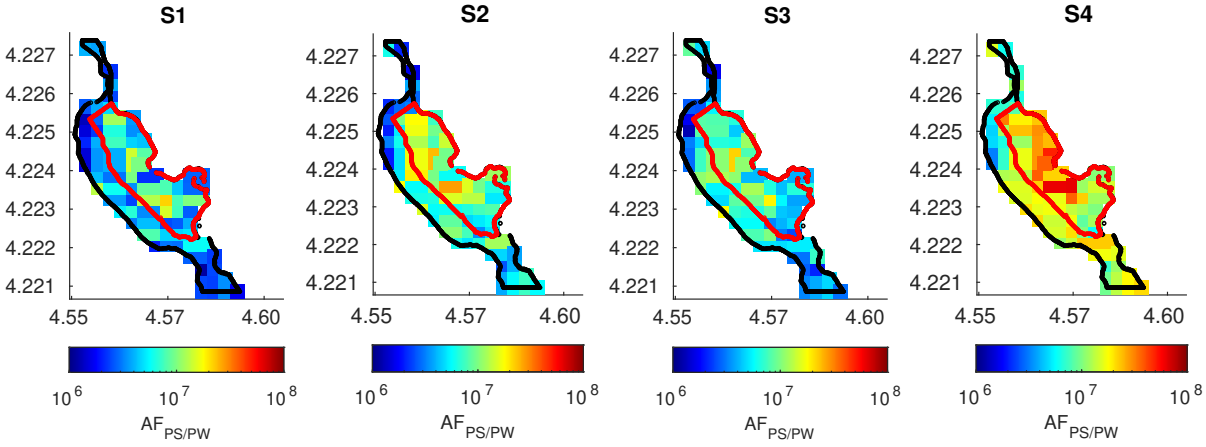

(b) Love waves

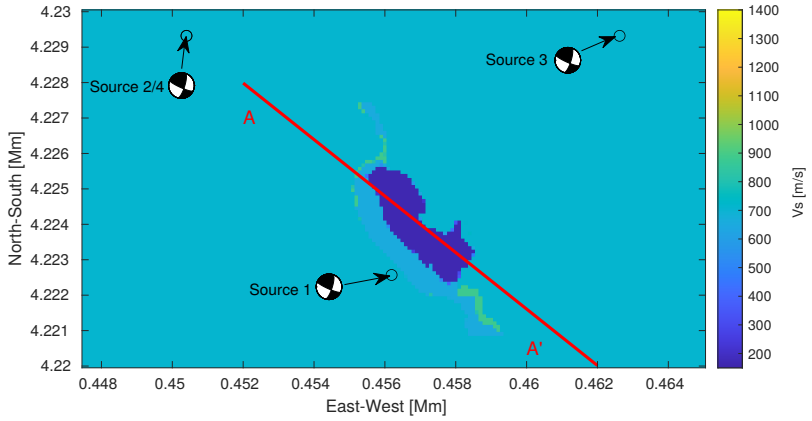

(c) Source position.

Figure 3.15: Maps of amplification $AF_{PS/PW}$ of the surface waves amplitudes depending on the source position.

3.3 Cadarache basin

A second simulation of a site is performed from the Cadarache basin, located in southern France. The site is of particular interest for the location of a research center with several nuclear facilities

and because is a high-seismicity area, so it has been the study case for numerous studies (Perron et al., 2018a; Guyonet-Benaize, 2011; Hollender et al., 2011; Dujardin et al., 2020; Castro-Cruz et al., 2021, 2022). The 3D simulation of wave propagation used in this work was performed and verified by Castro-Cruz et al. (2022, 2021) using the SEM3D code. Some of the features of this model is the inclusion of the topography and the simulation of realistic extended source scenarios for a M_w 6.0 earthquake in one of the faults with potential to cause middle to strong ground motion in the area: Middle Durance segment. For the fully explained description of the model please refer to its references.

The earthquake scenarios in this simulation present near field effects, where velocity pulses in the fault normal direction are observed, increasing spectral accelerations at large periods (Alavi and Krawinkler, 2004; Champion and Liel, 2012; Güneş, 2022). The effects of long period ground motions would be then a combination of near field ground motion and basin edge generated surface waves. For this reason, the near field ground motion are first identified and the signal is treated to focus only in the basin-generated surface waves. Then, the surface waves characteristics are investigated with the NIP.

3.3.1 Description of the model

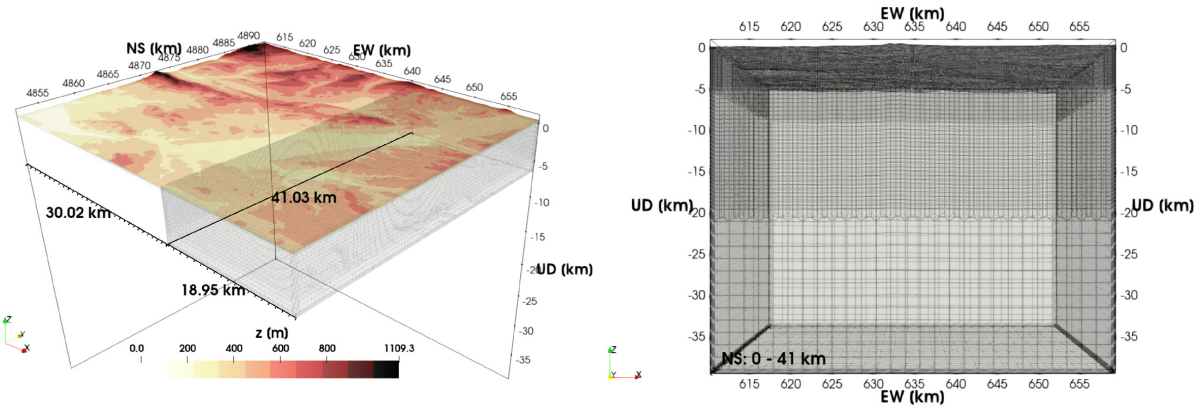

(a) Topography

(b) Mesh size and elements dimensions

Figure 3.16: Numerical domain in SEM3D of the Cadarache region: (a) Elevation and (b) Mesh elements. Retrieved from Castro-Cruz et al. (2022).

The mesh size, dimensions and local topography of the regional model are seen in Figure 3.16. The domain includes the basin and the different realizations of the extended sources (Figure 3.17). The Cadarache basin is described as an elongated basin of 3.5 km of maximum width in the northwest-southeast direction with a depth of approximately 50 to 160 m. The mechanical model is described by one regional velocity profile and one local velocity profile estimated at the Cadarache centre for the basin, retrieved from the studies of Guyonet-Benaize (2011) and Hollender et al. (2011). The local velocity model is defined by a simple function with minimum

wave velocity of $V_S = 400$ m/s and $V_P = 900$ m/s, homogeneous to the whole basin, given by

$$V_{s,soil}\,(h) = 400 + 130h^{0.5} \qquad \text{m/s} \tag{3.4}$$

$$V_{p,soil}\,(h) = \begin{cases} 900 & 0 \leq h \leq 7 \\ 1500 + 190h^{0.5} & h > 7 \end{cases} \qquad \text{m/s} \tag{3.5}$$

where h is the depth in meters.

The regional velocity model is given in Table 3.3, where the first layer (up to 60 m of depth) is a function of depth, followed by constant layers. The damping values Q were defined in terms of the velocity of the sediments as $Q_S = V_S/10$ and $Q_P = V_P/5$.

Table 3.3: Properties of the material for the crustal model proposed for the Cadarache region. V_p the P-wave velocity, V_s the S-wave velocity, ρ density. Retrieved from Castro-Cruz et al. (2021).

Depth [km]	V_p [km/s]	V_s [km/s]	ρ [kg/m^3]
0	2+1.054$z^{0.3}$	1+0.427$z^{0.4}$	2.4
0.06	5.60	3.20	2.8
3.0	5.92	3.43	2.8
27.0	6.60	3.81	2.9
35.0	8.00	3.81	2.9

In terms of the numerical model, the mesh was created using the non-houring approach, for a maximum frequency of 10.5 Hz. According to Castro-Cruz et al. (2022), most of the basin amplification were in the 1.0 to 10.5 Hz range, verified against H/V measurements of Hollender et al. (2011) in the basin. Moreover, the fundamental frequency is estimated close to 5 Hz.

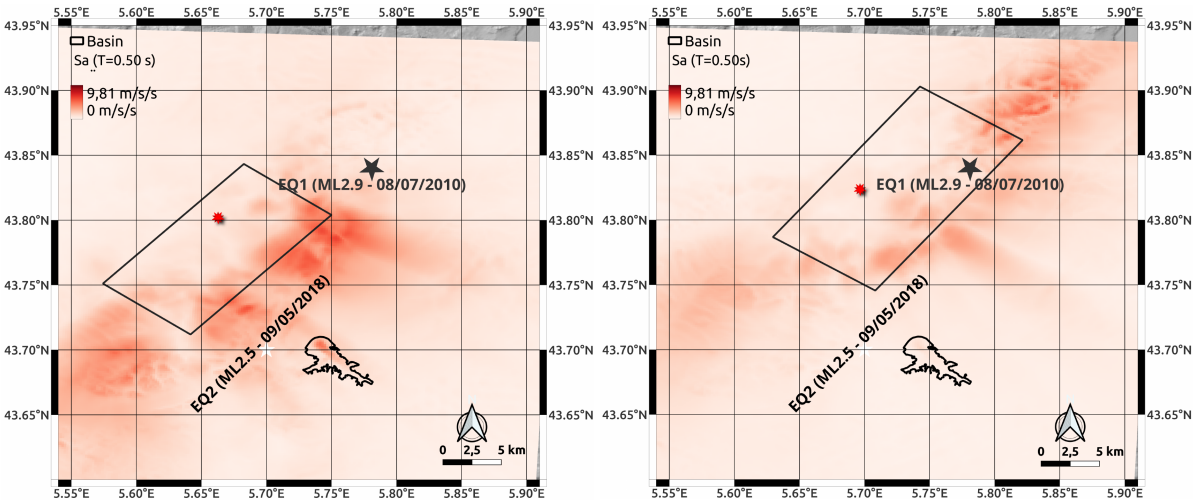

(a) EF2 (b) EF4

Figure 3.17: Distribution of $Sa[T = 0.5s]$ for two selected extended fault scenarios: (a) EF2 and (b) EF4 according to the names received in Castro-Cruz et al. (2022).

.

For the sake of brievity, and in order to evaluate the surface wave generation in this basin, two source scenarios were selected: EF2 and EF4 of the work of Castro-Cruz et al. (2022). Both of them represent segments of the Middle Durance fault. The target seismic moment is fixed at $1.04 \cdot 10^{18}$Nm. The kinematic description is based on the model for low-to-moderate seismicity regions for near fault zones of Dujardin et al. (2020). The pseudo-spectral accelerations (Sa) values for a period $T = 0.5$ s for the two extended source is displayed in Figure 3.17. This period was chosen as it is close to the natural period of vibration of the soft soil sediment within the basin (Perron et al., 2018a).

3.3.2 Results and discussion

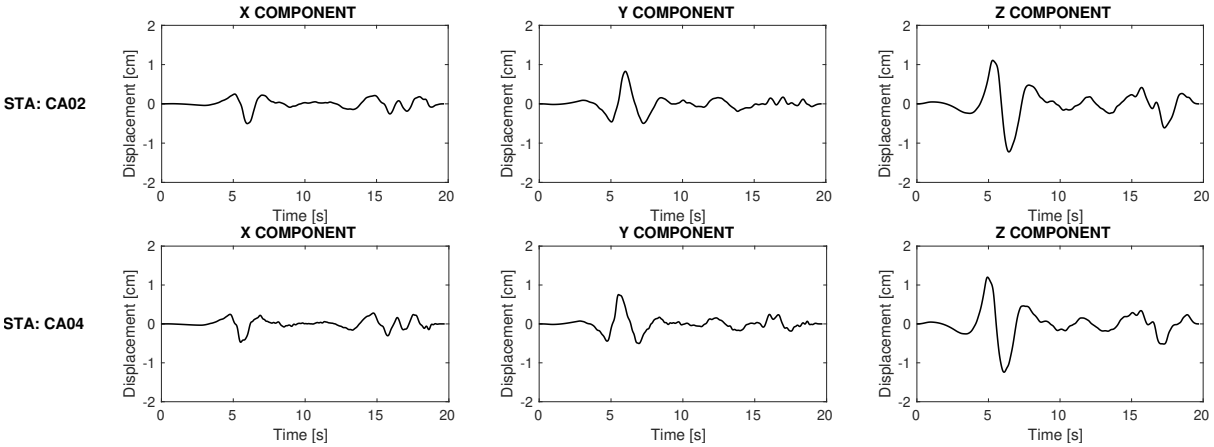

Figure 3.18: Displacement time histories stations (a) CA02, in rock site, and (b) CA04 in soft soil site.

First, two stations are selected to exemplify the ground motion obtained in this case scenario: CA04, located inside the basin and CA02, located at the bedrock. The displacements time histories for the source scenario EF4 in Figure 3.18 show clearly a long-period velocity pulse due to the near-field function used to model the sources. From a direct observation of the obtained seismograms, this velocity pulse does not seem to interact with the basin, as no amplification in the CA04 station is observed. Therefore, a quantitative approach is used to further identify near field ground motions present in the simulation results. Proposed by Baker (2007b), the method identify if the ground motion contains strong velocity pulses based on two predictors: the peak ground velocity (PGV) ratio and the energy ratio. The latter is a division between the residual and the original record, where the residual signal is the ground motion remaining after the substraction of the largest velocity pulse. The $Pulse\,indicator$ is defined as

$$Pulse\,indicator = \frac{1}{1 + \exp\left\{-23.3 + 14.6\,(PGVratio) + 20.5\,(energyratio)\right\}} \tag{3.6}$$

If the pulse indicator is close to 1, the ground motion is classified as "*pulse-like*".

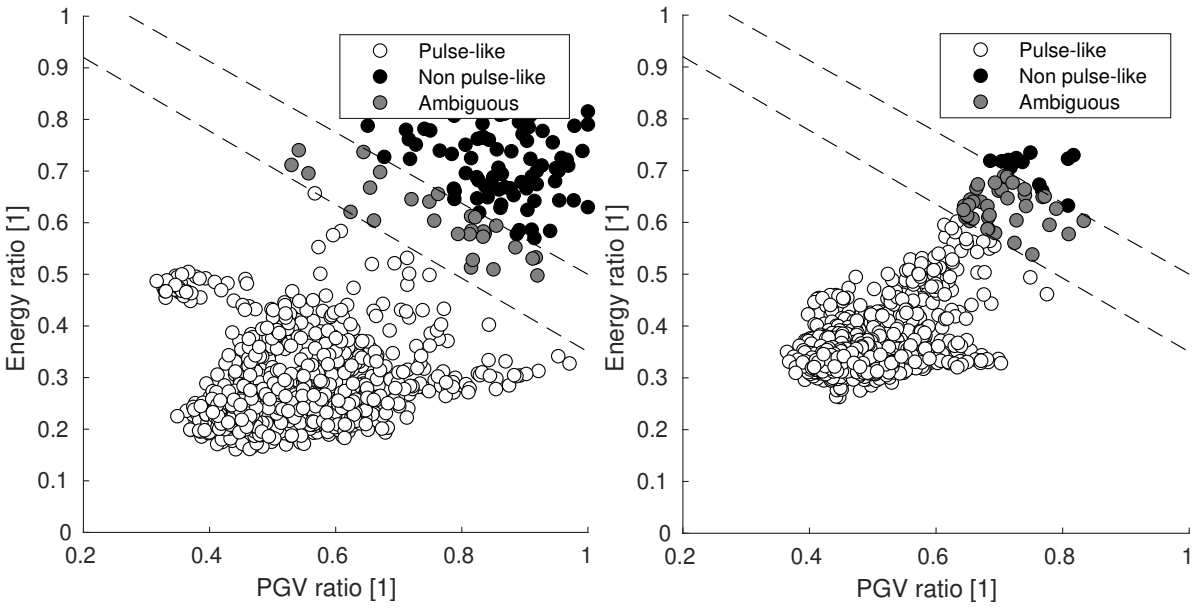

Figure 3.19: Predictor variables used for pulse-like classification for all the monitors at the surface inside and outside the basin for the two source scenarios.

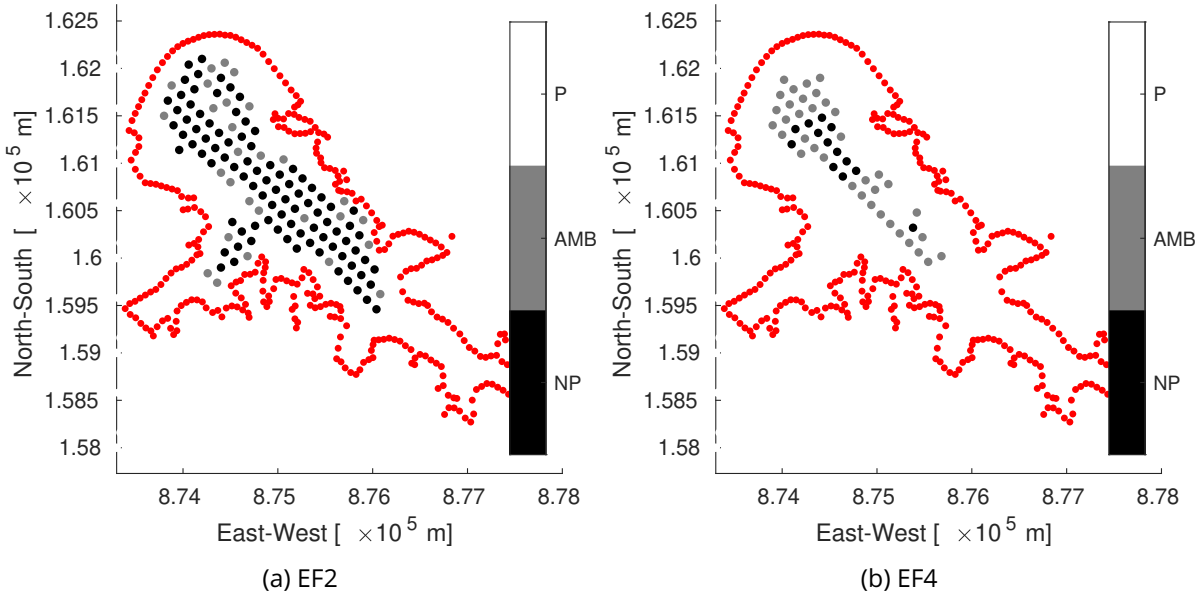

Figure 3.20: Map of the ground motion classified as pulse-like (P, in white) versus ambiguous (AMB, in gray) and not caused by directivity effects (NP, in black).

Figure 3.19 displays the PGV ratio versus the energy ratio of the obtained signals all over the surface for the EF2 and EF4, respectively. Between the zones indicating the pulse or non-pulse-like behavior there is a zone where the signals do not have a clear classification, so they are classified as ambiguous. As expected, it is observed that most of the signals are in the pulse-like zone, which means that near-fault effects are present in the signals. If the same indicator

is plotted against the position inside the basin, as in Figure 3.20, it is possible to observe that ground motions in a small area inside the basin are classified as nonpulses.

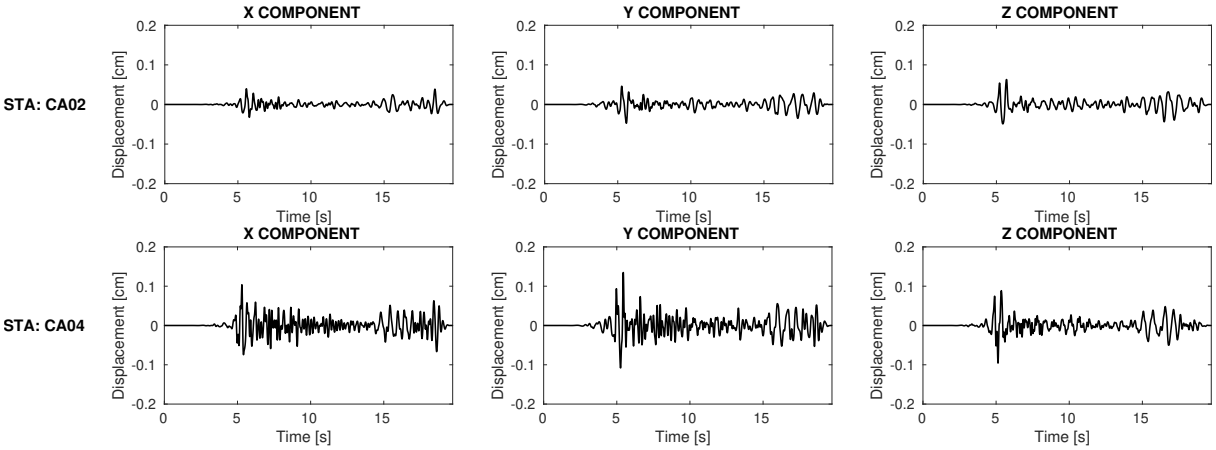

Figure 3.21: Time history displacement after bandpass filtering between 1-10 Hz to remove near-field effects at stations (a) CA02, in rock site, and (b) CA04 in soft soil site for the EF4 source scenario.

From this observation, the period of the substracted pulses using the identification procedure of Baker (2007b) vary between 1.6 and 3.9 seconds or analogously between 0.25 and 0.6 Hz. To focus in the basin-generated surface waves with frequencies closer to the fundamental frequency of the basin (4.4 Hz) , it was decided to remove the pulse from the signal. Thus, the results that follows are obtained by analyzing the results between 1 to 10 Hz, to avoid the influence of the long-period pulse in the surface waves (Figure 3.21).

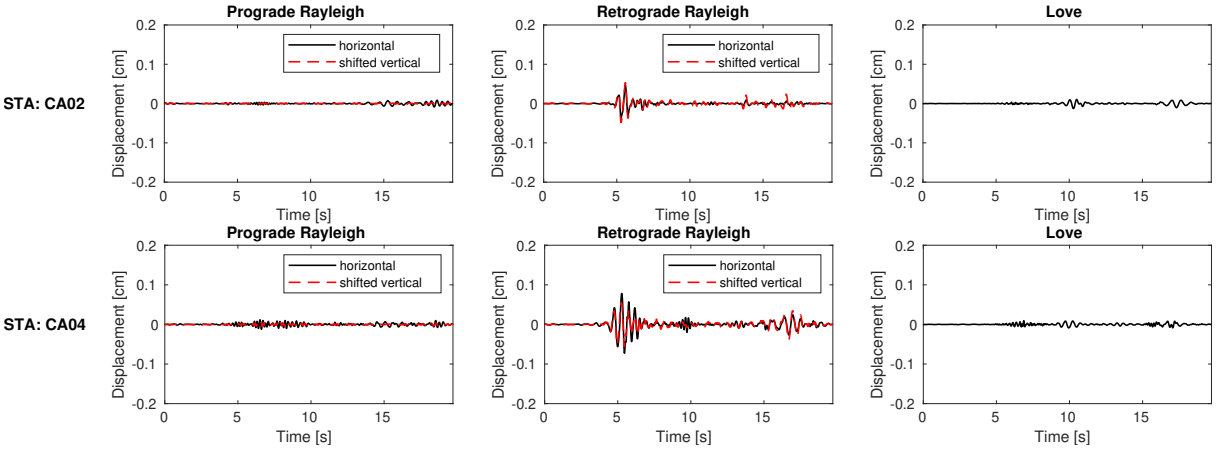

Figure 3.22: Surface waves extraction at stations (a) CA02, in rock site, and (b) CA04 in soft soil site for the EF4 source scenario after the bandpass filtering between 1 and 10 Hz to remove near-field effects.

The selection of 1 Hz for the application of this filter to the signals can be argued because low frequency shaking will not be able to interact with the basin (Drake, 1980; Ayoubi et al., 2021). For instance, Ayoubi et al. (2021) estimated that for wavelengths > 8 times the basin depth, the

basin is too small to experience mode conversion. In this case, a rough estimation can be made in terms of the fundamental frequency, shear wave velocity and depth of the sediments, and it is expected that the incoming waves start to interact with the basin at frequencies $f > 2.1$ Hz based on the literature results.

After the filtering, the time signals are analyzed with the NIP to extract the surface waves. As an example, Figure 3.22 show the results in the stations CA02 and CA04 after the latter consideration, where the basin amplification is clearly observed in the extracted Retrograde Rayleigh waves.

In the results that follows, the Normalized Inner Product (NIP) was applied at large scale over monitors across the whole surface (inside and outside the basin). Surface waves were extracted in a domain of dimensions of 4.7 km $\times$ 4.4 km, in monitors located at the surface spaced every 20 meters in order to have a good resolution of the spatial variability of the surface waves, analizing a total of 52000 monitors. Figure 3.23 shows the characteristics of the surface waves for the extended source EF2, which is located closer to the basin. It should be noted that the results are presented only if the coefficient of correlation C_{PV} between the polarized and vertical components at the station is higher than 0.7 in Rayleigh and lower than 0.1 in Love waves. The white areas in the Figures 3.23 and 3.24 means no surface waves are identified.

The results demonstrates the significant influence of the basin on the surface wave formation. Retrograde Rayleigh waves are concentrated in the western part of the basin and some strong amplification outside the basin could be related to topographic effects. Love waves, in contrast, exhibit a peculiar behavior because they are observed along most of the central part of the basin, but far from the edges. It is concluded from Figure 3.23b and 3.23c that, in general, Love waves characteristics interacts the most with the basin: the central frequency is close as the natural frequency of vibration and they clearly get deflected by the basin boundaries, compared to Rayleigh waves.

The effect of the distance to the source in the surface wave generation can be analized by comparing the previous results with the extended source EF4, located further north than EF2, as depicted in Figure 3.24. In this case, smaller amplitudes of the surface waves are found, because the ground motion amplification was also lower in this case scenario (Figure 3.17). The generation of basin-induced surface waves is favorized from the fact that the wavefield from the extended source EF2 arrives and interacts directly with the northwestern border. The central frequency of the Love waves seems to decrease in the deepest part of the basin. Therefore, a distinct feature of Love waves is found: their properties could be directly related to the basin properties, as only minor differences are observed between EF2 and EF4 source scenarios.

Finally, from Figures 3.23 and 3.24 a high spatial variability within close distances inside the basin is observed. This is described by a complex pattern of surface waves amplification, distinctively for each source scenario, caused by the multiple interaction of the wavefield from the extended source with the basin. This finding could remark the importance of realistic physics based simulations for the complete understanding of these types of waves.

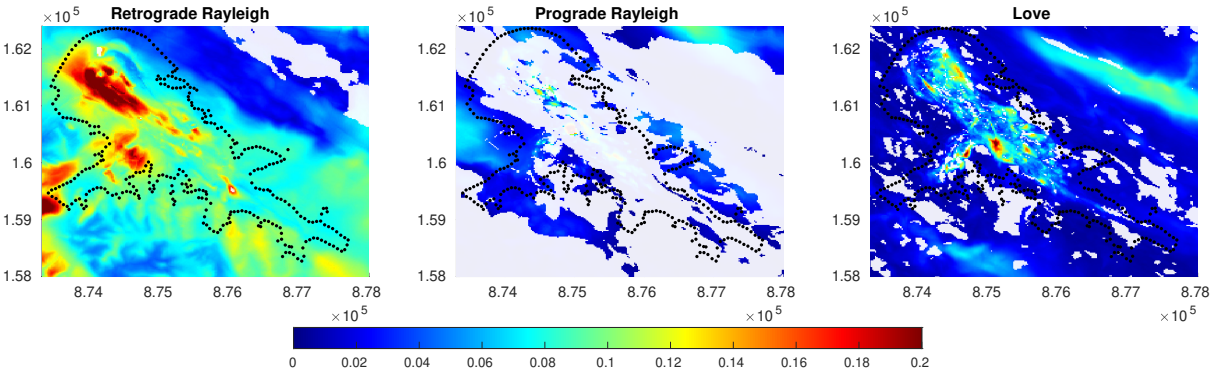

(a) Amplitude

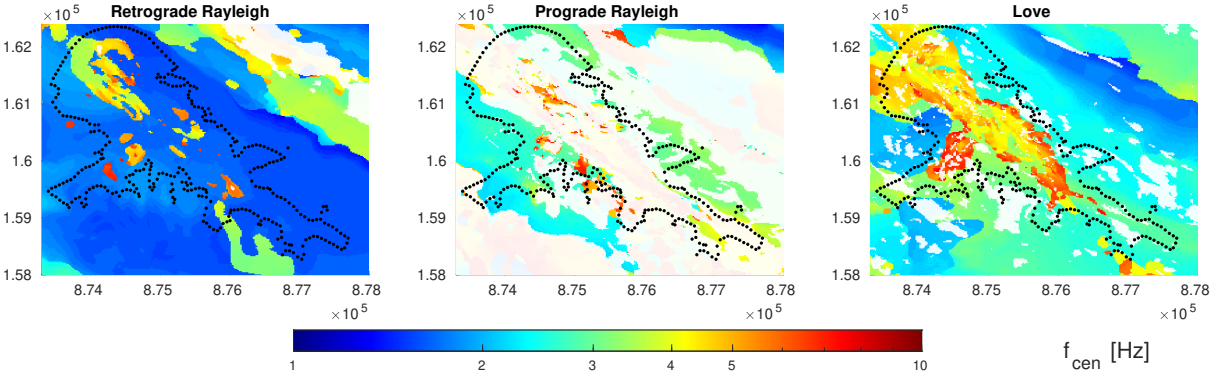

(b) Central frequency

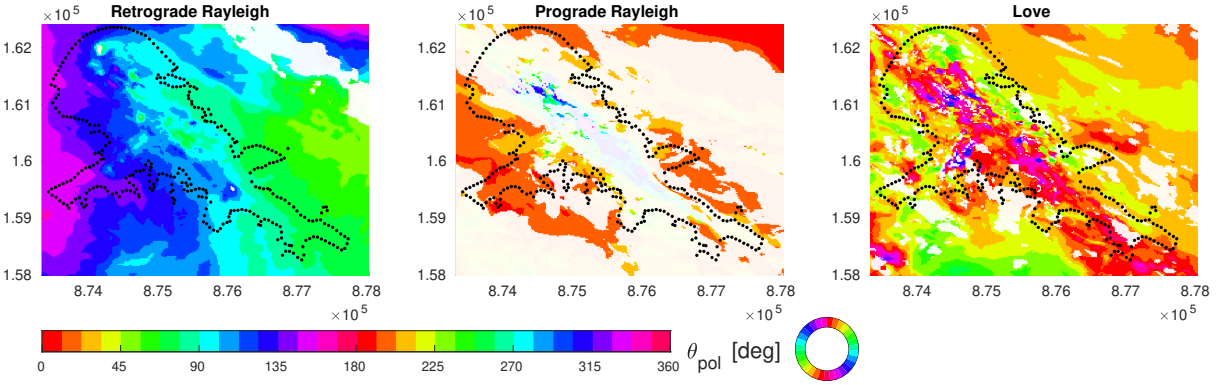

(c) Azimuth angle.

Figure 3.23: Surface wave characteristics map in the Cadarache basin (a) maximum amplitude of the polarized horizontal displacement A_{POL}, (b) central frequency f_{CEN} and (c) azimuth angle for the extended source EF2.

3.4 Concluding remarks

This Chapter focused on investigating basin-induced surface waves in realistic basins. Two physics-based simulations (PBS) were explored: the Argostoli basin in Cephalonia island, Greece, and the Cadarache basin, in southern France. The Normalized Inner Product (NIP, Meza-Fajardo et al., 2015) was used as the methodology to identify and extract the three types of surface waves due to its time efficiency. Specifically, the method has to be applied to multiple time histories (of the

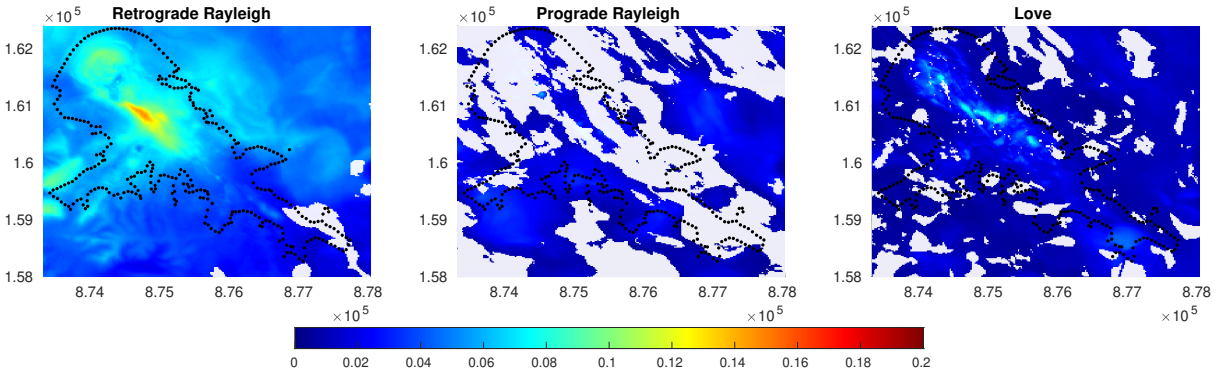

(a) Amplitude

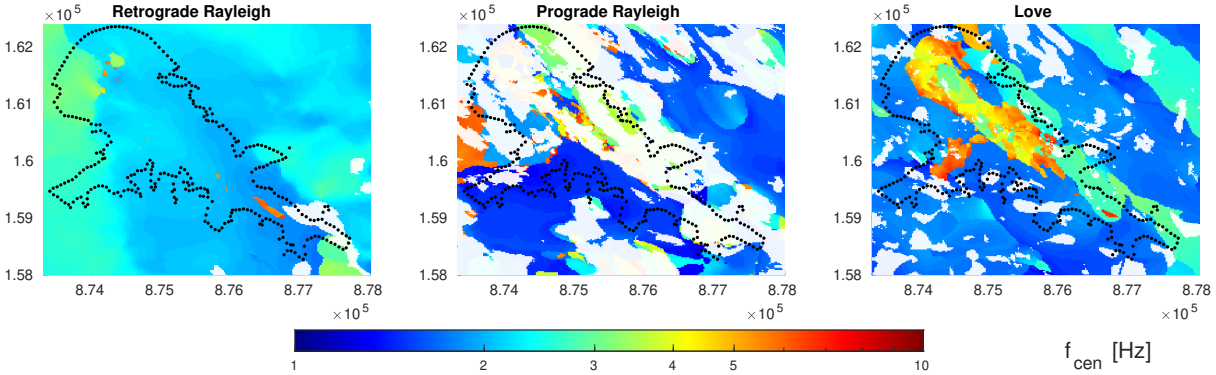

(b) Central frequency

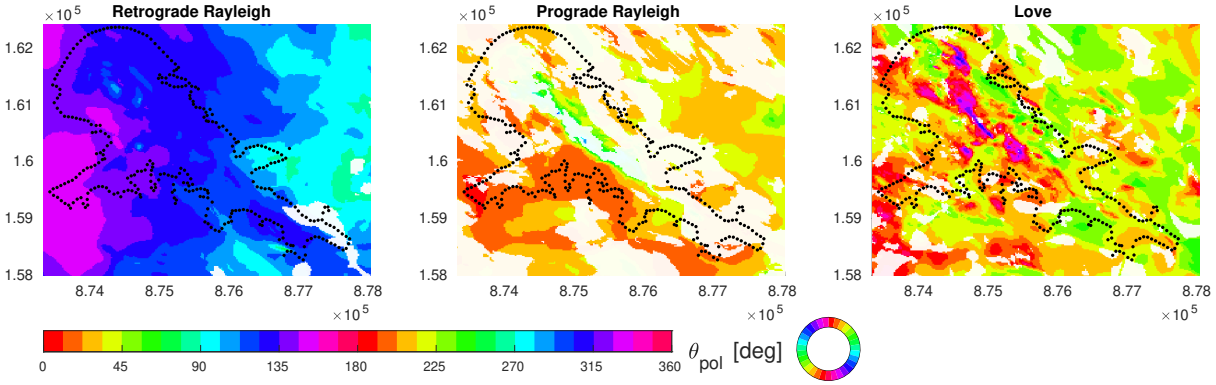

(c) Azimuth angle.

Figure 3.24: Surface wave characteristics map in the Cadarache basin (a) maximum amplitude of the polarized horizontal displacement A_{POL}, (b) central frequency f_{CEN} and (c) azimuth angle for the extended source EF4.

order of thousands) to evaluate the spatial variability of surface waves inside and outside the basins.

The results, in general, are defined by a more significant spatial variability than in the canonical basin of Chapter 2, explained from complexities in the models such as the basin geometry, material layering, source azimuth and topography. In this case, the development of a relation between surface wave generation and some basin proxies, as in amplification studies (e.g. Stambouli et al., 2018; Pilz et al., 2021; Bard, 2021), remains a complex task. However, from the results

of this Chapter, some patterns of the basin-induced surface waves can be disclosed.

Since the surface waves are generated at the basin edges and get trapped within the soft sediments, their polarization angle θ, which can be easily related to their propagation direction, is determined more by the basin edges geometry than by the source back azimuth. However, the source back azimuth is important because it influences the entrance of the basin and, therefore, the energy conversion at the border, i.e., the amplification of the surface waves. As for the central frequency (f_{cen}) of the basin-induced surface waves, the condition of $f_{cen} > f_0$, with f_0 the fundamental frequency of the site, is respected in all cases. Besides, in general, f_{cen} of Love waves is close to f_0 and f_{cen} of Rayleigh waves is higher. For instance, the latter can be related to the amplification response observed in the SSR ratio in higher frequencies (Bowden and Tsai, 2017).

These observations, i.e., the frequency-dependent amplification of the surface waves observed, contribute to the ground motion amplification, thus affecting the seismic hazard estimation. For example, this surface wave amplification would be present only when the 3D effect (basin geometry) is accounted for compared to a traditionally used 1D column with a vertically incident S-wave. In this case, the realistic physics-based simulation of basins are a powerful tool to generate complex earthquake ground motions. This shaking is necessary for the correct evaluation of seismic hazard for infrastructures located on sedimentary basins.

Chapter 4

Seismic performance of long-period large-scale infrastructures including basin effects

Contents

4.1 Introduction

This Chapter is focused in the influence of the basin effects on the structural demand, as part of the “final" steps of the performance based design or PBEE methodology formulation (e.g. Porter, 2003). The last two steps, related to the structural and damage analysis of the PBEE formulation rely on the definition of a engineering demand parameter (EDP) and damage parameter (DP) conditioned to the intensity measure (IM) defined earlier in the hazard analysis. The problem is solved in a probabilistic manner, relating the EDP with its annual rate of exceedance, computed as the combination of the likelihood of a ground shaking intensity with the probability of some adverse outcome (Baker et al., 2021), given by

$$\lambda_{EDP}(z) = \int P\left[EDP > z | IM = im\right] \cdot \frac{d\,\lambda_{IM}\left(im\right)}{d\,im} \cdot d\,im \tag{4.1}$$

The integral part $P\left[EDP > z | IM = im\right]$ is the probability that the engineering demand parameter level $EDP = z$ is exceeded given the ground intensity measure level $IM = im$. Moreover, the $\lambda_{EDP}(z)$ is computed from the *hazard curve* λ_{IM} estimated in the previous step of the hazard analysis. This mean annual rate of exceedance λ_{IM} at a site of a given im level is given by

$$\lambda_{IM}(im) = \lambda_0 \int_m \int_r P\left[IM > im | m, r\right] \cdot f_{m,r}\left(m, r\right) \cdot dm \cdot dr \tag{4.2}$$

The probability that a specified IM is exceeded at a given location for a set of source parameters m (magnitude) and r (distance) is represented by $P\left[IM > im | m, r\right]$ and $f_{m,r}$ is the joint probability density function (PDF) for magnitude and distance (Bazzurro and Cornell, 1999; Bommer, 2002). In realistic cases, the hazard dissagregation have to be performed for all seismic scenarios in the region of interest to measure the value λ_0, the annual rate of earthquakes greater than the minimum magnitude, in order to obtain the complete hazard curve λ_{IM}. The used IM will represent the seismic demand of the earthquake on the structure, and it should be able to correlate the ground motion with the damage to the buildings. In general, the most used IMs are the intensity and peak ground acceleration (PGA) or the response spectra linked to structural characteristics (Calvi et al., 2006).

When dealing with the structural response for the soil-structure interaction (SSI) analyses, several engineering approaches are used. Site effects are usually considered with simplified one-dimensional (1D) soil layers subjected to vertically propagating plane S-wave fields, thus inducing only shaking in the horizontal components. Additionally, this shaking is usually induced in one or two orthogonal directions applied along the principal axes of the structure (Rigato and Medina, 2007). Vertical component is usually neglected, as small deflections are assumed (Trifunac, 2006). Specifically, the site effects in the seismic hazard analysis are accounted by the defined *amplification factors* (AF), which as its name suggest, focus on the amplification due to the presence of the soil sediments (e.g. Bazzurro and Cornell, 2004; Marafi et al., 2017). The AFs are applied directly to the horizontal ground motions. However, the basin geometry, as seen in the previous chap-

ters, will generate a more complex ground motion, described by the generation of surface waves and rotational components, differential ground motion, and directionality effects.

The rotational components from ground motions are of interest in earthquake engineering, as they can increase the damage induced to a structure as much as usually considered translational components (Stupazzini et al., 2009a; Guidotti et al., 2018; Guéguen and Astorga, 2021; Kato and Wang, 2021; Vicencio and Alexander, 2019; Castellani et al., 2012; Smerzini et al., 2009; Nazarov et al., 2015; Falamarz-Sheikhabadi and Ghafory-Ashtiany, 2015; Meza Fajardo and Papageorgiou, 2018). To evaluate the significance of the effects of rocking and torsional effects on buildings, severals studies (Gupta and Trifunac, 1990, 1991; Çelebi et al., 2014) showed for simplified representation of structural systems that rocking and torsional excitations can be important for tall structures supported by soft sediments. For long period waves, Gičev et al. (2015) conducted a study of a building supported by a flexible foundation. They concluded that the response of a building can be approximated by the response of a rigid body translation combined with rotation input motions as long as the spatial variability in the foundation is small. Torsion in buildings from non-uniform ground motion can be determined by soil modeling as a subspace (Anagnostopoulos et al., 2015). In small buildings torsion from ground motion increase the displacement and drift ratios (Rahat Dahmardeh et al., 2020; Poudel et al., 2022). Besides, the importance of the vertical to the horizontal input motion is relevant to the effects of the rotational motions. When the acceleration spectra of the vertical components in the range of periods of interest is comparable to the horizontal components, important rotational effects can be expected (Castellani et al., 2012). Additionally, the ground motion directionality can also produce an increase of the expected values of demand parameters in different types of structures (Athanatopoulou, 2005; Boore, 2010; Banerjee Basu and Shinozuka, 2011; Noori et al., 2019, among others). For instance, Noori et al. (2019) investigated the problem for bridge structures, where it was found that the critical angle, the most damaged, is not always aligned with its orthogonal principal axes.

Therefore, a major challenge is the correct representation of realistic input motions, where complex wave-fields should be defined as a three-dimensional (3D) input motion (Abell et al., 2018; Zuchowski et al., 2018; McCallen et al., 2021a,b, among others). In this work, the basin effects are investigated simultaneously on the intensity measures (IM) and on the demand (EDP or DP). Thus, the severity of the input ground motion and the corresponding structural damage can be quantified and related. The questions seeked to be responded in this Chapter are:

- Can basin effects increase the observed structural demand in a structure?
- Can these basin effects on the structural demand be correctly estimated from amplification factors computed over the ground motions?

With this in mind, a complete numerical 3D simulation of wave propagation from the earthquake source to the structure is performed. Nonlinear response-history analysis is the most direct structural modeling method (Trifunac, 2006). This analysis does not require significant assumptions as other analytical models. However, there are some limitations in the approach: it

requires to well represent the reality since the results depend strongly on the selected input motions to perform the analysis. For that reason, the full SEM-FEM approach is selected, based on the domain reduction method (DRM) (Bielak et al., 2003). In this procedure, the finite soil foundation domain and the structure are explicitly modelled with finite element method (FEM) models. The formulation in the time domain allow to impose a full 3D input seismic excitation and to absorb outgoing waves arriving on the boundary of the finite domain.

This Chapter is structured as follows. First, it starts by introducing the modeling framework used for the basin effect quantification in Section 4.2. The description of the properties of the model are shown in Section 4.3. The reference structural case is developed using a traditional methodology in Section 4.4. Then, in Section 4.5 the basin effects on the ground motion amplification and structural response are explored. Finally, the basin effects are added on the seismic hazard and risk analysis following the PBEE methodology in Section 4.6.

4.2 Modeling approach for basin effect quantification on buildings response

In order to evaluate the beneficial or unfavorable effects of the presence of the basin on the structural response of a bridge pylon, a two-step dynamic approach is considered with the Domain Reduction Method (DRM) to model the wave propagation response from the earthquake source to the structure, first defined by Bielak et al. (2003). The methodology used in this work was implemented and validated by Korres (2021); Korres et al. (2023) for the coupling between the spectral element code SEM3D (CEA and CentraleSupélec and IPGP and CNRS, 2017) and the finite element method (FEM) software Code_Aster (Code_Aster, 2017). In the traditional DRM, the wave field is transferred from the regional scale model to the boundaries of a closer reduced domain of interest at the scale of the structure. Therefore, the boundaries of the reduced domain need to hold certain characteristics to approximate the infinite propagation of waves, avoid spurious reflections, and allow the dynamic excitation from outside the domain to be transferred as an input of the FEM. According to Korres et al. (2023), the SEM-FEM weak coupling in Code_Aster uses paraxial boundary conditions (Modaressi and Benzenati, 1994). The diffracted field is described by a zero-order paraxial approximation which allow to generate the evolution of dynamic impedance, locally in space and time. As a result, they simultaneously work as absorbing boundaries and allow the transfer of the dynamic excitation.

This dynamic input at the boundaries of the reduced domain needs two fields: (i) the nodal forces (or traction vector) and (ii) the velocity. In the formulation of Korres et al. (2023), due to the incompatibility between the two numerical formulations (i.e. shape functions, quadrature rules and degrees-of-freedoms), the traction vector needs to be reconstructed in a middle step. Hence, the traction vector is approximated on a FEM framework computed from the displacement field $\mathbf{u}$ obtained as the solution of the wave propagation in SEM3D. It is obtained in auxiliary layers neighboring to the reduced domain boundary, and a static problem is performed in Code_Aster

(FEM) to obtain the nodal forces $\mathbf{F}_{node}$ at the nodes of the reduced domain boundary, which are directly the traction vector. The detailed study of the SEM-FEM coupling is beyond the scope of this work but refer to Korres et al. (2023) for further details about this method.

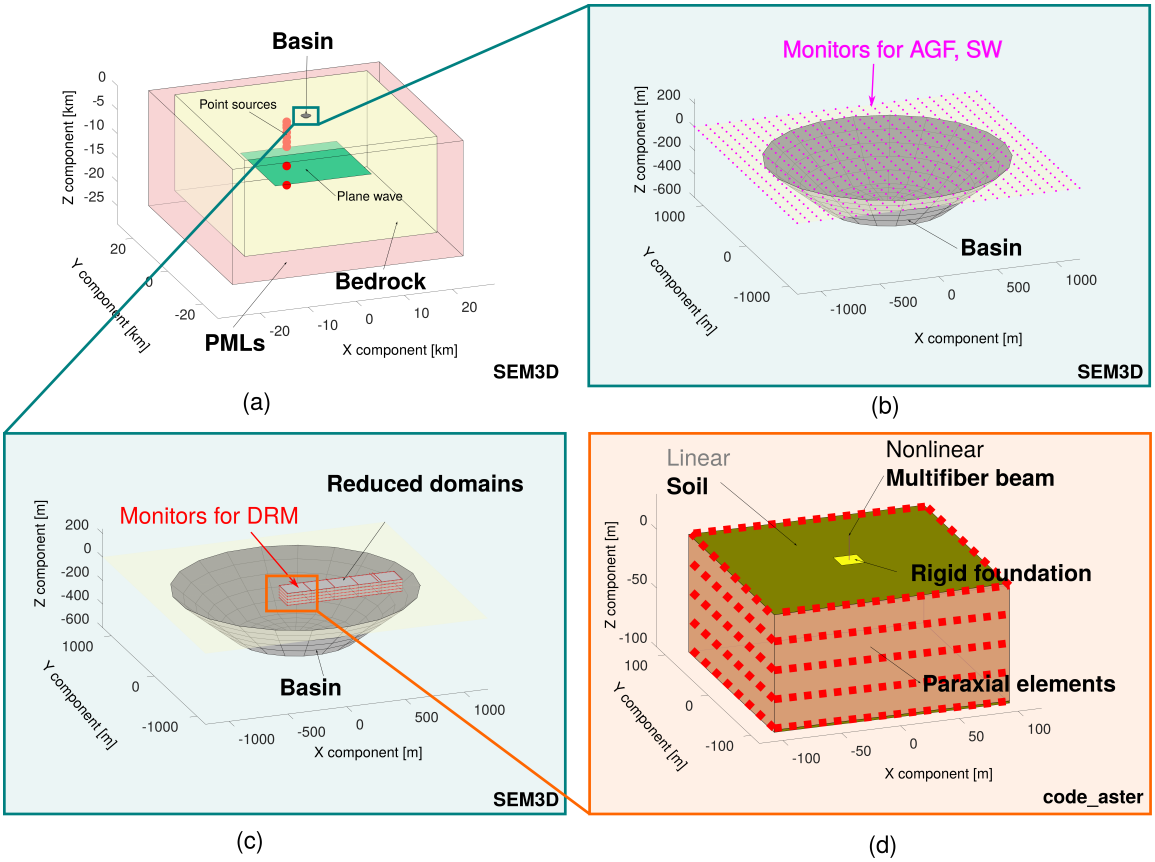

Figure 4.1: Schematic representation of the framework used in this work for the basin effect quantification on the structural response. The problem is assessed from the (a) regional scale of tens of kilometers, (b and c) including the basin, to the (d) local scale of tens of meters.

In this work, the framework to investigate the basin effects on the structural response is schematically presented in Figure 4.1:

1. SEM3D solves the wave propagation problem at the "*regional*" scale of tens of kilometers, including the sources and the basin.

2. The obtained field motion at the monitors of the DR model boundaries is extracted and them, it is imposed as 3D ground motion in the FE model. So as to take into account the spatial variability of both the basin amplification and surface waves generation from the "regional" scale, five different DR models are placed into the basin.

3. At the "*local*" scale of hundred of meters, a complete FE model including soil and inelastic structural behavior in Code_Aster is used to asses the effect of surface waves generation among others on the structural response.

4.2.1 Comparative approach for basin effect quantification

In order to quantify the basin geometry effects on the structural performance, the computed non linear response of the bridge pylon for the case models with and without basin are compared, as represented in Figure 4.2:

1. In a layered case (Figure 4.2a), where the sediment material constituting the basin is extended infinitely in the horizontal direction. This model is the one used traditionally for the site-effects assessment (Wills et al., 2000; Stambouli et al., 2021). Since a pure one-dimensional (1D) case is accomplished only in the case where a vertically incident plane wave is used as input motion, the definition of 2D instead of 1D have been selected to account the use of more complex sources, i.e., double couple (DC) point sources.

2. In a 3D basin (Figure 4.2b), where the basin geometry is included (e.g. Olsen and Archuleta, 1996).

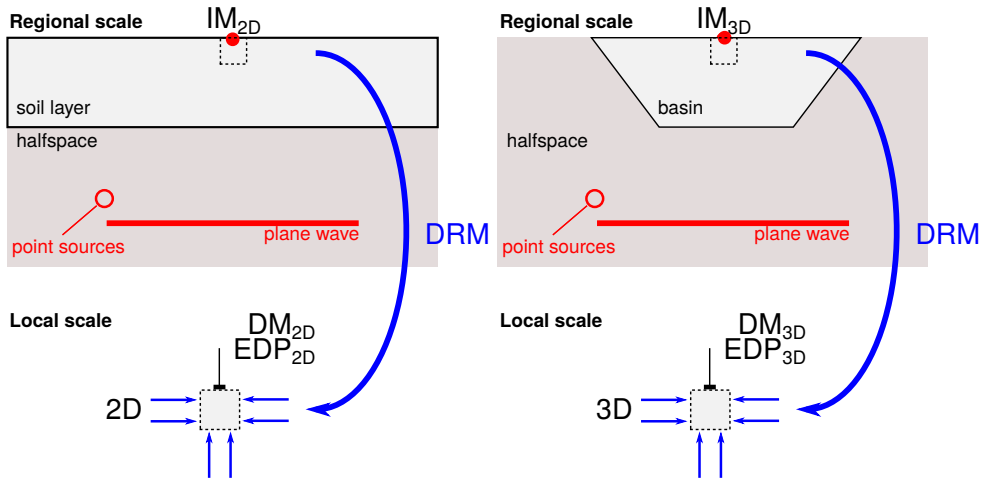

(a) 2D case (b) 3D case

Figure 4.2: Representation for the evaluation of basin effects on the structural response. Two cases are performed for each source scenario: (a) 2D, where the sediment material are extended infinitely and (b) 3D, where the geometry of the basin is included.

It is crucial to note that the two approaches take into account the soil and the material non linearities of structure. The 2D approach takes into account the fully seismic soil-structure interaction problem, the non-linear behavior of superstructure and the induced surface waves from the sources depth, but neglects all interaction effects with the basin and the induced surface waves from the basin edges. This comparative approach was developed in order to provide two groups of consistent responses.

4.3 Studied case description and modeling

In order to quantify the basin effects on tall structures, a simplified FE model is used. The dynamic system consists of two sub-domains (Figure 4.3), the superstructure and the foundation soil. The superstructure model represents a bridge pylon proposed by Chatzigogos and Meza Fajardo (2020). It is composed of a column representing a reinforced concrete, masses at the top, associated to the deck of the bridge and a spring-dashpot element between the deck and the pylon to represent deck isolation. The concrete structural elements are modeled by 3D multifiber beam (Kotronis et al., 2004). With a limited number of degrees of freedom, the model reduces the computational time while including the main characteristics of the structural response (e.g. nonlinear behavior). The main characteristics of the multifiber model are presented hereafter. The soil foundation has a shear wave velocity (V_s) equal to 900 m/s and a mass density (ρ) of 2000 kg/m^3. A linear isotropic elasticity behavior for the constituent soil material is assumed. The minimum size of elements is of 6.25 m $\times$ 6.25 m $\times$ 4 m. It was chosen in order to have 8 to 10 elements per wavelength which are sufficient to prevent numerical dispersion. In this work, the structure is introduced into the reduced domain of soil coming from SEM 3D (i.e. at the paraxial boundary level) and the dynamic time analysis is performed using the Finite Element Method (FEM) software Code_Aster, so the Soil-Structure Interaction is considered directly (Figure 4.3).

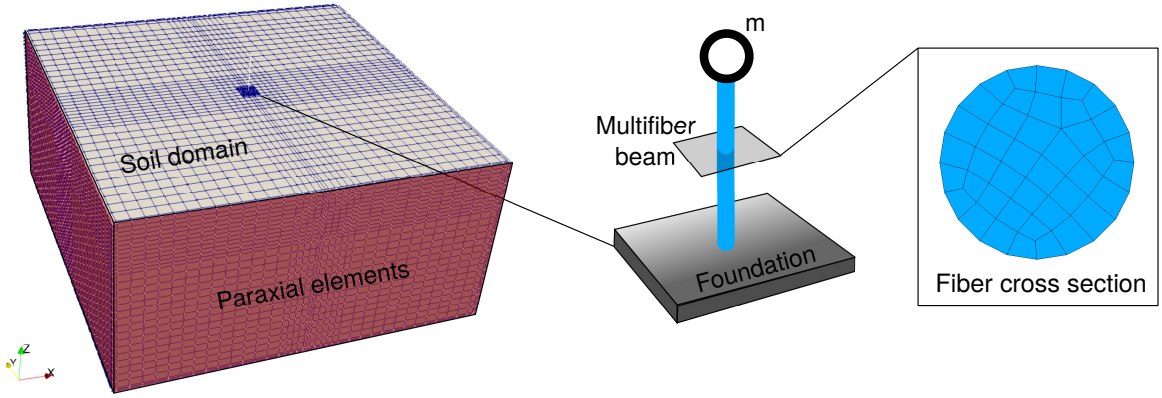

Figure 4.3: Representation of the model used for the time analysis in order to compute the coupled site-to-structure response of the bridge pylons. At the left, the mesh of the soil reduced domain, where the input motion coming from the regional model is inserted at the paraxial boundary level. The structure is superposed on the soil, and it is composed of a volumetric rigid foundation with a fiber-beam element. The latter is constituted by a cross section where nonlinear behavior is added.

4.3.1 Structural model

A simplification of the bridge pier can be made using a multifiber or fiber-beam elements in order to perform nonlinear dynamic time history calculations without the excessive computational cost (Mazars et al., 2006). The procedure has been widely used in the literature to investigate the structural response for different kinds of ground motion phenomena (Feng et al., 2014; Kashani et al., 2017; Salami et al., 2019; Ibrahim et al., 2022; Shen et al., 2021; Rodríguez et al., 2022; Özcebe et al., 2020, among others). The beam element is representative of the real behavior of concrete (as represented in Figure 4.4a, Kotronis et al. (2004)). The hypothesis of the fiber-beam is that the structure is discretized in 1D elements (Figure 4.4c), and plasticity is distributed in a cross-section (Figure 4.4b), which is discretized into fibers, depicted in different colors (Spacone et al., 1996; Carol and Murcia, 1989; Neuenhofer and Filippou, 1997). The representation allows the definition of independent uniaxial constituve laws at each fiber. For instance, the RC section will have fibers of concrete and fibers of steel.

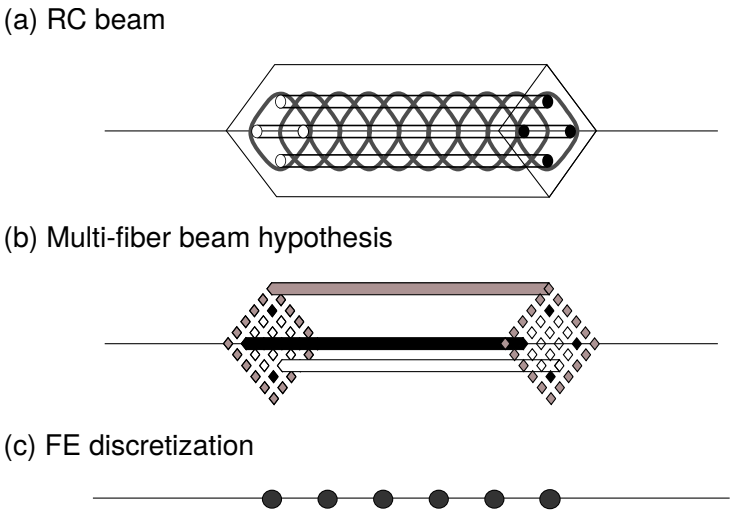

Figure 4.4: Multifiber description. Retrieved from Kotronis et al. (2004).

In general, there are two types of multifiber (Mazars et al., 2006), depending on the beam-hypothesis considered. On the Euler-Bernoulli theory, the shear effects are neglected, and the sections remain plane and perpendicular to the neutral axis of the beam (Poliotti et al., 2021). Alternatively, on the Timoshenko theory, the shear is possible through the beam as well as the shear due to torsion, and the sections remain plane but not necessarily perpendicular to the neutral axis.

4.3.1.1 Formulation of multifiber model in Code_Aster

In Code_Aster, the multifiber implemented follows the Euler hypothesis. In one beam element, the discretization have two nodes and six DOFs per node (in three dimensions, 3D): three nodal translations u, v, w and three nodal rotations $\theta_x, \theta_y, \theta_z$, represented by the vector of nodal displacements $\mathbf{U} = \{u, v, w, \theta_x, \theta_y, \theta_z\}^T$, where the beam is oriented in the x axis on a right-

handed coordinate system. The displacement field of the neutral axis $\mathbf{U}_s$ at any point $s \in [0, L]$ of the beam can be obtained as:

$$\mathbf{U}_s = \mathbf{NU} \tag{4.3}$$

where **N** is the matrix containing the linear interpolation functions and

$$\mathbf{U}_s = \{u_s(x), \theta_{sy}(x), \theta_{sz}(x), \theta_{sx}(x)\}^T \tag{4.4}$$

is the generalized displacement field reduced by the Euler theory. In the multifiber formulation, the beam element is divided into a number of cross sections, of surface S, located on the control point of the numerical integration (i.e. on the Gauss points, represented as black dots in Figure 4.4(c)). From the assumption of Euler hypothesis, all strains and stresses act parallel to the longitudinal axis (Spacone et al., 1996), and the deformation at each part of the section (x, y, z) can be correspondingly computed in function of the displacement field at the neutral axis $\mathbf{U}_s$. At the cross section level, the relation between $\mathbf{U}_s$ and the generalized forces $\mathbf{F}_s = \{N, M_y, M_z, M_x\}^T$ is given by

$$\mathbf{K}_s \cdot \mathbf{U}_s = \mathbf{F}_s \tag{4.5}$$

where $\mathbf{K}_s$ is the rigidity matrix over the section S. The generalized forces N, M_y, M_z, M_x are integrals of the stresses over the cross section. In Code_Aster, the section is discretized in n fibers, so the integrals can be approximated as sums over the n fibers, since on each fiber the stresses are constant. The vector $\mathbf{F}_s$ does not include torsion, since is assumed to remain linear elastic in torsion and uncoupled from the flexural and axial response. Finally, from Equation 4.4 the resolution is performed in order to find a solution to the classic linear system at each integration point of the element (nodes):

$$\mathbf{K} \cdot \mathbf{U} = \mathbf{F} \tag{4.6}$$

where **F** are the nodal forces and the matrix **K** is the rigidity of the element, computed as the integral over the length of the beam.

4.3.1.2 Structural model parameters

More specifically, the multifiber model of Chatzigogos and Meza Fajardo (2020); Perraud et al. (2022) used in this work represents a uniform bridge pier of height H_p = 21 m, with a cross section of circular form of diameter $D_p = 3$ m (as observed in Figure 4.5). The cross section is characterized by a homogeneous material, and, at each fiber, the nonlinear constitutive law of Figure 4.6a is implemented. This bi-linear law is defined by the initial elastic Young modulus $E_p = 30$ GPa, a yield stress $f_y = 16.22$ MPa, and a post-yielding Young Modulus $E'_p = \alpha_p E_p$ with $\alpha_p = 3 \times 10^{-14}$, which defines practically an elastoplatic perfect behavior. An example of the nonlinearities generated by this behavior on the multifiber model is represented in the bending moment M versus curvature ϕ in Figure 4.6b. Additional parameters of the bridge pylon are

described in Table 4.1. With this characteristics the structural fundamental period (T_{st}) is equal to 1.21 s.

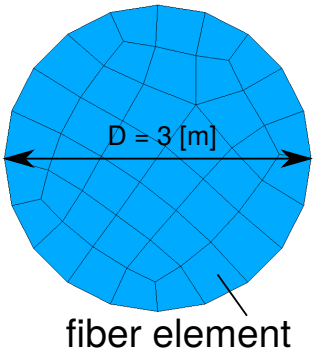

Figure 4.5: Fiber beam section, where each element (fiber) has a nonlinear behavior.

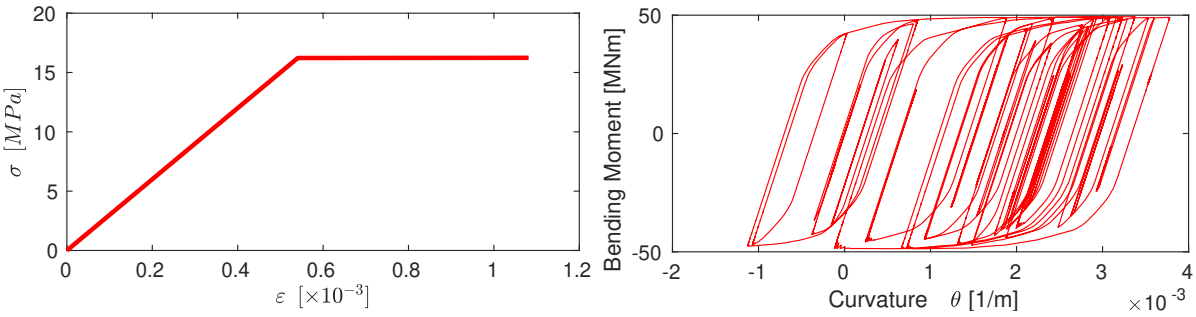

Figure 4.6: (a) Bilinear behavior adopted at each fiber of the beam structure and their impact into the (b) Moment-curvature curve at the bottom of the structure.

Table 4.1: Superstructure input parameters. From Perraud et al. (2022).

Parameter	Symbol	Value
Column height [m]	H_p	21.0
Diameter [m]	D_p	3.0
Mass density [kg/m^3]	ρ_p	2500
Mass of the deck [10^3 kg]	m_d	1200
Mass of inertia of the deck [10^3 kg m^2]	J_d	23400
Young Modulus of the pier [GPa]	E_p	30
Poisson' ratio of the pier [1]	ν_p	0.2
Hysteretic damping ratio [%]	ξ_p	5
Yield stress of pier fibers [MPa]	f_y	16.22
Hardening parameter of pier fibers [1]	α_p	3×10^{-14}
Fundamental period [s]	T_{st}	1.206

The superstructure is completed by nodal masses (m_d for the translational component and J_d for the rotational component) at the top of the beam representing the deck section of the

bridge. The masses are connected to the beam with a spring-dashpot element to represent potential bearing or deck isolation with values of rigidity $\mathbf{K}_d = \infty$ and damping $\mathbf{C}_d = \infty$.

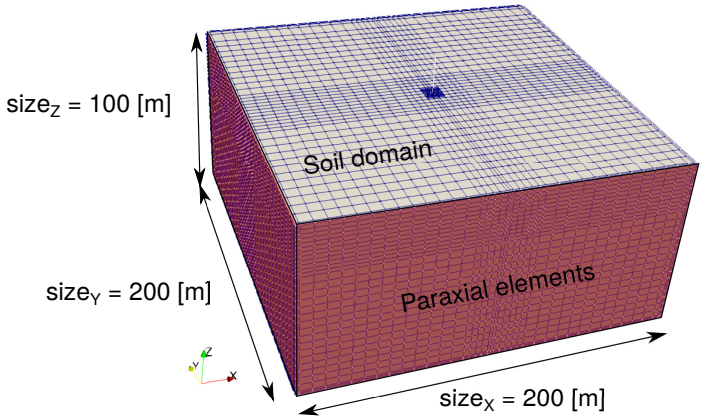

Figure 4.7: Mesh of the soil domain in Code_Aster.

Finally, in the original work of Chatzigogos and Meza Fajardo (2020), the foundation-soil domain is modeled by a macroelement. In this work, conversely, the soil portion is modeled with 3D volumetric elements in the FE code in order to have a direct coupling of soil and structure. The dimensions (x, y, z) of the soil domain are 200 m $\times 200$ m $\times 100$ m (Figure 4.7). The model parameters associated to the soil domain are described in Table 4.2.

Table 4.2: Model parameters of the soil in Code_Aster.

Parameter	Value
V_s^{min} [m/s]	900.0
Max. element size [m]	$6.25 \times 6.25 \times 4.5$
Number of elements [1]	49200
Targeted frequency [Hz]	14.5

The structure is positioned at the center of the soil domain. The connection of the superstructure with the soil portion is generated by a rigid square foundation modeled with 2D plate elements, using the same characteristics as in Chatzigogos and Meza Fajardo (2020). The foundation is then described by a density $\rho_f = 2500$ kg/m^3, height $H_f = 2$ m and width $B = 10$ m. For the sake of simplicity, this foundation is fully attached to the ground, which allows all ground displacements to be transmitted to the superstructure.

4.4 Plane wave dynamic response of the structure

The objective of this section is to conduct a nonlinear seismic analysis of the structure with a traditional strategy (Saez et al., 2008, 2011; Karatzetzou and Pitilakis, 2018a,b; de Silva, 2020, among

others), for both the assessment of seismic structural vulnerability and to define the most appropriate damage index allowing to characterize the potential structural failure for each structural element (local) and for the entire structure (global) (Cosenza and Manfredi, 2000).

In this section, the structure is excited with a large number of input ground motions to conduct the damage analysis following the Performance-Based Earthquake Engineering (PBEE) methodology. A first assessment of the dynamic response is performed to evaluate the effect of the inelastic soil-structure interaction (SSI) and the effect of the input directivity on the structural response. The comparative dynamic analysis is solved in two models as proposed by Saez et al. (2011):

1. The structure is subjected to a ground motion imposed at the base considering a rigid base (RB) condition.

2. A complete FEM model including the structure and the soil foundation is generated (Figure 4.7), and the ground motion is imposed at the base of the soil model as a vertically incident plane wave. Thus, the soil-structure interaction (SSI) effect is considered. In this case, the soil column has absorbing boundaries.

4.4.1 Input ground motion

A high-intensity earthquake database is specially selected to induce a wide range of nonlinear structural behavior. A total of 192 unscaled time-histories in two horizontal directions (a total of 384 signals) were chosen. The ground motion characteristics are displayed in terms of the intensity measures (IM) distribution (e.g. PGA, PSA, T_{VA} and I_a), presented in Figure 4.8. The parameter T_{VA} is the period of a equivalent harmonic wave representing the earthquake loading, given by

$$T_{VA} = \alpha \frac{PGV}{PGA} \tag{4.7}$$

with $\alpha = 4.89$ (Kawase, 2011; Lopez-Caballero and Khalil, 2018).

First, and remembering that in the complete study (i.e. from the source to the structure including the basin effects), the structural problem is three dimensional, the 384 signals are imposed in only one direction (1DIR) on the horizontal component x to evaluate the structural response when the shaking is applied in its principal directions. In addition, as observed in Chapter 2, in the problem of basin effects, the fault mechanism and the tridimensional geometry induce ground shaking in multiple horizontal and vertical directions, defined as directionality (Boore et al., 2006; Boore, 2010; Laouami et al., 2006; Shahi and Baker, 2014; Baron et al., 2022, among others). For this reason, it is important to assess the directionality effect of the excitation on the structure's response. Thus, a second charge scenario is performed by imposing the 192 input motion in the two x and y directions simultaneously (2DIR).

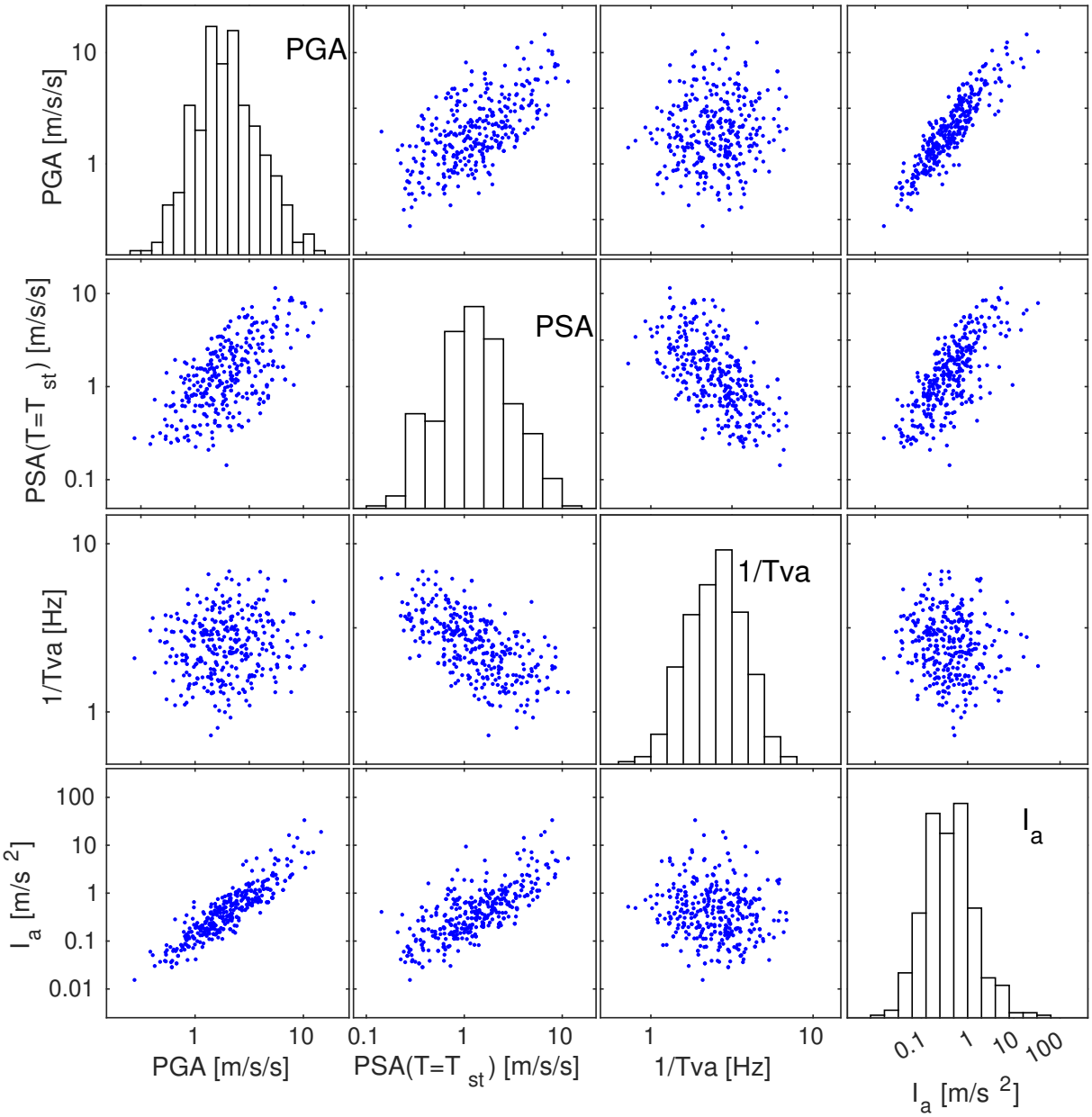

Figure 4.8: IM distribution of selected records for plane wave analysis.

4.4.2 Damage index and structural mechanical behavior

In the framework of performance-based design, one of the key points is to define the most appropriate damage index, able to provide a reliable description of the structural damage level which could be linked to an engineering demand parameter (EDP) for structural vulnerability assessment (Cosenza and Manfredi, 2000; Colombo and Negro, 2005; Mitropoulou et al., 2018, among others).

According to Cosenza and Manfredi (2000); Colombo and Negro (2005) among others, a damage index relates a given damage situation (i.e. loss of the capacity of a structural member) resulting from complex non-linear deformation or energy dissipation, to a unique point in the

monotonic skeleton curve. It could be defined either for each structural element (local) or related to the entire structure (global) (Cosenza and Manfredi, 2000). For instance, Ghobarah et al. (1999); Park and Ang (1985) defined different damage indicators (DI), differentiated in two types: *based on strength* or *based on response*. The most used indicators can be summarized as follows (Baker et al., 2021),

- ductility (Krawinkler et al., 2003; Farrow and Kurama, 2003),
- eigen-frequency drop-off (Stocchi and Richard, 2019) and
- plastic energy (Ke et al., 2017).

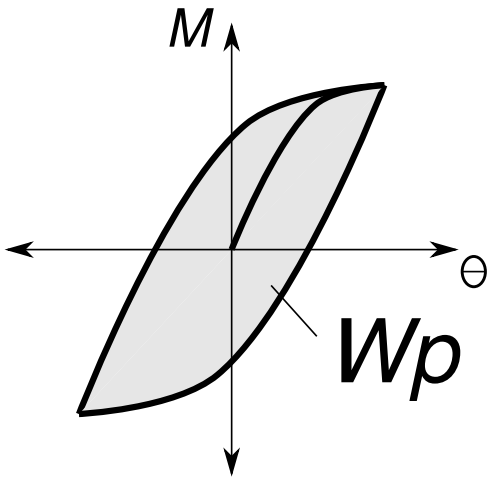

Figure 4.9: Representation of the plastic energy dissipation, W_p.

For the sake of brevity, in this case the structural response is evaluated by quantifying a inelastic seismic demand index, namely the plastic energy dissipation (W_P). This parameter represents the hysteretic nonlinear behavior and is defined as the cumulative energy under the moment (M) -curvature (ϕ) curve (Figure 4.9) at the base of the structure, given by the expression

$$W_p = \int_S M\phi dS \tag{4.8}$$

On the other hand, typical demand parameters (EDP) of bridge columns are the lateral drift and the maximum top displacement (u_{top}) (Krawinkler et al., 2003; Lehman et al., 2004; Miranda and Akkar, 2006; Hatzigeorgiou and Beskos, 2009; Yang et al., 2010; Wang et al., 2014; Fox et al., 2015, among others). In behalf of brevity only, the demand of the structure is evaluated with the u_{top} as EDP.

As an example, one signal time history is selected to plot in the Figure 4.10 the evolution of displacements at the top u_{top} versus the hysteretic loops in the moment-curvature curve that imply the increasing of the plastic energy at the base W_p. According to this Figure, it is clear that the nonlinear behavior starts only when the u_{top} passes a certain threshold at the beginning of

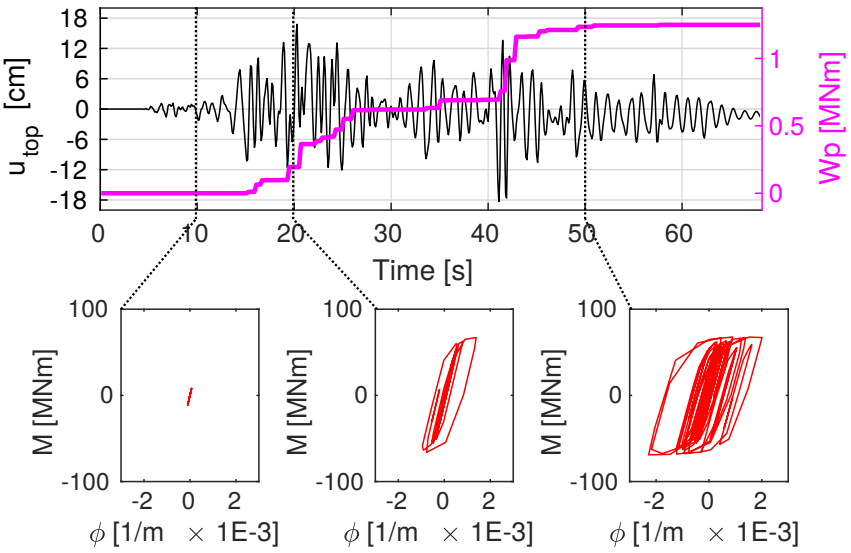

Figure 4.10: Evolution in time of the top deck displacement u_{top} versus the nonlinear behavior quantified by the W_p for one specified ground motion.

the shaking. Then, W_p is constant until a second strong shaking occurs which results in a second large increasing of W_p at $t = 40$ s. Therefore, it is possible to visually conclude that a link exist between the damage indicator (DI) and the deck horizontal displacements (EDP) due to the pier bending, the same behavior as observed by Perraud et al. (2022).

The relation between the structural response in terms u_{top} and W_p can be analyzed with the results of the whole database under different hypotheses on the modeling. The Figure 4.11 shows this relation with the SSI or RB considerations, and also by injecting the seismic shaking in one (1DIR) or two (2DIR) directions for all the dataset. To account for the directionality of the ground motions, the top displacement is computed as the square root of the sum of squares (SRSS) of the two horizontal components as

$$u_{top}^{SRSS} = \sqrt{(u_{top,X})^2 + (u_{top,Y})^2} \tag{4.9}$$

and the plastic energy dissipation is computed as the sum over the two horizontal directions as

$$W_{p*} = W_{px} + W_{py} \tag{4.10}$$

Figure 4.11 demonstrates that imposing the load in one or two directions change slightly the damage response of the structure. A small difference in the elastic part ($u_{top} < 7$ cm) is observed between the $1DIR$ and $2DIR$ cases, associated possibly to a small torsion produced when the loading is applied in two directions.

The limit damage states (performance thresholds) are also represented in this Figure. They were adopted from those proposed by Penna et al. (2004) and are summarized in Table 4.3. The ultimate displacement of bridge pier (Δ_u) is defined at 70 cm.

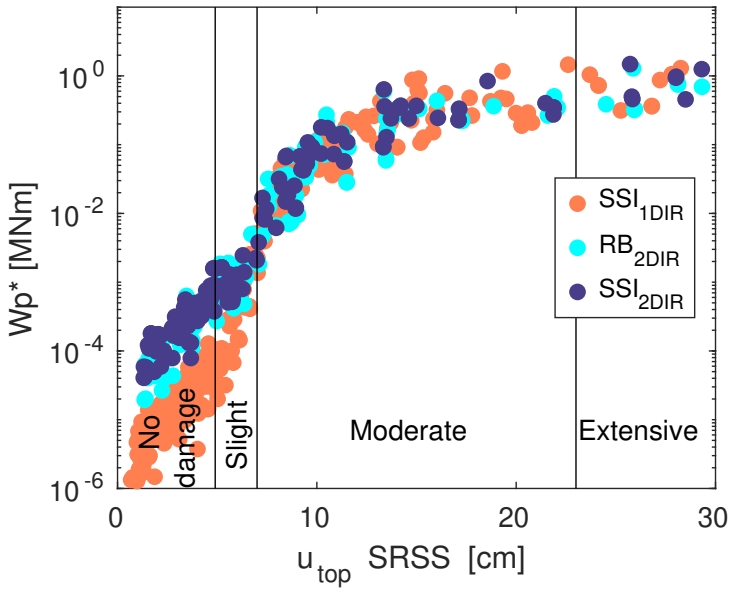

Figure 4.11: Link between the structural response (EDP and DI), for different traditional model hypotheses, including soil structure interaction and directionality of the ground motions.

Table 4.3: Displacement limit states adopted from Penna et al. (2004)

Damage state	Displacement threshold	Displacement value u_{top} [cm]
Slight	$0.7 \cdot \Delta_y$	4.9
Moderate	Δ_y	7.0
Extensive	$\Delta_y + 0.25 \cdot (\Delta_u - \Delta_y)$	22.75

The second level of the physics-based desing, i.e, the structural analysis, conduce to evaluate the structural response (with an Engineering Demand Parameter, EDP) with respect to a ground motion characteristic (Stewart et al., 2002; Porter, 2003; Baker et al., 2021, among others). As the ground motion is only accounted by the Intensity Measures (IM), they must be well chosen in order to correctly relate EDP and IM (Baker, 2007a). According to Tothong and Luco (2007), the IMs should be (i) efficient, in order to correlate strongly with multiple measures of the structural response, and (ii) sufficient, in order to provide a good prediction on the structural response with a reduced variability. Therefore, the efficiency and sufficiency of different IMs for the selected structure is assessed to choose a single IM adapted for the analysis. As for the IM, different measures can be compared, such as peak ground acceleration (PGA), peak ground velocity (PGV), peak ground displacement (PGD), Arias Intensity (I_a) and Cumulative Velocity (CAV), and the pseudo spectral response in acceleration and displacement (PSa and PSd, respectively). The spectral response are evaluated in the fundamental frequency of the structure. Because of lack of space, only four IMs have been contrasted in Figure 4.12, for the loading case in 1 direction.

Thus, the results are depicted in Figure 4.12, from where it is possible to clearly visualize

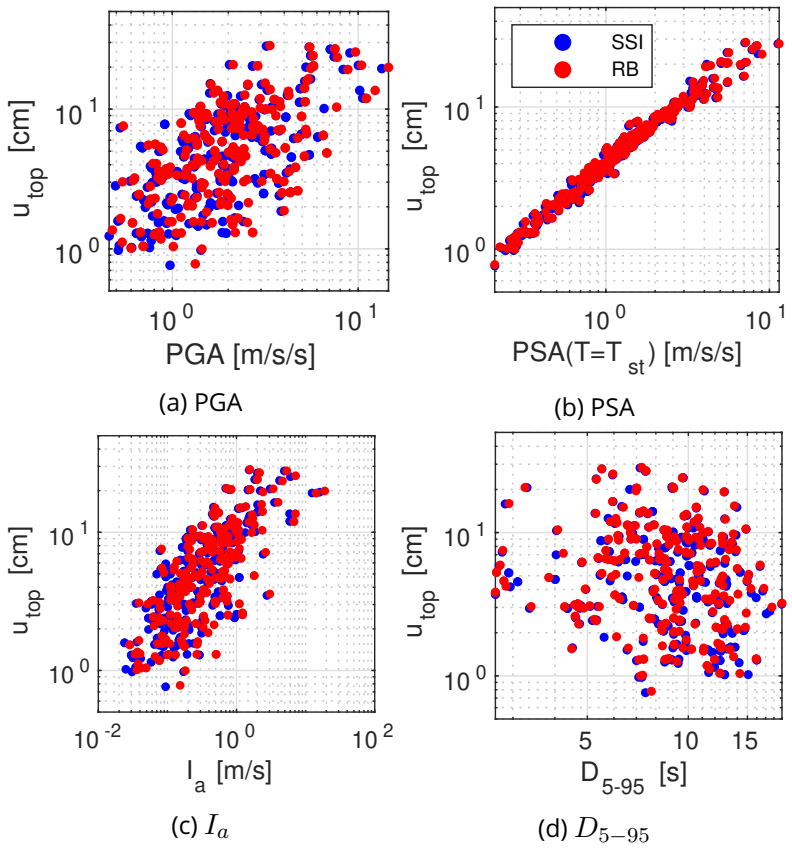

(a) PGA (b) PSA

(c) I_a (d) D_{5-95}

Figure 4.12: Scatter plot of IMs and EDP (u_{top}) for the case of loading in one direction (RB_{1DIR} and SSI_{1DIR}).

that structural response under dynamic loads is better related to the spectral response (PSA) rather than any other IM, since the variability or dispersion of the seleted EDP is the lowest. Additionally, some other trends are observed, such as the no evident link between the PGA and D_{5-95} and the structural damage u_{top}. The IMs in the SSI case have been computed from the signals at the base of the foundation. The consideration of the soil-structure interaction does not seems to influence the response. This could be due to the high shear wave velocity of the sediment layer ($V_s = 900$ m/s) which is determinant into the soil-structure response (e.g., NEHRP Consultants Joint Venture, 2012). Accordingly, the PSA is the IM used in the following sections to relate the basin effects to the structural performance, which is also the measure typically used in the computation of structural fragility (de Silva, 2020). The unique horizontal $PSA(T = T_{st})$ is defined as the geometric mean (GM) of the two horizontal components.

Moreover, a simple relationship can be obtained to evaluate the dependance of the $PSA(T = T_{st})GM$ as IM versus the $u_{top}SRSS$ as EDP. According to several authors (Cornell et al., 2002; Ghosh et al., 2015; de Silva, 2020, among others), the EDP-IM relationship can be expressed by a equation of the type

$$EDP = a \cdot IM^b + \epsilon \tag{4.11}$$

where a and b are calibrated by a linear regression in a log-log plot (as in Figure 4.13), and ϵ is the

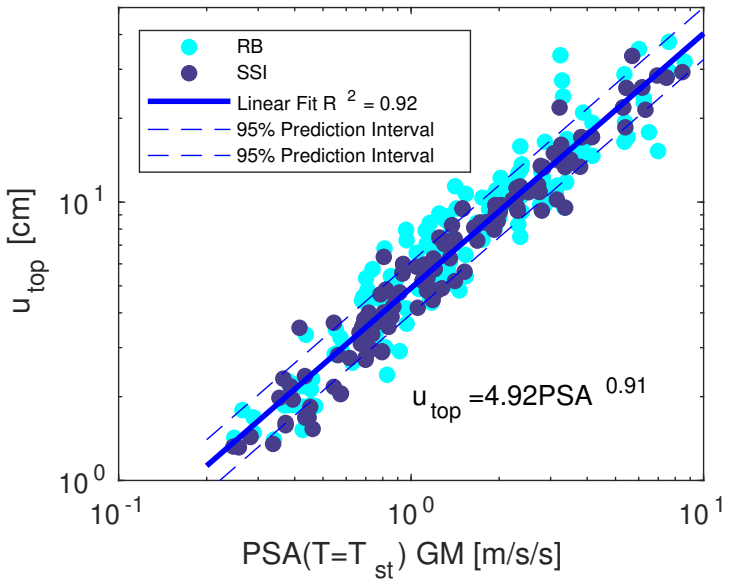

Figure 4.13: $PSA^{GM}(T = T_{st})$ - u_{top}^{SRSS} obtained relationship for the loading in two directions (RB and SSI cases). A linear regression model have been fitted to the data.

error associated. A simple linear fit using all the results of the response in two directions (RB_{2DIR} and SSI_{2DIR}), allow to obtain the values $a = 4.92$, $b = 0.91$ with a coefficient $R^2 = 0.92$.

4.4.3 Non-linear analysis and results

So as to define the structural reference case, the dynamic responses obtained by the bridge pylon model in fixed base condition are analyzed. With regard to seismic demand evaluation on the structure, the maximum top displacement (u_{top}) and its corresponding base shear force (V_{base}) observed during the dynamic computation are presented in Figure 4.14. This curve corresponds to the dynamic capacity curve (Push-over) of the bridge pylon.

According to this Figure, it is noted that a structural non-linear behavior appears when $u_{top} > 7$ cm, thus, this is the displacement corresponding to the yield capacity of the bridge pylon (Δ_y, Table 4.3). The maximum drift is equal to 3%. A problem that can appear during the computation of the structure's response is that some earthquake time histories produce a displacement larger than Δ_u. In these cases, the validity of the non-linear model is not guaranteed for large deformation levels. Thus, in this study, the displacements greater than Δ_u are considered as the collapse apparition in the structure.

The bridge pylon's response in terms of top displacement has been analyzed, so as to assess the capability of the multifiber beam's model to vary the rigidity of the building beyond its yield capacity. The acceleration time histories obtained at the top of the pylon for one case with u_{top} greater than Δ_y (i.e. yield behavior) is studied using wavelet transform with a Morlet function (Torrence and Compo, 1998). Figure 4.15 displays the normalized energy spectral density as a function of time of the wavelet transform of top acceleration for a case where u_{top} = 18 cm. As expected, it is observed before the main shock the structure's response is in the first mode

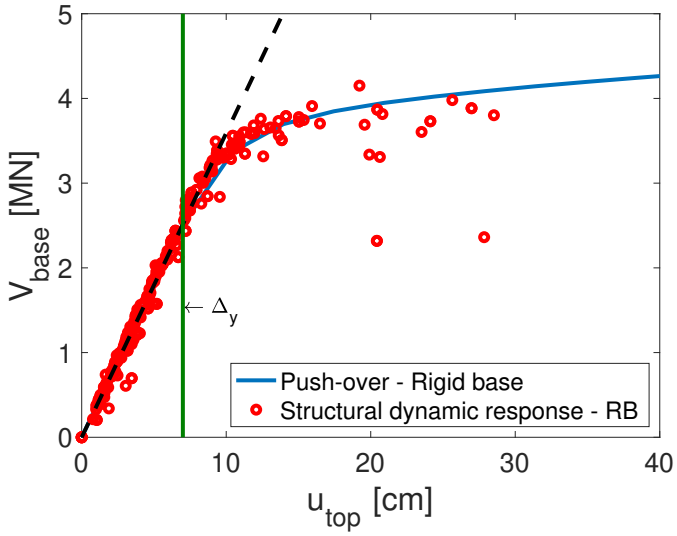

Figure 4.14: Structural dynamic response obtained for the bridge pylon at fixed base condition.

frequency, $f_{st} = 0.82$ Hz (dashed red line). Then, during the main shock phase of the seismic loading, the structure's response drops from f_{st} to $f_2 = 0.76$ Hz showing the apparition of a non-linear behavior and a stiffness degradation. It is followed by an apparent recovery at the end of the loading showing that the spectral ratio of the pre-event noise is similar to the spectral ratio of the coda-window (see the dashed red line after 45 s).

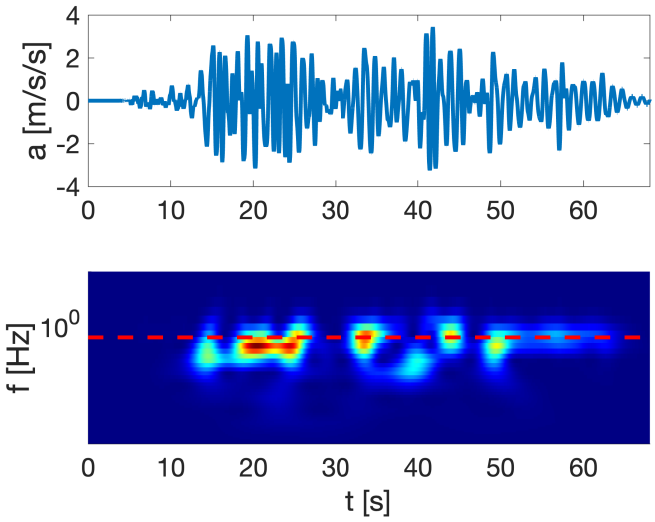

Figure 4.15: Time-frequency analysis (wavelet transform) of top bridge pylon's acceleration time histories.

Finally, according to Ruiz and Saragoni (2009) among others, both natural frequency and damping of the structure could be estimated from an acceleration time histories using the auto-correlation function or autocorrelogram technique. The shape of the autocorrelogram could be

assimilate to the response of single degree-of-freedom model to free oscillation :

$$y(t) \quad = \quad \exp(-\beta \cdot (2 \cdot \pi \cdot t \cdot f_{st})) \cdot \cos(2 \cdot \pi \cdot t \cdot f_{st}) \tag{4.12}$$

where f_{st} is the natural frequency and β is the damping ratio. Now, using the autocorrelation function of the three acceleration time histories (EQ01, EQ03 and EQ70), it is noted that due to induced damage, the structural damping (β) shifts from 0.5% in the elastic case (i.e. $u_{top} < \Delta_y$ in earthquake signal EQ01) to $\approx 5\%$ for the case when $u_{top} > \Delta_y$ in EQ70 (Figure 4.16).

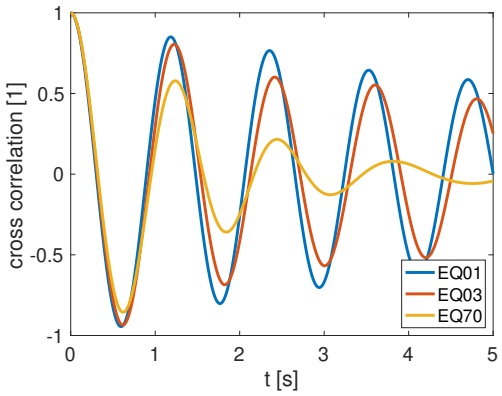

Figure 4.16: Normalized autocorrelograms of three top pylon's acceleration time histories.

4.5 Basin effects on the induced structural damage

In order to evaluate the damage due to basin effects, the auxiliary domain of the DRM methodology is inserted in a basin. The basin corresponds to a canonical truncated cone basin, with homogeneous properties, which has been the object of study in Chapter 2, denominated TC (truncated cone) with a shear wave velocity of the sediments of $V_s = 900$ m/s. The effect of the spatial variability on the structural response is evaluated by inserting the structure in five different positions of the basin, from DRM_1, at the basin center to DRM_5 at the basin edge (Figure 4.17), distributed along the X axis. In this section, the source effects (type and point source-depth) are partially investigated with the comparison of a vertically incident plane wave (PW) to more realistic point sources. The complete input source description is available in Section 2.4.2 of Chapter 2. The computational resources are summarized in Table 4.4.

In the following, the variability of the DRM location (i.e, spatial variability) and of the source depth and type (i.e, source variability) are compared. In order to find the coupled basin effects on the seismic hazard and on the structural demand, first, the ground motion variability is computed in terms of the selected IM (PSA), the aggravation factor, the basin generated surface waves and the rotational components. Second, the variability is assessed in the structural seismic demand. Finally, the basin effects on the seismic hazard and demand are discussed.

It is common knowledge that the level of the nonlinear behavior of the structure is related directly to the amplitudes of the ground motions. Therefore, in order to have a comparable am-

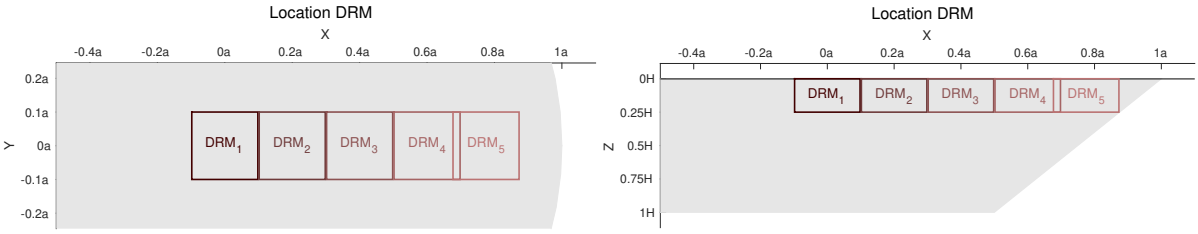

(a) XY (b) XZ

Figure 4.17: Location of the auxiliar domains DRM_1, at the center of the basin, to DRM_5, at the eastern edge of the basin, to evaluate the spatial variability in the (a) XY (b) XZ planes.

Table 4.4: Summary of simulations performed and computational resources used for the structural analysis in Code_Aster.

Parameter	Value
Number of positions evaluated	5
Number of sources	8
Total DRM simulations	80
Delta time [s]	0.001
Simulation time [s]	15
Wall clock time per source (wave prop. SEM3D) [hours]	3
Wall clock time per simulation (transfer of dynamic input) [hours]	4
Wall clock time per simulation (time domain analysis) [hours]	16

plitude in the results from every source, a reference model without the basin (only the bedrock) is simulated, and the ground motion at the position [0,0,0] m is obtained. A normalizing factor F_{source} is computed for every source, such that the horizontal peak ground displacement, defined as the square root of the sum of squares (SRSS) of the two horizontal seismic components PGD_H, given by

$$PGD_H = \sqrt{PGD_X^2 + PGD_Y^2} \tag{4.13}$$

is equal to a reference value of $PGD_{H,Rock} = 3$ cm in this reference model. Then, the factor F_{source} multiplies the input forces and displacements when applied to the reduced domain computation in Code_Aster. Since most the results are presented in terms of aggravation factors (3D case divided by 2D case), the normalizing factor F_{source} is meaningful only when the absolute values are presented.

4.5.1 Ground motion variability

Inside the basin, the ground motion response at a specific location will be a combination of source and basin geometry effects. For that reason, the two phenomena are separated by observing the variability of the resulting IM in terms of the source depth (Figures 4.18a and 4.18c) and of the location of the auxiliar domain inside the basin (Figures 4.18b and 4.18d). The results of this section are focused to the specific location to where the structure is emplaced, but the full

interpretation of the data, please refer to Chapter 2.

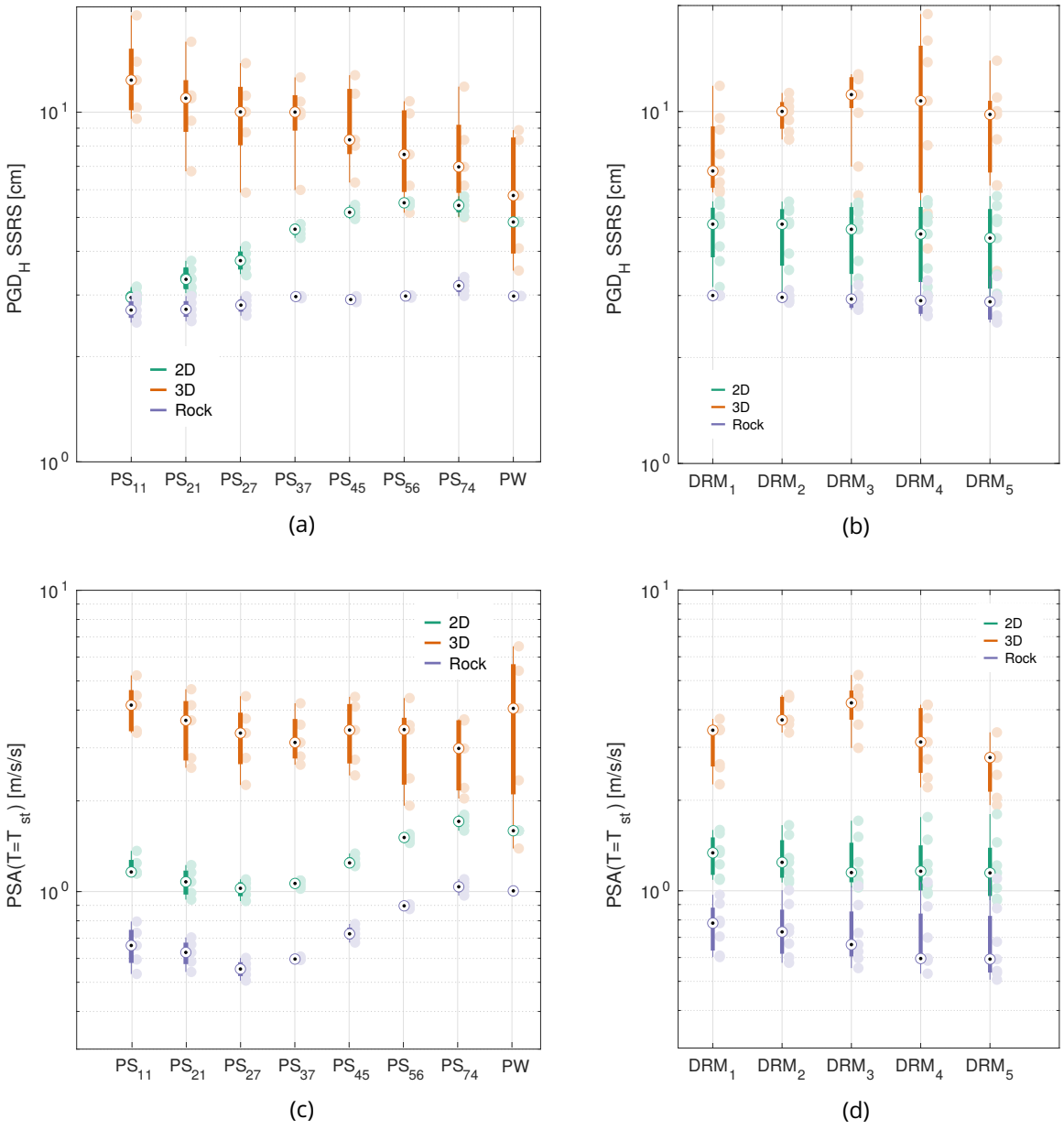

Figure 4.18: Variability of the intensity measures (a and b) PGD_H SRSS and (c and d) $PSA_H(T = T_{st})$ with source depth and basin location.

The colors of the scattered points refers to the three material cases: $2D$, corresponding to the infinetely layered model, $3D$, where the basin geometry has been added and $Rock$, where only the halfspace is modelled. The selected IMs are the PGD_H and the geometric mean (GM) of the pseudo spectral acceleration PSA_H,

$$PSA_H(T = T_{st}) = \sqrt{PSA_X \cdot PSA_Y} \tag{4.14}$$

evaluated at the period of the structure T_{st}. In the Figures, basin and source effects are clearly recognized comparing the three material models. More specifically, for the $Rock$ and the layered model $2D$, only the source effects appears. In these models, most of the variability in the IMs comes from the selected normalization and the source position. Higher IMs are obtained for deeper sources in the layered model ($2D$). The amplification factor AF_{2D} computed with the median values is defined as

$$AF_{2D} = \frac{IM_{2D}}{IM_{Rock}} \tag{4.15}$$

and ranges from 1 up to values of 2 for both IMs.

When the $3D$ model is adopted, both source- and geometry effects are present, except for the vertically incident plane wave (PW), affected only by the basin geometry. The PW is the source showing the higher variability of the PSA_H with DRM location as observed in Figure 4.18c, with PSA_H values ranging from 1.4 up to 6.5 m/s^2. When the input is a DC point source, while the basin geometry undoubtfully amplifies the PSA, the DRM location is less important than in the PW case. Regarding the different DRM locations in the basin (Figures 4.18b and 4.18d), most of the source depth variability is observed for the DRM_1, at the center, and DRM_4 closer to the basin edges. The amplification factor of the $3D$ model, defined analogously as in Equation 4.15, is given by

$$AF_{3D} = \frac{IM_{3D}}{IM_{Rock}} \tag{4.16}$$

The AF_{3D} reaches values up to 5.9 and it is higher for the shallower sources and the DRM_3. The average AFs, dependent of the DRM position are presented in Table 4.5. More variability is observed for the 3D case.

Table 4.5: Average values of the amplification and aggravation factors.

DRM Location	AF_{1D}	AF_{3D}	AGF
DRM_1	1.714 ± 0.076	4.318 ± 0.915	2.539 ± 0.654
DRM_2	1.716 ± 0.085	5.407 ± 0.807	3.147 ± 0.430
DRM_3	1.715 ± 0.082	5.879 ± 2.024	3.394 ± 1.066
DRM_4	1.737 ± 0.117	4.675 ± 2.207	2.647 ± 1.158
DRM_5	1.786 ± 0.180	4.121 ± 1.800	2.260 ± 0.871
average	1.730 ± 0.109	4.819 ± 1.751	2.767 ± 0.958

4.5.2 Comparative ground motion response: 2D vs 3D

Figure 4.19 compares the ground motion intensity with the $PSA(T = T_{st})$ observed in the layered model (2D) versus the basin model (3D) in the five positions inside the basin (DRM_1 to DRM_5), for the two horizontal components of motion (X and Y) independently. In the PW the ground motion is polarized only in the X component, while the point sources impose a horizontal motion in both X and Y components. Thus, this Figure assesses the basin and source effects on the directivity of the IMs.

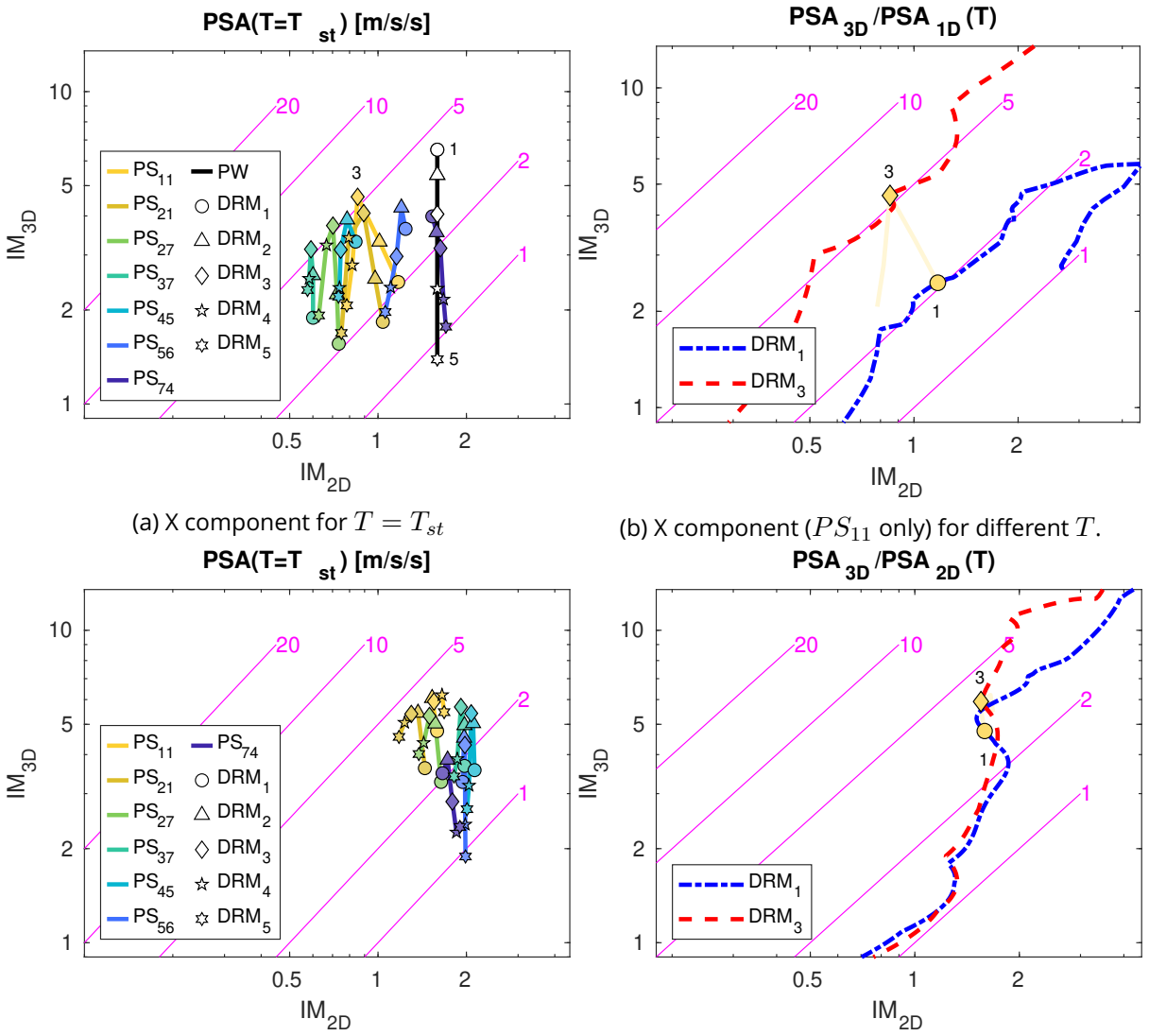

(a) X component for $T = T_{st}$

(b) X component (PS_{11} only) for different T.

(c) Y component for $T = T_{st}$

(d) Y component (PS_{11} only) for different T.

Figure 4.19: Comparison of the ground motion parameter $PSa(T)$ in the 2D model (horizontal axis) versus 3D basin model (vertical axis). (a,c) show the results evaluated at the period of the structure $T = T_{st}$ for 5 positions of the structure (DRM_{1-5}) and sources (shallow PS_{11} to deep PS_{74} and plane PW). (b,d) show the $PSa(T)$ for the DRM_1 (center of the basin) and DRM_3 for the source PS_{11}, where the points are a specific result of the continuous line of $PSa_{3D}/PSa_{2D}(T)$ when $T = T_{st}$. The diagonal lines represent the AGF values computed as the ratio 3D/2D.

The diagonal lines on each plot represent the AGF, computed as the ratio given by

$$AGF = \frac{AF_{3D}}{AF_{2D}} = \frac{IM_{3D}}{IM_{2D}} \tag{4.17}$$

Figures 4.19b and 4.19d on the right pretend to show the frequency-dependent ground motion response, which will have different amplification values on the 2D and 3D cases for each structural period T. The resulting IM on the left are only a specific evaluation for the studied structure.

The AGFs clearly show differences in the two components of motions, explained by the position of the DRM (all aligned along the X-axis). In the X component, the source effects are observed mainly in the IM of the 2D model, while the IMs in the 3D model are similar for all the point sources. Since the PSA in the 2D model reaches higher values for the deeper sources (PS_{11} and PS_{21}), the AGF values are minimized. A value of AGF = 5 is the maximum obtained to the X component in the DRM_3. Conversely, the AGF in the Y components is maximum for the shallow sources (PS_{11} and PS_{21}), explained by the increase of IM_{3D} combined with a slight decrease of the IM_{2D}. From the results, it can be drawn that the source depth affects the AGF due to a change in the response of the 3D and 2D models simultaneously and that shallow sources (PS_{11} and PS_{45}) impact the most the response (which have been previously related to surface wave generation, see Figures 2.21 and 2.22).

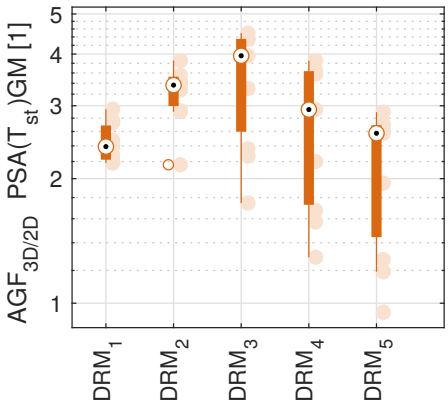

Figure 4.20: Spatial variability of the aggravation factor $AGF\,\{IM = PSA_H\}$.

The spatial variability of the AGFs computed with the PSA_H can be summarized by Figure 4.20 and third colum of Table 4.5. Within the literature regarding the aggravation factors, Stambouli et al. (2018) compared the spatial effects on the aggravation factors by defining zones in the basin. Largest AGFs were obtained for embankment ratios $E_r = Z_{max}/Width > 0.08$, to where the studied basin here has a $E_r = 400/2000 = 0.2$, and close to the central region and the near-edge region. In this case, the spatial variability observed in this case behaves as expected, since the higher amplitudes are located in the DRM_3, where a high concentration of energy due to surface waves interference coming from the basin edge (Zhu et al., 2020).

4.5.3 Non horizontal induced ground motion: surface waves and rotational components

Besides the amplification produced by the inclusion of the basin edge which is accounted in the AGFs, other types of shaking are present in the seismic wavefield: surface waves and rotational components. The surface waves are identified with the normalized inner product (NIP, Meza-Fajardo et al., 2015) and the maximum horizontal displacement amplitude is computed from the extracted time-signals. For the layered model (2D), the surface waves are formed due to the

non vertical incidence of the waves as, for instance, Love waves are generated by interference of SH waves within the sediment layer. However, while both Rayleigh and Love type waves are expected to be generated on the 2D and 3D models, in the latter the basin edge contributes to an additional wave generation (Drake, 1980).

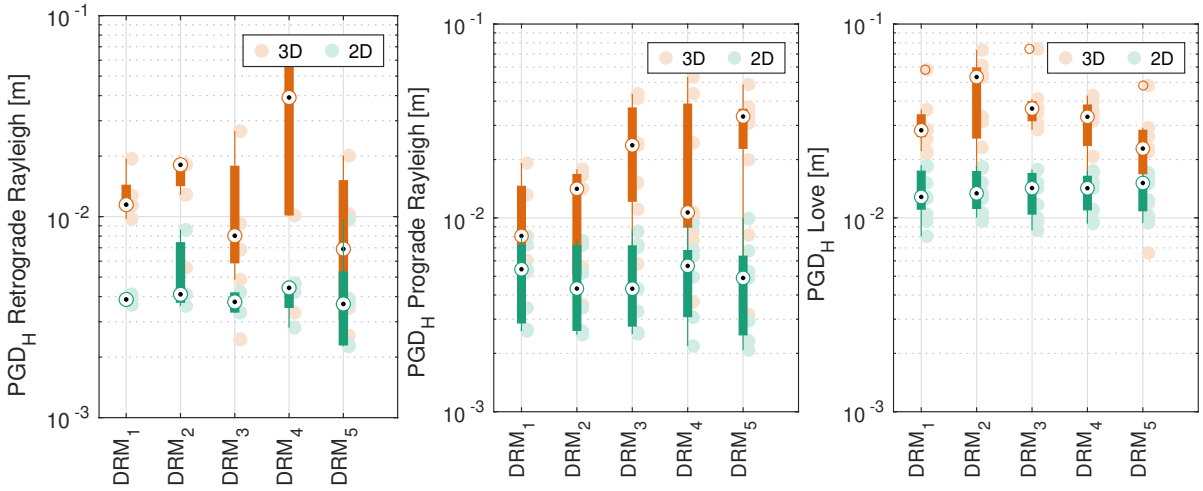

(a) Retrograde Rayleigh (b) Prograde Rayleigh (c) Love

Figure 4.21: Spatial variability of the extracted surface waves.

The spatial variability for the 5 DRM positions is plotted in Figure 4.21. The modification produced by the inclusion of the basin edge is observed as an amplification, more evident in the DRM_4 and DRM_5 (the closest to the basin edges) for the Rayleigh waves. In a relative narrow basin (such as the one in this study, defined with a high E_r value) it is expected that surface waves propagate all over the basin, including the central part (Bard and Bouchon, 1985; Zhu et al., 2020), which is observed only for the Love waves. An explanation for the higher amplitudes of Rayleigh waves observed near the edges can be the three-dimensionality of the problem (wave incidence plus geological geometry), which may play a role in the directionality of propagation of the waves.

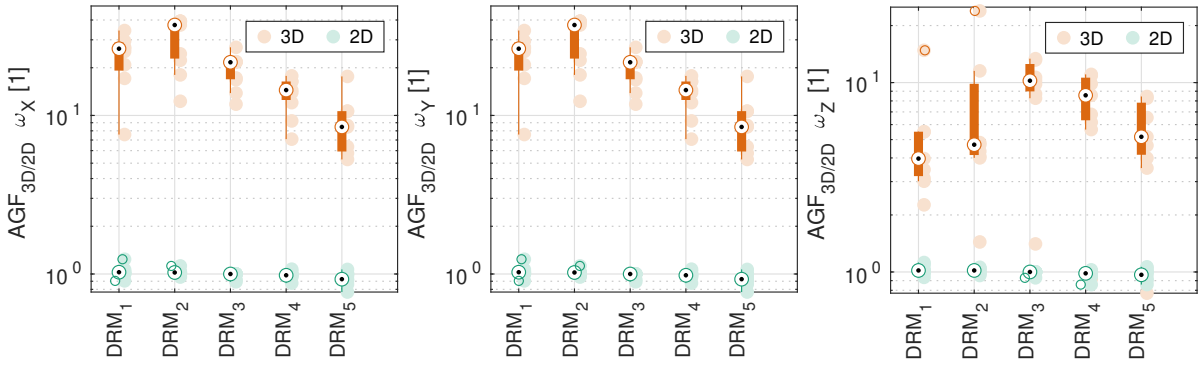

(a) Rocking X component (b) Rocking Y component (c) Torsion

Figure 4.22: Spatial variability of the aggravation factor of rotational displacement components.

Moreover, due to the local surface waves, some rotational components will be part of the ground motions and they could be perjudicial to buildings. In general, the rotation over the

horizontal axes, defined as *rocking*, is associated to Rayleigh waves, and the rotation over the vertical component, defined as *torsion*, to Love waves (Sbaa et al., 2017; Guéguen and Astorga, 2021; Perraud et al., 2022, among others). The AGFs of the rotational components are plotted in the Figure 4.22. The aggravation of the rocking component is comparable in the two horizontal directions. From a direct observation, these rotational components are not directly related to the surface waves. The discrepances could be due to other waves types present as complicated reflections and refractions taking place within the basin edges. This would explain also the high values of the AGF, up to 40 in the central part of the basin (DRM_1 and DRM_2).

4.5.4 Influence of the basin geometry and source position on the structural seismic demand

The effects of the basin geometry and source type is observed in the ground motion as an increase in the horizontal, rotational ground motions. In this section, the structure is positioned in the 2D model and 3D model. An important observation refers to the directivity effect due to the propagation path exerted by the point source (PS) compared to a vertically incident plane wave (PW).

As an example, Figure 4.23 compares the damage level with the normal stress (σ) at each Gauss point of the multifiber beam, placed in the basin model ($3D$) for the PW and the shallow PS_{11} input motions. An arbitrary time step is selected where high-nonlinear behavior ($\sigma > \sigma_y = 16.22$ MPa) is being induced in some parts of the model. As observed, the damage is concentrated on the base of the bridge pylon. The structure disturbed by the PW concentrate the damage mainly in the lateral edges of the pylon. In contrast, and due to the directionality of the ground motion, the damage in the bridge pylon during the dynamic analysis for the PS rotates along the edges with time. This is confirmed by the top deck displacement motion displayed in Figure 4.24. Because of this uneven directional damage, the following uses the geometric mean of the PSA_H (Equation 4.14) as intensity measure, the u_{top} SRSS (Equation 4.9) as engineering demand parameter (EDP) and the dissipation energy in both directions W_p* (Equation 4.10) as damage measure (DM).

The effect of the source depth and DRM location on the EDP and DM are plotted in Figures 4.25 and 4.26, respectively. Top deck displacements vary between 5 and 23 cm approximately, which induce slight to moderate damage according to the picked limit states. An interesting result comes from the fact that while maximum head displacements are obtained in the deeper sources for the layered (2D) model, higher values are expected for shallow sources in the basin (3D). The influence of the basin edges in the structural response is therefore exemplified by the increased u_{top} and W_{p*} due to the generation of surface waves in shallow sources.

From the point of view of ground motion characterization, the structural response usually depends on multiple IMs. Figure 4.27 relates different IM and the structural damage. The quantification of the basin geometry effect on the structural response can be contrasted in the 2D (Figure 4.27a) and 3D (Figure 4.27b) cases, observed simultaneously in the dissipated plastic energy W_p

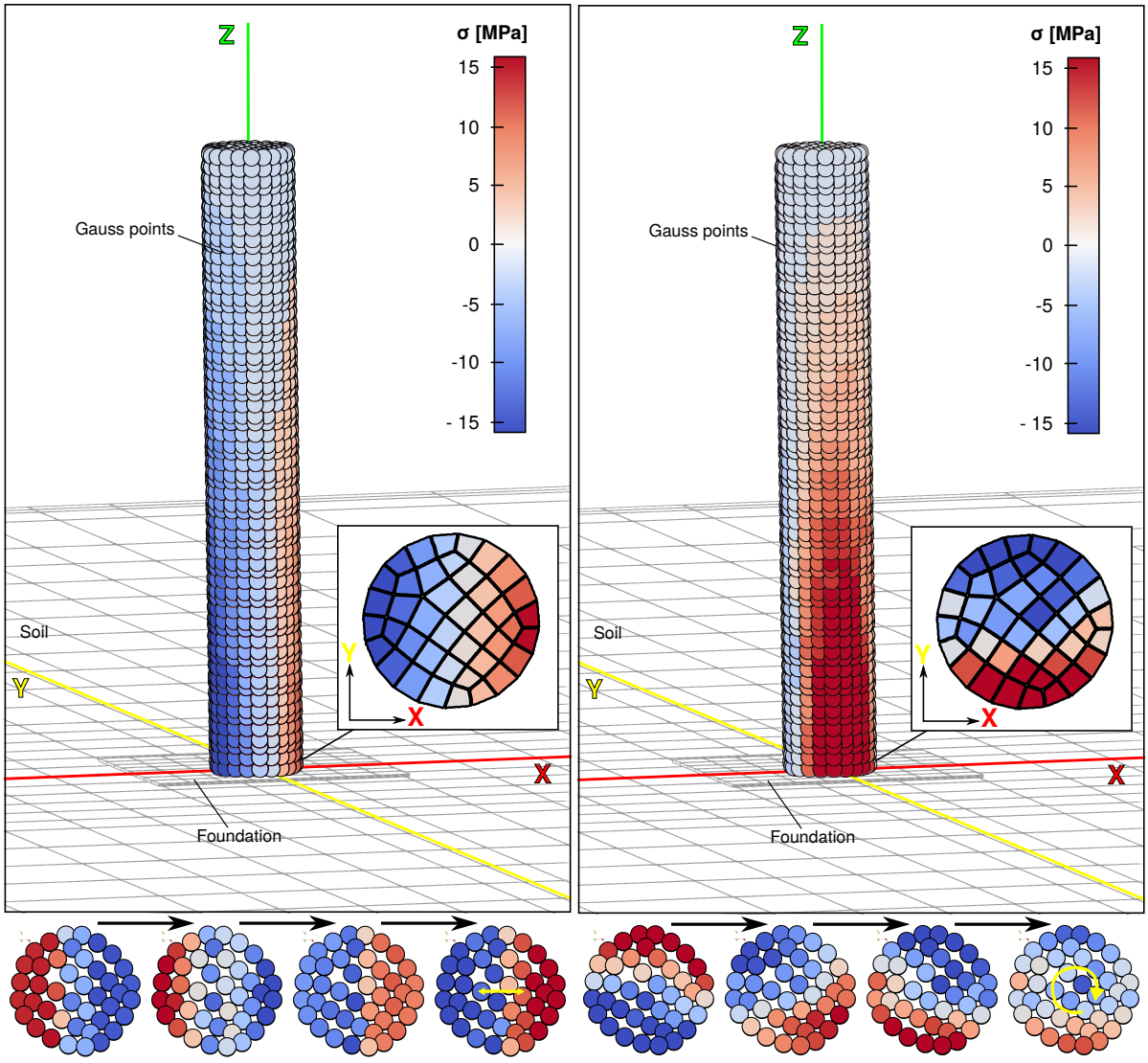

(a) PW, at the location of DRM_1

(b) PS_{11}, at the location of DRM_3

Figure 4.23: Structural damage observed at the Gauss point level for an arbitrary time step. The section shows the distribution of normal stress σ at each fiber on the bottom section of the bridge pylon.

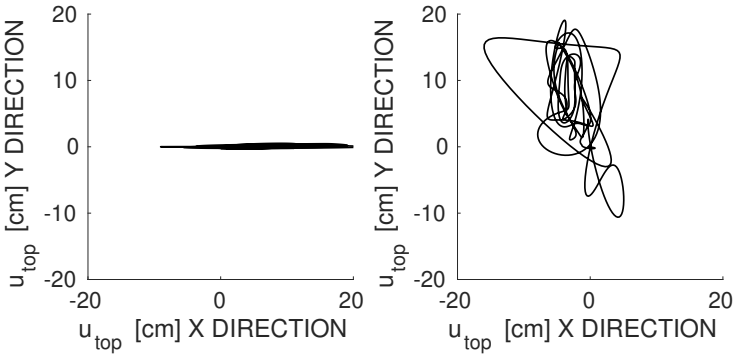

(a) PW, at the location of DRM_1 (b) PS_{11}, at the location of DRM_3

Figure 4.24: Top deck horizontal displacements u_{top} distribution with time for the same cases as Figure 4.23, showing directionality differences between the plane wave of vertical incidence and the double couple point sources.

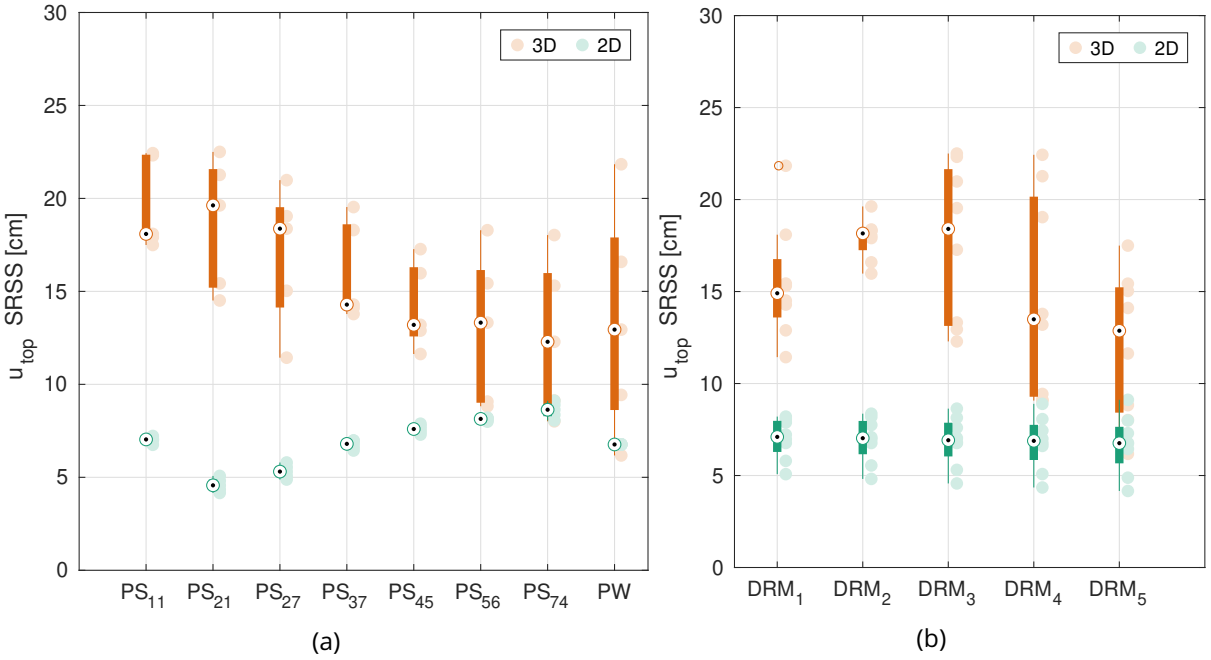

Figure 4.25: Variability of the engineering demand parameter u_{top} with source depth and basin location.

and of three IMs from recorded time signals at diferent positions: the *inverse* of the predominant harmonic period, 1/TVA, the maximum acceleration a_{max} (PGA) and iso-peak ground velocity PGV values (dashed diagonal lines). In this case, each component of the W_p is individually plotted. The 1/TVA slighty varies between 2 and 4 Hz, showing that the ground motion is dominated by similar harmonic components, caused by the source and basin settings (equal source time function, homogeneous sedimentary layer). However, the inclusion of the basin border increases both the PGA and PGV, with the corresponding observed structural damage W_p.

Regarding the structural response, Figure 4.28 superposes the computed u_{top} and W_{p*} to

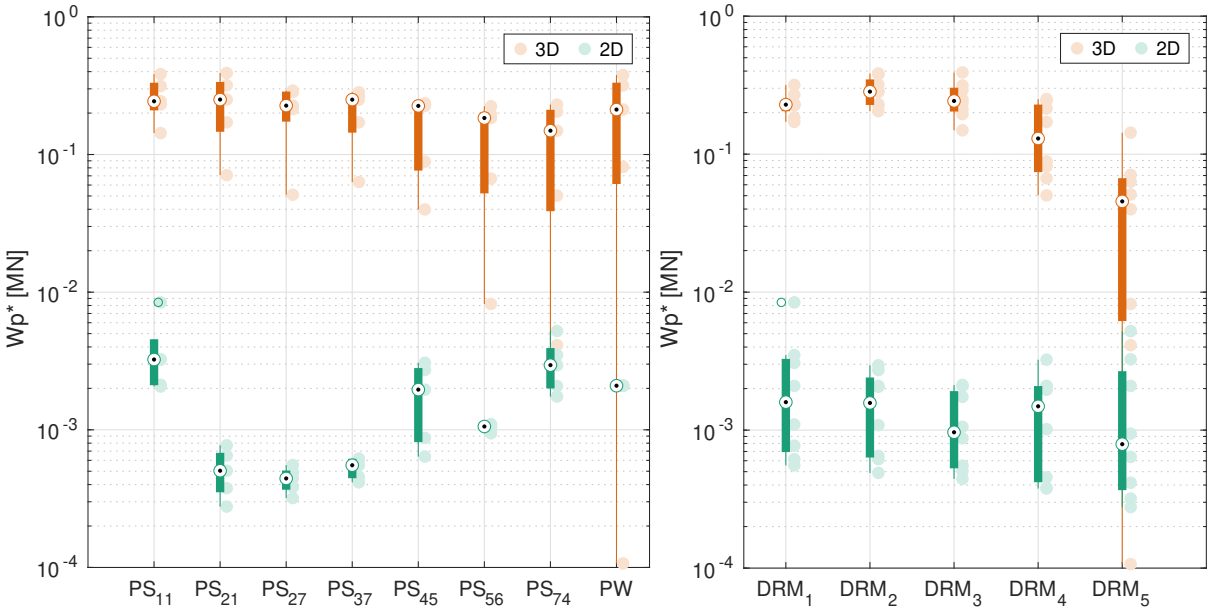

Figure 4.26: Variability of the damage measure $Wp*$ with source depth and basin location.

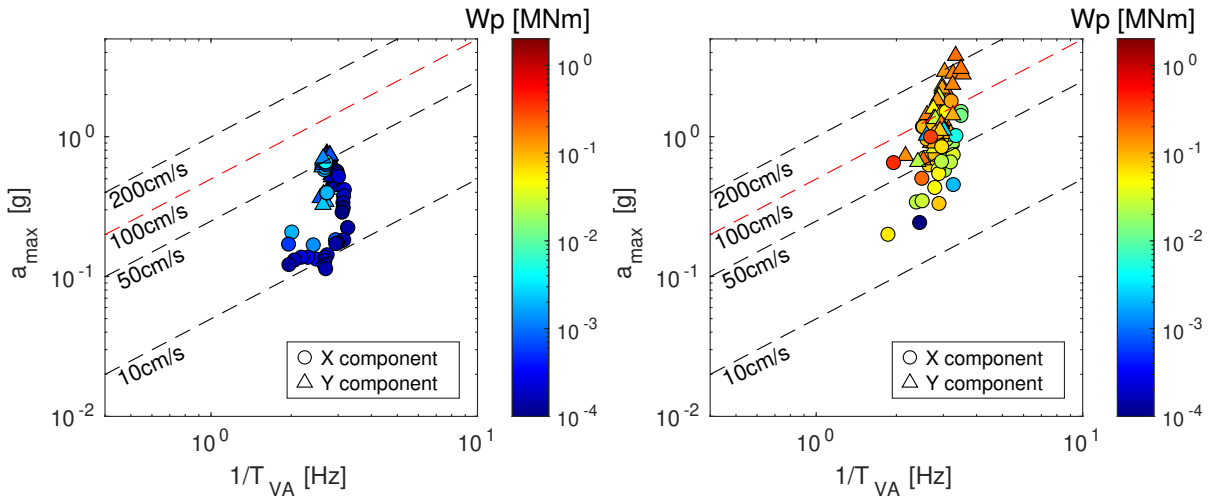

Figure 4.27: Distribution of IMs (a_{max} and $1/T_{VA}$) versus structural damage (W_p) depending on the geometry used: layered case (2D) and basin (3D).

the reference case defined in Section 4.4. As expected, the observed damage response in the structure follows the reference values. The plots show that while the basin effects induce an additional damage, for this structure specifically, the relation between EDP and DI is still the same, i.e, the damage response does not change. Therefore, it would be possible to approximate them from an uncoupled analysis. However, the directionality of the ground motions has to be accounted. It is esential to recall that this result is specifically for this structure, and to the selected EDP and IM. Other structures could be more affected to surface waves or rotational

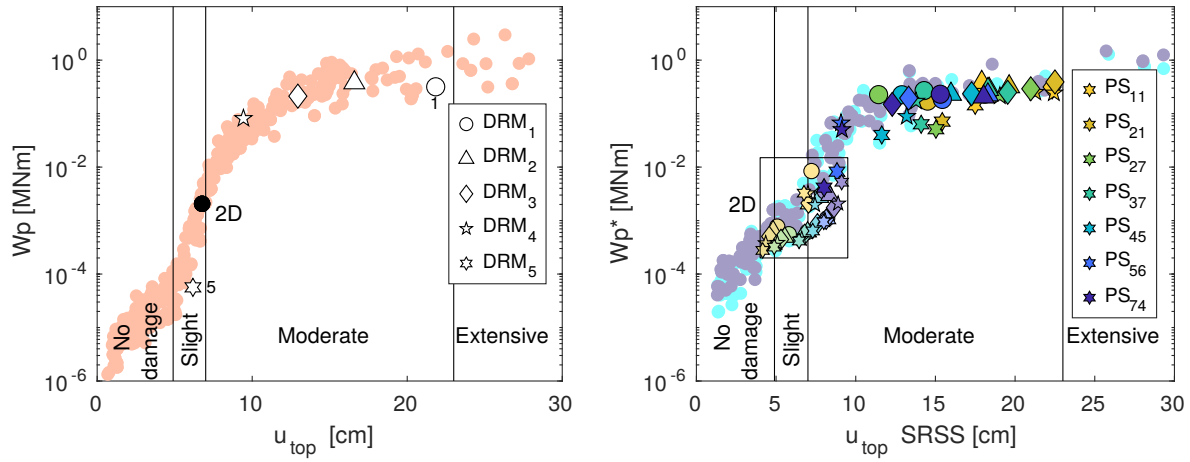

(a) PW vs reference SSI_{1DIR}

(b) PS vs reference RB_{2DIR} and SSI_{2DIR}.

Figure 4.28: Obtained structural response: (a) The vertically incident plane wave (PW) is compared to the reference case when the loading was applied in one direction and (b) the point sources (PS) to the reference case in two directions. The results for the layered case (2D) are in black and delimited by a square, respectively.

components.

4.6 Basin effects following the PBEE methodology

This last part focuses on the effects of basin inclusion on the computation of the seismic hazard and on the demand of the structure following a PBEE methodology. Traditionally, the seismic hazard analysis relates the ground motion level (IM) with its mean annual rate of exceedence (MRE or λ) (Bazzurro and Cornell, 2004; Rathje and Saygili, 2008; Tarbali et al., 2018, among others), given by

$$\lambda_{IM}(im) = MRE_{IM}(im) = \lambda_0 \int_m \int_r P[IM > im|m,r] \cdot f_{m,r}(m,r) \cdot dm \cdot dr \tag{4.18}$$

where all the faults in the area, all the potential earthquakes scenarios on each source are accounted, in terms of a magnitude m and distance to the site r. In this work, λ_0, defined as the annual rate of earthquakes greater than the minimum magnitude, is impossible to compute because a simplified non realistic case is being used. Therefore, the estimation of IM is computed in terms of the complementary cumulative distribution function (CCDF) (Bazzurro and Cornell, 2004), described by the integral

$$CCDF_{IM} = \int_m \int_r P[IM > im|m,r] \cdot f_{m,r}(m,r) \cdot dm \cdot dr \tag{4.19}$$

The aim of a seismic hazard analysis is to first evaluate the IM prediction (in terms of GMPE or any other way of IM estimation) on standard rock, to which then the 1D linear site response is first

considered, and in a following step the underground geometry (3D) (Bard, 2021). Therefore, to account for site effects, an additional term is added in the Equation 4.19, resulting the following equation

$$CCDF_{IM,UG}(im) = \int_m \int_r P\left[IM > im | m, r, UG\right] \cdot f_{m,r,UG}\left(m, r, UG\right) \cdot dm \cdot dr \tag{4.20}$$

where UG represents the site term, $UG = [2D, 3D]$, depending if a one-dimensional layer or the whole basin are considered.

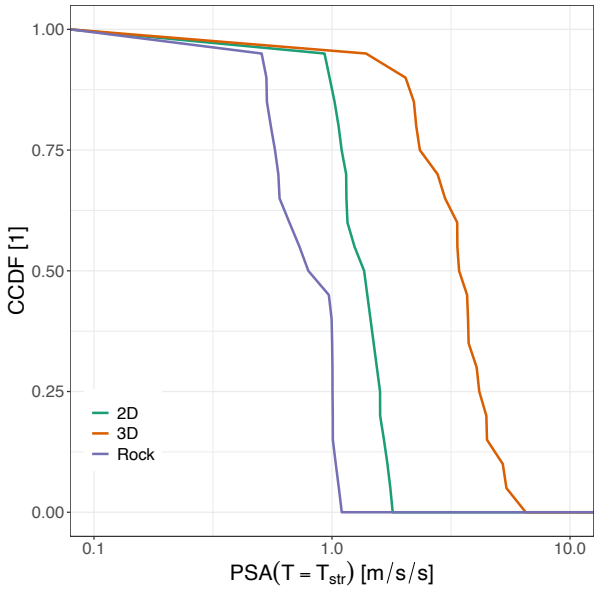

Figure 4.29: $CCDF_{IM}$ for the three subsurface geometries: *Rock*, layered model (2D) and basin model (3D).

For the hazard calculation, the selected IM is the geometric mean of the horizontal components of the pseudo spectral acceleration (PSA) in the period of the structure $PSA_H(T = T_{st})$ at the free field. Three CCDF curves are generated in Figure 4.29: for rock conditions, for a layered model to account for site effects (2D) and when a basin geometry is included (3D), considering all the responses for all the sources and all the positions.

The site term plays a significant role in the hazard as observed in Figure 4.29. It is clear that the inclusion of a layer of soil increases the spectral hazard, but the biggest change is observed for the 3D case. For instance, the PSA with a 25% probability of excedance is about 1 m/s^2 for rock conditions, versus 1.6 and 4.2 m/s^2 for 2D and 3D cases, respectively. The effects of the soil layering can be accounted correspondingly by the amplification factor $AF(f)$, defined as in Bazzurro and Cornell (2004),

$$AF(f) = \frac{PSA^s(f)}{PSA^r(f)} \tag{4.21}$$

where s refers to the soil and r refers to the bedrock. Thus, this formulation is comparable to the presented in Subsection 4.5.1.

Correspondingly, the probabilistic evaluation of seismic demand is related to its mean annual rate of exceedance (λ_D or MRE$_D$), given by

$$\lambda_D(d) = MRE_D(d) = \int P[D > d|IM = im] \cdot MRD_{IM}(im) \cdot dim \tag{4.22}$$

where MRD_{IM} is the probability density function represented by the derivative of the hazard curve as

$$MRD_{IM} = \frac{d}{dz}[MRE_{IM}(im)] \tag{4.23}$$

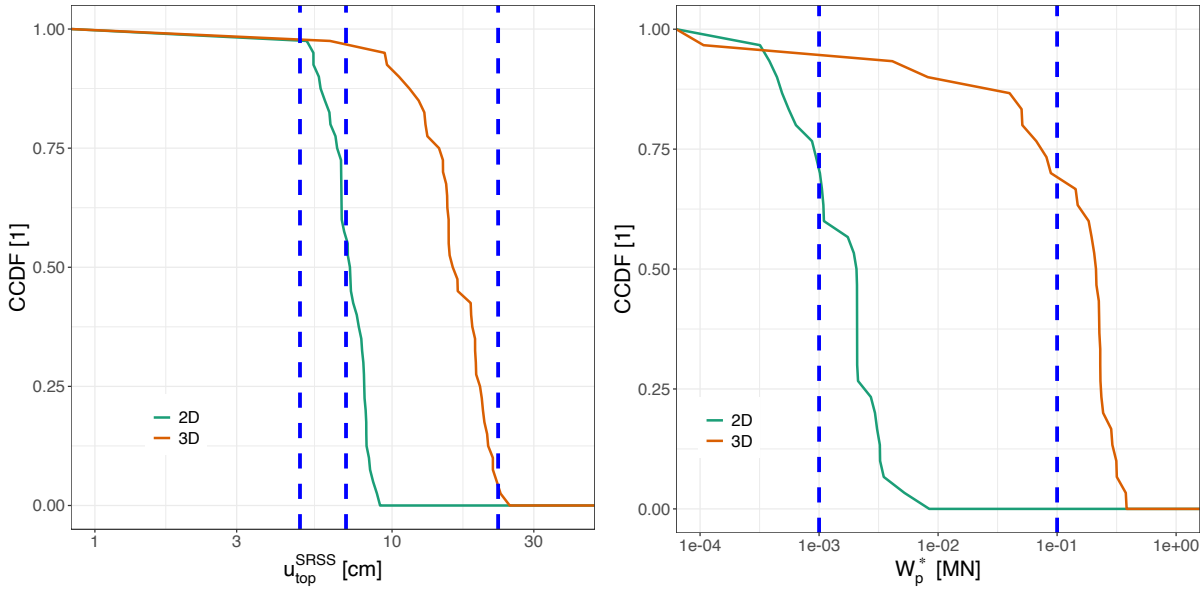

(a) (b)

Figure 4.30: (a) $CCDF_{EDP}$ and (b) $CCDF_{DI}$ for the three subsurface geometries: layered model (2D) and basin model (3D). The vertical blue lines represent the threshold for different limit states.

In a analogous form, λ_D is also computed by the CCDF. The response distribution of the engineering demand parameter (horizontal deck displacement, u_{top}) and damage index (plastic energy, W_{p*}) in the 2D and 3D cases can be contrasted in Figures 4.30a and 4.30b, respectively. The threshold values for *slight, moderate* and *extensive* damage are also presented for the u_{top}, and estimated for the W_{p*}. According to the Figures, the values of W_{p*} and u_{top} for the 2D geometry are substancially smaller than the ones obtained from the 3D geometry. Specifically, it is observed that the expected damage levels shift from *slight* (defined by a $W_p \approx 1$ kN) to *moderate* ($W_p \approx 0.1$ MN), also observed in Figure 4.28.

4.6.1 Influence of the modeling approach on the seismic demand

In the previous section, the demand CCDF curves were measured directly from a "coupled" modelling technique, in the sense that the wave propagation process goes directly from the source

to the structure with the DRM, including the complex wavefield produced by basins. In order to conclude the analysis of the structure, these results can be further contrasted with an estimation using the simple approach developed in Section 4.4. The following steps are used to estimate basin effects on the uncoupled demand:

1. First, the hazard curves, or the $CCDF$, are determined for the selected IM in the 2D and 3D cases (Figure 4.29). In this case they are directly the ones obtained from the numerical simulations, but they could also be estimated only with the $CCDF_{Rock}$ and then consider the site effect with amplification factors (such as the ones presented in Table 4.5).

2. Then, the estimated $CCDF_D$ curves can be obtained by the convolution of the probability of exceeding the demand (Equation 4.11) with the “hazard curves" of Figure 4.29.

The term “uncoupled” means that first the seismic hazard is computed and then, in an independent step, the structural demand. Therefore, the discrepancies in the measured (subscript $_M$) versus estimated (subscript $_E$) demand CCDFs come from (i) the differences in the ground motion characteristics not accounted with the selected IM (for instance, the PSA_H accounts for horizontal part of surface waves but not for vertical or rotational components) and (ii) the efficiency and sufficiency of the selected IM for the selected EDP. The soil-structure interaction is partially included in the simple approach because the EDP-IM relationship have been calculated from models including the soil and the structure.

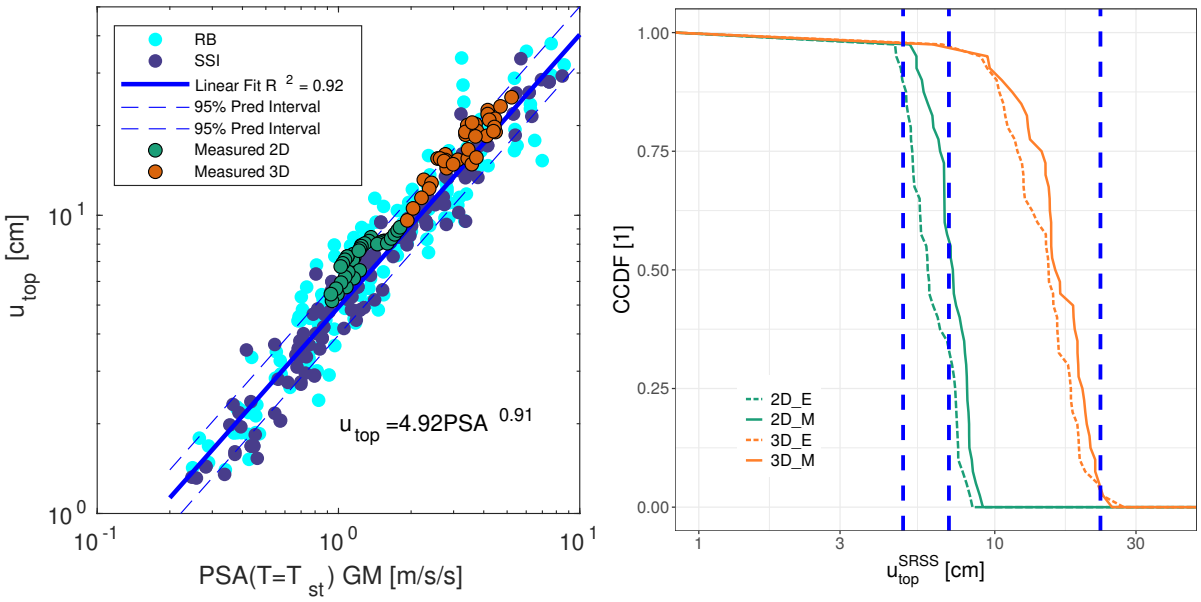

Figure 4.31: (a) EDP-IM reference relationship, where the numerical results from the 2D and 3D cases were superposed, and (b) comparison of the estimated versus measured demand CCDF curves. Two geometry cases are plotted: layered (2D) and basin (3D).

The Figure 4.31a shows the measured IM-EDP response in the 2D and 3D cases superposed to the traditional method from Section 4.4. The comparison of the estimated versus measured

$CCDF_{u_{top}}$ results is plotted in Figure 4.31b for the layered (2D) and the basin (3D) geometries. The threshold values for *slight, moderate* and *extensive* damage are also presented. It is observed that the estimated values of u_{top}^{SRSS} are only slighty lower than the ones measured. This finding demonstrates that most of the differences on the measured structural demand between the 2D and 3D cases come directly from the increase in the IM. This IM is computed only with the horizontal components. For a *moderate* damage, in the 2D case, the simple approach provides a underestimation of the structural demand ($\approx 35\%$) compared to the measured value ($\approx 50\%$). The differences are observables for the 2D and 3D cases. This result can lead to the conclusion that the complex 3D excitation may lead to higher damages for the structure. To recall, complex ground motions are present in the 2D case due to the nonvertical incidence of waves and in the 3D case plus the basin geometry.

4.7 Concluding remarks

This Chapter assesses the effect of the basin geometry on the strong ground motion amplification as well as on the seismic demand of nonlinear structures. The coupled response uses the domain reduction method (DRM), in order to propagate the seismic wavefield from the earthquake fault to a nonlinear infrastructure. Regarding the structural response, a first analysis was performed to recover the reference nonlinear response.

As expected, the inclusion of the basin geometry increases the hazard, which is dependent on the source depth and location inside the basin. Besides the amplification of the horizontal components, the nonvertical incidence and basin geometry induces surface waves, rocking and torsion (Bard and Bouchon, 1980b), although not all of the rotational components can be associated to surface waves. The amplification of the ground motion is correspondingly observable in the structural response, where directionality effects from the use of point sources induces a three-dimensional damage pattern in the structure. The inclusion of the underground geometry generates a general shift in the observable damage limit state, passing from a *Slight* to a *Moderate* level. This finding highlights the importance of the consideration of the the basin geometry for seismic design.

Regarding the results of the PBEE methodology, the numerical results were the base to perform the analysis of the second to fourth steps (Porter, 2003), namely the hazard, structural and damage analysis. The results were expressed in terms of the cumulative distribution function (CCDF) for the selected intensity measure (IM), engineering demand parameter (EDP) and and damage index (DI), which links the probability of exceedance with the previous step. Finally, in last subsection, the results were contrasted to a simple approach, where the seismic hazard and structural demand were calculated in two separate steps, i.e., the hazard is convoluted with the nonlinear response of the structure, similar to the work of Bazzurro and Cornell (2004). This simple approach involves the disminution of the calculation time since the simulation on the FEM reduced domains with the 3D inputs are no longer necessary. It was observed a good accuracy with this approximative method, revealing that most of the differences on the damage between

the 2D and 3D models can be explained by the increase of the hazard in the latter case, accounted by the horizontal spectral acceleration component $PSA_H(T = T_{st})$. This increase is a combination of amplification due to the sediment materials plus the horizontal components of surface waves. Therefore, for this specific source, basin and infrastructural setting, the structural demand could be estimated from amplification factors obtained from the ground motions.

Nevertheless, using an approximation would slightly underestimate the structural response. This is probably due to the fact that the complex shaking is not correctly characterized with only one intensity measure focused on the horizontal component, not accounting for the increased response due to rotational components (Castellani et al., 2012; Falamarz-Sheikhabadi and Ghafory-Ashtiany, 2015; Guidotti et al., 2018; Meza Fajardo and Papageorgiou, 2018; Vicencio and Alexander, 2019, among others). These are present on the ground motion only when a nonvertical shaking is imposed.

The aforementioned conclusions are based only on the results for the specific source, basin and infrastructural setting. Admittedly, the presented investigation represents a basis for further numerical simulations, where different aspects can be analyzed:

1. Because of numerical limitations, the CCDF curves were presented undistinguished on the spatial variability inside the basin (DRM location). Yet, the propagation phenomena taking place inside basins is usually different if the site location is closer to the edges or closer to the central part, hence explaining why almost all amplification or aggravation factors proposed in the literature are location-dependent (Iyisan and Khanbabazadeh, 2013; Ayoubi et al., 2021; Bard, 2021, among others). For that reason, the CCDF should also account for the spatial variation inside the basin. This can be accomplished by definition of zones (e.g., Stambouli et al., 2018) for the computation of the CCDFs. This would allow, for instance, to determine which zones are influenced the most with damage due to surface wave generation.

2. The seismic structural damages seem to be affected by the horizontal components of the ground motion in a higher order of magnitude than the other components (vertical and rotational). The limits of this conclusion could be further investigated. For instance, assymetrical models could be analyzed in the same framework. In this case, the influence of the torsion exerted from Love waves could be more significant (e.g., de la Llera and Chopra, 1994; Dahmardeh et al., 2020), and therefore should be considered in seismic analysis and design.

Conclusion and Perspectives

The earthquake wavefield characterization and three-dimensional numerical simulations of basin models, from the source to the structure, have led to partial conclusions already given in each chapter. Still, the principal results regarding their contribution to the research questions stated in the document's introduction are addressed herein.

The first part of the work has been devoted to validating the surface wave identification and characterization procedure called the *normalized inner product* (NIP). A comparison has been performed with two other methodologies (MUSIC and 6CPol). Regarding the posterior hazard analysis, the surface wave characterization searches for parameters associated with a measure of ground motion intensity (e.g., polarization angle, maximum amplitudes, frequency content). Results demonstrate the correct identification of the selected strategy, besides the advantage of lower computational time for implementation in large-scale domains.

Thus, a second part of the work focused on a parametric study performed in canonical and realistic basins to highlight the influence of material and geometrical settings of the input source and basin on the surface wave generation. These models showed that three-dimensionality patterns in surface wave propagation can quickly become a complex problem. The influence of local soil structure on surface waves was observed primarily in the frequency content. It has also been noted that basin-induced surface waves partially influence the amplification response inside the basin. This surface wave amplification is controlled because the two types (Love and Rayleigh) have a distinguished frequency range: for the Love waves, the values are close to the fundamental soil frequency, while for Rayleigh waves are higher.

The third part of the work has been dedicated to the basin effect on the structural demand of a simplified nonlinear structure model. For this purpose, the evaluation of the structural demand of a simplified nonlinear beam column is considered in this study. The innovation is that a coupled numerical simulation is performed, including a complex 3D input ground motion that excites the structure. The "coupled" model was contrasted to evaluate the influence of the 3D complex wave field (i.e., surface waves and rotational components) compared to a traditional excitation (i.e., vertically incident plane S-wave) arriving at the base of the foundation. The analysis was performed in the framework of the PBEE methodology. The traditional methodology worked to define seismic vulnerability curves and EDP-IM relations. Due to the properties of the evaluated structural case, the structural response is dominated by the horizontal components of the ground motion input, and the rotational components increase only slightly the expected demand.

It should be noted that the amplification observed in the IM partially considers the surface wave energy. Therefore, the amplification factor, defined with the pseudo-spectral acceleration evaluated in the frequency of the structure, is a good indicator of the structural damage in basins. Nevertheless, the limitations of this conclusion should be examined in future works.

Perspectives

Several research suggestions can be established from this work in the direction of further work:

- One of the final aims of the project to which this work is placed, **MODULATE**, is the development of tools and guidelines to the seismic risk assessment of infrastructures affected by the surface waves produced by sedimentary basins.

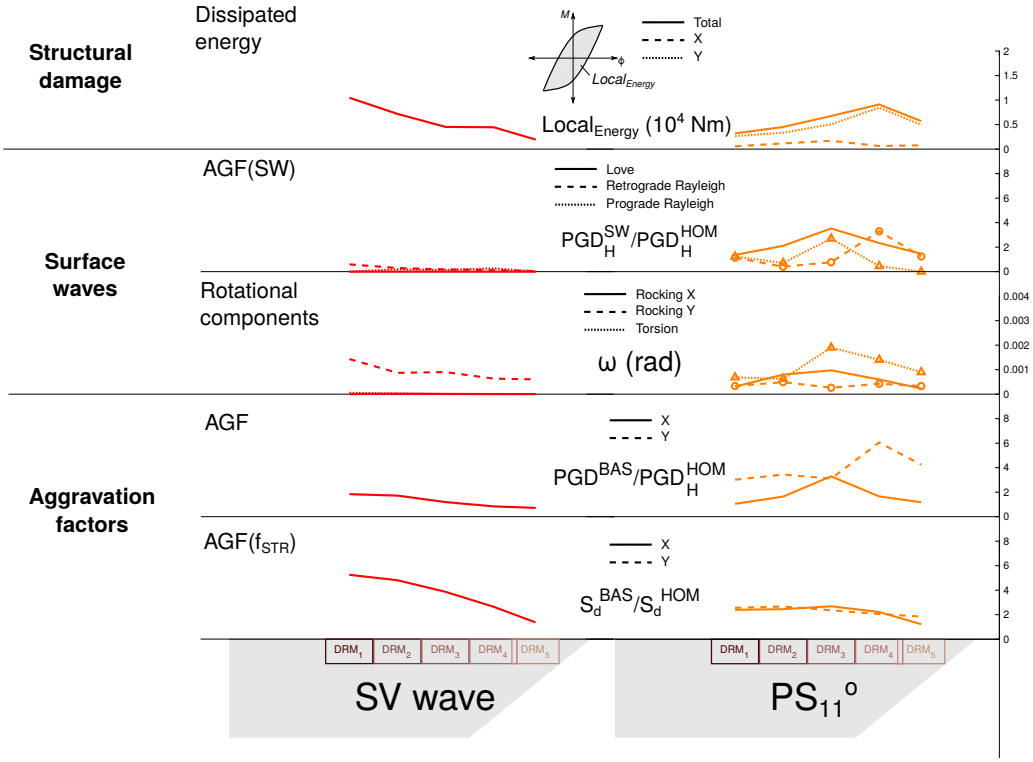

Figure C.1: Spatial variability of (from top to bottom) seismic damage as dissipated energy, AGF of displacement spectra of the extracted surface waves, rotational components, AGF(PGD) of total signal and AGF of displacement spectra evaluated at fSTR, for plane wave (left, in red) and shallow DC point source (right, in orange) cases.

Some relations were obtained between the generation of surface waves with the basin and seismic setting, which, as summarized in Figure C.1, are location- and source-dependent. A more extensive parametric study could be conducted to find a correlation in simple equations. This equation, for instance, could be in the form of an aggravation factor that includes surface waves and can predict structural damage. This implementation could be easily added to the PBEE analyses used by practicing earthquake engineers.

- Other parameters could also be added to evaluate the surface wave propagation in basins, such as non-linear soil behavior, attenuation in the material properties, which have yet to be investigated (e.g. Aggelis and Shiotani, 2007; De Martin et al., 2021).

- Regarding the structural performance, effects from 3D complex ground motions observed in realistic seismic scenarios (e.g., extended faults, heterogeneous media) could be examined. Their influence on more complicated structures, such as asymmetrical-plan and high-rise buildings and long-span bridges, which are prone to rotational-induced damage, is an ongoing research topic (e.g., Nazarov et al., 2015; Vicencio and Alexander, 2019, 2021; Özşahin and Pekcan, 2020) and could be easily studied with the methodology used in this work. Another foundation system can be further investigated: including soil-structure interface for sliding or using flexible foundations (Gičev et al., 2015; Perraud et al., 2022, among others).

- A reduced-order modeling technique applied to the DRM framework was proposed by the works of Korres (2021); Castro-Cruz et al. (2021), in terms of synthetic Green's functions (SGFs). A similar study could be performed to complement the hazard analysis (λ_{EDP}) for the investigation of basin effects.

Appendices

Appendix A

Physics-Based Numerical simulation in SEM3D

As stated by Igel (2016), the importance of 3D numerical physics-based simulations is variated, from the computation of ground shaking for seismic hazard studies, to the understanding of physical phenomena concerning the seismic rupture and wave propagation through the Earth. One of the most used numerical methodologies is the spectral element method (SEM), introduced by Faccioli et al. (1997); Komatitsch et al. (1999); Komatitsch and Tromp (1999). The method is recommended because it combines an interpolation scheme based on the Gauss-Lobato-Legendre (GLL) collocation points with spectral convergence of function interpolation for the usage of Lagrange polynomials as basis functions. The latter results in an explicit time scheme and makes the mass matrix diagonal, which has advantages in terms of efficiency and parallelization flexibility. In this work, the 3D Spectral Element Method code SEM3D (CEA and CentraleSupélec and IPGP and CNRS, 2017) is used.

The resolution of the mesh is defined by solving the minimum element size Δh given by

$$\Delta h \leq \frac{V_{min}}{f_{max}} \frac{N}{N_{GLL}} \tag{A.1}$$

where V_{min} is the minimum shear wave velocity, f_{max} is the maximum target frequency to resolve, N_{GLL} is the number of GLL points per wavelength and N the polynomial degree. For instance, a value of 5 GLL points correspond to a Lagrange interpolant of degree $N = 4$.

In the following, the main features in in SEM3D are discussed: the representation of seismic sources, the *not-honouring* meshing technique and the absorbing boundary conditions. A basin amplification validation is performed against an analytical reference solution.

A.1 Representation of the seismic sources in SEM3D

The earthquake source is assumed as a discontinuity having an infinitesimal thickness, where the elastic equation does not hold (Aki and Richards, 1980). The first simplification arises if the finite

size of the source is ignored, then the source can be approximated by a system of equivalent body forces acting at a point. This is valid for observations at sufficiently large distances compared with source dimensions and if the wavelenghts of the observations are larger than the source dimensions. The time-dependent body forces $F_i(t)$ can be represented by the integral over a infinitesimal volume V_0 as

$$F_i(t) = \lim_{V_0 \to 0} \int_{V_0} F_i(\mathbf{x}, t)\, dV \tag{A.2}$$

where **x** are the coordinates of the point source. In a more generalized way, a seismic source can be represented through a moment tensor M_{ij} (Udias et al., 2013), expressed as

$$M_{ij} = \int_{V_0} m_{ij} dV \tag{A.3}$$

where m_{ij} is the moment tensor volume density in the case of volumetric sources (an analogous case is the case to a surface). The relation between the body forces produced by the fracture and relative displacement and the moment tensor density is given by

$$F_i(t) = -m_{ij}, j \tag{A.4}$$

Each component of the moment tensor m_{ij} correspond to couples of forces or dipoles. The moment tensor is represented by elementary components (Figure A.1) in a matrix form as

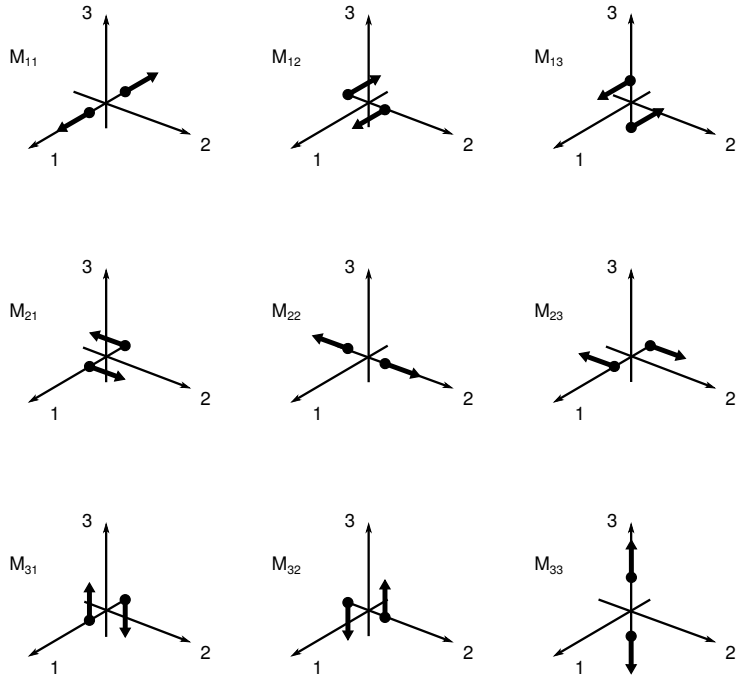

Figure A.1: Moment tensor elementary components.

$$M = \frac{1}{3}\begin{bmatrix} M_{11} & M_{21} & M_{13} \\ M_{12} & M_{22} & M_{23} \\ M_{13} & M_{23} & M_{33} \end{bmatrix} \tag{A.5}$$

where the components m_{11}, m_{22} and m_{33} are linear dipoles, without a moment as the arms are in the same direction as the forces (Udias et al., 2013). The other components, have arms perpendicular to the forces so are couples with a moment. In this particular case, they receive the name of doble couple (DC), represented by two sources with the same moment acting in opposite directions. The DC is the system most frequently used to represent the source of earthquakes as they represent the shear facture, which is normally the process which tectonic earthquakes are though as.

Supposing that all components of the moment tensor have the same temporal dependance, the $M_{i,j}(t) = M(t) m_{ij}$ are the time-independent normalized components and $M(t)$ is the total time-dependent scalar seismic moment. If the moment tensor corresponds to a DC, then the scalar seismic moment M_0 is equal to

$$M_0 = \mu \Delta \overline{u} S \tag{A.6}$$

where μ is the shear or rigidity modulus of the material at the fault. The scalar seismic moment M_0 which is a measure of the size of an earthquake, can be obtained by the integration of $\dot{M}_0(t)$. The function $M(t)$ is called the source time function (STF). It represents, for a shear fracture, the slip $\Delta u(t)$ at the source.

The condition of zero net moment implies that the moment tensor is symmetric (Udias et al., 2013), so a restrictive form can be derived based in only four parameters: the source time function, to vector components of slip and one normal vector. Hence, the fault plane can be represented in function of the strike of the plane with respect to the north, ϕ, dip δ and rake λ, which is the angle of the slip vector with respect to the horizontal.

It is important to recall that the moment tensor is a function of time and position ($M(\mathbf{x}, t)$) so the extended dimension of the source can be considered. In the following subsections, the implementation of kinematic extended sources is discussed, as well as one particular case, the plane wave approximation. In a kinematic model, the rupture process is specified by a spatial distribution of the slip vector, and a rupture velocity (the velocity of propagation of the slip).

A.1.1 Kinematics of extended sources

By the theory of elastic superposition, any extended source can be defined as a sequence of double couple point sources. The earthquake faulting in SEM3D is simulated by means of the kinematic slip source model. In this model, the representation of the rupture is given by a series of double-couple sub-sources distributed along the plane. The slip is initiated from the hypocenter and then propagates according to the rupture velocity.

In SEM3D, the extended fault modelling is represented using the Ruiz Integral Kinematic (RIK)

source model. The full description is available in the original work of Ruiz et al. (2011) and the implementation in SEM3D is specifically based on Gallovič (2015).

The source rupture is simulated as a series of multiple sub-events, described as circular cracks (multi-cracks model). The size of the circles is related to the number of sources and dimensions of the fault (along-strike length L and width W) based on a fractal distribution. The distribution of radii R ranges within a minimum $R_{min} = \Delta x/2$ of half the minimum distance between and the center of two cracks, and a maximum $R_{max} = \alpha \min(W, L)$ with $\alpha < 0.5$ an user-defined value. The slip distribution $\Delta u_c(r)$ at each sub-source along the crack surface is defined as (Eshelby and Peierls, 1957)

$$\Delta u_c(r) = \frac{24}{7\pi} \frac{\Delta\sigma_d}{\mu} \sqrt{R^2 - r^2} \tag{A.7}$$

which is dependent of r, the distance from a point on the crack surface to it center, with μ the rigidity and σ_d the stress drop of the sub-source, considered constant. The crack's center position is defined by source inversion techniques, so that the slip distribution patch represents the target seismic moment defined for the seismic scenario. However, a stochastic component of the number/size of each sub-source is used in order to have a good representation of the high frequency directivity, based on a random distribution. Besides, the nucleation point within each crack is randomly chosen.

When the nucleation starts, the rise time of the slip function is defined as a function of the sub-source radius R as

$$\tau(R) = \begin{cases} \frac{2R}{V_r} & R < R_p \\ \frac{2R_P}{V_r} & R \geq R_p \end{cases} \tag{A.8}$$

where V_r is the rupture velocity and R_p is the subevent size that has the maximum rise-time $\tau_{max} = R_p/V_r$.

A.1.2 Plane wave approximation

In order to compute amplification of the ground motions due to local effects or soil-structure interaction analyses, one of the main simplifications in numerical simulation models is the use of vertically incident plane waves as input motion. This excitation is generally inserted into the model by effective forces in small domains. In SEM3D the dynamic excitation is introduced by point forces/moment, so a plane wave could be implemented as a spatial distribution of point-wise forces in a plane thanks to Huyguens principle, which states that every point on a wavefront can be regarded as a new source of waves as in Figure A.2.

With all the sub-sources having the same moment tensor and slip function, a plane wave incidence can be approximated. The idea is that the spherical wave field produced by the point sources constructively interfere in order that only the normal incidence ray-path prevails. For that, a sufficiently small lag-distance L between each point source has to be selected. Special attention has also to be given to the distance source-surface for the plane wavefront to develop and to the dimensions of the grid to avoid nonplanar waves. The methodology implemented in

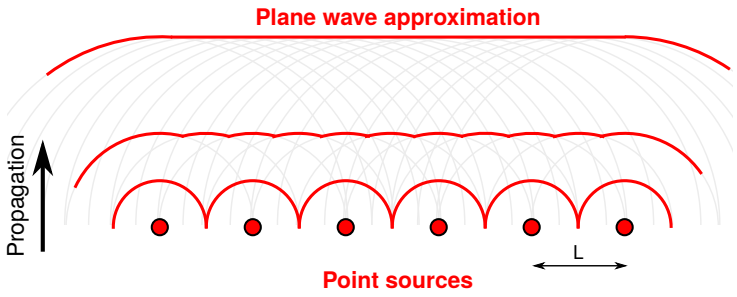

Figure A.2: Huyguens' principle representation for a vertically propagating plane wavefront.

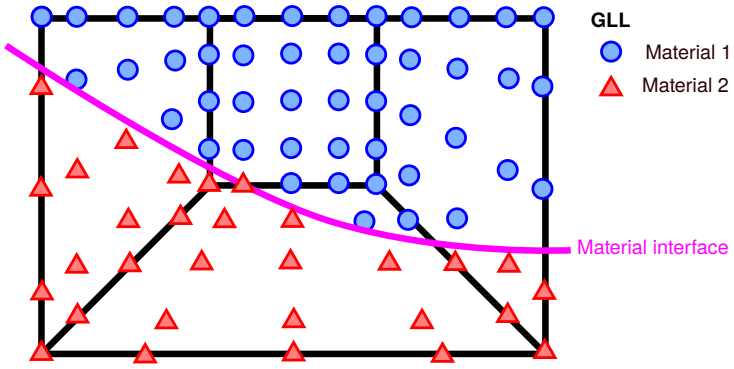

Figure A.3: Not honouring meshing technique. Modified from Touhami (2020).

SEM3D was validated for a simple case of a 3D domain with two horizontal layers by Gatti (2017). To obtain a desired amplitude of the incident motion, the amplitude of each sub-source function has to be calibrated.

A.2 Non honouring meshing technique

Hexahedral meshes is one advantage of the spectral approximation but also one limitation, as it is difficult to generate complex geology of the sub-surface with geometrical discontinuities, such as the case of a basin. For that, the mesh can be treated by the not-honouring approach: the mesh elements do not follow the geometrical discontinuities, so hexahedral meshes can be constructed. Instead, the material properties are defined at the GLL level of the element as represented in Figure A.3 for elements with a polynomial degree of 4, depicting that one element could have different material properties.

The advantages of the method lie in the reduction in computing cost due to a more simpler and regular mesh without compromising the accuracy of the results (e.g., Pelties et al., 2010; Igel et al., 2015; Touhami, 2020). However, it is important to consider some limitations associated with the dimension of the transition, which should be much smaller than the shear wavelength, and to avoid strong contrasts between different geological materials. The non honouring approach in SEM3D have been validated by Touhami (2020) for a simplified basin.

Table A.1: Material properties for the semi-spherical basin of reference.

Layer	$\rho\,(kg/m^3)$	V_p (m/s)	V_s (m/s)
Soil	2600	1600	855
Halfspace	4333	2094	1209

A.3 Validation of the amplification on a simplified basin model with SEM3D

In order to verify some of the approximations discussed previously, the amplification observed by a three-dimensional simplified basin will be verified against a reference solution of Sanchez-Sesma (1983). The model consist in a canonical semi-spherical basin. The basin was positioned at the surface in the middle of the SEM3D domain and a vertically incident plane-P wave is applied.

The material properties of the basin and halfspace (denoted by the subscript B and R, respectively) are defined in the original case as

$$\frac{\mu_B}{\mu_H} = 0.3 \tag{A.9}$$

$$\frac{\rho_B}{\rho_H} = 0.6 \tag{A.10}$$

$$\nu_B = 0.3 \tag{A.11}$$

$$\nu_H = 0.25 \tag{A.12}$$

where μ, ρ and ν are respectively the shear modulus, mass density and Poisson coefficient. Into the SEM3D model, the properties translate as the found in Table A.1.

The mesh was generated with the non-honoring approach, with regular elements of dimension 50 m $\times\, 50$ m $\times\, 50$ m to attain a maximum frequency of 17 Hz. Figure A.4 shows the density at the surface, where the use of a non honouring strategy at the basin/halfspace interface is clearly recognized. In SEM3D, the material interface that separate the two materials represented in Figure A.3 is not continuous, but in fact given to the software by means of a regularly spaced matrix (a *point cloud* of discretized values). This three dimensional matrix provides one material attribute to each XYZ coordinate, and is the reason why some averaged values are seen at the interface.

To inyect the vertically incident plane wave into the simulation, the extended plane wave source was generated by a grid of equally spaced point sub-sources placed every 10 meters, positioned at a depth of 3 km. The total dimensions of the grid is of 5 km $\times\, 5$ km, sufficiently larger than the basin radius. At each subsource, a source time function representing a 1Hz-Ricker

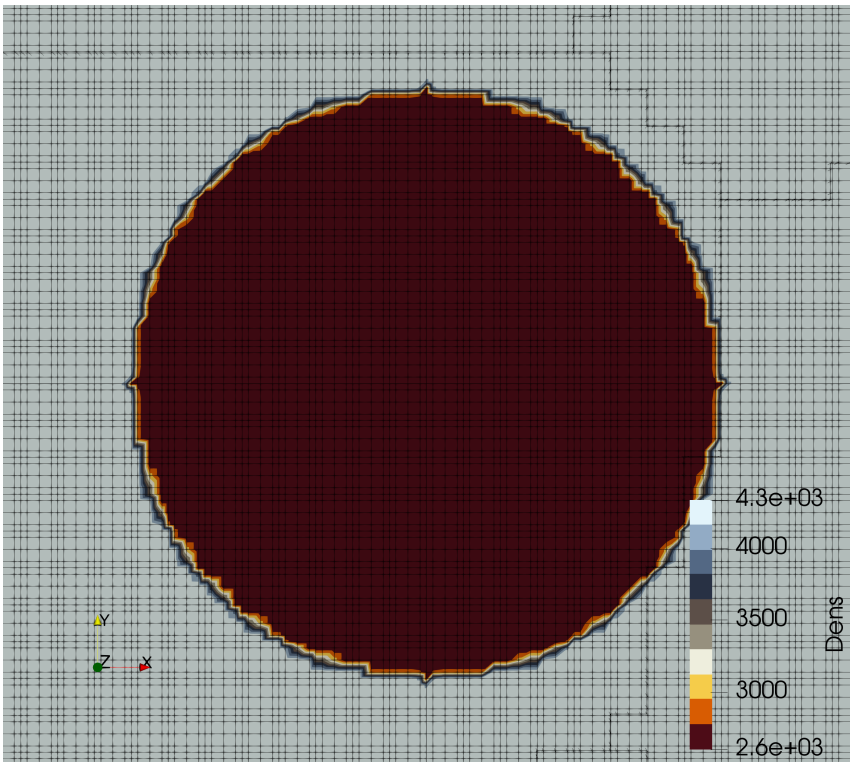

Figure A.4: Density distribution using the non honouring technique for a semi-spherical basin model observed at the surface. The mesh is discretized at the GLL points described by a non regular distance.

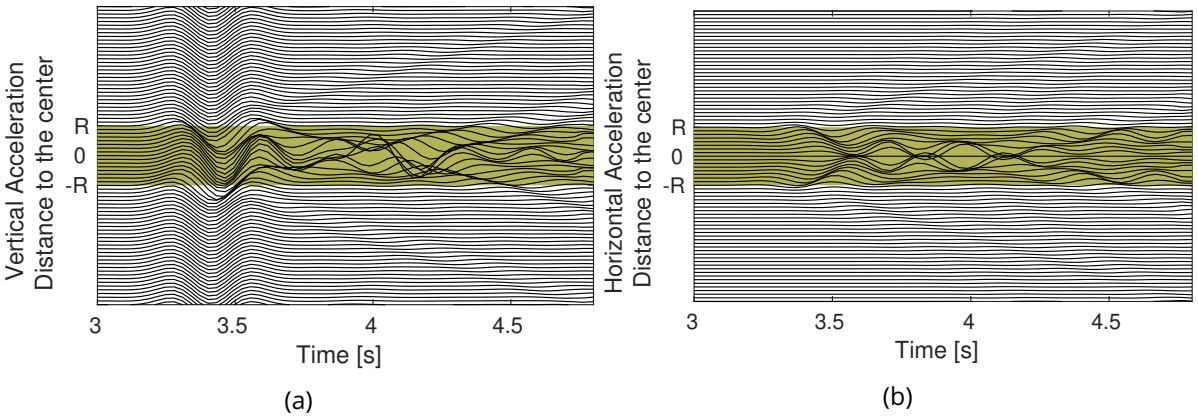

Figure A.5: Seismograms of a vertically incident plane P wave arriving to a semi-spherical basin of radius R in the (a) vertical and (b) horizontal components.

wavelet was considered and a moment tensor M,

$$M = \frac{1}{3}\begin{bmatrix} 1 & 0 & 0 \\ 0 & 1 & 0 \\ 0 & 0 & 1 \end{bmatrix} \tag{A.13}$$

associated to a strike $\phi = 90°$, dip $\delta = 45°$ and rake $\lambda = 90°$ according to a simple fault model (Subsection A.1).

The simulation of the P-wave propagation is observed in the time domain in Figure A.5, over a profile along the X-axis. As expected, amplification is observed in the vertical component plus the mode conversion to SH waves in the horizontal components (inside the green area in Figure A.5). The comparison with the reference study have been carried out by means of the amplification factor, computed as the ratio between the maximum displacement in the basin against the same model but without a basin. The results are computed in the frequency domain at one particular frequency. From Sanchez-Sesma (1983), the amplification is analyzed in the normalized frequency η_P

$$\eta_P = 2R/\Lambda_P = 0.5 \tag{A.14}$$

where $R = 400$ m, the radius of the basin and Λ_P is the wavelength of the incident P wave. For a normalized frequency of $\eta_P = 0.5$, the results in SEM3D are determined for a frequency of 1.3 Hz. Very good agreement is found with the reference study (Figure A.6). From these results, it is concluded that the non honouring approach does not generate a relevant modification close to the interest frequencies. Therefore, the non honouring meshing technique in addition to the plane wave approximation can be used in order to simplify the seismic wave propagation for the evaluation of basin effects.

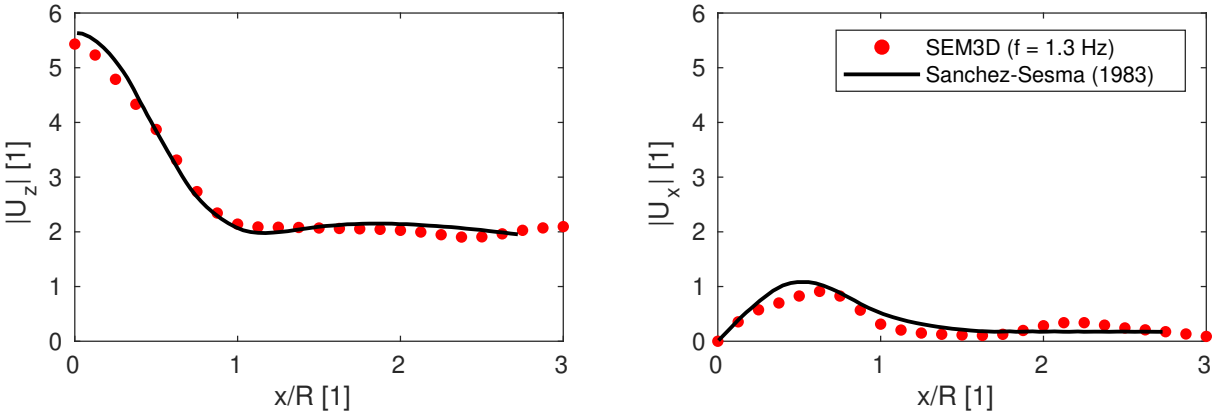

Figure A.6: Verification of a 3D semi-spherical basin model: Amplification of the vertical (left) and horizontal (right) displacement for a vertically propagated P-wave. In solid line, the reference solution by Sanchez-Sesma (1983), against the results obtained in SEM3D in red dots. The horizontal axis is normalized by the radius R of the basin.

Bibliography

Abell, J. A., Orbović, N., McCallen, D. B., and Jeremić, B. (2018). Earthquake soil-structure interaction of nuclear power plants, differences in response to 3-D, 3 1-D, and 1-D excitations. *Earthquake Engineering and Structural Dynamics*.

Abrahamson, N. A., Schneider, J. F., and Stepp, J. C. (1991). Empirical Spatial Coherency Functions for Application to Soil-Structure Interaction Analyses. *Earthquake Spectra*, 7(1):1–27.

Achenbach, J. D. (1973). *Wave propagation in elastic solids*. NorthHolland/American Elsevier.

Adams, B. M., Osborne, N. M., and Taber, J. J. (2003). The basin-edge effect from weak ground motions across the fault-bounded edge of the Lower Hutt Valley, New Zealand. *Bulletin of the Seismological Society of America*, 93(6):2703–2716.

Aggelis, D. G. and Shiotani, T. (2007). Experimental study of surface wave propagation in strongly heterogeneous media. *The Journal of the Acoustical Society of America*, 122(5):EL151.

Aki, K. and Richards, P. G. (1980). *Quantitative seismology*. W.H. Freeman, San Francisco.

Alavi, B. and Krawinkler, H. (2004). Behavior of moment-resisting frame structures subjected to near-fault ground motions. *Earthquake Engineering and Structural Dynamics*, 33(6):687–706.

Alcaraz-Castaño, M., Alcolea-González, J. J., de Andrés-Herrero, M., Castillo-Jiménez, S., Cuartero, F., Cuenca-Bescós, G., Kehl, M., López-Sáez, J. A., Luque, L., Pérez-Díaz, S., Piqué, R., Ruiz-Alonso, M., Weniger, G. C., and Yravedra, J. (2021). First modern human settlement recorded in the Iberian hinterland occurred during Heinrich Stadial 2 within harsh environmental conditions. *Scientific Reports*, 11(1):1–24.

Ameri, G., Hollender, F., Perron, V., and Martin, C. (2017). Site-specific partially nonergodic PSHA for a hard-rock critical site in southern France: adjustment of ground motion prediction equations and sensitivity analysis. *Bulletin of Earthquake Engineering*, 15(10):4089–4111.

Amini, D., Gatmiri, B., and Maghoul, P. (2022). Seismic Response of Alluvial Valleys Subject to Oblique Incidence of Shear Waves. *Journal of Earthquake Engineering*, 26(12):6304–6328.

Anagnostopoulos, S. A., Kyrkos, M. T., and Stathopoulos, K. G. (2015). Earthquake induced torsion in buildings: Critical review and state of the art. *Earthquake and Structures*, 8(2):305–377.

Anderson, J. G. (2007). Physical Processes That Control Strong Ground Motion. *Treatise on Geophysics: Second Edition*, 4:505–557.

Anderson, J. G. and Brune, J. N. (1999). Probabilistic seismic hazard analysis without the ergodic assumption. *Seismological Research Letters*, 70(1):19–28.

Aochi, H., Ducellier, A., Dupros, F., Delatre, M., Ulrich, T., De Martin, F., and Yoshimi, M. (2013). Finite difference simulations of seismic wave propagation for the 2007 mw 6.6 Niigata-ken Chuetsu-Oki earthquake: Validity of models and reliable input ground motion in the near-field. *Pure and Applied Geophysics*, 170(1):43–64.

Aquib, T. A., Sivasubramonian, J., and Mai, P. M. (2022). Analysis of Ground Motion Intensity Measures and Selection Techniques for Estimating Building Response. *Applied Sciences (Switzerland)*, 12(23).

Arboleda-Monsalve, L. G., Mercado, J. A., Terzic, V., and Mackie, K. R. (2020). Soil–Structure Interaction Effects on Seismic Performance and Earthquake-Induced Losses in Tall Buildings. *Journal of Geotechnical and Geoenvironmental Engineering*, 146(5):1–14.

Arias, A. (1970). Measure of earthquake intensity. Technical report, Massachusetts Inst. of Tech., Cambridge. Univ. of Chile, Santiago de Chile.

Arias, A. (1996). Local directivity of strong ground motion. In *Eleventh World Conference on Earthquake Engineering*.

Athanatopoulou, A. M. (2005). Critical orientation of three correlated seismic components. *Engineering Structures*, 27(2):301–312.

Ayoubi, P., Mohammadi, K., and Asimaki, D. (2021). A systematic analysis of basin effects on surface ground motion. *Soil Dynamics and Earthquake Engineering*, 141:106490.

Baker, J., Bradley, B., and Stafford, P. (2021). *Seismic Hazard and Risk Analysis*. Cambridge University Press.

Baker, J. W. (2007a). Probabilistic structural response assessment using vector-valued intensity measures. *Earthquake Engineering and Structural Dynamics*, 36(1):1861–1883.

Baker, J. W. (2007b). Quantitative classification of near-fault ground motions using wavelet analysis. *Bulletin of the Seismological Society of America*, 97(5):1486–1501.

Banerjee Basu, S. and Shinozuka, M. (2011). Effect of ground motion directionality on fragility characteristics of a highway bridge. *Advances in Civil Engineering*, 2011.

Baraschino, R., Baltzopoulos, G., and Iervolino, I. (2022). Reconciling eurocode 8 part 1 and part 2 two-component record selection. *Journal of Earthquake Engineering*, 26(13):6918–6942.

Bard, P.-Y. (2021). Physics-Based Site-Amplification Prediction Equations: A dream at reach? In *Proceedings of the 6th IASPEI / IAEE International Symposium: Effects of Surface Geology on Seismic Motion. Kyoto (on line), Japan*.

Bard, P.-Y., Bora, S. S., Hollender, F., Laurendeau, A., and Traversa, P. (2020). Are the Standard VS-Kappa Host-to-Target Adjustments the Only Way to Get Consistent Hard-Rock Ground Motion Prediction? *Pure and Applied Geophysics*, 177(5):2049–2068.

Bard, P.-Y. and Bouchon, M. (1980a). The Seismic Response Of Sediment-Filled Valleys. Part 1. The Case Of Incident Sh Waves. *Bulletin of the Seismological Society of America*, 70(4):1263–1286.

Bard, P.-Y. and Bouchon, M. (1980b). The Seismic Response Of Sediment-Filled Valleys. Part 2. The Case Of Incident P And Sv Waves. *Bulletin of the Seismological Society of America*, 70(5):1921–1941.

Bard, P.-Y. and Bouchon, M. (1985). The two-dimensional resonance of sediment-filled valleys. *Bulletin of the Seismological Society of America*, 75(2):519–541.

Baron, J., Primofiore, I., Klin, P., Vessia, G., Laurenzano, G., Vessia, G., Laurenzano, G., and Vessia, G. (2022). Investigation of Topographic Site Effects using 3D Waveform Modelling: Amplification, Polarization and Torsional Motions in the Case Study of Arquata del Tronto (Italy). *Bulletin of Earthquake Engineering*, 20(1):677–710.

Bazzurro, P. and Cornell, C. A. (1999). Disaggregation of seismic hazard. *Bulletin of the Seismological Society of America*, 89(2):501–520.

Bazzurro, P. and Cornell, C. A. (2004). Nonlinear soil-site effects in probabilistic seismic-hazard analysis. *Bulletin of the Seismological Society of America*, 94(6):2110–2123.

Berenger, J.-P. (1994). A perfectly matched layer for the absorption of electromagnetic waves. *Journal of Computational Physics*, 114(2):185–200.

Berge-Thierry, C., Svay, A., Laurendeau, A., Chartier, T., Perron, V., Guyonnet-Benaize, C., Kishta, E., Cottereau, R., Lopez-Caballero, F., Hollender, F., Richard, B., Ragueneau, F., Voldoire, F., Banci, F., Zentner, I., Moussallam, N., Lancieri, M., Bard, P.-Y., Grange, S., Erlicher, S., Kotronis, P., Le Maoult, A., Nicolas, M., Régnier, J., Bonilla, F., and Theodoulidis, N. (2017). Toward an integrated seismic risk assessment for nuclear safety improving current french methodologies through the SINAPS@ research project. *Nuclear Engineering Design*, 323(1):185–201.

Berge-Thierry, C., Voldoire, F., Ragueneau, F., Lopez-Caballero, F., and Le Maoult, A. (2019). Main Achievements of the Multidisciplinary SINAPS@ Research Project: Towards an Integrated Approach to Perform Seismic Safety Analysis of Nuclear Facilities. *Pure and Applied Geophysics*.

Berge-Thierry, C., Voldoire, F., Ragueneau, F., Lopez-Caballero, F., and Le Maoult, A. (2020). Main achievements of the multidisciplinary sinaps@ research project: Towards an integrated approach to perform seismic safety analysis of nuclear facilities. *Pure and Applied Geophysics*, 177(5):2299–2351.

Berger, J. F., Lespez, L., Kuzucuoğlu, C., Glais, A., Hourani, F., Barra, A., and Guilaine, J. (2016). Interactions between climate change and human activities during the early to mid-Holocene in the eastern Mediterranean basins. *Climate of the Past*, 12(9):1847–1877.

Bielak, J., Hisada, Y., Bao, H., Xu, J., and Ghattas, O. (2000). One- vs two- or three-dimensional effects in sedimentary valleys. In *Proceedings of the 12th WCEE*, pages 1–8.

Bielak, J., Loukakis, K., Hisada, Y., and Yoshimura, C. (2003). Domain reduction method for three-dimensional earthquake modeling in localized regions, part I: Theory. *Bulletin of the Seismological Society of America*, 93(2):817–824.

Bommer, J. and Acevedo, B. (2004). The use of real earthquake accelerograms as input to dynamic analysis. *Journal of Earthquake Engineering*, 8(sup1):43–91.

Bommer, J. J. (2002). Deterministic vs. Probabilistic seismic hazard assessment: An exaggerated and obstructive dichotomy. *Journal of Earthquake Engineering*, 6:43–73.

Bonilla, L. F., Steidl, J. H., Gariel, J. C., and Archuleta, R. J. (2002). Borehole response studies at the Garner Valley Downhole Array, Southern California. *Bulletin of the Seismological Society of America*, 92(8):3165–3179.

Boore, D. M. (2003). Simulation of ground motion using the stochastic method. *Pure and Applied Geophysics*, 160(3):635–676.

Boore, D. M. (2004). Can site response be predicted? *Journal of Earthquake Engineering*, 8(1):1–41.

Boore, D. M. (2010). Orientation-independent, nongeometric-mean measures of seismic intensity from two horizontal components of motion. *Bulletin of the Seismological Society of America*, 100(4):1830–1835.

Boore, D. M., Watson-Lamprey, J., and Abrahamson, N. A. (2006). Orientation-independent measures of ground motion. *Bulletin of the Seismological Society of America*, 96(4):1502–1511.

Bowden, D. C. and Tsai, V. C. (2017). Earthquake ground motion amplification for surface waves. *Geophysical Research Letters*, 44(1):121–127.

Brissaud, Q., Bowden, D. C., and Tsai, V. C. (2020). Extension of the basin rayleigh-wave amplification theory to include basin-edge effects. *Bulletin of the Seismological Society of America*, 110(3):1305–1322.

Brune, J. (1970). Tectonic stress and the spectra of seismic shear waves from earthquakes. *Journal of Geophysical Research*, 75:4997–5009.

Bustos, J., Pastén, C., Pavez, D., Acevedo, M., Ruiz, S., and Astroza, R. (2023). Two-dimensional simulation of the seismic response of the Santiago Basin, Chile. *Soil Dynamics and Earthquake Engineering*, 164(September 2022).

Cadet, H., Bard, P. Y., Duval, A. M., and Bertrand, E. (2012). Site effect assessment using KiK-net data: Part 2-site amplification prediction equation based on f0 and Vsz. *Bulletin of Earthquake Engineering*, 10(2):451–489.

Calvi, G. M., Pinho, R., Magenes, G., Bommer, J. J., Restrepo-Vélez, L. F., and Crowley, H. (2006). Development of seismic vulnerability assessment methodologies over the past 30 years. *ISET Journal of Earthquake Technology*, 43(3):75–104.

Carol, I. and Murcia, J. (1989). Nonlinear time-dependent analysis of planar frames using an 'exact' formulation-II. Computer implementation for R.C. structures and examples. *Computers and Structures*, 33(1):89–102.

Castellani, A., Stupazzini, M., and Guidotti, R. (2012). Free-field rotations during earthquakes: Relevance on buildings. *Earthquake Engineering and Structural Dynamics*, 41(5):875–891.

Castro-Cruz, D., Gatti, F., and Lopez-Caballero, F. (2021). High-fidelity broadband prediction of regional seismic response: a hybrid coupling of physics-based synthetic simulation and empirical Green functions. *Natural Hazards*, 108(2):1997–2031.

Castro-Cruz, D., Gatti, F., Lopez-Caballero, F., Hollender, F., El Haber, E., and Causse, M. (2022). Blind broad-band (0–10 Hz) numerical prediction of the 3-D near field seismic response of an MW6.0 extended fault scenario: application to the nuclear site of Cadarache (France). *Geophysical Journal International*, 232(1):581–600.

CEA and CentraleSupélec and IPGP and CNRS (2017). SEM3D Ver 2017.04 Registered at French Agency for Protection of Programs (Dépôt APP).

Chaljub, E., Maufroy, E., Moczo, P., Kristek, J., Hollender, F., Bard, P.-Y., Priolo, E., Klin, P., De Martin, F., Zhang, Z., et al. (2015). 3-d numerical simulations of earthquake ground motion in sedimentary basins: testing accuracy through stringent models. *Geophysical Journal International*, 201(1):90–111.

Chammas, R., Abraham, O., Cote, P., Pedersen, H. A., and Semblat, J. F. (2003). Characterization of Heterogeneous Soils Using Surface Waves: Homogenization and Numerical Modeling. *International Journal of Geomechanics*, 3(1):55–63.

Champion, C. and Liel, A. (2012). The effect of near-fault directivity on building seismic collapse risk. *Earthquake Engineering & Structural Dynamics*, 41:1391–1409.

Chatzigogos, C. T. and Meza Fajardo, K. C. (2020). Incremental dynamic analyses of bridge pylons with consideration of the effect of surface waves. In *Proceedings of the International Conference on Structural Dynamic , EURODYN, Greece*, pages 2893–2908.

Choi, Y., Stewart, J. P., and Graves, R. W. (2005). Empirical model for basin effects accounts for basin depth and source location. *Bulletin of the Seismological Society of America*, 95(4):1412–1427.

Code_Aster (2017). General public licensed structural mechanics finite element software, included in the Salomé-Méca simulation platform. Website http://www.code-aster.org.

Colombo, A. and Negro, P. (2005). A damage index of generalised applicability. *Engineering Structures*, 27(8):1164–1174.

Cornell, C. A., Jalayer, F., Hamburger, R. O., and Foutch, D. A. (2002). Probabilistic Basis for 2000 SAC Federal Emergency Management Agency Steel Moment Frame Guidelines. *Journal of Structural Engineering*, 128(4):526–533.

Cornell C. Allin (1968). Engineering Seismic Risk Analysis. *Bulletin of the Seismological Society of America*, 58(5):1583–1606.

Cornou, C. and Bard, P.-Y. (2003). Site-to-bedrock over 1D transfer function ratio: An indicator of the proportion of edge-generated surface waves? *Geophysical Research Letters*, 30(9):1–5.

Cornou, C., Bard, P.-Y., and Dietrich, M. (2003a). Contribution of Dense Array Analysis to the Identification and Quantification of Basin-Edge-Induced Waves , Part II : Application to Grenoble Basin (French Alps). *Bulletin of the Seismological Society of America*, 93(6):2624–2648.

Cornou, C., Bard, P.-Y., and Dietrich, M. (2003b). Contribution of dense array analysis to the identification and quantification of basin-edge-induced waves, part I: Methodology. *Bulletin of the Seismological Society of America*, 93(6):2604–2623.

Cosenza, E. and Manfredi, G. (2000). Damage indices and damage measures. *Progress in Structural Engineering and Materials*, 2(1):50–59.

Cruz-Atienza, V. M., Tago, J., Sanabria-Gómez, J. D., Chaljub, E., Etienne, V., Virieux, J., and Quintanar, L. (2016). Long Duration of Ground Motion in the Paradigmatic Valley of Mexico. *Scientific Reports*, 6(1):1–9.

Cushing, E. M., Hollender, F., Guyonnet-Benaize, C., Perron, V., Imtiaz, A., Svay, A., Mariscal, A., Bard, P.-Y., Cottereau, R., Lopez-Caballero, F., Theodoulidis, N., Moiriat, D., and Gelis, C. (2016). Close to the lair of Odysseus Cyclops : the SINAPS @ postseismic campaign and accelerometric network installation on Cephal ... In *Proceedings of the 7th INQUA on paleoseismology, active tectonics and archeoseismology, Crestone, Colorado, USA*, pages 74–76.

Cushing, E. M., Hollender, F., Moiriat, D., Guyonnet-Benaize, C., Theodoulidis, N., Pons-Branchu, E., Sépulcre, S., Bard, P.-Y., Cornou, C., Dechamp, A., Mariscal, A., and Roumelioti, Z. (2020). Building a three dimensional model of the active Plio-Quaternary basin of Argostoli (Cephalonia Island, Greece): An integrated geophysical and geological approach. *Engineering Geology*, 265:105441.

Dahmardeh, S. R., Aziminejad, A., and Motamedi, M. (2020). Effect of torsional component of earthquakes on response of symmetric/asymmetric buildings. *Proceedings of the Institution of Civil Engineers: Structures and Buildings*, 173(11):858–878.

Day, R. W. (2012). *Geotechnical Earthquake Engineering Handbook*. McGraw-Hill USA, second edition.

Day, S., Bielak, J., Dreger, D., Graves, R., Larsen, S., Olsen, K. B., Pitarka, A., and Ramirez-Guzman, L. (2006). Numerical simulation of basin effects on long-period ground motion. In *8th National Conference on Earthquake Engineering*, pages 1–10.

Day, S., Bielak, J., Dreger, D., Graves, R., Larsen, S., Olsen, K. B., Pitarka, A., and Ramirez-Guzman, L. (2013). Numerical Simulation Of Basin Effects On Long-Period Ground Motion. In *Integral Equations, Boundary Value Problems and Related Problems: Dedicated to Professor Chien-Ke Lu on the Occasion of his 90th Birthday: Yinchuan, Ningxia, China, 19-23 August 2012*, pages 211–223.

Day, S. M., Graves, R., Bielak, J., Dreger, D., Larsen, S., Olsen, K. B., Pitarka, A., and Ramirez-Guzman, L. (2008). Model for basin effects on long-period response spectra in southern California. *Earthquake Spectra*, 24(1):257–277.

Daza, J., Riano, A. C., Soto, V., Lopez-Caballero, F., and Reyes, J. C. (2023). Surface waves study of the Bogota Basin - Part 1 : Identification and extraction. *[Manuscript in preparation]*, pages 1–20.

de Carvalho Paludo, L., Bouvier, V., and Cottereau, R. (2019). Scalable parallel scheme for sampling of Gaussian random fields over very large domains. *International Journal for Numerical Methods in Engineering*, 117(8):845–859.

de la Llera, J. C. and Chopra, A. K. (1994). Accidental torsion in buildings due to base rotational excitation. *Earthquake Engineering & Structural Dynamics*, 23(9):1003–1021.

De Martin, F., Chaljub, E., Thierry, P., Sochala, P., Dupros, F., Maufroy, E., Hadri, B., Benaichouche, A., and Hollender, F. (2021). Influential parameters on 3-D synthetic ground motions in a sedimentary basin derived from global sensitivity analysis. *Geophysical Journal International*, 227(3):1795–1817.

de Silva, F. (2020). Influence of soil-structure interaction on the site-specific seismic demand to masonry towers. *Soil Dynamics and Earthquake Engineering*, 131(1):106023.

Douglas, J. and Aochi, H. (2008). A survey of techniques for predicting earthquake ground motions for engineering purposes. *Surveys in Geophysics*, 29(3):187–220.

Douglas, J., Gehl, P., Bonilla, L. F., Scotti, O., Régnier, J., Duval, A. M., and Bertrand, E. (2009). Making the most of available site information for empirical ground-motion prediction. *Bulletin of the Seismological Society of America*, 99(3):1502–1520.

Drake, L. (1980). Love and Rayleigh waves in an irregular soil layer. *Bulletin of the Seismological Society of America*, 70(2):571–582.

Dujardin, A., Hollender, F., Causse, M., Berge-Thierry, C., Delouis, B., Foundotos, L., Ameri, G., and Shible, H. (2020). Optimization of a Simulation Code Coupling Extended Source (k-2) and Empirical Green's Functions: Application to the Case of the Middle Durance Fault. *Pure and Applied Geophysics*, 177(5):2255–2279.

El Haber, E., Cornou, C., Jongmans, D., Youssef Abdelmassih, D., Lopez-Caballero, F., and AL-Bittar, T. (2019). Influence of 2d heterogeneous elastic soil properties on surface ground motion spatial variability. *Soil Dynamics and Earthquake Engineering*, 123:75–90.

Elgamal, A. W., Zeghal, M., Taborda, V., and Dobry, R. (1996). Analysis of Site Liquefaction and Lateral Spreading Using Centrifuge Testing Records. *Soils and Foundations*, 36(2):111–121.

Eshelby, J. D. and Peierls, R. E. (1957). The determination of the elastic field of an ellipsoidal inclusion, and related problems. *Proceedings of the Royal Society of London. Series A. Mathematical and Physical Sciences*, 241(1226):376–396.

Faccioli, E. and Chavez-Garcia, F. (2000). Complex site effects and building codes: Making the leap. *Journal of Seismology*, 4:23–40.

Faccioli, E., Maggio, F., Paolucci, R., and Quarteroni, A. (1997). 2D and 3D elastic wave propagation by a pseudo-spectral domain decomposition method. *Journal of Seismology*, 1(3):237–251.

Falamarz-Sheikhabadi, M. R. and Ghafory-Ashtiany, M. (2015). Rotational components in structural loading. *Soil Dynamics and Earthquake Engineering*, 75:220–233.

Farrow, K. T. and Kurama, Y. C. (2003). SDOF Demand Index Relationships for Performance-Based Seismic Design. *Earthquake Spectra*, 19(4):799–838.

Feng, Y., Kowalsky, M. J., and Nau, J. M. (2014). Fiber-based modeling of circular reinforced concrete bridge columns. *Journal of Earthquake Engineering*, 18(5):714–734.

Foti, S., Lai, C. G., Rix, G. J., and Strobbia, C. (2015). *Surface Wave Methods for Near-Surface Site Characterization*. Taylor & Francis.

Fox, M. J., Sullivan, T. J., and Beyer, K. (2015). Evaluation of seismic assessment procedures for determining deformation demands in RC wall buildings. *Earthquake and Structures*, 9(4):911–936.

Frankel, A., Carver, D., Cranswick, E., Bice, T., Sell, R., and Hanson, S. (2001). Observations of basin ground motions from a dense seismic array in San Jose, California. *Bulletin of the Seismological Society of America*, 91(1):1–12.

Furumura, T., Hayakawa, T., Nakamura, M., Koketsu, K., and Baba, T. (2008). Development of long-period ground motions from the nankai trough, japan, earthquakes: Observations and computer simulation of the 1944 tonankai (mw 8.1) and the 2004 se off-kii peninsula (mw 7.4) earthquakes. *Pure and Applied Geophysics*, 1:1–23.

Gallovič, F. (2015). Modeling Velocity Recordings of the Mw 6.0 South Napa, California, Earthquake: Unilateral Event with Weak High-Frequency Directivity. *Seismological Research Letters*, 87(1):2–14.

Gao, W., Hu, H., Hou, W., Zhang, P., Gong, P., Jia, W., Liu, X., and Li, K. (2022). The Spatiotemporal Patterns of Human Settlement during the Longshan and Erlitou Periods in Relation to Extreme Floods and Subsistence Strategy in the Upper and Middle Qin River Reaches, Central China. *Land*, 11(7):1–15.

Gatti, F. (2017). *Analyse physics-based de scénarios sismiques "de la faille au site" : prédiction de mouvement sismique fort pour l'étude de vulnérabilité sismique de structures critiques.* Phd thesis, Université Paris Saclay (COmUE) ; Politecnico di Milano.

Gatti, F., Carvalho Paludo, L. D., Svay, A., Lopez-Caballero, F., Cottereau, R., and Clouteau, D. (2017). Investigation of the earthquake ground motion coherence in heterogeneous non-linear soil deposits. *Procedia Engineering*, 199:2354–2359.

Gatti, F., Touhami, S., Lopez-Caballero, F., Paolucci, R., Clouteau, D., Alves Fernandes, V., Kham, M., and Voldoire, F. (2018). Broad-band 3-d earthquake simulation at nuclear site by an all-embracing source-to-structure approach. *Soil Dynamics and Earthquake Engineering*, 115:263–280.

Gelagoti, F., Kourkoulis, R., Anastasopoulos, I., and Gazetas, G. (2012). Nonlinear dimensional analysis of trapezoidal valleys subjected to vertically propagating SV waves. *Bulletin of the Seismological Society of America*, 102(3):999–1017.

Ghisbain, P. (2014). *Damage-based Earthquake Engineering*. WIT Press.

Ghobarah, A., Abou-Elfath, H., and Biddah, A. (1999). Response-based damage assessment of structures. *Earthquake Engineering and Structural Dynamics*, 28:79 – 104.

Ghofrani, H. and Atkinson, G. M. (2015). Duration of the 2011 Tohoku earthquake ground motions. *Journal of Seismology*, 19(1):9–25.

Ghosh, J., Padgett, J. E., and Sánchez-Silva, M. (2015). Seismic damage accumulation in highway bridges in earthquake-prone regions. *Earthquake Spectra*, 31(1):115–135.

Gičev, V., Trifunac, M. D., and Orbović, N. (2015). Translation, torsion, and wave excitation of a building during soil-structure interaction excited by an earthquake SH pulse. *Soil Dynamics and Earthquake Engineering*, 77:391–401.

Gil-Zepeda, S. A., Luzón, F., Aguirre, J., Morales, J., Sánchez-Sesma, F. J., and Ortiz-Alemán, C. (2002). 3D seismic response of the deep basement structure of the Granada Basin (southern Spain). *Bulletin of the Seismological Society of America*, 92(6):2163–2176.

Gilbert, G. K., Humphrey, R. L., Sewell, J. S., and Soulé, F. (1907). The San Francisco Earthquake and Fire of April 18, 1906 and their effects on structures and structural materials. Technical Report 324, Department of the Interior, United States Geological Survey, Washington, USA.

Graves, R. (1993). Modeling three-dimensional site response effects in the Marina District basin, San Francisco, California. *Bulletin of the Seismological Society of America*, 83(4):117–125.

Greenhalgh, S., Sollberger, D., Schmelzbach, C., and Rutty, M. (2018). Single-station polarization analysis applied to seismic wavefields: A tutorial. *Advances in Geophysics*, 59:123–170.

Greenhalgh, S. A., Zhou, B., and Rutty, M. (2008). Effect of coherent noise on single-station direction of arrival estimation. *Journal of Seismology*, 12(3):377–385.

Gribler, G. and Mikesell, T. D. (2019). Methods to isolate retrograde and prograde Rayleigh-wave signals. *Geophysical Journal International*, 219(2):975–994.

Guéguen, P. and Astorga, A. (2021). The torsional response of civil engineering structures during earthquake from an observational point of view. *Sensors (Switzerland)*, 21(2):1–21.

Guidotti, R., Castellani, A., and Stupazzini, M. (2018). Near-field earthquake strong ground motion rotations and their relevance on tall buildings. *Bulletin of the Seismological Society of America*, 108(3):1171–1184.

Günay, M. S. and Mosalam, K. M. (2012). PEER Performance Based Earthquake Engineering Methodology , Revisited. In *15th World Conference on Earthquake Engineering (15WCEE). Lisbon, Portugal*.

Güneş, N. (2022). Effects of near-fault pulse-like ground motions on seismically isolated buildings. *Journal of Building Engineering*, 52(1):1–17.

Gupta, V. and Trifunac, M. (1990). Response of multistoried buildings to ground translation and rocking during earthquakes. *Probabilistic Engineering Mechanics*, 5(3):138–145.

Gupta, V. and Trifunac, M. (1991). Effects of ground rocking on dynamic response of multistoried buildings during earthquakes. *Doboku Gakkai Ronbunshu*, 432(1):43–50.

Guyonet-Benaize, C. (2011). *Modélisation 3D multi-échelle des structures géologiques de la region de la faille de la moyenne Durance (SE France)*. PhD thesis, Ecole Doctorale Sciences de l'Environnement (Aix-en-Provence).

Haskell, N. (1953). The dispersion of surface waves on multilayered media. *Bulletin of the Seismological Society of America*, 43(1):17–34.

Haslinger, F., Kissling, E., Ansorge, J., Hatzfeld, D., Papadimitriou, E., Karakostas, V., Makropoulos, K., Kahle, H.-G., and Peter, Y. (1999). 3D crustal structure from local earthquake tomography around the Gulf of Arta (Ionian region, NW Greece). *Tectonophysics*, 304(3):201–218.

Hatzigeorgiou, G. D. and Beskos, D. E. (2009). Inelastic displacement ratios for SDOF structures subjected to repeated earthquakes. *Engineering Structures*, 31(11):2744–2755.

Hendrick, N. and Hearn, S. (1999). Polarisation analysis: What is it? why do you need it? how do you do it? *Exploration Geophysics*, 30(4):177–190.

Heresi, P., Ruiz-García, J., Payán-Serrano, O., and Miranda, E. (2020). Observations of Rayleigh waves in Mexico City Valley during the 19 September 2017 Puebla–Morelos, Mexico earthquake. *Earthquake Spectra*, 36:62–82.

Hobiger, M. (2011). *Polarization of surface waves : Characterization , inversion and application to seismic hazard assessment*. PhD thesis, Université de Grenoble.

Hobiger, M., Cornou, C., Bard, P.-Y., Bihan, N. L., and Imperatori, W. (2016). Analysis of seismic waves crossing the Santa Clara Valley using the three-component MUSIQUE array algorithm. *Geophysical Journal International*, 207(1):439–456.

Hobiger, M., Cornou, C., Bard, P. Y., and Le Bihan, N. (2011). MUSIQUE: A quaternion-based array processing technique for surface wave polarization analysis. In *IEEE Workshop on Statistical Signal Processing Proceedings. Nice, France*, pages 5–8.

Hökelekli, E. and Al-Helwani, A. (2020). Effect of soil properties on the seismic damage assessment of historical masonry minaret–soil interaction systems. *Structural Design of Tall and Special Buildings*, 29(2):1–12.

Hollender, F., Andre, M., Guyonnet-benaize, C., Cornou, C., Caillot, V., and Bard, P.-y. (2011). Can High Daily-Variation Of Noise Level Alter Results Of Ambient Vibration H/V Technique? In *Effects of Surface Geology on Seismic Motion, 4th IASPEI / IAEE International Symposium*, pages 1–6.

Hollender, F., Roumelioti, Z., Regnier, J., Perron, V., and Bard, P.-y. (2018). Respective Advantages of Surface and Downhole Reference Stations for Site Effect Studies : Lessons Learnt From the

Argonet (Cephalonia Island , Greece) and Cadarache (Provence , France) Vertical Arrays. In *16Th European Conference on Earthquake Engineering*, pages 1–12.

Hori, M., Ichimura, T., Wijerathne, L., Ohtani, H., Chen, J., Fujita, K., and Motoyama, H. (2018). Application of high performance computing to earthquake hazard and disaster estimation in urban area. *Frontiers in Built Environment*, 4(February).

Ibrahim, A. R., Makhloof, D. A., and Ren, X. (2022). Numerical collapse simulation based critical state analysis for framed-wall structure subjected to earthquakes. *Structural Design of Tall and Special Buildings*, 32(2):1–24.

Ichimura, T., Agata, R., Hori, T., Satake, K., Ando, K., Baba, T., and Hori, M. (2017a). Tsunami analysis method with high-fidelity crustal structure and geometry model. *Journal of Earthquake and Tsunami*, 11(5):1–18.

Ichimura, T., Fujita, K., Yoshiyuki, A., Quinay, P. E., Hori, M., and Sakanoue, T. (2017b). Performance enhancement of three-dimensional soil structure model via optimization for estimating seismic behavior of buried pipelines. *Journal of Earthquake and Tsunami*, 11(5):1–17.

Igel, H. (2016). *Computational Seismology: A Practical Introduction*. Oxford University Press.

Igel, H., Kaser, M., and Stupazzini, M. (2015). Seismic Wave Propagation in Media with Complex Geometries, Simulation of. In *Encyclopedia of Complexity and Systems Science*. Springer Science+Business Media.

Imtiaz, A., Cornou, C., Bard, P. Y., and Hobiger, M. (2014). Diffracted Wave Field And Coherency Analysis: An Example From Dense Array Network In Argostoli Basin, Cephalonia, Greece. In *Proceedings of the Second European Conference on Earthquake Engineering and Seismology (2ECEES), Istanbul, Turkey, 24-29 August*.

Imtiaz, A., Cornou, C., Bard, P. Y., and Hobiger, M. (2020). Diffracted wave-field decomposition and multi-dimensional site effects in the Argostoli valley, Greece. *Geophysical Journal International*, 224(3):1849–1869.

Imtiaz, A., Perron, V., Svay, A., Hollender, F., Bard, P. Y., and Theodoulidis, N. (2017). Wavefield characteristics and coherency of seismic ground motion from a rocksite at Argostoli Greece. In *Proceedings of the 16th World Conference on Earthquake Engineering, Santiago, Chile, 9-13 January*.

Iwaki, A. and Iwata, T. (2008). Validation of 3-D basin structure models for long-period ground motion simulation in the Osaka basin, western Japan. *Journal of Seismology*, 12(2):197–215.

Iyisan, R. and Khanbabazadeh, H. (2013). A numerical study on the basin edge effect on soil amplification. *Bulletin of Earthquake Engineering*, 11(5):1305–1323.

Jeremić, B., Jie, G., Preisig, M., and Tafazzoli, N. (2009). Time domain simulation of soil-foundation-structure interaction in non-uniform soils. *Earthquake Engineering and Structural Dynamics*, 38(5):699–718.

Joyner, W. B. (2000). Strong motion from surface waves in deep sedimentary basins. *Bulletin of the Seismological Society of America*, 90(6 B):95–112.

Kamal and Narayan, J. P. (2015). 3D basin-shape ratio effects on frequency content and spectral amplitudes of basin-generated surface waves and associated spatial ground motion amplification and differential ground motion. *Journal of Seismology*, 19(2):293–316.

Kamal and Rani, K. (2017). Study of Effects of Basin Shape , Shape-Ratio and Angle of Incidence of SH-Wave on Ground Motion Characteristics and Aggravation Factors. *J. Ind. Geophys. Union*, 21(6):490–499.

Karatzetzou, A. and Pitilakis, D. (2018a). Modification of Dynamic Foundation Response Due to Soil-Structure Interaction. *Journal of Earthquake Engineering*, 22(5):861–880.

Karatzetzou, A. and Pitilakis, D. (2018b). Reduction factors to evaluate acceleration demand of soil-foundation-structure systems. *Soil Dynamics and Earthquake Engineering*, 109(3):199–208.

Kashani, M. M., Málaga-Chuquitaype, C., Yang, S., and Alexander, N. A. (2017). Influence of non-stationary content of ground-motions on nonlinear dynamic response of RC bridge piers. *Bulletin of Earthquake Engineering*, 15(9):3897–3918.

Kato, B. and Wang, G. (2021). Regional seismic responses of shallow basins incorporating site-city interaction analyses on high-rise building clusters. *Earthquake Engineering and Structural Dynamics*, 50(1):214–236.

Kawase, H. (1996). The cause of the damage belt in Kobe:"The basin-edge effect," constructive interference of the direct S-wave with the basin-induced diffracted/Rayleigh waves. *Seismological Research Letters*, 67(5):25–34.

Kawase, H. (2003). Site effects on strong ground motions. *International Geophysics Series*, 81:1013–1030.

Kawase, H. (2011). Strong motion characteristics and their damage impact to structures during the Off Pacific Coast of Tohoku earthquake of march 11, 2011; How extraordinary was this M9.0 earthquake? In *In 4th IASPEI / IAEE International Symposium: Effects of Surface Geology on Seismic Motion. University of California Santa Barbara, USA.*, pages 1–10.

Kawase, H. and Aki, K. (1989). A study of the response of a soft basin for incident S, P, and Rayleigh waves with special reference to the long duration observed in Mexico City. *Bulletin of the Seismological Society of America*, 79(5):1361–1382.

Ke, K., Yam, M. C., and Ke, S. (2017). A dual-energy-demand-indices-based evaluation procedure of damage-control frame structures with energy dissipation fuses. *Soil Dynamics and Earthquake Engineering*, 95(1):61–82.

Keilis-Borok, V. I. (1989). *Surface Waves in Media with Weak Lateral Inhomogeneity*, pages 35–69. Springer Netherlands, Dordrecht.

Kennett, B. and Fichtner, A. (2020). *Exploiting Seismic Waveforms: Correlation, Heterogeneity and Inversion*. Cambridge University Press.

Khalil, C. and Lopez-Caballero, F. (2021). Survival analysis of a liquefiable embankment subjected to sequential earthquakes. *Soil Dynamics and Earthquake Engineering*, 140(10):106436.

Kim, B. and Hashash, Y. M. (2013). Site response analysis using downhole array recordings during the March 2011 Tohoku-Oki earthquake and the effect of long-duration ground motions. *Earthquake Spectra*, 29(SUPPL.1):37–54.

Knott, C. G. (1899). Reflection and Refraction of Elastic Waves with Seismological Applications. *Philosophical Magazine*, 48(1):64–97.

Koketsu, K. and Miyake, H. (2008). A seismological overview of long-period ground motion. *Journal of Seismology*, 12(2):133–143.

Komatitsch, D. and Tromp, J. (1999). Introduction to the spectral element method for three-dimensional seismic wave propagation. *Geophysical journal international*, 139(3):806–822.

Komatitsch, D., Vilotte, J.-P., Vai, R., Castillo-Covarrubias, J. M., and Sánchez-Sesma, F. J. (1999). The spectral element method for elastic wave equations—application to 2-d and 3-d seismic problems. *International Journal for numerical methods in engineering*, 45(9):1139–1164.

Korres, M. (2021). *Coupled 3D physics-based simulations for seismic source-to-structure response: Application to the Kashiwazaki-Kariwa nuclear power plant (Japan) case)*. PhD thesis, Université Paris-Saclay.

Korres, M., Lopez-Caballero, F., Alves Fernandes, V., Gatti, F., Zentner, I., Voldoire, F., Clouteau, D., and Castro-Cruz, D. (2023). Enhanced Seismic Response Prediction of Critical Structures via 3D Regional Scale Physics-Based Earthquake Simulation. *Journal of Earthquake Engineering*, 27(3):546–574.

Kotronis, P., Davennem, L., and Mazars, J. (2004). Poutre 3D multifibre Timoshenko pour la modélisation des structures en béton armé soumises à des chargements sévères. *Revue Francaise de Genie Civil, Taylor & Francis*, 8(2-3):329–343.

Kramer, S. L. (1996). *Geotechnical Earthquake Engineering*. Prentice-Hall International Series.

Krawinkler, H. (1999). Challenges and progress in performance-based earthquake engineering. *International Seminar on Seismic Engineering for Tomorrow - In Honor of Professor Hiroshi Akiyama. Tokyo, Japan*, pages 1–10.

Krawinkler, H., Medina, R., and Alavi, B. (2003). Seismic drift and ductility demands and their dependence on ground motions. *Engineering Structures*, 25(5):637–653.

Krebes, E. (2019). *Seismic Wave Theory*. Cambridge University Press.

Kristek, J., Moczo, P., Bard, P.-Y., Hollender, F., and Stripajová, S. (2018). Computation of amplification factor of earthquake ground motion for a local sedimentary structure. *Bulletin of Earthquake Engineering*, 16(6):2451–2475.

Ktenidou, O. J., Chávez-García, F. J., Raptakis, D., and Pitilakis, K. D. (2016). Directional dependence of site effects observed near a basin edge at Aegion, Greece. *Bulletin of Earthquake Engineering*, 14(3):623–645.

Kusanovic, D. S., Seylabi, E., and Asimaki, D. (2023). Seismo-VLAB: An open-source finite element software for seismic meso-scale simulations. *SoftwareX*, 21:101300.

Lai, V. H., Graves, R. W., Yu, C., Zhan, Z., and Helmberger, D. V. (2020). Shallow Basin Structure and Attenuation Are Key to Predicting Long Shaking Duration in Los Angeles Basin. *Journal of Geophysical Research: Solid Earth*, 125(10):1–15.

Laouami, N., Slimani, A., Bouhadad, Y., Chatelain, J. L., and Nour, A. (2006). Evidence for fault-related directionality and localized site effects from strong motion recordings of the 2003 Boumerdes (Algeria) earthquake: Consequences on damage distribution and the Algerian seismic code. *Soil Dynamics and Earthquake Engineering*, 26(11):991–1003.

Lehman, D., Moehle, J., Mahin, S., Calderone, A., and Henry, L. (2004). Experimental evaluation on the seismic performance of reinforced concrete bridge columns. *Journal of Structural Engineering*, 130(6):869 – 879.

Liu, Z. X., Huang, Z. E., and Meng, S. B. (2022). Three-dimensional IBEM solution to seismic wave scattering by a near-fault sedimentary basin. *Engineering Analysis with Boundary Elements*, 140:220–242.

Liu, Z. X., Huang, Z. E., Zhang, Z., Meng, S. B., and Huang, L. (2021). Three-dimensional preconditioned FM-IBEM solution to broadband-frequency seismic wave scattering in a layered sedimentary basin. *Engineering Analysis with Boundary Elements*, 133(8):1–18.

Lombaert, G. and Clouteau, D. (2006). Resonant multiple wave scattering in the seismic response of a city. *Waves in Random and Complex Media*, 16(3):205–230.

Lombaert, G., Clouteau, D., and Soize, C. (2005). A comparison of the city-site effect for the case of nice and mexico city. In *6th European Conference on Structural Dynamics: Eurodyn 2005. Paris, France*, pages 1329 – 1334.

Lopez-Caballero, F. and Khalil, C. (2018). Vulnerability assessment for earthquake liquefaction and induced settlements of an embankment using gaussian processes. *ASCE-ASME Journal of Risk and Uncertainty in Engineering Systems, Part A: Civil Engineering*, 4(2):04018010.

Makra, K. and Chávez-García, F. J. (2016). Site effects in 3D basins using 1D and 2D models: an evaluation of the differences based on simulations of the seismic response of Euroseistest. *Bulletin of Earthquake Engineering*, 14(4):1177–1194.

Makra, K., Chávez-García, F. J., Raptakis, D., and Pitilakis, K. (2005). Parametric analysis of the seismic response of a 2D sedimentary valley: Implications for code implementations of complex site effects. *Soil Dynamics and Earthquake Engineering*, 25(4):303–315.

Makra, K., Rovithis, E., Riga, E., Raptakis, D., and Pitilakis, K. (2021). Amplification features and observed damages in İzmir (Turkey) due to 2020 Samos (Aegean Sea) earthquake: identifying basin effects and design requirements. *Bulletin of Earthquake Engineering*, 19(12):4773–4804.

Malischewsky, P. G., Scherbaum, F., Lomnitz, C., Thanh, T., Wuttke, F., and Shamir, G. (2008). The domain of existence of prograde Rayleigh-wave particle motion for simple models. *Wave Motion*, 45(4):556–564.

Manea, E., Michel, C., Hobiger, M., Fäh, D., Cioflan, C., and Radulian, M. (2017). Analysis of the seismic wave field in the moesian platform (bucharest area) for hazard assessment purposes. *Geophysical Journal International*, 210:1609–1622.

Mao, S., Mordret, A., Campillo, M., Fang, H., and van der Hilst, R. D. (2020). On the measurement of seismic traveltime changes in the time-frequency domain with wavelet cross-spectrum analysis. *Geophysical Journal International*, 221(1):550–568.

Marafi, N. A., Eberhard, M. O., Berman, J. W., Wirth, E. A., and Frankel, A. D. (2017). Effects of deep basins on structural collapse during large subduction earthquakes. *Earthquake Spectra*, 33(3):963–997.

Maranò, S. and Fäh, D. (2013). Processing of translational and rotational motions of surface waves: Performance analysis and applications to single sensor and to array measurements. *Geophysical Journal International*, 196(1):317–339.

Maranò, S., Hobiger, M., and Fäh, D. (2017). Retrieval of Rayleigh wave ellipticity from ambient vibration recordings. *Geophysical Journal International*, 209(1):334–352.

Matinmanesh, H. and Asheghabadi, M. S. (2011). Seismic analysis on soil-structure interaction of buildings over sandy soil. *Procedia Engineering*, 14:1737–1743.

Maufroy, E., Chaljub, E., Hollender, F., Bard, P.-Y., Kristek, J., Moczo, P., De Martin, F., Theodoulidis, N., Manakou, M., Guyonnet-Benaize, C., Hollard, N., and Pitilakis, K. (2016). 3d numerical simulation and ground motion prediction: Verification, validation and beyond – lessons from the e2vp project. *Soil Dynamics and Earthquake Engineering*, 91:53–71.

Mazars, J., Kotronis, P., Ragueneau, F., and Casaux, G. (2006). Using multifiber beams to account for shear and torsion. Applications to concrete structural elements. *Computer Methods in Applied Mechanics and Engineering*, 195(52):7264–7281.

McCallen, D., Petersson, A., Rodgers, A., Pitarka, A., Miah, M., Petrone, F., Sjogreen, B., Abrahamson, N., and Tang, H. (2021a). EQSIM—A multidisciplinary framework for fault-to-structure earthquake simulations on exascale computers part I: Computational models and workflow. *Earthquake Spectra*, 37(2):707–735.

McCallen, D., Petrone, F., Miah, M., Pitarka, A., Rodgers, A., and Abrahamson, N. (2021b). EQSIM—A multidisciplinary framework for fault-to-structure earthquake simulations on exascale computers, part II: Regional simulations of building response. *Earthquake Spectra*, 37(2):736–761.

Meza-Fajardo, K. C., Aochi, H., and Papageorgiou, A. S. (2021). Comparative analysis of Rayleigh and Love waves detected propagating in the Nobi and Kanto basins during the 2004-, 2007-Chuetsu and 2011 Tohoku earthquakes. *Soil Dynamics and Earthquake Engineering*, 143(1):1–18.

Meza-Fajardo, K. C. and Papageorgiou, A. S. (2016). Estimation of rocking and torsion associated with surface waves extracted from recorded motions. *Soil Dynamics and Earthquake Engineering*, 80:225–240.

Meza Fajardo, K. C. and Papageorgiou, A. S. (2018). Response of tall buildings to base rocking induced by Rayleigh waves. *Earthquake Engineering and Structural Dynamics*, 47(8):1755–1773.

Meza-Fajardo, K. C., Papageorgiou, A. S., and Semblat, J. F. (2015). Identification and extraction of surface waves from three-component seismograms based on the normalized inner product. *Bulletin of the Seismological Society of America*, 105(1):210–229.

Meza-Fajardo, K. C., Semblat, J.-f., Chaillat, S., and Lenti, L. (2016). Seismic-wave amplification in 3d alluvial basins: 3d/1d amplification ratios from fast multipole BEM simulations. *Bulletin of the Seismological Society of America*, 106(3):1267–1281.

Meza-Fajardo, K. C., Varone, C., Lenti, L., Martino, S., and Semblat, J.-f. (2019). Surface wave quantification in a highly heterogeneous alluvial basin: Case study of the Fosso di Vallerano valley, Rome, Italy. *Soil Dynamics and Earthquake Engineering*, 120(November 2018):292–300.

Miranda, E. and Akkar, S. D. (2006). Generalized Interstory Drift Spectrum. *Journal of Structural Engineering*, 132(6):840–852.

Mitropoulou, C. C., Marano, G. C., and Lagaros, N. D. (2018). Damage index-based lower bound structural design. *Frontiers in Built Environment*, 4(32):1–12.

Miura, H. and Midorikawa, S. (2001). Effects of 3-D Deep Underground Structure on Characteristics of Rather Long-Period Ground Motion. *Zisin (Journal of the Seismological Society of Japan. 2nd ser.)*, 54(3):381–395.

Moczo, P., Kristek, J., Bard, P.-Y., Stripajová, S., Hollender, F., Chovanová, Z., Kristeková, M., and Sicilia, D. (2018). Key structural parameters affecting earthquake ground motion in 2D and 3D sedimentary structures. *Bulletin of Earthquake Engineering*, 16(6):2421–2450.

Modaressi, H. and Benzenati, I. (1994). Paraxial approximation for poroelastic media. *Soil Dynamics and Earthquake Engineering*, 13(2):117–129.

Narayan, J. P. (2012). Effects of angle of incidence of sh-wave at the basin-edge on the charactristics of basin-edge induced love wave. *Journal of Earthquake and Tsunami*, 6(1):1–21.

Nazarov, Y. P., Poznyak, E., and Filimonov, A. V. (2015). A brief theory and computing of seismic ground rotations for structural analyses. *Soil Dynamics and Earthquake Engineering*, 71:31–41.

NEHRP Consultants Joint Venture (2012). Soil-Structure Interaction for Building Structures. Technical report, Engineering Laboratory of the National Institute of Standards, U.S. Department of Commerce.

Neuenhofer, A. and Filippou, F. C. (1997). Evaluation of nonlinear frame finite-element models. *Journal of Structural Engineering*, 123(7):958–966.

Nguyen, K. T., Kusanovic, D. S., and Asimaki, D. (2022). Three-dimensional nonlinear soil–structure interaction for Rayleigh wave incidence in layered soils. *Earthquake Engineering and Structural Dynamics*, 51(11):2752–2770.

Noori, H. R., Memarpour, M. M., Yakhchalian, M., and Soltanieh, S. (2019). Effects of ground motion directionality on seismic behavior of skewed bridges considering SSI. *Soil Dynamics and Earthquake Engineering*, 127(August):105820.

Novikova, E. I. and Trifunac, M. D. (1994). Duration of strong ground motion in terms of earthquake magnitude, epicentral distance, site conditions and site geometry. *Earthquake Engineering & Structural Dynamics*, 23(9):1023–1043.

O'Kane, A. and Copley, A. (2021). The controls on earthquake ground motion in foreland-basin settings: the effects of basin and source geometry. *Geophysical Journal International*, 225(1):512–529.

Olsen, K. B. (2000). Site amplification in the Los Angeles basin from three-dimensional modeling of ground motion. *Bulletin of the Seismological Society of America*, 90(6B):S77–S94.

Olsen, K. B. and Archuleta, R. J. (1996). Three-dimensional simulation of earthquakes on the Los Angeles fault system. *Bulletin of the Seismological Society of America*, 86(3):575–596.

Özcebe, A. G., Smerzini, C., and Bhanu, V. (2020). Insights into the Effect of Spatial Variability of Recorded Earthquake Ground Motion on the Response of a Bridge Structure. *Journal of Earthquake Engineering*, 24(6):920–946.

Özşahin, E. and Pekcan, G. (2020). Assessment of Seismic Demand Due to Torsional Ground Motions on Symmetric Skew Bridges. *Journal of Earthquake Engineering*, 00(00):1–16.

Panji, M. and Mojtabazadeh-Hasanlouei, S. (2021). Surface Motion of Alluvial Valleys Subjected to Obliquely Incident Plane SH-Wave Propagation. *Journal of Earthquake Engineering*, pages 1–26.

Paolucci, R., Mazzieri, I., Smerzini, C., and Stupazzini, M. (2014). Physics-based earthquake ground shaking scenarios in large urban areas. In *Perspectives on European earthquake engineering and seismology*, pages 331–359. Springer, Cham.

Park, C., Miller, R., and Xia, J. (1998). Multichannel analysis of surface waves. *Geophysics*, 64.

Park, Y. and Ang, A. H. (1985). Mechanistic Seismic Damage Model for Reinforced Concrete. *Journal of Structural Engineering*, 111(4):722–739.

Parla, R. and Somala, S. N. (2022). Seismic ground motion amplification in a 3d sedimentary basin: Source mechanism and intensity measures. *Journal of Earthquake and Tsunami*, 16(04):2250008.

Parvez, I. A. and Rosset, P. (2014). Chapter 11 - the role of microzonation in estimating earthquake risk. In Shroder, J. F. and Wyss, M., editors, *Earthquake Hazard, Risk and Disasters*, Hazards and Disasters Series, pages 273–308. Academic Press, Boston.

Pelties, C., Käser, M., Hermann, V., and Castro, C. E. (2010). Regular versus irregular meshing for complicated models and their effect on synthetic seismograms. *Geophysical Journal International*, 183(2):1031–1051.

Penna, A., Cattari, S., Galasco, A., and Lagomarsino, S. (2004). Seismic assessment of masonry structures by non-linear macro-element analysis. In *IV International Seminar on Structural Analysis of Historical Construction-Possibilities of Numerical and Experimental Techniques*, volume 2, pages 1157–1164.

Perraud, Y., Chatzigogos, C. T., Meza-Fajardo, K. C., and Labbé, P. (2022). Effect of Rayleigh waves on seismic response of bridge pylons via Incremental Dynamic Analyses. *Soil Dynamics and Earthquake Engineering*, 152(4):1–17.

Perron, V., Gélis, C., Froment, B., Hollender, F., Bard, P.-Y., Cultrera, G., and Cushing, E. M. (2018a). Can broad-band earthquake site responses be predicted by the ambient noise spectral ratio? Insight from observations at two sedimentary basins. *Geophysical Journal International*, 215(2):1442–1454.

Perron, V., Hollender, F., Mariscal, A., Theodoulidis, N., Andreou, C., Bard, P.-Y., Cornou, C., Cottereau, R., Cushing, E. M., Frau, A., Hok, S., Konidaris, A., Langlaude, P., Laurendeau, A., Savvaidis, A., and Svay, A. (2018b). Accelerometer, velocimeter dense-array, and rotation sensor datasets from the sinaps@ postseismic survey (Cephalonia 2014-2015 aftershock sequence). *Seismological Research Letters*, 89(2A):678–687.

Pilz, M., Cotton, F., and Zhu, C. (2021). How much are sites affected by 2-D and 3-D site effects? A study based on single-station earthquake records and implications for ground motion modelling. *Geophysical Journal International*, 228(3):1992–2004.

Pilz, M., Parolai, S., Petrovic, B., Silacheva, N., Abakanov, T., Orunbaev, S., and Moldobekov, B. (2018). Basin-edge generated Rayleigh waves in the almaty basin and corresponding consequences for ground motion amplification. *Geophysical Journal International*, 213(1):301–316.

Pitilakis, K., Riga, E., Anastasiadis, A., and Makra, K. (2015). New Elastic Spectra, Site Amplification Factors and Aggravation Factors for Complex Subsurface Geology, Towards the Improvement of Ec8. In *6th International Conference on Earthquake Geotechnical Engineering*, number November, pages 1–20.

Poggi, V., Ermert, L., Burjanek, J., Michel, C., and Fäh, D. (2014). Modal analysis of 2-D sedimentary basin from frequency domain decomposition of ambient vibration array recordings. *Geophysical Journal International*, 200(1):615–626.

Poliotti, M., Bairán, J. M., and Möller, O. (2021). A variable order framework for 3D nonlinear analysis of reinforced concrete frames under general loading. *Engineering Structures*, 242:1–12.

Porter, K. A. (2003). An Overview of PEER's Performance-Based Earthquake Engineering Methodology. In *Ninth International Conference on Applications of Statistics and Probability in Civil Engineering (ICASP9) July 6-9, 2003, San Francisco*, pages 1–8.

Poudel, B., Özşahin, E., and Pekcan, G. (2022). Effect of Torsional Ground Motions on Floor Acceleration Response in Flexible SMRF Buildings. *Journal of Earthquake Engineering*, 26(4):2168–2185.

Poursartip, B., Fathi, A., and Tassoulas, J. L. (2020). Large-scale simulation of seismic wave motion: A review. *Soil Dynamics and Earthquake Engineering*, 129(December 2018):105909.

Psarropoulos, P. N., Tazoh, T., Gazetas, G., and Apostolou, M. (2007). Linear and nonlinear valley amplification effects on seismic ground motion. *Soils and Foundations*, 47(5):857–871.

Rahat Dahmardeh, S., Motamedi, M., and Aziminejad, A. (2020). A study on the effects of torsional component of ground motions on seismic response of low- and mid-rise buildings. *Structural Design of Tall and Special Buildings*, 29(4):1–25.

Rathje, E. M. and Saygili, G. (2008). Probabilistic Seismic Hazard Analysis for the Sliding Displacement of Slopes: Scalar and Vector Approaches. *Journal of Geotechnical and Geoenvironmental Engineering*, 134(6):804–814.

Riaño, A. C., Reyes, J. C., Yamín, L. E., Bielak, J., Taborda, R., and Restrepo, D. (2020). Integration of 3d large-scale earthquake simulations into the assessment of the seismic risk of bogota, colombia. *Earthquake Engineering & Structural Dynamics*, 50(1):155–176.

Riaño, A. C. and Lopez-Caballero, F. (2021). Development of a multi-tool virtual site for a benchmark on nonlinear site response analysis. Deliverable 2. Technical report, SIGMA2, Research and Development Program on Seismic Ground Motion.

Riga, E., Makra, K., and Pitilakis, K. (2016). Aggravation factors for seismic response of sedimentary basins: A code-oriented parametric study. *Soil Dynamics and Earthquake Engineering*, 91(9):116–132.

Riga, E., Makra, K., and Pitilakis, K. (2018). Investigation of the effects of sediments inhomogeneity and nonlinearity on aggravation factors for sedimentary basins. *Soil Dynamics and Earthquake Engineering*, 110(1):284–299.

Rigato, A. B. and Medina, R. A. (2007). Influence of angle of incidence on seismic demands for inelastic single-storey structures subjected to bi-directional ground motions. *Engineering Structures*, 29(10):2593–2601.

Rodríguez, J., Khan, S., Riyadh, M. M., Bruton, D., and Alam, M. S. (2022). Assessment of the seismic behavior of short-to-medium overall length girder bridges under asynchronous ground motions. *Soil Dynamics and Earthquake Engineering*, 162(7):107446.

Ruiz, J. A., Baumont, D., Bernard, P., and Berge-Thierry, C. (2011). Modelling directivity of strong ground motion with a fractal, k^{-2}, kinematic source model. *Geophysical Journal International*, 186(1):226–244.

Ruiz, S. and Saragoni, G. R. (2009). Free vibration of soils during large earthquakes. *Soil Dynamics and Earthquake Engineering*, 29(1):1–16.

Saez, E., Lopez-Caballero, F., and Modaressi-Farahmand Razavi, A. (2008). Influence of nonlinear SSI on the seismic response of reinforced concrete multistory frames. *12th International Conference on Computer Methods and Advances in Geomechanics 2008*, 4(5):2766–2773.

Saez, E., Lopez-Caballero, F., and Modaressi-Farahmand-Razavi, A. (2011). Effect of the inelastic dynamic soil-structure interaction on the seismic vulnerability assessment. *Structural Safety*, 33(1):51–63.

Salami, M. R., Kashani, M. M., and Goda, K. (2019). Influence of advanced structural modeling technique, mainshock-aftershock sequences, and ground-motion types on seismic fragility of low-rise RC structures. *Soil Dynamics and Earthquake Engineering*, 117(6):263–279.

Salichon, J., Kohrs-Sansorny, C., Bertrand, E., and Courboulex, F. (2010). A Mw 6.3 earthquake scenario in the city of Nice (southeast France): Ground motion simulations. *Journal of Seismology*, 14(3):523–541.

Sanchez-Sesma, F. J. (1983). Diffraction of elastic waves by three-dimensional surface irregularities. *Bulletin of the Seismological Society of America*, 73(6):1621–1636.

Sanchez-Sesma, F. J. (1987). Site effects on strong ground motion. *Soil Dynamics and Earthquake Engineering*, 6(2):124–132.

Sanchez-Sesma, F. J. and Luzon, F. (1995). Seismic response of three-dimensional alluvial valleys for incident P,S, and Rayleigh waves. *Bulletin of the Seismological Society of America*, 85(1):269–284.

Sbaa, S., Hollender, F., Perron, V., Imtiaz, A., Bard, P.-Y., Mariscal, A., Cochard, A., and Dujardin, A. (2017). Analysis of rotation sensor data from the SINAPS@ Kefalonia (Greece) post-seismic experiment—link to surface geology and wavefield characteristics. *Earth, Planets and Space*, 69(1):124.

Schmidt, R. O. (1986). Multiple emitter location and signal parameter estimation. *IEEE Transactions on Antennas and Propagation*, 34(3):190–194.

Semblat, J. and Pecker, A. (2009). *Waves and vibrations in soils: Earthquakes, Traffic, Shocks, Construction works*. IUSS Press.

Semblat, J. F., Kham, A., Parara, E., Bard, P.-y., Pitilakis, K., Makra, K., and Raptakis, D. (2009). Seismic wave amplification : Basin geometry vs soil layering. *Soil Dynamics and Earthquake Engineering*, 25(7):529–538.

Semblat, J. F., Lokmane, N., Driad-Lebeau, L., and Bonnet, G. (2010). Local amplification of deep mining induced vibrations part.2: Simulation of ground motion in a coal basin. *Soil Dynamics and Earthquake Engineering*, 30(10):947–957.

Semblat, J.-F., Paolucci, R., and Duval, A.-M. (2003). Simplified vibratory characterization of alluvial basins. *Comptes Rendus Geoscience*, 335(4):365–370.

Seylabi, E., Restrepo, D., Taborda, R., and Asimaki, D. (2021). Deterministic ground motion simulations with shallow crust nonlinearity at Garner Valley in Southern California. *Earthquake Engineering and Structural Dynamics*, 50(1):43–59.

Shahi, S. K. and Baker, J. W. (2014). NGA-West2 models for ground motion directionality. *Earthquake Spectra*, 30(3):1285–1300.

Shearer, P. M. (1999). *Introduction to Seismology*. Cambridge University Press.

Shen, J., Ren, X., and Chen, J. (2021). Effects of spatial variability of ground motions on collapse behaviour of buildings. *Soil Dynamics and Earthquake Engineering*, 144(1):106668.

Smerzini, C., Paolucci, R., and Stupazzini, M. (2009). Experimental and numerical results on earthquake-induced rotational ground motions. *Journal of Earthquake Engineering*, 13(1 SUPPL. 1):66–82.

Smerzini, C., Paolucci, R., and Stupazzini, M. (2011). Comparison of 3D, 2D and 1D numerical approaches to predict long period earthquake ground motion in the Gubbio plain, Central Italy. *Bulletin of Earthquake Engineering*, 9(6):2007–2029.

Smerzini, C., Vanini, M., Paolucci, R., Renault, P., and Traversa, P. (2022). Regional physics-based simulation of ground motion within the Rhône Valley, France, during the MW 4.9 2019 Le Teil earthquake. *Bulletin of Earthquake Engineering*, (0123456789).

Sohrabi-Bidar, A., Kamalian, M., and Jafari, M. K. (2010). Seismic response of 3-D Gaussian-shaped valleys to vertically propagating incident waves. *Geophysical Journal International*, 183(3):1429–1442.

Sollberger, D., Greenhalgh, S. A., Schmelzbach, C., Van Renterghem, C., and Robertsson, J. O. (2018). 6-C polarization analysis using point measurements of translational and rotational ground-motion: Theory and applications. *Geophysical Journal International*, 213(1):77–97.

Sollberger, D., Igel, H., Schmelzbach, C., Edme, P., van Manen, D. J., Bernauer, F., Yuan, S., Wassermann, J., Schreiber, U., and Robertsson, J. O. (2020). Seismological processing of six degree-of-freedom ground-motion data. *Sensors (Switzerland)*, 20(23):1–32.

Spacone, E., Filippou, F. C., and Taucer, F. F. (1996). Fibre beam-column model for non-linear analysis of R/C frames : Part I. Formulation. *Earthquake Engineering & Structural Dynamics*, 25:711–725.

Stambouli, A., Zendagui, D., Bard, P.-Y., and Derras, B. (2017). Deriving amplification factors from simple site parameters using generalized regression neural networks: Implications for relevant site proxies. *Earth, Planets and Space*, 69(1).

Stambouli, A. B., Bard, P.-y., Chaljub, E., Kristek, J., Stripajová, S., Durand, C., Zendagui, D., and Derras, B. (2018). 2D / 1D Aggravation Factors : From a Comprehensive Study To Estimation With a Neural Network Model. In *16lth European Conference of Earthquake Engineering*, pages 1–12.

Stambouli, A. B., Zendagui, D., Bard, P.-Y., and Dif, H. (2021). Influence of site parameters on fourier amplification application for 1d linear viscoelastic method. *Periodica Polytechnica Civil Engineering*, 65(1):229–241.

Stewart, J. P., Chiou, S. J., Bray, J. D., Graves, R. W., Somerville, P. G., and Abrahamson, N. A. (2002). Ground motion evaluation procedures for performance-based design. *Soil Dynamics and Earthquake Engineering*, 22(9-12):765–772.

Stocchi, A. and Richard, B. (2019). Sensitivity of engineering demand parameters as a function of structural typology and assessment method. *Nuclear Engineering and Design*, 343:151–165.

Stockwell, R. G., Mansinha, L., and Lowe, R. P. (1996). Localization of the complex spectrum: The S transform. *IEEE Transactions on Signal Processing*, 44(4):998–1001.

Stupazzini, M., De La Puente, J., Smerzini, C., Käser, M., Igel, H., and Castellani, A. (2009a). Study of rotational ground motion in the near-field region. *Bulletin of the Seismological Society of America*, 99(2 B):1271–1286.

Stupazzini, M., Paolucci, R., and Igel, H. (2009b). Near-fault earthquake ground-motion simulation in the Grenoble Valley by a high-performance spectral element code. *Bulletin of the Seismological Society of America*, 99(1):286–301.

Svay, A., Perron, V., Imtiaz, A., Zentner, I., Cottereau, R., Clouteau, D., Bard, P. Y., Hollender, F., and Lopez-Caballero, F. (2017). Spatial coherency analysis of seismic ground motions from a rock site dense array implemented during the Kefalonia 2014 aftershock sequence. *Earthquake Engineering and Structural Dynamics*, 46(12):1895–1917.

Taborda, R. and Bielak, J. (2014). Ground-motion simulation and validation of the 2008 Chino Hills, California, earthquake using different velocity models. *Bulletin of the Seismological Society of America*, 104(4):1876–1898.

Taborda, R. and Roten, D. (2015). Physics-based ground-motion simulation. In Beer, M., Kougioumtzoglou, I. A., Patelli, E., and Au, S.-K., editors, *Encyclopedia of Earthquake Engineering*, pages 1898–1926. Springer Berlin Heidelberg, Berlin, Heidelberg.

Takemura, S., Akatsu, M., Masuda, K., Kajikawa, K., and Yoshimoto, K. (2015). Long-period ground motions in a laterally inhomogeneous large sedimentary basin: Observations and model simulations of long-period surface waves in the northern Kanto basin, Japan. *Earth, Planets and Space*, 67(1):1–17.

Tan, B., Wang, H., Wang, X., Yi, S., Zhou, J., Ma, C., and Dai, X. (2022). The study of early human settlement preference and settlement prediction in Xinjiang, China. *Scientific Reports*, 12(1):1–18.

Tarbali, K., Bradley, B., Huang, J., Lee, R., Lagrava, D., Bae, S., Polak, V., Motha, J., and Zhu, M. (2019). Cybershake nz v18.5: New zealand simulation-based probabilistic seismic hazard analysis. In *Earthquake Geotechnical Engineering for Protection and Development of Environment and Constructions- Proceedings of the 7th International Conference on Earthquake Geotechnical Engineering, 2019*, pages 1–8.

Tarbali, K., Bradley, B. A., and Baker, J. W. (2018). Consideration and propagation of ground motion selection epistemic uncertainties to seismic performance metrics. *Earthquake Spectra*, 34(2):587–610.

Tchawe, F. N., Gelis, C., Bonilla, L. F., and Lopez-Caballero, F. (2021). Effects of 2-D random velocity perturbations on 2-D SH short-period ground motion simulations in the basin of Nice, France. *Geophysical Journal International*, 226(2):847–861.

Thompson, E. M., Baise, L. G., Tanaka, Y., and Kayen, R. E. (2012). A taxonomy of site response complexity. *Soil Dynamics and Earthquake Engineering*, 41:32–43.

Tokimatsu, K. (1997). Geotechnical site characterization using surface waves. In *Earthquake Geotechnical Engineering: Proceedings of IS-Tokyo'95, The First International Conference on Earthquake Geotechnical Engineering, Rotterdam*, pages 1333–136. AA Balkema.

Torrence, C. and Compo, G. P. (1998). A Practical Guide to Wavelet Analysis. *Bulletin of the American Meteorological Society*, 79(1):61–78.

Tothong, P. and Luco, N. (2007). Probabilistic seismic demand analysis using advanced ground motion intensity measures. *Earthquake Engineering & Structural Dynamics*, 36(056):1837–1860.

Touhami, S. (2020). *Numerical modeling of seismic field and soil interaction : application to the sedimentary basin of Argostoli (Greece)*. PhD thesis, Université Paris-Saclay.

Touhami, S., Gatti, F., Lopez-Caballero, F., Cottereau, R., de Abreu Corrêa, L., Aubry, L., and Clouteau, D. (2022). SEM3D: A 3D High-Fidelity Numerical Earthquake Simulator for Broadband (0–10 Hz) Seismic Response Prediction at a Regional Scale. *Geosciences (Switzerland)*, 12(3):0–27.

Trifunac, M. D. (1971). Surface motion of a semi-cylindrical alluvial valley for incident plane SH waves . *Bulletin of the Seismological Society of America*, 61(6):1755–1770.

Trifunac, M. D. (2006). *Effects of Torsional and Rocking Excitations on the Response of Structures*, pages 569–582. Springer Berlin Heidelberg, Berlin, Heidelberg.

Trifunac, M. D. (2012). Earthquake response spectra for performance based design-A critical review. *Soil Dynamics and Earthquake Engineering*, 37:73–83.

Trifunac, M. D. and Brady, A. G. (1976). Correlations of peak acceleration, velocity and displacement with earthquake magnitude, distance and site conditions. *Earthquake Engineering & Structural Dynamics*, 4(5):455–471.

Tsuno, S., Noyori, M., and Yamanaka, H. (2022). Azimuthal dependence on amplifications for long-period ground motions propagating in the Kanto Basin, Japan. *Journal of Seismology*, 26(2):373–385.

Udias, A., Madariaga, R., and Buforn, E. (2013). Source mechanisms of earthquakes: Theory and practice. *Source Mechanisms of Earthquakes: Theory and Practice*, pages 1–302.

Vamvatsikos, D. (2015). Analytic fragility and limit states [p(edp|im)]: Nonlinear dynamic procedures. In Beer, M., Kougioumtzoglou, I. A., Patelli, E., and Au, S.-K., editors, *Encyclopedia of Earthquake Engineering*, pages 87–94. Springer Berlin Heidelberg, Berlin, Heidelberg.

Vicencio, F. and Alexander, N. A. (2019). A parametric study on the effect of rotational ground motions on building structural responses. *Soil Dynamics and Earthquake Engineering*, 118(January):191–206.

Vicencio, F. and Alexander, N. A. (2021). Method to evaluate the dynamic structure-soil-structure interaction of 3-D buildings arrangement due to seismic excitation. *Soil Dynamics and Earthquake Engineering*, 141(1):106494.

Viens, L. and Denolle, M. A. (2019). Long-period ground motions from past and virtual megathrust earthquakes along the nankai trough, Japan. *Bulletin of the Seismological Society of America*, 109(4):1312–1330.

Wang, P., Han, Q., and Du, X. (2014). Seismic performance of circular RC bridge columns with flexure-torsion interaction. *Soil Dynamics and Earthquake Engineering*, 66:13–30.

Wills, C. J., Petersen, M., Bryant, W. A., Reichle, M., Saucedo, G. J., Tan, S., Taylor, G., and Treiman, J. (2000). A site-conditions map for California based on geology and shear-wave velocity. *Bulletin of the Seismological Society of America*, 90(6 SUPPL.):187–208.

Wirth, E. A., Vidale, J. E., Frankel, A. D., Pratt, T. L., Marafi, N. A., Thompson, M., and Stephenson, W. J. (2019). Source-Dependent Amplification of Earthquake Ground Motions in Deep Sedimentary Basins. *Geophysical Research Letters*, 46(12):6443–6450.

Wong, H. L. and Trifunac, M. D. (1974). Surface motion of a semi-elliptical alluvial valley for incident plane SH waves . *Bulletin of the Seismological Society of America*, 64(5):1389–1408.

Woodhouse, J. (1974). Surface waves in a laterally varying layered structure. *Geophysical Journal International*, 37(3):461–490.

Xu, J., Bielak, J., Ghattas, O., and Wang, J. (2003). Three-dimensional nonlinear seismic ground motion modeling in basins. *Physics of the earth and planetary interiors*, 137(1-4):81–95.

Yang, D., Pan, J., and Li, G. (2010). Interstory drift ratio of building structures subjected to near-fault ground motions based on generalized drift spectral analysis. *Soil Dynamics and Earthquake Engineering*, 30(11):1182–1197.

Yoshimoto, K. and Takemura, S. (2014). Surface wave excitation at the northern edge of the Kanto Basin, Japan. *Earth, Planets and Space*, 66(1):1–7.

Zalachoris, G. and Rathje, E. M. (2015). Evaluation of One-Dimensional Site Response Techniques Using Borehole Arrays. *Journal of Geotechnical and Geoenvironmental Engineering*, 141(12):1–15.

Zentner, I. (2014). A procedure for simulating synthetic accelerograms compatible with correlated and conditional probabilistic response spectra. *Soil Dynamics and Earthquake Engineering*, 63:226–233.

Zentner, I. (2017). A general framework for the estimation of analytical fragility functions based on multivariate probability distributions. *Structural Safety*, 64:54–61.

Zerva, A. and Zhang, O. (1996). Estimation of signal characteristics in seismic ground motions. *Probabilistic Engineering Mechanics*, 11(1):229–242.

Zhang, L., Wang, J. T., Xu, Y. J., He, C. H., and Zhang, C. H. (2020). A procedure for 3D seismic simulation from rupture to structures by coupling SEM and FEM. *Bulletin of the Seismological Society of America*, 110(3):1134–1148.

Zhang, W. and Taciroglu, E. (2021). 3D time-domain nonlinear analysis of soil-structure systems subjected to obliquely incident SV waves in layered soil media. *Earthquake Engineering and Structural Dynamics*, 50(8):2156–2173.

Zhu, C., Chávez-García, F. J., Thambiratnam, D., and Gallage, C. (2018). Quantifying the edge-induced seismic aggravation in shallow basins relative to the 1D SH modelling. *Soil Dynamics and Earthquake Engineering*, 115(11):402–412.

Zhu, C., Riga, E., Pitilakis, K., Zhang, J., and Thambiratnam, D. (2020). Seismic Aggravation in Shallow Basins in Addition to One-dimensional Site Amplification. *Journal of Earthquake Engineering*, 24(9):1477–1499.

Zhu, C. and Thambiratnam, D. (2016). Interaction of geometry and mechanical property of trapezoidal sedimentary basins with incident SH waves. *Bulletin of Earthquake Engineering*, 14(11):2977–3002.

Zhu, C., Thambiratnam, D. P., and Zhang, J. (2016). Response of sedimentary basin to obliquely incident SH waves. *Bulletin of Earthquake Engineering*, 14(3):647–671.

Zoeppritz, K. (1919). On reflection and transmission of seismic waves by surfaces of discontinuity. *Nachrichten von der Königlichen Gesellschaft der Wissenschaften zu Göttingen, Mathematisch-physikalische Klasse*, 48(1):66–84.

Zuchowski, L., Brun, M., and De Martin, F. (2018). Co-simulation coupling spectral/finite elements for 3D soil/structure interaction problems. *Comptes Rendus - Mecanique*, 346(5):408–422.

Çelebi, M., Okawa, I., Kashima, T., Koyama, S., and Iiba, M. (2014). Response of a tall building far from the epicenter of the 11 march 2011 m 9.0 great east japan earthquake and aftershocks. *The structural design of tall and special buildings*, 23(6):427–441.